Optical Spectroscopy And Ab-Initio Study On Biocompatible Nanohybrids For Their Potential Biomedical And Environmental Applications

THESIS

SUBMITTED FOR THE DEGREE OF

DOCTOR OF PHILOSOPHY (SCIENCE)

IN

NANOSCIENCE AND NANOTECHNOLOGY

BY

MD NUR HASAN

CENTRE FOR RESEARCH IN NANOSCIENCE AND NANOTECHNOLOGY

UNIVERSITY OF CALCUTTA

2023

This Thesis is dedicated to My Family

For their Endless Love, Support and Encouragement

Acknowledgements

First and foremost, I owe my sincere and humble gratitude to my enthusiastic supervisor Professor Samir Kumar Pal, for providing me the opportunity to work under his supervision. I am very grateful for his constant motivation, belief in my capabilities, and persistent availability to clarify my doubts despite his extremely busy schedule. His immense knowledge in the multidisciplinary field of science and technology, commitment to the highest scientific standards, and unconditional support during crises, taken together make him an exemplary mentor. I feel to be fortunate enough to learn from his instrumental expertise and detailed insight into various experimental problems. This thesis would not have been possible without his thoughtful guidance, warm encouragement, unconditional support, constructive criticism with simultaneous allocation to express my ideas to work independently and his inexhaustible help. He has given me with many opportunities to improve my scientific knowledge, allowing me to explore new areas of research, and to interact several talented researchers from various parts of the globe. His positive vibes, everlasting energy, disciplined nature, great leadership quality and enduring willingness for learning motivate me substantially and thank you very much Sir for inspiring me to believe in my dreams.

I would like to express my deepest gratitude to my associate supervisor Dr. Debjani Karmakar for allowing me to learn under her supervision. I feel to be fortunate to learn the details of the computational calculation and to deal with the different perspectives of the problem, from her. Especially grateful for her constant availability, great interest and numerous helpful discussions for my work. She has provided me with many opportunities to gain scientific experience, allowing me to explore new areas of research, and interact and collaborate with talented researchers from many different national and international institutes.

I am grateful to get the opportunity to actively work with talented researchers from various parts of the globe. I would like to thank Prof. Dr. Saleh A. Ahmed, Umm Al-Qura University, Makkah, Saudi Arabia, Prof. Dr. Ranjan Das, West Bengal State University, Prof. Dr. Olle Eriksson, Uppsala University, Sweden, Prof. Dr. Dipankar Das Sarma, IISc Bangalore, India, Prof. Dr. Tanusri Saha-dasgupta, Director, S. N. Bose National Centre for Basic Sciences, India, Dr. Arpita Chattopadhyay, Techno International, Kolkata, India, Prof. Dr. Anna Delin, KTH Royal, Sweden, Prof. Dr. Mala Mitra, Sister Nivedita University, Kolkata, India, Prof. Dr. K. V. Adarsh, IISER, Bhopal, India, Dr. Patrik Thunström, Uppsala University, Sweden, Dr. Goutam Sheet, IISER, Mohali, India, Dr. Manuel Pereiro, Uppsala University, Sweden, Prof. Dr. Peter Lemmens and Dr. Dirk Wulferding, Institute for Condensed Matter Physics, Braunschweig, Germany, Dr. Tatini Rakshit, Shiv Nadar University, Greater Noida, India, Prof. Dr. Chinmoy Bhattacharya, IIEST, Howrah, India.

I express my gratitude to all the faculty members and the staff of S. N. Bose National Centre for Basic Sciences for their assistance in my research career. A sincere appreciation goes to all other non-academic staff and gardeners of SNBNCBS who have actively maintained the magnificent ambiance of the centre. I would like to give special thanks to all technical cell members (Joy Da, Shakti Da, Amit Da, Samik Da, Urmi Di, and Dipayan Da) for their help during performing different experiments. I acknowledge the Council of Scientific & Industrial Research for providing the fellowship, and SNBNCBS for providing a good research atmosphere and such a beautiful and green campus. I would like to thank SERB for funding me Psi-k conference (EPFL, Switzerland). Also, I pay tribute to all my teachers throughout my life. It was them, who kept faith in me first.

I'd like to express my sincere thanks to all my seniors and colleagues for providing a stimulating and enriching environment. Special thanks to Dr. Tuhin Kumar Maji for holding my hand at the initial stage of my

research work. I am grateful to Dr. Damayanti Bagchi for helping me with the experiments related to biology. I am also thankful to Nivedita, Lopa di and Amrita for their assistance in formatting and proof-reading of my thesis. My sincere appreciation goes to all my seniors: Dr. Tuhin Kumar Maji, Dr. Arka Chatterjee, Dr. Damayanti Bagchi, Dr. Priya Singh, Dr. Jayita Patwari, Dr. Anirudhha Adhikari, Dr. Soumendra Singh, Dr. Animesh Halder, Dr. Pritam Biswas, Dr. Tatini Rakshit, Dr. Gulmi Chakraborty, Dr. Soumendra Darbar, Dr. Probir Kumar Sarkar, Dr. Tanushree Dutta, and all the present group members: Dipanjan, Arpan, Nivedita, Ria, Susmita, Neha, Amrita, Lopa Di and Monojit Da for providing a homely and a cheerful environment as well as assisting me in research. My appreciation goes to other past members of my group; Deepsikha, Alisha, Debanjana, Harmit, Rajdeep, Aman, Manali, Mahasweta, Debdatta, Nairika and Nairit. A very special thanks to Arka da, Dipanjan and Arpan who have been a source of oxygen for me in the lab. I shared many glorious moments over a long period and will always miss their company in the future. I also want to thank all my friends for the good times, I shared with them.

I wanted to take a moment to express my sincere appreciation to Saswati Madam for her kind affection, good wishes and several times she has graciously prepared wonderful dinners for us. Your culinary skills never cease to amaze me, and the flavours of the dishes were simply outstanding. It is truly exceptional and I feel incredibly fortunate to have had the opportunity to enjoy the precious time with you. I want to express my deepest gratitude for the effort and dedication you put during my Ph.D. journey.

Finally, I would like to pay high regard to my family and all of my relatives for their love, affection, praise, and good wishes. Especially, I would like to thank my father who sacrificed his happiness for my education and always provide moral support. Without the enormous sacrifices of my Father and mother, encouragement and support from my elder sisters, brothers, brother-in-law and sister-in-law, and their blessing, this thesis would not have acquired its shape. I hereby acknowledge and thank all those who directly or indirectly supported me in this mesmerizing venture.

Finally, I would like to thank everybody who played an important role throughout my journey. I apologize if I missed anyone, who has helped me through these testing years.

Dated:
Department of Chemical and Biological Sciences,
S. N. Bose National Centre for Basic Sciences,
Salt Lake, Kolkata 700106, India *(Md Nur Hasan)*

CONTENTS

Chapter 1: Introduction

Chapter 2: An Overview of Experimental Techniques and Systems

Chapter 3: Instrumentation and Sample Preparation

Chapter 1

Introduction

1.1. Background:

Over the past two decades, there has been a significant technological advancement that has led to revolutionary breakthroughs in the field of medical diagnosis. This has made it easier to detect diseases at an early stage. Despite this, conventional therapeutics seem to be inadequate in overcoming many life-threatening illnesses. [1, 2]. A concerning problem in the healthcare industry is the emergence of drug resistance, which occurs when medicines become less effective in treating diseases, particularly bacterial infections, and cancer. Drug resistance begins when there is a mutation in the target protein site of the affected cells [3, 4]. The pharmaceutical industry and the Governments have not been working together to combat the problem of drug resistance. Additionally, the natural ability of microbes to develop resistance at a faster rate than the creation of new drugs [5], implies that current methods of developing effective and lasting anti-microbial treatments are likely to fail in the long run. One of the most significant threats to public health in the 21st century is the development of drug resistance in pathogenic microorganisms [6], suggesting the urgency of alternative therapeutic strategies. The invention of smart functional materials possessing target-specific action instigated through external stimuli (such as light, pH, ions, etc.) could be considered as an effective substitute for conventional drugs, and evaluation of such materials in terms of fabrication, characterization and application, should be considered as an impactful new-age research topic.

On the other hand, two significant challenges confronted in the 21st century are the increasing need for energy and its ecological consequences [7]. Fossil fuel has been

predominantly utilized as a primary energy source for decades [8]. However, the accessibility of non-renewable energy sources is declining with time and the burning of such fuels is resulting in environmental contamination due to the discharge of harmful greenhouse gases [9]. Therefore, there is a growing interest in developing strategies for utilizing diverse green and renewable energy sources as sustainable solutions to meet the energy demand. Solar radiation is deemed as the primary green and renewable energy source among others, owing to its consistent and abundant existence on the Earth's surface [10]. The amount of solar power reaching the Earth's crust is approximately $1.2x10^5$ terawatts which is 10^4 times greater than the world's energy consumption [11]. Nevertheless, existing light-harvesting technologies rely on wide bandgap semiconductors that are inadequate for capturing low-energy photons [12, 13]. Hence, it is imperative to develop solar technologies that can effectively harness solar radiation. Moreover, monitoring environmental pollution and designing technologies to restore it are crucial steps toward achieving sustainable solutions to environmental degradation.

1.2. Nanomaterials:

nanomaterials are considered systems in which at least half of the particles in terms of number have at least one dimension between 1 and 100 nm [14]. Sometimes, the term is used to describe particles of larger sizes of up to 500 nm, or fibers and tubes that have dimensions less than 100 nm in only two directions. However, for metal particles smaller than 1 nm, are typically referred to as atom clusters instead [15]. Nanoparticles are commonly differentiated from microparticles (1-1000 μm), "fine particles" (ranging from 100 to 2500 nm), and "coarse particles" (ranging from 2500 to 10,000 nm) due to their smaller size, which gives rise to distinct physical and chemical properties. These properties include colloidal characteristics, ultrafast optical effects and electric properties [16]. Due to their significantly smaller size compared to the wavelengths of visible light (400-700 nm), nanoparticles are not visible through standard optical microscopes. Instead, electron microscopes are

needed for their visualization. This size difference also affects the behavior of nanoparticle dispersions in transparent media, as they can remain transparent, unlike suspensions of larger particles which typically scatter visible light. Moreover, nanoparticles can readily pass through commonly used filters like ceramic candles, necessitating the use of specialized nanofiltration techniques for liquid separation.

Typically, nanoparticles have a reduced concentration of point defects compared to their larger counterparts in bulk materials. However, they can still exhibit various dislocations mechanics due to their unique surface structures. Consequently, their mechanical properties differ from those of bulk materials. Moreover, non-spherical nanoparticles, such as prisms, cubes, and rods, showcase properties that are dependent on their shape and size, both in terms of chemical and physical aspects, resulting in anisotropic characteristics [17]. The attractive optical properties of non-spherical nanoparticles made of gold (Au), silver (Ag), and platinum (Pt) are leading to their wide range of applications. The unique geometries of these non-spherical nanoparticles result in increased effective cross-sections and more intense colors in colloidal solutions. The ability to adjust the resonance wavelengths by modifying the particle geometry makes them suitable for various purposes, including molecular labeling, biomolecular assays, trace metal detection, and nano technological applications [18]. Under unpolarized light, anisotropic nanoparticles exhibit a unique absorption behavior and random orientation of particles. This characteristic arises from continuous advancements in the synthesis of these nanoparticles, allowing for their efficient preparation in high quantities on a daily basis.

1.3. An Overview of Nanohybrids:

Nanohybrids are a type of nanomaterial that consist of two or more components, each with nanoscale dimensions, that are combined in order to create a new material with unique properties [19] which are different from its counterparts. The different

components can be organic or inorganic and can be in the form of nanoparticles, nanowires, nanotubes, or other nanostructures. The term "nanohybrid" is often used interchangeably with "nanocomposite", which is a broader term that includes any composite material containing nanoscale components. However, nanohybrids typically refer to materials where the components have distinct and separate functions, whereas nanocomposites may have more homogeneous properties. The field of hybrid materials is relatively new but already it has an immense impact on material science; they are anticipated to provide a strong impact in the field of design and development of new materials [20]. A reduction of the constituent dimensions of the hybrid system down to the molecular scale makes it possible to tune the material properties preciously [21, 22]. The molecular-level interaction at the surface or interface between the two constituents can produce novel properties of the hybrid material and thus can improve their activities compared to their pristine [23]. Depending on molecular interaction and parent constituent nanohybrid can be categorized into different categories. In terms of the possible interaction, connecting two species, a hybrid system can be classified into two categories: *Class I* hybrid materials are those that show weak non-covalent interactions between the two phases, such as van der Waals (vdW), hydrogen bonding, or weak electrostatic interactions. In contrast, *Class II* materials are those which show strong covalent interactions between two constituents [24]. The properties of the hybrid system are highly dependent on the strength of the interaction between the two constituents. Apart from bond strength depending upon the nature of two-parent counterparts of hybrid materials, there are several different classes of nanohybrids, each with their unique characteristics and potential applications:

1.3.1. Inorganic-organic Nanohybrids: Inorganic-organic nanohybrids are a class of nanomaterials that combine inorganic and organic components at the nanoscale [25]. These hybrid materials can exhibit unique properties that arise from the

combination of the different components. Inorganic components typically include metals, metal oxides, and ceramics, while organic components can include organic ligands, dyes, and surfactants. There are several methods for synthesizing inorganic-organic nanohybrids, including sol-gel processes, co-precipitation, and self-assembly. The combination of inorganic and organic components can provide enhanced mechanical, thermal, and chemical stability, as well as increased surface area and tunable electronic properties.

1.3.2. Inorganic-inorganic Nanohybrids: Inorganic-inorganic nanohybrids are a type of nanomaterial that consist of two or more inorganic components integrated at the nanoscale [26]. These hybrid materials can exhibit new or enhanced properties that arise from the synergistic interactions between the components. They have a wide range of applications in the field of catalysis, sensing, energy storage, and environmental remediation. For example, they can be used as photocatalysts for water splitting, as electrodes for supercapacitors, or as adsorbents for heavy metal ions. Inorganic-inorganic nanohybrids can also exhibit enhanced mechanical and thermal properties and high surface area, which make them promising materials for energy conversion and storage applications.

1.3.3. Organic-organic Nanohybrids: Organic-organic nanohybrids consist of two or more organic components integrated at the nanoscale [27]. Electrostatic interactions involve the attraction between positively and negatively charged components. They can be used as drug delivery vehicles, where the combination of different organic components can provide enhanced biocompatibility, drug loading capacity, and controlled drug release. They can also be used as sensors, where the combination of different organic components can provide enhanced selectivity and sensitivity.

1.3.4. Carbon-based Nanohybrids: This class of nanohybrids consists of carbon-based materials, such as graphene, carbon nanotubes, or nanodiamonds, combined

with other materials [28]. These materials have unique electrical, mechanical, and thermal properties and have the potential to be used in a wide range of applications, including energy storage, optoelectronics, and nanomedicine.

1.3.5. Polymer Based Nanohybrids: This class of nanohybrids consists of two or more types of nanoparticles combined in a matrix material, such as a polymer or ceramic [29]. These materials have the potential to be used in a variety of applications, including structural materials, sensing, and drug delivery.

However, among all, the most common type of hybrid material is the inorganic-organic hybrid system [30]. They have a wide diversity of potentialities to introduce novel structural designs in material sciences [31-33]. Combining inorganic and organic components allows for the creation of materials with improved or entirely new properties, such as enhanced mechanical strength, thermal stability, conductivity, and optical properties. They can be designed to exhibit specific functionalities by carefully selecting and controlling the composition and arrangement of the components. The combination of inorganic and organic components often results in synergistic effects, where the hybrid system exhibits properties superior to its components. They offer a wide range of possibilities for material design and synthesis. They can be tailored at the molecular level, enabling precise control over properties and functionalities. They can bridge the gap between traditionally incompatible materials, allowing for the integration of different materials into a single system [34]. They can contribute to sustainability efforts by improving the efficiency and performance of energy storage devices, such as batteries and supercapacitors. Additionally, the combination of organic components with inorganic materials can provide biocompatibility, making them suitable for biomedical applications with potential environmental benefits.

The challenges associated with nanohybrids, include controlling the size and morphology of the hybrid particles, ensuring good dispersion of the components,

good efficiency, and avoiding unwanted interactions between the components. Additionally, there may be concerns about the potential toxicity of the inorganic components, particularly in biomedical applications. Understanding the interactions between the components and their long-term stability and biocompatibility is essential for optimizing their properties and minimizing potential risks. Further research and development in the synthesis and characterization of nanohybrids will be essential to harness their full potential.

1.4. Applications of Nanohybrids: Biomedical Field and Environmental Remediation:

Hybrid materials represent a fundamentally interdisciplinary field of research and development connecting a variety of groups of material sciences such as hybrid interfaces, organometallics, colloids, soft matter, coordination polymers, metal-organic frameworks (MOFs), etc. [34]. Nanohybrid and heterostructure are contributing as emergent materials in different important fields including energy harvesting, healthcare and drug delivery, environment remedy, optoelectronics, supercapacitor, superconductor, sensing, optoelectronics, catalysis and surfaces, nanocomposites, nanoporous and mesoporous materials, sensing, biomedicine, biomaterials, biochemistry, and engineering materials, etc. [35-37] Another important aspect of nanohybrid material is the multifunctionality due to the synergistic effect of its two components. In recent years, nanohybrids have shown great potential in various fields of biomedical and environmental remediation. Some of their applications and potential problems are discussed below;

1.4.1. Biomedical Applications: *In drug delivery*, nanohybrids can be used to deliver drugs to specific cells or tissues, increasing efficacy and reducing side effects. However, the potential problem with this is the toxicity of the nanohybrid itself. *In tissue engineering*, nanohybrids can be used as scaffolds for tissue engineering, providing a suitable microenvironment for cells to grow and differentiate.

Nonetheless, there is a risk of toxicity and immune response when the nanohybrid comes in contact with living cells. *In diagnostic imaging*, when developing nanohybrids for diagnostic imaging, researchers take great care to ensure their safety. This involves a thorough evaluation of the nanohybrid's toxicity profile, biocompatibility, and potential long-term effects.

To minimize toxicity concerns, several strategies can be employed: *Surface modification*, the surface of nanohybrids can be modified with biocompatible coatings to improve their stability, reduce potential toxicity, and enhance their compatibility with the biological environment. *Biodegradability,* designing nanohybrids with biodegradable components allows for their gradual breakdown and elimination from the body over time, reducing long-term effects. *Size and shape control,* nanohybrids can be engineered to have specific sizes and shapes, which can influence their interactions with cells and tissues. Optimization of these parameters can minimize potential toxicity. *Rigorous testing,* nanohybrids undergo comprehensive toxicity assessments, including biocompatibility tests, cytotoxicity assays, and long-term animal studies, to evaluate their safety profile before clinical translation.

1.4.2. Environmental Applications: *In water treatment*, nanohybrids can be used to remove contaminants from water, such as heavy metals, organic pollutants, and pathogens. However, the potential problem is the release of nanoparticles into the environment, which can have harmful effects on aquatic organisms. *In air pollution control,* nanohybrids can be used to remove pollutants from the air, such as carbon dioxide, nitrogen oxides, and volatile organic compounds. Nonetheless, the potential problem is the release of nanoparticles into the atmosphere, which can have harmful effects on human health and the environment. *In soil remediation,* nanohybrids can be used to remove contaminants from soil, such as pesticides, herbicides, and heavy metals. However, it can have negative impacts on soil

organisms, such as earthworms and beneficial bacteria due to the long-term effects of the nanohybrid.

To mitigate the potential harmful effects, researchers and engineers focus on several strategies; *Nanoparticle stability*, the design and fabrication of nanohybrids aim to improve their stability and minimize the release of nanoparticles into the water. This can involve surface modifications, encapsulation techniques, or immobilization of nanoparticles onto solid supports to prevent their leaching. *Material selection,* the choice of nanomaterials for water treatment applications is crucial. Selecting materials that are inherently stable and less likely to release nanoparticles can minimize environmental risks. Additionally, biodegradable or environmentally kind nanomaterials can be utilized, which degrade over time without causing long-term harm. *System design and containment*, implementing well-designed water treatment systems with appropriate containment measures can help prevent the release of nanoparticles into the environment. Efficient filtration or separation techniques can be employed to remove and recover the nanohybrids after water treatment, minimizing the potential for environmental exposure.

1.5. Scope of the Optical Spectroscopic Studies for the Investigation of Hybrid Nanomaterials:

Optical spectroscopy is a powerful technique that has been widely used to investigate the properties of materials in the nanoscale. It measures the interaction of light with matter and provides information on the electronic and vibrational structure of materials [38]. By measuring the absorption and emission spectra of materials, researchers can determine the size, shape, and composition of the systems that make up the composite material. The absorption and emission spectra at different temperatures, researchers can investigate the energy transfer processes between the different nanomaterials and the influence of the surrounding environment. It can be used to study the surface plasmon resonance (SPR) of

nanohybrid materials. SPR is a phenomenon that occurs when light interacts with free electrons on the surface of a material, resulting in a resonance effect [39]. By measuring the SPR spectra of nanohybrid materials, researchers can investigate the surface properties of the composite material, such as surface charge density, surface roughness, and surface area. The optical properties of nanohybrid materials can be investigated by measuring the absorption and emission spectra at different wavelengths, researchers can determine the optical bandgap, exciton energy, and exciton binding energy of the composite material. Apart from that optical spectroscopy can also be used for sensing applications.

The scope of optical spectroscopic investigation on hybrid materials is vast and offers exciting possibilities for developing new materials with enhanced properties for various applications. This field contributes to advancements in diverse applications, including sensors, imaging, optoelectronics, and energy-related technologies. Continued research in optical spectroscopy of nanohybrid holds promise for the development of innovative materials and devices with improved functionalities and practical applications. So, there are lots of opportunities in optical spectroscopic studies on nanohybrid to investigate and develop new systems for enhanced multifunctional activity in various fields.

In one of our studies, by using optical spectroscopic techniques, we studied a new class of MOFs that constitute a significant class of hybrid inorganic-organic crystalline porous materials and its structures can be manipulated at the atomic scale by an appropriate choice of metal ions and organic ligands [40, 41]. The optical spectroscopic studies on mixed metal MOFs show enhanced thermal stability, water stability and pH-responsive dissolution characteristics. The mixed metal MOFs show significant antibacterial photodynamic therapeutic activity towards drug-resistant bacteria and they can also degrade model pollutant MB under white light illumination [42].

In one of our works, we have encapsulated rifampicin (RF), an antituberculosis drug [43] on the surface of ZIF8. The detailed characteristics and properties of ZIF8 and ZIF8-RF, have been performed in optical spectroscopic-based techniques [44]. The drug release profile experiment has been performed in UV-visible absorbance which demonstrates that ZIF8-RF carries on as pH-responsive drug delivery and is ideal for targeting bacterial disease. The spectroscopic investigation shows ZIF8 can effectively deliver phototherapeutic drugs into a bacterial infection site and significantly kill the infectious bacteria using antimicrobial photodynamic therapeutic strategies [45].

We have also synthesized norfloxacin (NF) functionalized ZnO-based (ZnO-NF) nanohybrid. The newly synthesized nanohybrid has been characterized using various microscopic and spectroscopic techniques. To investigate the optical spectroscopic properties of the systems, we have used UV-visible, steady-state fluorescence and picosecond resolved time correlated single photon counting (TCSPC) studies which demonstrate the efficient electron transfer from NF to ZnO nanoparticle. This enhances the reactive oxygen species (ROS) generation capability of the system. Thus, it shows tremendous antimicrobial activity that can be beneficial for manifold biomedical application purposes.

Since the ZnO-based hybrids nanomaterials are the most promising and encouraging system for the modulation of drug activity. The implementation of a dual-responsive mechanism could be a very useful technique to achieve enhanced efficacy in antibacterial photodynamic therapy (aPDT). Here, we study the fabrication of metal hybrid nanomaterials which is Au-decorated ZnO (Au_ZnO). The morphology and composition of the samples were characterized by several techniques including microscopic and optical spectroscopic. We encapsulated an antibacterial agent TC with Au_ZnO system to make a novel Au_ZnO-TC tri-hybrid [46]. The steady state photoluminescence and time-resolved fluorescence transient study demonstrate the FRET from TC to Au as well as charge transfer from TC to

ZnO in the Au_ZnO-TC tri-hybrid system. The investigation has suggested that the energy transfer from TC to Au nanoparticle triggers an enormous electron separation in the Au_ZnO-TC tri-hybrid system which enhanced the production of ROS in the presence of white light.

Light harvesting materials that capture solar photons and convert them for light-mediated applications are considered to be one of the ground breaking research in today's world [47, 48]. Different kind of semiconductor nanoparticle has been utilized to harvest solar light. However, widely used semiconducting metal oxides such as TiO_2 [13] and ZnO [12], can harvest only the ultraviolet portion of solar spectra which is ~4% of the full solar spectrum due to their large bandgap (TiO_2 (~3.2 eV) or ZnO (~3.37eV)). So it is highly required to design a nanomaterial that can harvest the NIR part of solar light. In one of our works, we have synthesized IR820 encapsulated ZIF-8 nano-MOF, characterized using various electron microscopic and optical spectroscopic techniques to confirm the formation of hybrid nanomaterials. The time-resolved fluorescence transient depicts the excited state charge transfer process from IR820 to ZIF-8 in functionalized nano-MOF [49]. It shows efficient NIR light-induced dose-dependent antibacterial activity due to enhanced ROS generation capability.

Chelation therapy is one of the most effective and widely accepted methods of treatment to reduce metal toxicity caused by an excess amount of essential metals. Chelating complexes can efficiently capture the targeted metal and can easily be excreted from the body. In this work, we have investigated the iron chelating property of curcumin through various optical spectroscopic tools by synthesizing and characterizing the iron–curcumin complex [50].

The experimental tools used for studying the dynamical processes involved are picosecond-resolved carrier relaxation dynamics such as photoinduced electron transfer (PET) [51] and FRET [52, 53]. Different experimental techniques have been

employed for the structural and functional characterization of the hybrid materials such as steady-state UV-vis absorption and fluorescence, thermogravimetric analysis (TGA), Fourier transform infrared spectroscopy (FTIR), Raman scattering, dynamic light scattering (DLS), powder X-Ray diffraction (XRD), field emission scanning electron microscopy (FESEM) and high-resolution transmission electron microscopy (HRTEM).

1.6. Scope of the Computational Investigation on Nanomaterials:

Ab-initio studies have become an essential part of the field of material science, engineering, physics, biology, chemistry and many other fields. The scope of computational studies is vast and continuously expanding with new applications emerging regularly [54]. It has been used in the development of advanced materials [55], the behavior of particles and systems at the atomic and molecular levels. The unique benefit of ab-initio modeling lies in the possibility to calculate the macroscopic properties of materials based on calculations of microscopic quantities. In the last few decades, many experimental phenomena including photochemical reaction pathways, and radiative and nonradiative decay processes have drawn substantial attention from computational scientists to offer explanations for several unanswered queries in photophysics and photochemistry. Using computational calculation it is possible to investigate the comprehensive mechanisms of unexplored complicated chemical reactions, ground state and excited state charge delocalization pathway, excitonic feature, and device transport characteristics of the systems. Density functional theory (DFT) based ab-initio calculation is a widely used method for studying the electronic structure of materials and their magnetic properties. In DFT, the electronic structures of a material are described by the density of its electrons, which is determined by solving the Schrödinger equation with an effective potential [56]. To study the magnetism of a material using DFT, one can calculate the magnetic moment associated with each atom in the material. The magnetic moment is defined as the magnetic dipole moment per unit volume

and is a measure of the strength and direction of the magnetic field produced by the atom. DFT calculations can predict the magnetic properties of materials by calculating the total energy of a system in different magnetic states [57]. The magnetic configuration with the lowest total energy is the ground state configuration which represents the most stable magnetic structure of the material. DFT can also be used to study the magnetic anisotropy of materials, which is the dependence of the magnetic properties on the direction of an applied magnetic field. Magnetic anisotropy is an important property in the design of magnetic materials for applications such as data storage and spintronic.

By using first principles DFT calculations, we investigate structural relaxations and orbital decomposition on ReX_2 (X = S, Se) materials to explain the existing conflicts [58, 59]. We have explained the semiconductor to metal transition under moderately high pressure in the light of orbital decomposition. We have also computed different X-ray spectral properties of ReS_2 and $ReSe_2$. For kagome stibnite series AV_3Sb_5 (A = K, Rb, and Cs), with first-principles electronic structure and phonon calculations, we found that the bulk system stabilizes in the collinear spin-polarized ferromagnetic state with finite vanadium moments and conforms as a frustrated spin cluster [60]. We have also predicted a new series of magnetic transition metal hydroxide semiconductors $X(OH)_2$ (X= Mn, Fe, Co Ni). We explored the layer-dependent magnetic properties and the formation as well as exfoliation energies [61].

The prediction of highly efficient nanohybrid and investigation of unexpected behavior in hybrid systems are the main motives to include DFT-based computational calculation. In this thesis, we have carried out ab-initio investigations on different nanohybrid to understand the fascinating intrinsic property at the interfaces. In one of our works, we prepared ZnO-NF nanohybrid system and investigated the electronic structure. We calculated the efficient charge separation from norfloxacin to ZnO nanoparticle in a nanohybrid system that

supports the experimental ligand to metal charge transfer mechanism [62]. In another work, we have investigated the electronic property and charge transfer mechanism in the ZIF8-IR820 hybrid system by using first principles DFT investigations [49]. The experimental findings of ZIF8 and ZIF8-IR820 are well explained by DFT-based calculations. We have also investigated the fabrication of metal hybrid systems which is Au nanoparticle decorated ZnO (Au_ZnO) [46]. The morphology and composition of the samples were characterized by DFT-based computational techniques. The experimental findings are well explained by first-principles DFT analysis.

The computational tools used for studying the electronic interaction include DFT as implemented in Vienna Ab initio Simulation Package (VASP) [63, 64] with projector augmented wave (PAW) pseudopotentials and generalized gradient approximated (GGA), and Perdew-Burke-Ernzerhof (PBE) exchange-correlation functionals [65] with the incorporation of spin-orbit coupling. The vdW corrections are incorporated by following the semi-empirical Grimme DFT-D3 method [66]. The time-dependent optical properties are calculated by using the all-electron full-potential linearized augmented plane wave approach including local orbitals within the framework of DFT as implemented in the ELK 4.3.6 code [67].

1.7. Objective:

The prime objective of this thesis is the use of nanohybrid materials for their benefits in biomedical and environmental applications. Among them, metal-drug complexes, organic nanoparticles encapsulating drug molecules and inorganic nanoparticles attached to antibiotics need to be evaluated in detail to understand the interfacial properties that are responsible for betterment in medicinal activity which could give rise to the design of heterostructures with efficient charge separation and useful for various diseased conditions. One of the important objectives of this thesis is to fabricate various types of hybrid materials and unravel

the ultrafast dynamical processes across the interface of heterostructures by using both spectroscopic and computational techniques to enhance medicinal efficiency. Special emphasis has been given to the correlation between the ultrafast processes at the interface and their implications in terms of improved biomedicinal and environmental applications.

Depending upon the nature and strength of the interaction, the functionalities of the hybrids get altered. Thus, there is a necessity to study the interfacial processes using experimental and computational tools to fully understand the interfacial dynamics at the nano-junction. Hybrid materials with improved properties often depict superior functionalities. The current generation of hybrids formed using commercially available drug molecules with some inorganic counterparts often enhances the bioavailability and activity of the drug with an enhanced permeability and retention (EPR) effect at the target site [68]. Besides, the fabricated hybrid materials can incorporate 'sense and act' like stimuli responsive drug action and thus lowers the side effects of treatment [69-71]. The precise knowledge of interfacial charge transfer properties is important to fully understand the mechanism of drug action and their alteration upon hybrid formation within the scope of our studies. In this regard, light-mediated treatment methodologies such as photodynamic therapy (PDT) involve photosensitizer molecules, which could be activated by specific photon energy followed by the production of reactive oxygen species (ROS) for therapeutic use [72]. Metal-organic frameworks (MOFs) constitute a significant class of hybrid inorganic-organic crystalline porous materials and its structures can be manipulated at the atomic scale by an appropriate choice of metal ions and organic ligands [40, 41]. We have written a review article on sensitization of nontoxic MOF for their potential drug delivery application against microbial infection [47]. Several important features of MOFs as drug carriers for biological adaptabilities were investigated. Then, various types of methodologies to functionalize MOFs with satisfying agents were abbreviated. In the end, this review

proposes a thorough summary of the biomedical applications of MOF nanoparticles focusing on the antimicrobial activity. Finally, the challenges and predictions were expansively discussed to provide important context for the improvement of MOFs as proficient antibacterial and antiviral actions.

In one of our studies, we employed a mixed metal approach to get both water stability and activity in one single MOF system [42]. The mixed metal MOF (Zn_50Co_{50}-ZIF) shows enhanced thermal stability, water stability and pH-responsive dissolution characteristics. It depicts antibacterial photodynamic therapeutic activity towards drug-resistant bacterial strains. It can also degrade model pollutant MB under white light illumination. In another study, we encapsulated rifampicin (RF), an antituberculosis drug [43] on the surface of ZIF8. The synthesized ZIF8-RF nano-MOF has been characterized by using experimental and computational methods. The drug release profile experiment demonstrates that ZIF8-RF carries on as pH-responsive drug delivery and is ideal for targeting the bacterial disease. We have investigated that, ZIF8 can effectively deliver phototherapeutic drugs into a bacterial infection site and pronouncedly killed the infection using antimicrobial photodynamic therapeutic strategies [45].

In another work, we have used norfloxacin (NF) with wide bandgap semiconductor ZnO due to its advantages such as targeted delivery vehicles, nontoxic, chemically reliable, biodegradable, excellent wide bandgap, greater binding energy (60 MeV), lower cost and abundance in nature [73-76]. The detailed characteristics are performed in both experimental and theoretical techniques. The synthesized antibiotic-implanted nanohybrids (ZnO-NF) depict tremendous antimicrobial activity due to the enormous ROS production capability in the presence of light.

Light harvesting materials that capture solar photons and convert them for light-mediated applications are considered to be one of the groundbreaking research topics of the present era [47]. The NIR part of solar light contains almost 50% of the

solar spectra. So to harvest full solar light, it is highly required to design a nanomaterial that can harvest the NIR part of solar light. To explore the NIR light activated nanohybrid systems, we have synthesized ZIF8-IR820 nanohybrid by encapsulating the IR820 dye (a typical cyanine dye) on the surface of the ZIF8 nanoparticle. The electronic charge transfer mechanism has been described by using experimental as well as first-principles DFT calculation techniques. It shows efficient NIR light-induced dose-dependent antibacterial activity due to enhanced ROS generation capability that would be beneficial for bacterial remediation.

Utilization of duel sensitization in photodynamic therapy can be very useful to get more efficiency. Although, the approach has been earlier utilized to increase the efficacy in dye-sensitized solar cells [77-79]. We report the fabrication of metal hybrids nanomaterials which is Au-decorated ZnO (Au_ZnO). We encapsulated an antibacterial agent tetracycline (TC) with Au_ZnO system to make a novel Au_ZnO-TC tri-hybrid and achieved enormous ROS in the presence of white light. The dual sensitization in the tri-hybrids leads to huge antimicrobial activity against gram-positive bacteria due to immense ROS under white light irradiation.

In another work, we investigated the iron chelating property of curcumin through various spectroscopic tools by synthesizing and characterizing the iron–curcumin (Fe–Cur) complex. Our study unravels the improved antioxidant activity of the synthesized chelate complex in the dark. We further demonstrate that the proposed complex generates no significant ROS under dark conditions, which makes it a promising candidate for chelation therapy of iron toxicity.

The results acquired from all these studies of nanohybrid heterojunction systems using combined spectroscopic and computational study could be very promising in designing new-age materials for benefit in different practical fields including energy harvesting, device fabrication, magnetism in superconductivity, development of medicine, photocatalysis, etc.

1.8. Summary of the Work Done:

1.8.1. Synthesis and Optical Characterization of a Nontoxic Nanohybrid for their Potential Drug Delivery Application:

1.8.1.1. Enhanced Water Stability and Photoresponsivity in Metal Organic Framework (MOF): A Potential Tool to Combat Drug Resistant Bacteria [42]: In this work, we have successfully synthesized a bimetallic (Zinc and Cobalt) Zeolitic Imidazolate Framework ($Zn_{50}Co_{50}$-ZIF), a class in a wider microporous Metal-Organic Framework (MOF) family. The synthesized nanostructures maintain both water stability like ZIF-8 (solely Zn containing) and charge transfer electronic band in the visible optical spectrum as ZIF-67 (solely Co containing). Crystal structure from XRD, high resolution transmission electron microscopy (HRTEM) followed by elemental mapping (EDAX) confirm structural stability and omnipresence of the metal atoms (Zn and Co) across the nanomaterial with equal proportion. The existence of a charge transfer state consistent with ZIF67 and intact ultrafast excited state dynamics of the imidazolate moiety in both ZIF-8 and ZIF-67, is evidenced from steady state and time resolved optical spectroscopy. The thermal and aqueous stabilities of $Zn_{50}Co_{50}$-ZIF are found to be better than ZIF-67 but comparable to ZIF-8 as evidenced by solubility, scanning electron microscopy (SEM) and XRD studies of the material in water. We have evaluated the photoinduced ROS generation by the mixed ZIF employing dichloro-dihydro-fluorescein diacetate (DCFH-DA) assay. We have also explored the potentiality of the synthesized material for the alternate remediation of methicillin-resistant *Staphylococcus aureus* (MRSA) infection through the photoinduced reactive oxygen species (ROS) generation and methylene blue (MB) degradation kinetics.

1.8.1.1. Nano MOFs as Targeted Drug Delivery Agents to Combat Antibiotic Resistant Bacterial Infections [44]: The drug resistance of bacteria is a significant threat to human civilization while the action of antibiotics against drug-resistant

bacteria is severely limited due to the hydrophobic nature of drug molecules, which unquestionably inhibits its permanency for clinical applications. The antibacterial action of nanomaterials offers major modalities to combat drug-resistant bacteria. The current work reports, the use of nano MOFs encapsulating drug molecules to enhance their antibacterial activity against model drug-resistant bacteria and biofilm of the bacteria. We have attached rifampicin (RF), a well-documented antituberculosis drug with tremendous pharmacological significance, into the pore surface of zeolitic imidazolate framework 8 (ZIF8) by a simple synthetic procedure. The synthesized ZIF8 has been characterized using the X-ray diffraction (XRD) method before and after drug encapsulation. The electron microscopic strategies such as scanning electron microscope (SEM) and transmission electron microscope (TEM) methods were performed to characterize the binding between ZIF8 and RF. We have also performed picosecond resolved fluorescence spectroscopy to validate the formation of the ZIF8-RF nanohybrids (NHs). The drug release profile experiment demonstrates that ZIF8-RF depicts pH-responsive drug delivery and is ideal for targeting bacterial disease corresponding to its inherent acidic nature. Most remarkably, ZIF8-RF gives enhanced antibacterial activity against methicillin-resistant *S. aureus* (MRSA) bacteria and also prompts entire damage of structurally robust bacterial biofilms. Overall, the present study depicts a detailed physical insight into nanohybrids, presenting tremendous antimicrobial activity that can be beneficial for manifold practical applications.

1.8.2. A Combined Optical Spectroscopy and Computational Studies on Nanohybrids with wide band Semiconductor for Potential Biomedical Applications:

1.8.2.1. Wide Bandgap Semiconductor Based Novel Nanohybrid for Potential Antibacterial Activity: Ultrafast Spectroscopy and Computational Studies [62]: The properties of nanomaterials generated by external stimuli are considered an

innovative and promising replacement for the annihilation of bacterial infectious disease. The present study demonstrates the possibility of getting the antibiotic-like drug action from our newly synthesized nanohybrid which consists of norfloxacin (NF), as the photosensitive material, covalently attached to the ZnO nanoparticle. The synthesized nanohybrid has been characterized using various microscopic and spectroscopic techniques. Steady state fluorescence and time-correlated single photon counting (TCSPC) based spectroscopic studies demonstrate the efficient electron transfer from NF to ZnO. This enhances the reactive oxygen species (ROS) production capability of the system. First principles density functional theory has been calculated to get an insight into the charge separation mechanism. To explore the electron densities of occupied and unoccupied levels of the nanohybrid, we have verified the nature of the electronic structure. It is observed that there is a very high possibility of electron transfer from NF to ZnO in the nanohybrid system which validates the experimental findings. Finally, the efficacy of the nanohybrid compared to NF and ZnO has been estimated on the *in vitro* culture of *E. coli* bacteria. We have obtained a significant reduction in bacterial viability by the nanohybrid with respect to control in the presence of light. These results suggest that synthesized nanohybrid could be a potential candidate in new-generation alternative antibacterial drugs.

1.8.2.2. Functionalized Nano-MOF for NIR Induced Bacterial Remediation: A Combined Spectroscopic and Computational Study [49]: Antimicrobial infection has emerged as one of the principal health problems in the world that requires urgent effective prevention. In order to deal with this reality, antibacterial photodynamic therapy of photosensitizers such as IR820 is one of the most encouraging and innovative methodologies to combat bacteria-caused infections. However, their activity is limited due to low photostability, short circulation, and lack of targeted bio-distribution. Herein, we have developed a user-friendly and universal approach to overcome such limitations of cyanine dye IR820 by

encapsulating it with zeolitic imidazolate framework-8 (ZIF-8) keeping its activity intact. The synthesized ZIF8-IR820 nano-MOFs are characterized using electron microscopic and optical spectroscopic techniques. Moreover, the formation of hybrids is confirmed from the charge transfer process obtained from time resolved fluorescence transient and first principles DFT-based analysis. The ultrafast charge transfer dynamic enhances the red-light sensitive reactive oxygen species (ROS) production capability which is further catalyzed in acidic pH and DFT-based calculation validates the experimental results. The enhanced ROS production of ZIF8-IR820 nano-MOFs makes it superior in NIR-induced antibacterial activity. Overall, the study demonstrates a detailed physical understanding of photosensitizer encapsulated nano-MOF system which shows efficient NIR light-induced photo-dose dependent antibacterial activity that can be beneficial for potential bacterial remediation.

1.8.3. A Combined Spectroscopic and Computational Studies on Tri-hybrid Nanomaterial for Potential Removal of Antibiotic Burden and Bacterial Remediation:

1.8.3.1. Tetracycline Encapsulated in Au Nanoparticle-Decorated ZnO Nanohybrids for Enhanced Antibacterial Activity [46]: Infections caused by antibiotic-resistant bacteria are one of the most perilous health threats in today's world due to its fast-increasing pace in recent years and less availability of new treatment strategies. In this regard, the development of novel antibacterial agents is needed to combat bacterial infections. Stimuli responsive nanomaterials especially light-mediated treatment applications using ZnO-based nanohybrids for targeted biomedical aspects are leading the field with high interest. However, pure ZnO has low activity in practical applications due to the faster recombination rate of photo-generated electron-hole pairs. In this work, we reported the one-step fabrication of Au-decorated ZnO hybrids nanomaterials (Au_ZnO) and further attached it with

traditional antibiotic tetracycline (TC). The morphology and composition of the samples were characterized by electron microscopic, ultrafast optical spectroscopic and density functional theory-based computational techniques. The steady state photoluminescence and time-resolved fluorescence transient studies demonstrate the Förster resonance energy transfer (FRET) from TC to Au as well as efficient electron transfer from TC to ZnO in the Au_ZnO-TC tri-hybrid system. The multiple charge transfer processes present in the Au_ZnO-TC tri-hybrids show a significant increment of reactive oxygen species (ROS) generation in the presence of white light due to a higher extent of electron-hole separation. The antibacterial properties of Au_ZnO-TC tri-hybrids and other control samples such as ZnO nanoparticles, TC and Au_ZnO nanohybrids against *Staphylococcus hominis* were studied systematically. The results obtained by this study confirm that the Au_ZnO-TC tri-hybrid has great potential as a new antibacterial agent for the remediation of bacterial infections with less chance of resistance generation.

1.8.4. Synthesis and Optical Spectroscopic Studies on Properties of Nanohybrids after Doping with Ions for Their Potential Applications:

1.8.4.1. Combating Essential Metal Toxicity: Key Information from Optical Spectroscopy [50]: Essential minerals play an important role to maintain healthy human physiology. However, the presence of an excess amount of such essential metals can cause cell injury which finally leads to severe life-threatening diseases. Chelating complexes can efficiently capture the targeted metal and can easily be excreted from the body. Commonly utilized metal chelators have major side effects including long-term damage to some organs which has pointed out the need for less harmful biocompatible chelating agents. In this work, we have investigated the iron chelating property of curcumin through various spectroscopic tools by synthesizing and characterizing the iron-curcumin (Fe-Cur) complex. We have also investigated whether the synthesized materials can retain their antioxidant activity after the

chelation of the substantial metal ion. Our study unravels the improved antioxidant activity of the synthesized chelate complex. We further investigate that the proposed complex generates no significant reactive oxygen species (ROS) under dark conditions, which makes it a promising candidate for chelation therapy of iron toxicity. Femtosecond resolved fluorescence studies further give an insight into the mechanism of activity of the new complex where electron transfer from ligand to metal has been observed prominently. Thus, the Fe-Cur complex has the potential to act as a dual-activity medicine for the excretion of toxic metal ions via chelation and as a therapeutic agent of oxidative stress caused by the metal ion as well.

1.9. Plan of the Thesis:

The plan of the thesis is as follows:

Chapter 1: This chapter includes a concise introduction and motivation for the entire thesis work. Scope of the optical spectroscopy and first principles density functional theory for the investigation of the nanomaterials for manifold applications. A summary of the work done is also presented in this chapter.

Chapter 2: This chapter provides an overview of the steady-state and dynamical tools, the structural aspects of dyes, and fluorescent probes used in the experiments.

Chapter 3: This chapter includes the details of instrumentation, data analysis, and experimental procedures that have been used during the entire thesis work. A summary of the working principle of the instruments and synthesis procedure of materials has been described here.

Chapter 4: This chapter contains the detail of the theoretical methodology of DFT-based computational calculation. Furthermore, we discuss the time-dependent DFT and its application. We have also described all the methods of computational calculations including phonon vibrational modes. In addition, we have explained a

combined full-potential DFT+MLFT approach [80, 81] to calculate the X-ray spectral properties. In a case study, with the help of electronic structure and phonon calculations, we correct the structures of both of ReS_2 and $ReSe_2$ systems, capable of resolving the existing disputes of the structure-property relationship. We pointed out the effects of structural relaxations and orbital decomposition to explain the existing conflicts.

Chapter 5: In this chapter, we have successfully synthesized a bimetallic (Zinc and Cobalt) Zeolitic Imidazolate Framework ($Zn_{50}Co_{50}$-ZIF). The synthesized nanostructures maintain both water stability like ZIF-8 (solely Zn containing) and charge transfer electronic band in the visible optical spectrum as ZIF-67 (solely Co containing). We have evaluated the photoinduced ROS generation by the mixed ZIF employing dichloro-dihydro-fluorescein diacetate (DCFH-DA) assay. Also, we have attached rifampicin (RF) into the pore surface of ZIF8 to prepare ZIF8-RF nanohybrids. We have performed picosecond resolved fluorescence spectroscopy to validate the formation of the ZIF8-RF. The drug release profile experiment demonstrates that ZIF8-RF depicts acidic pH-responsive drug delivery capability, ideal for targeting bacterial disease due to its characteristic acidic nature. We have also explored the potentiality of the synthesized material for the alternate remediation of MRSA infection through the photoinduced reactive oxygen species (ROS) generation and methylene blue (MB) degradation kinetics.

Chapter 6: In this chapter, we have investigated the possibility of getting antibiotic-like drug action from our newly synthesized nanohybrids. The synthesized nanohybrids have been characterized using various microscopic and spectroscopic techniques. Steady state fluorescence and time-correlated single photon counting (TCSPC) studies demonstrate the efficient electron transfer from drugs to inorganic nanoparticles. First-principles density functional theory calculations reveal the charge separation mechanism which validates the experimental findings. The

synthesized nanohybrids show light-induced photo-dose-dependent antibacterial activity that can be beneficial for potential bacterial remediation.

Chapter 7: In this chapter, we reported a one-step fabrication of Au-decorated ZnO hybrids nanomaterials (Au_ZnO) and further attached it with traditional antibiotic tetracycline (TC). The multiple charge transfer processes present in the Au_ZnO-TC tri-hybrids show a significant increment of reactive oxygen species (ROS) generation in the presence of white light due to a higher extent of electron-hole separation. The antibacterial properties of Au_ZnO-TC tri-hybrids and other control samples such as ZnO nanoparticles, TC and Au_ZnO nanohybrids against *Staphylococcus hominis* were studied systematically. The results obtained by this study confirm that the Au_ZnO-TC tri-hybrid has great potential as a new antibacterial agent for the remediation of bacterial infections with less chance of resistance generation.

Chapter 8: In this chapter, we have investigated the iron chelating property of curcumin through various spectroscopic tools by synthesizing and characterizing the iron-curcumin (Fe-Cur) complex. Our study unravels the improved antioxidant activity of the synthesized chelate complex due to insignificant reactive oxygen species (ROS) under dark conditions. Femtosecond resolved fluorescence studies further give an insight into the mechanism of activity of the new complex where electron transfer from ligand to metal has been observed prominently.

References

[1] C. J. Murray, A. D. Lopez, Measuring the global burden of disease, *N. Engl. J. Med.* 369 (2013) 448.

[2] X. Guo, N. Yang, W. Ji, H. Zhang, X. Dong, Z. Zhou, L. Li, H.-M. Shen, S. Q. Yao, W. Huang, Mito-bomb: Targeting mitochondria for cancer therapy, *Adv. Mater.* 33 (2021) 2007778.

[3] R. Friedman, Computational studies of protein–drug binding affinity changes upon mutations in the drug target, *WIREs Comput. Mol. Sci.* 12 (2022) e1563.

[4] F. C. Tenover, Mechanisms of antimicrobial resistance in bacteria, *Am. J. Med.* 119 (2006) S3.

[5] J. P. Verma, D. K. Jaiswal, R. Sagar, Pesticide relevance and their microbial degradation: A-state-of-art, *Rev. Environ. Sci. Biotechnol.* 13 (2014) 429.

[6] F. Prestinaci, P. Pezzotti, A. Pantosti, Antimicrobial resistance: A global multifaceted phenomenon, *Pathog. Glob. Health* 109 (2015) 309.

[7] H. Ishaq, I. Dincer, C. Crawford, A review on hydrogen production and utilization: Challenges and opportunities, *Int. J. Hydrog. Energy* 47 (2022) 26238.

[8] J. Goldemberg, Ethanol for a sustainable energy future, *Science* 315 (2007) 808.

[9] S. Y. Tee, K. Y. Win, W. S. Teo, L. D. Koh, S. Liu, C. P. Teng, M. Y. Han, Recent progress in energy-driven water splitting, *Adv. Sci.* 4 (2017) 1600337.

[10] L. Al-Ghussain, Global warming: Review on driving forces and mitigation, *Environ. Prog. Sustain. Energy* 38 (2019) 13.

[11] Y. Shang, S. Hao, C. Yang, G. Chen, Enhancing solar cell efficiency using photon upconversion materials, *Nanomaterials* 5 (2015) 1782.

[12] A. Omar, H. Abdullah, Electron transport analysis in zinc oxide-based dye-sensitized solar cells: A review, *Renew. Sustain. Energy Rev.* 31 (2014) 149.

[13] J. Yan, T. Wang, G. Wu, W. Dai, N. Guan, L. Li, J. Gong, Tungsten oxide single crystal nanosheets for enhanced multichannel solar light harvesting, *Adv. Mater.* 27 (2015) 1580.

[14] H. Rauscher, B. Sokull-Klüttgen, H. Stamm, The european commission's recommendation on the definition of nanomaterial makes an impact, *Nanotoxicology* 7 (2013) 1195.

[15] E. Roduner, Size matters: Why nanomaterials are different, *Chem. Soc. Rev.* 35 (2006) 583.

[16] E. Khosropour, L. Hakimi, W. Weisany, Role of engineered nanomaterials in biotic stress managements in engineered nanomaterials for sustainable agricultural production, soil improvement and stress management, *Academic Press*, Massachusetts, 2023.

[17] F. Villanueva-Flores, A. Castro-Lugo, O. T. Ramírez, L. A. Palomares, Understanding cellular interactions with nanomaterials: Towards a rational design of medical nanodevices, *Nanotechnology* 31 (2020) 132002.

[18] A. W. Clark, J. M. Cooper, Nanogap ring antennae as plasmonically coupled SERRS substrates, *Small* 7 (2011) 119.

[19] S. Mourdikoudis, A. Kostopoulou, A. P. LaGrow, Magnetic nanoparticle composites: Synergistic effects and applications, *Adv. Sci.* 8 (2021) 2004951.

[20] J. Wen, G. L. Wilkes, Organic/inorganic hybrid network materials by the sol−gel approach, *Chem. Mater.* 8 (1996) 1667.

[21] A. E. Nel, L. Mädler, D. Velegol, T. Xia, E. M. Hoek, P. Somasundaran, F. Klaessig, V. Castranova, M. Thompson, Understanding biophysicochemical interactions at the nano–bio interface, *Nat. Mater.* 8 (2009) 543.

[22] J. E. Gagner, S. Shrivastava, X. Qian, J. S. Dordick, R. W. Siegel, Engineering nanomaterials for biomedical applications requires understanding the nano-bio interface: A perspective, *J. Phys. Chem. Lett.* 3 (2012) 3149.

[23] P. Gómez-Romero, C. Sanchez, Functional hybrid materials, *John Wiley & Sons*, New York, 2006.

[24] H. Ishii, K. Sugiyama, E. Ito, K. Seki, Energy level alignment and interfacial electronic structures at organic/metal and organic/organic interfaces, *Adv. Mater.* 11 (1999) 605.

[25] J. Wang, X. Tan, X. Pang, L. Liu, F. Tan, N. Li, MoS_2 quantum dot@polyaniline inorganic–organic nanohybrids for *in vivo* dual-modal imaging guided synergistic photothermal/radiation therapy, *ACS Appl. Mater. Interfaces* 8 (2016) 24331.

[26] G. Choi, N. S. Rejinold, H. Piao, J.-H. Choy, Inorganic–inorganic nanohybrids for drug delivery, imaging and photo-therapy: Recent developments and future scope, *Chem. Sci.* 12 (2021) 5044.

[27] X. Xie, J. Tang, Y. Xing, Z. Wang, T. Ding, J. Zhang, K. Cai, Intervention of polydopamine assembly and adhesion on nanoscale interfaces: State-of-the-art designs and biomedical applications, *Adv. Healthcare Mater.* 10 (2021) 2002138.

[28] Y. Fu, G. Zeng, C. Lai, D. Huang, L. Qin, H. Yi, X. Liu, M. Zhang, B. Li, S. Liu, L. Li, M. Li, W. Wang, Y. Zhang, Z. Pi, Hybrid architectures based on noble metals and carbon-based dots nanomaterials: A review of recent progress in synthesis and applications, *J. Chem. Eng.* 399 (2020) 125743.

[29] W. Park, H. Shin, B. Choi, W.-K. Rhim, K. Na, D. Keun Han, Advanced hybrid nanomaterials for biomedical applications, *Prog. Mater. Sci.* 114 (2020) 100686.

[30] P. J. Hagrman, D. Hagrman, J. Zubieta, Organic-inorganic hybrid materials: From "simple" coordination polymers to organodiamine-templated molybdenum oxides, *Angew. Chem.* 38 (1999) 2638.

[31] R. Vendamme, S.-Y. Onoue, A. Nakao, T. Kunitake, Robust free-standing nanomembranes of organic/inorganic interpenetrating networks, *Nat. Mater.* 5 (2006) 494.

[32] K. Vallé, P. Belleville, F. Pereira, C. Sanchez, Hierarchically structured transparent hybrid membranes by in situ growth of mesostructured organosilica in host polymer, *Nat. Mater.* 5 (2006) 107.

[33] Y. Otsuka, Y. Okamoto, H. Y. Akiyama, K. Umekita, Y. Tachibana, S. Kuwabata, Photoinduced formation of polythiophene/TiO_2 nanohybrid heterojunction films for solar cell applications, *J. Phys. Chem. C* 112 (2008) 4767.

[34] C. Sanchez, P. Belleville, M. Popall, L. Nicole, Applications of advanced hybrid organic–inorganic nanomaterials: From laboratory to market, *Chem. Soc. Rev.* 40 (2011) 696.

[35] X. Liu, J. Iocozzia, Y. Wang, X. Cui, Y. Chen, S. Zhao, Z. Li, Z. Lin, Noble metal–metal oxide nanohybrids with tailored nanostructures for efficient solar energy conversion, photocatalysis and environmental remediation, *Energy Environ. Sci.* 10 (2017) 402.

[36] S. Prakash, M. Malhotra, W. Shao, C. Tomaro-Duchesneau, S. Abbasi, Polymeric nanohybrids and functionalized carbon nanotubes as drug delivery carriers for cancer therapy, *Adv. Drug Delivery Rev.* 63 (2011) 1340.

[37] S. Chang, X. Wu, Y. Li, D. Niu, Z. Ma, W. Zhao, J. Gu, W. Dong, F. Ding, W. Zhu, A hydrophobic dye-encapsulated nano-hybrid as an efficient fluorescent probe for living cell imaging, *Adv. Healthc. Mater.* 1 (2012) 475.

[38] G. Sharma, S. Pandey, S. Ghatak, G. Watal, P. K. Rai, Chapter 3 - potential of spectroscopic techniques in the characterization of "green nanomaterials" in nanomaterials in plants, algae, and microorganisms, *Academic Press*, Massachusetts, 2018.

[39] V. Amendola, R. Pilot, M. Frasconi, O. M. Maragò, M. A. Iatì, Surface plasmon resonance in gold nanoparticles: A review, *J. Condens. Matter Phys.* 29 (2017) 203002.

[40] Y. Zhao, X.-G. Yang, X.-M. Lu, C.-D. Yang, N.-N. Fan, Z.-T. Yang, L.-Y. Wang, L.-F. Ma, $\{Zn_6\}$ cluster based metal–organic framework with enhanced room-temperature phosphorescence and optoelectronic performances, *Inorg. Chem.* 58 (2019) 6215.

[41] Introduction to metal–organic frameworks, *Chem. Rev.* 112 (2012) 673.

[42] S. A. Ahmed, D. Bagchi, H. A. Katouah, M. N. Hasan, H. M. Altass, S. K. Pal, Enhanced water stability and photoresponsivity in metal-organic framework (MOF): A potential tool to combat drug-resistant bacteria, *Sci. Rep.* 9 (2019) 19372.

[43] T. Mondol, S. Batabyal, S. K. Pal, Interaction of an antituberculosis drug with nano-sized cationic micelle: Förster resonance energy transfer from dansyl to rifampicin in the microenvironment, *Photochem. Photobiol.* 88 (2012) 328.

[44] S. A. Ahmed, M. N. Hasan, D. Bagchi, H. M. Altass, M. Morad, I. I. Althagafi, A. M. Hameed, A. Sayqal, A. E. R. S. Khder, B. H. Asghar, H. A. Katouah, S. K. Pal, Nano-MOFs as targeted drug delivery agents to combat antibiotic-resistant bacterial infections, *R. Soc. Open Sci.* 7 (2020) 200959.

[45] D. Bagchi, A. Bhattacharya, T. Dutta, S. Nag, D. Wulferding, P. Lemmens, S. K. Pal, Nano MOF entrapping hydrophobic photosensitizer for dual-stimuli-responsive unprecedented therapeutic action against drug-resistant bacteria, *ACS Appl. Bio Mater.* 2 (2019) 1772.

[46] S. A. Ahmed, M. N. Hasan, H. M. Altass, A. Bera, R. I. Alsantali, N. Pan, A. Y. A. Alzahrani, D. Bagchi, J. H. Al-Fahemi, A. S. Khder, S. K. Pal, Tetracycline encapsulated in Au nanoparticle-decorated ZnO nanohybrids for enhanced antibacterial activity, *ACS Appl. Nano Mater.* 5 (2022) 4484.

[47] M. N. Hasan, A. Bera, T. K. Maji, S. K. Pal, Sensitization of nontoxic MOF for their potential drug delivery application against microbial infection, *Inorg. Chim. Acta* 523 (2021) 120381.

[48] S. Kundu, A. Patra, Nanoscale strategies for light harvesting, *Chem. Rev.* 117 (2017) 712.

[49] M. N. Hasan, A. Bera, T. K. Maji, D. Mukherjee, N. Pan, D. Karmakar, S. K. Pal, Functionalized nano-MOF for NIR induced bacterial remediation: A combined spectroscopic and computational study, *Inorg. Chim. Acta* 532 (2022) 120733.

[50] S. A. Ahmed, M. N. Hasan, D. Bagchi, H. M. Altass, M. Morad, R. S. Jassas, A. M. Hameed, J. Patwari, H. Alessa, A. Alharbi, S. K. Pal, Combating essential metal toxicity: Key information from optical spectroscopy, *ACS Omega* 5 (2020) 15666.

[51] P. Piotrowiak, Photoinduced electron transfer in molecular systems: Recent developments, *Chem. Soc. Rev.* 28 (1999) 143.

[52] J. R. Lakowicz, Topics in fluorescence spectroscopy: Principles, *Springer Science & Business Media*, New York, 1992.

[53] A. Periasamy, Fluorescence resonance energy transfer microscopy: A mini review, *J. Biomed. Opt.* 6 (2001) 287.

[54] S. G. Louie, Y.-H. Chan, F. H. da Jornada, Z. Li, D. Y. Qiu, Discovering and understanding materials through computation, *Nat. Mater.* 20 (2021) 728.

[55] Y. Liu, T. Zhao, W. Ju, S. Shi, Materials discovery and design using machine learning, *J. Materiomics* 3 (2017) 159.

[56] W. Kohn, Nobel lecture: Electronic structure of matter-wave functions and density functionals, *Rev. Mod. Phys.* 71 (1999) 1253.

[57] M. S. Si, D. S. Xue, Magnetic properties of vacancies in a graphitic boron nitride sheet by first-principles pseudopotential calculations, *Phys. Rev. B* 75 (2007) 193409.

[58] M. N. Hasan, F. Sorgenfrei, N. Pan, D. Phuyal, M. Abdel-Hafiez, S. K. Pal, A. Delin, P. Thunström, D. D. Sarma, O. Eriksson, D. Karmakar, Re-dichalcogenides: Resolving conflicts of their structure–property relationship, *Adv. Phys. Res.* 1 (2022) 2200010.

[59] M. N. Hasan, F. Sorgenfrei, N. Pan, S. K. Pal, A. Delin, P. Thunstrom, D. Sarma, O. Eriksson, D. Karmakar, Resolving conflicts in rhenium dichalcogenides (ReS_2 and $ReSe_2$), *Bull. Am. Phys. Soc.* 9 (2023) UU09.00004.

[60] M. N. Hasan, Q. Xu, A. Delin, A. Bergmann, P. M. Oppeneer, M. Pereiro, O. Eriksson, D. Karmakar, Magnetism in kagome superconductors, *Psi-k Conference* 3 (2022) C3.23.

[61] N. Pan, M. N. Hasan, M. Pereiro, P. Thunstrom, S. Pal, A. Delin, O. Eriksson, D. Karmakar, Hydroxide semiconductors: New series of van der Waals magnets, *Bull. Am. Phys. Soc.* 2 (2023) AAA02.00002.

[62] M. N. Hasan, T. K. Maji, U. Pal, A. Bera, D. Bagchi, A. Halder, S. A. Ahmed, J. H. Al-Fahemi, T. M. Bawazeer, T. Saha-Dasgupta, S. K. Pal, Wide bandgap semiconductor-based novel nanohybrid for potential antibacterial activity: Ultrafast spectroscopy and computational studies, *RSC Adv.* 10 (2020) 38890.

[63] G. Kresse, J. Furthmüller, Efficient iterative schemes for ab initio total-energy calculations using a plane-wave basis set, *Phys. Rev. B* 54 (1996) 11169.

[64] G. Kresse, D. Joubert, From ultrasoft pseudopotentials to the projector augmented-wave method, *Phys. Rev. B* 59 (1999) 1758.

[65] M. Ernzerhof, G. E. Scuseria, Assessment of the Perdew–Burke–Ernzerhof exchange-correlation functional, *J. Chem. Phys.* 110 (1999) 5029.

[66] S. Grimme, J. Antony, S. Ehrlich, H. Krieg, A consistent and accurate ab initio parametrization of density functional dispersion correction (DFT-D) for the 94 elements H-Pu, *J. Chem. Phys.* 132 (2010) 154104.

[67] A. Sanna, J. A. Flores-Livas, A. Davydov, G. Profeta, K. Dewhurst, S. Sharma, E. Gross, Ab initio Eliashberg theory: Making genuine predictions of superconducting features, *J. Phys. Soc. Japan* 87 (2018) 041012.

[68] X. Wang, Z. Guo, Targeting and delivery of platinum-based anticancer drugs, *Chem. Soc. Rev.* 42 (2013) 202.

[69] S. Mura, J. Nicolas, P. Couvreur, Stimuli-responsive nanocarriers for drug delivery, *Nat. Mater.* 12 (2013) 991.

[70] M. A. C. Stuart, W. T. Huck, J. Genzer, M. Müller, C. Ober, M. Stamm, G. B. Sukhorukov, I. Szleifer, V. V. Tsukruk, M. Urban, Emerging applications of stimuli-responsive polymer materials, *Nat. Mater.* 9 (2010) 101.

[71] R. Cheng, F. Meng, C. Deng, H.-A. Klok, Z. Zhong, Dual and multi-stimuli responsive polymeric nanoparticles for programmed site-specific drug delivery, *Biomaterials* 34 (2013) 3647.

[72] D. E. Dolmans, D. Fukumura, R. K. Jain, Photodynamic therapy for cancer, *Nat. Rev. Cancer* 3 (2003) 380.

[73] Z. L. Wang, Zinc oxide nanostructures: Growth, properties and applications, *J. Phys. Condens. Matter* 16 (2004) R829.

[74] D. Bagchi, V. S. Rathnam, P. Lemmens, I. Banerjee, S. K. Pal, NIR-light-active ZnO-based nanohybrids for bacterial biofilm treatment, *ACS omega* 3 (2018) 10877.

[75] T. K. Maji, P. K. Sarkar, P. Kar, B. Liu, P. Lemmens, D. Karmakar, S. K. Pal, A combined experimental and computational study on a nanohybrid material for potential application in NIR photocatalysis, *Appl. Catal. A: Gen.* 583 (2019) 117124.

[76] F. Lu, W. Cai, Y. Zhang, ZnO hierarchical micro/nanoarchitectures: Solvothermal synthesis and structurally enhanced photocatalytic performance, *Adv. Funct. Mater.* 18 (2008) 1047.

[77] E. Lee, C. Kim, J. Jang, High-performance förster resonance energy transfer (FRET)-based dye-sensitized solar cells: Rational design of quantum dots for wide solar-spectrum utilization, *Chem. Eur. J.* 19 (2013) 10280.

[78] S. Sarkar, A. Makhal, K. Lakshman, T. Bora, J. Dutta, S. Kumar Pal, Dual-sensitization via electron and energy harvesting in CdTe quantum dots decorated ZnO nanorod-based dye-sensitized solar cells, *J. Phys. Chem. C* 116 (2012) 14248.

[79] M. Ambapuram, R. Ramireddy, G. Maddala, S. Godugunuru, P. V. S. Yerva, R. Mitty, Effective upconverter and light scattering dual function $LiYF_4:Er^{3+}/Yb^{3+}$ assisted photoelectrode for high performance cosensitized dye sensitized solar cells, *ACS Appl. Electron. Mater.* 2 (2020) 962.

[80] J. Lüder, J. Schött, B. Brena, M. W. Haverkort, P. Thunström, O. Eriksson, B. Sanyal, I. Di Marco, Y. O. Kvashnin, Theory of L-edge spectroscopy of strongly correlated systems, *Phys. Rev. B* 96 (2017) 245131.

[81] M. W. Haverkort, M. Zwierzycki, O. K. Andersen, Multiplet ligand-field theory using Wannier orbitals, *Phys. Rev. B* 85 (2012) 165113.

Chapter 2

An Overview of Experimental Techniques and Systems

In order to investigate the dynamical processes involved in the synthesis of light harvesting hybrid materials, different steady-state and dynamical tools have been employed. These include photoinduced electron transfer (PET), Förster resonance energy transfer (FRET), distance distribution from FRET etc. In this chapter, we have included a brief discussion about the above-mentioned tools. An overview of the various systems, probes, and dyes used in the studies has also been provided.

2.1. Steady-state and Dynamical Tools:

2.1.1. Photoinduced Electron Transfer (PET): PET can be described as the movement of an electron caused by the absorption of light from an electron-rich species (D) to an electron-deficient species (A), as shown in Eq. 2.1.

$$D + A \rightarrow D^+ + A^- \tag{2.1}$$

The first law of photochemistry tells us that a photo-induced process must be initiated by the absorption of light. In PET, the absorbing species can either be a donor, the acceptor, or a ground-state complex between the donor and acceptor, often referred to as a charge transfer complex. These possibilities are shown in Eqs. 2.2−2.4.

$$D \xrightarrow{h\upsilon} D^* + A \longrightarrow D^+ + A^- \tag{2.2}$$

$$A \xrightarrow{h\upsilon} A^* + D \longrightarrow D^+ + A^- \tag{2.3}$$

$$(D \cdots A) \xrightarrow{h\upsilon} (D \cdots A)^* \longrightarrow D^+ + A^- \tag{2.4}$$

Transport of charges or excitons is commonly seen as a fundamental process in many optoelectronic devices as well as biological systems. The creation, diffusion, and annihilation of excitons and the mobility of charges are some of

the key processes in many devices that interconvert electric and light energies [1, 2]. PET is an important process in many biochemical systems, such as those in respiration and photosynthesis [3, 4]. To gain a deep understanding of these systems, it is important to describe the rates of these processes with a few empirically derived parameters [5, 6]. Therefore, it has become increasingly important to develop computational techniques that allow us to calculate the rate of charge or energy transport. In our systems, the apparent rate constants, k_{nr}, were determined for the nonradiative processes by comparing the lifetimes of the donor in the absence (τ_0) and the presence (τ) of an acceptor, using Eq. 2.5 [7].

$$k_{nr} = 1/\langle \tau \rangle - 1/\langle \tau_0 \rangle \tag{2.5}$$

The direction of electron transfer in the excited state is determined by the oxidation and reduction potential of the ground and excited states. Upon excitation the electron donor transfers an electron to the acceptor with a rate k_{nr}, forming the charge transfer complex. This complex may emit as an exciplex ($h\nu_E$) or be quenched and return to the ground state. The important part of this process is the decrease in the total energy of the charge transfer complex. The energy decreases because the ability to donate or accept electrons changes when a fluorophore is in excited state. Excitation provides the energy to drive charge separation. D and A do not form a complex when both are in the ground state because this is energetically unfavorable. The energy released by electron transfer can also change if the ions become solvated and/or separated in a solvent with a high dielectric constant. Upon excitation the electron donor transfers an electron to the acceptor with a rate k_P, forming the charge transfer complex $[D^+A^-]^*$ (Figure 2.1). This complex may emit as an exciplex ($h\nu_E$) or be quenched and return to the ground state.

This thesis demonstrates several PET processes, particularly in light-harvesting materials, and discusses the consequences of various interfacial electron transfer processes. In heterogeneous photocatalysis, photoinduced charge

separation in the photocatalyst is necessary and several strategies have been employed to facilitate charge separation. In heterostructure/dye-sensitized semiconductor nanohybrid, a series of charge transfer processes had to occur cooperatively so that the solar light can be harnessed efficiently. These include (i) electron injection from excited dye into the conduction band of the semiconductor, (ii) electron transport from one semiconductor to another semiconductor in the semiconductor nanohybrid, (iii) electron shuttling pathway from the conduction band of the semiconductor. The matching of the band energies of the two semiconductors facilitates desired functionality either to induce electron−hole recombination (e.g., light-emitting diodes) or to improve charge separation by driving electrons and holes in two different nanoparticles (e.g., photocatalysis in semiconductor heterostructure). In each instance where semiconductor nanocrystals are implemented into a practical device, PET reactions are intimately involved, and they dictate the overall functionality. This thesis focuses on the recent progress made in understanding the kinetics and mechanistic aspects of various PET processes at the semiconductor interface and their role in the direction of efficient solar light harvesting.

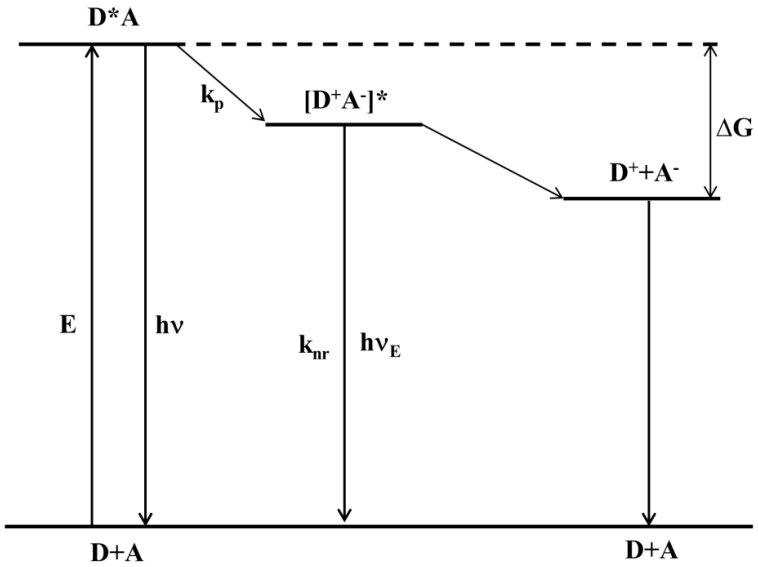

Figure 2.1: *Energy diagram for photoinduced electron transfer (PET). The excited molecule is assumed to be the electron donor.* ν *and* ν_E *are emission from the fluorophore and exciplex, respectively.*

2.1.2. Förster Resonance Energy Transfer (FRET): FRET is an electrodynamic phenomenon involving nonradiative transfer of the excited state energy from the donor dipole (D) to an acceptor dipole (A) in the ground state (Figure 2.2a). FRET is of two types: (i) Homo-molecular FRET and (ii) hetero-molecular FRET. In the former case, the same fluorophore acts both as an energy donor and acceptor, while in the latter case, two different molecules act as donor and acceptor.

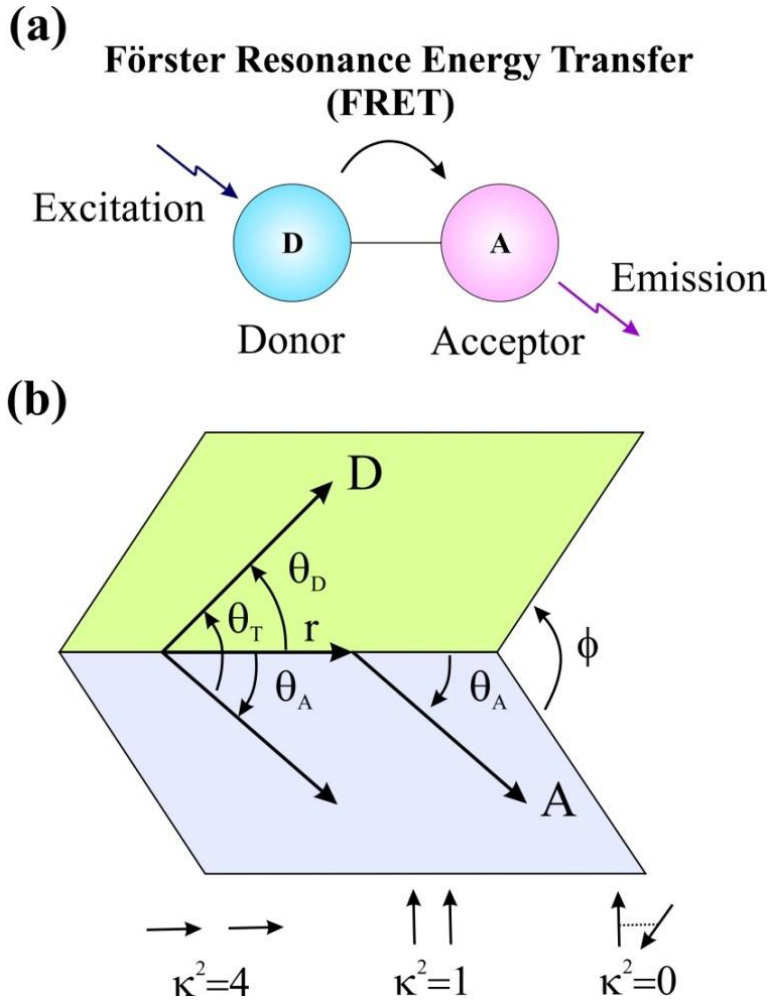

Figure 2.2: *(a) Schematic illustration of the FRET process. (b) Dependence of the orientation factor κ^2 on the directions of the emission and absorption dipoles of the donor and acceptor, respectively.*

Each donor-acceptor (D-A) pair participating in FRET is characterized by a distance known as Förster distance (R_0) i.e., the D-A separation at which energy transfer is 50% efficient. The rate of resonance energy transfer (k_T) from a donor to an acceptor is given by Eq. [8],

$$k_T = \frac{1}{\tau_D}\left(\frac{R_0}{r}\right)^6 \tag{2.6}$$

where τ_D is the lifetime of the donor in the absence of the acceptor and r is the donor to acceptor (D-A) distance. The rate of transfer of donor energy depends upon the extent of overlap of the emission spectrum of the donor with the absorption spectrum of the acceptor ($J(\lambda)$), the quantum yield of the donor (Q_D), the relative orientation of the donor and acceptor transition dipoles (κ^2) and the distance between the donor and acceptor molecules (r) (Figure 2.2b). The methodology to estimate the FRET efficiency of the donor and distances between donor-acceptor pairs are described below:

The Förster distance R_0 is given by [8],

$$R_0 = 0.211\left[\kappa^2 n^{-4} Q_D J(\lambda)\right]^{1/6} \text{ (in Å)} \tag{2.7}$$

where n is the refractive index of the medium, Q_D is the quantum yield of the donor, and $J(\lambda)$ is the overlap integral. κ^2 is defined as,

$$\kappa^2 = \left(\cos\theta_T - 3\cos\theta_D \cos\theta_A\right)^2 = \left(\sin\theta_D \sin\theta_A \cos\varphi - 2\cos\theta_D \cos\theta_A\right)^2 \tag{2.8}$$

where θ_T is the angle between the emission transition dipole of the donor and the absorption transition dipole of the acceptor, θ_D and θ_A are the angles between these dipoles and the vector joining the donor and acceptor, and φ is the angle between the planes of the donor and acceptor (Figure 2.2b). κ^2 value can vary from 0 to 4. For collinear and parallel transition dipoles, $\kappa^2 = 4$; for parallel dipoles, $\kappa^2 = 1$; and for perpendicularly oriented dipoles, $\kappa^2 = 0$. For donors and acceptors that randomize by rotational diffusion before an energy transfer, the magnitude of κ^2 is assumed to be 2/3. However, in systems where there is a definite site of attachment of the donor and acceptor molecules, to get physically relevant results, the value of κ^2 has to be estimated from the angle between the donor emission and acceptor absorption dipoles [9]. $J(\lambda)$, the

overlap integral, which expresses the degree of spectral overlap between the donor emission and the acceptor absorption, is given by,

$$J(\lambda) = \frac{\int_0^\infty F_D(\lambda)\varepsilon_A(\lambda)\lambda^4 d\lambda}{\int_0^\infty F_D(\lambda)d\lambda} \tag{2.9}$$

where $F_D(\lambda)$ is the fluorescence intensity of the donor in the wavelength range of λ to $\lambda+d\lambda$ and is dimensionless. $\varepsilon_A(\lambda)$ is the extinction coefficient (in $M^{-1} cm^{-1}$) of the acceptor λ. If λ is in nm, then $J(\lambda)$ is in units of $M^{-1} cm^{-1} nm^4$. Once the value of R_0 is known, the efficiency of energy transfer can be calculated. The efficiency of energy transfer (E) is the fraction of photons absorbed by the donor which are transferred to the acceptor and is defined as,

$$E = \frac{k_T(r)}{\tau_D^{-1} + k_T(r)} \tag{2.10}$$

$$\text{Or, } E = \frac{R_0^6}{r^6 + R_0^6} \tag{2.11}$$

For D-A systems decaying with multiexponential lifetimes, E is calculated from the amplitude weighted lifetimes $\langle\tau\rangle = \sum_i \alpha_i \tau_i$ of the donor in the absence (τ_D) and presence (τ_{DA}) of the acceptor as,

$$E = 1 - \frac{\tau_{DA}}{\tau_D} \tag{2.12}$$

The D-A distances can be measured using Eq. (2.11) and (2.12).

2.1.3. Data Analysis of Time-Resolved Fluorescence Transients: Curve fitting of the time-resolved fluorescence transients was carried out using a nonlinear least square fitting procedure to a function (Eq. 2.13) comprised of convolution of the IRF

$$(X(t) = \int_0^t E(t')R(t - t')dt') \tag{2.13}$$

(E(t)) with a sum of exponentials (Eq. 2.14) with pre-exponential factors (B_i),

$$(R(t) = A + \sum_{i=1}^{N} B_i e^{-t/\tau_i}) \tag{2.14}$$

characteristic lifetimes (τ_i) and a background (A). Relative concentration in a multiexponential decay is expressed as (Eq. 2.15).

$$c_n = \frac{B_n}{\sum_{i=1}^{N} B_i} \times 100 \tag{2.15}$$

The average lifetime (amplitude-weighted) of a multiexponential decay is expressed as,

$$\tau_{av} = \sum_{i=1}^{N} c_i \tau_i \tag{2.16}$$

2.2. Systems:

2.2.1. Molecular Probes: In this section, we will discuss the different probe molecules that have been used in the course of the study.

2.2.1.1. Indocyanine Green (IR820): IR820 is an indocyanine dye (Figure 2.3), which has a broad absorption band at 820 nm in methanol [10].

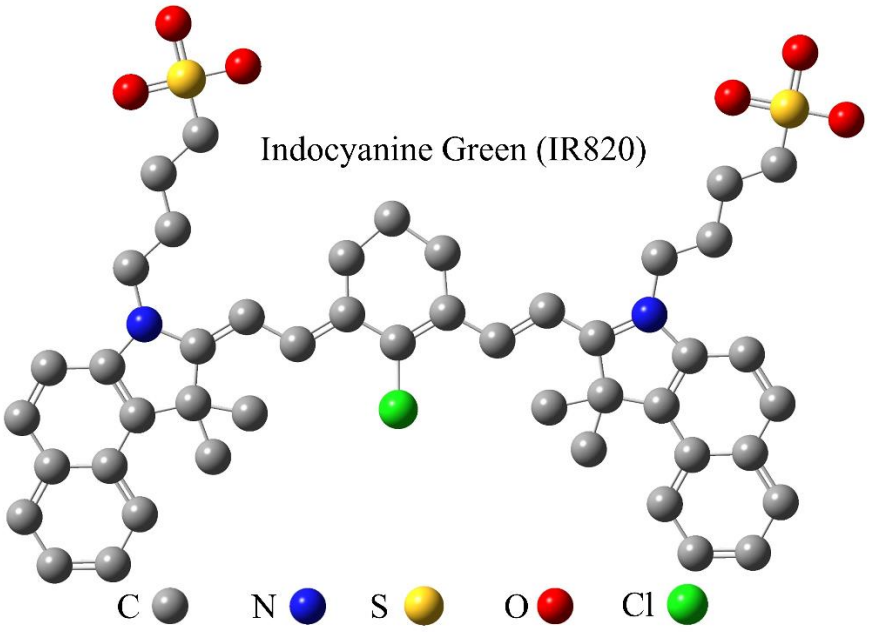

Figure 2.3: *Structure of indocyanine green (IR820), a benzoindole and a 1,1-diunsubstituted alkanesulfonate.*

It is a near-infrared (NIR) dye with a molar absorptivity of 72 x 10^4 dm^3 mol^{-1} cm^{-1} in water [11]. It is a cost-effective imaging agent with low cytotoxicity. It can be used for image guided photothermal therapy for the treatment of cancer. It is also used as a contrasting agent for the detection and quantification of infected tissues in animals.

2.2.1.2. Methylene Blue (MB): MB is a heterocyclic aromatic chemical compound with molecular formula: $C_{16}H_{18}ClN_3S$. It has many uses in a range of different fields. At room temperature, it appears as a solid and dark green powder, which yields a blue solution when dissolved in water. They are widely used as model water contaminants [12]. Its structure is given in Figure 2.4. When dissolved in water, the UV-visible spectrum of MB showed three absorption maxima. The first band was observed at 246 nm and then at 291 nm and more intensely at 663 nm [13]. The absorption maxima wavelength of MB (λ_{max} = 663 nm) was used for the analysis during the decolorization of MB dye.

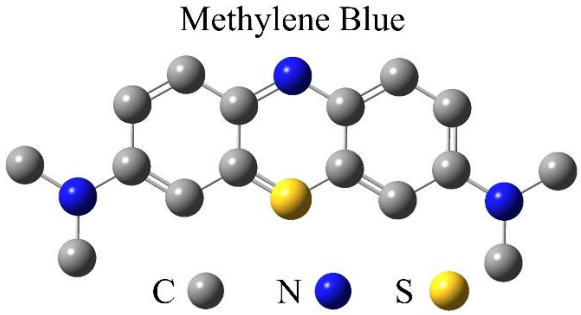

Figure 2.4: *Chemical structure of methylene blue.*

2.2.1.3. Norfloxacin (NF): NF is a broad-spectrum antibiotic that belongs to the class of drugs known as fluoroquinolones [14] as shown in Figure 2.5. It works by interfering with the DNA replication processes in bacteria, thereby preventing their growth and multiplication. NF is primarily used to treat bacterial infections in the urinary tract, prostate, and gastrointestinal tract. It can be effective against both gram-positive and gram-negative bacteria, including *Escherichia coli*, *Salmonella, Shigella*, and *Pseudomonas aeruginosa*. NF is typically taken orally, with or without food, and is usually prescribed for a period of 3-14 days, depending on the severity of the infection being treated. It

is important to complete the full course of treatment, even if symptoms improve before the medication is finished, to prevent the development of antibiotic-resistant bacteria.

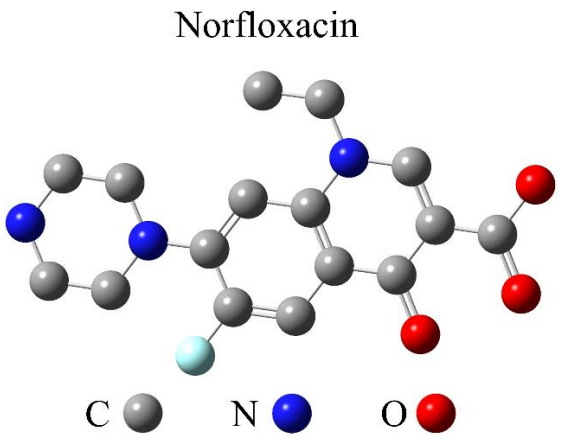

***Figure* 2.5:** *Chemical structure of norfloxacin (NF).*

2.2.1.4. Riboflavin (RBF): Riboflavin is a water-soluble member of the B-vitamin family [15] as shown in Figure 2.6. It is essential to the formation of two major coenzymes, flavin mononucleotide and flavin adenine dinucleotide. These coenzymes are involved in energy metabolism, cellular respiration, and antibody production, as well as normal growth and development.

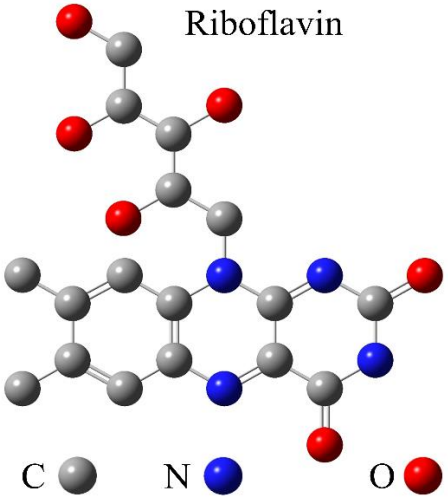

***Figure* 2.6:** *Chemical structure of riboflavin, a water-soluble member of the B-vitamin family.*

The coenzymes are also required for the metabolism of niacin, vitamin B6 and folate. Riboflavin is prescribed to treat corneal thinning, and taken orally, may

reduce the incidence of migraine headaches in adults. It is found in food and sold as a dietary supplement. Sufficient dietary and supplemental RF intake appears to have a protective effect on various medical conditions such as sepsis, ischemia etc. While it also contributes to the reduction in the risk of some forms of cancer in humans. These biological effects of RF have been widely studied for their anti-oxidant, anti-aging, anti-inflammatory, anti-nociceptive and anti-cancer properties. Moreover, the combination of RF and other compounds or drugs can have a wide variety of effects and protective properties and diminish the toxic effect of drugs in several treatments.

2.2.1.5. Tetracycline (TC): Tetracycline is a broad-spectrum antibiotic (Figure 2.7) that is used to treat a variety of bacterial infections. It was first discovered in 1948 and has been widely used ever since [16]. Tetracycline works by inhibiting the growth and multiplication of bacteria, thereby helping the body's immune system to fight the infection [17]. Tetracycline is commonly used to treat respiratory infections, urinary tract infections, skin infections, and sexually transmitted diseases, among others.

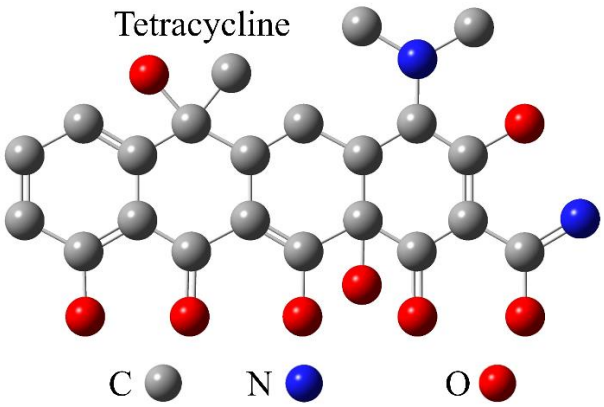

Figure 2.7: *Chemical structure of tetracycline, a class of medication used to manage and treat various bacterial infections.*

It is also used in the treatment of acne and rosacea. It is available in several forms, including capsules, tablets, and oral suspension. It is usually taken orally and should be taken on an empty stomach, as food can interfere with its absorption. Although tetracycline is generally considered safe and effective, it can cause several side effects [18]. These can include nausea, diarrhea,

vomiting, and abdominal pain. Tetracycline can also cause sensitivity to sunlight, so it is important to avoid prolonged exposure to the sun while taking this medication. In addition, tetracycline can interact with other medications, including oral contraceptives and antacids, so it is important to inform your doctor of any other medications you are taking before starting treatment with tetracycline.

2.2.1.6. Curcumin (Cur): Curcumin (Figure 2.8) is a natural yellowish-orange diarylheptanoid derived from the rhizomes of *Curcuma longa L.* popularly known as turmeric, a member of the ginger family [19]. The diverse pharmacological applications of curcumin towards various diseases include Alzheimer's disease, breast cancer, pancreatic cancer, colon cancer, arthritis, and oxidative stress-induced pathogenesis [20]. Furthermore, its promising antioxidant activity anticipates its possible use as a novel drug also for other lethal diseases.

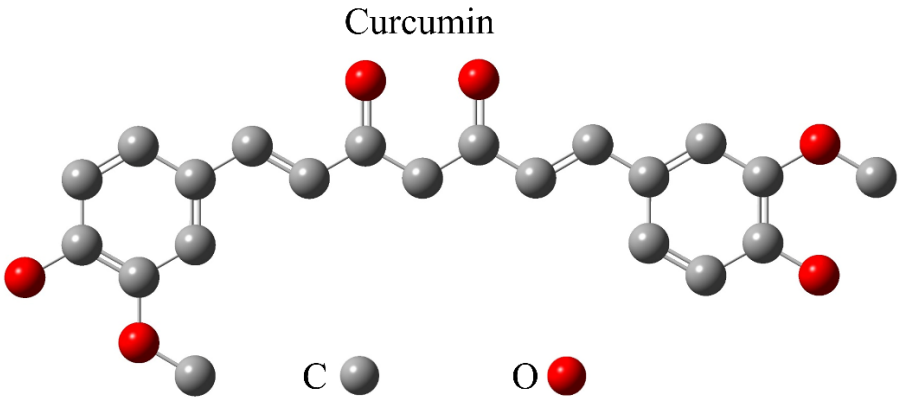

Figure 2.8: *Chemical structure of curcumin, a natural yellowish-orange diarylheptanoid.*

Curcumin is a linear polyphenol consisting of two o-methoxy phenolic groups that are connected by a seven-carbon linker consisting of an α, β-unsaturated β-diketo moiety (Figure 2.8). The diketo group exhibits keto-enol tautomerism and can also exist in different types of conformers depending on the nature of the solvent [21]. Due to the presence of β-diketone linkers in the seven-carbon chain, curcumin tends to chelate with metal. Sometimes, this metal chelating property can be detrimental, as it can attach to toxic metals like mercury or lead.

2.2.1.7. Rifampicin (RF): Rifampicin (also known as rifampin) is an antibiotic medication that belongs to a class of drugs known as rifamycins as shown in Figure 2.9. It is primarily used in the treatment of bacterial infections caused by organisms susceptible to rifampin. Rifampin is a key component of standard TB treatment regimens. It is highly effective against Mycobacterium tuberculosis and/or the bacterium responsible for causing tuberculosis.

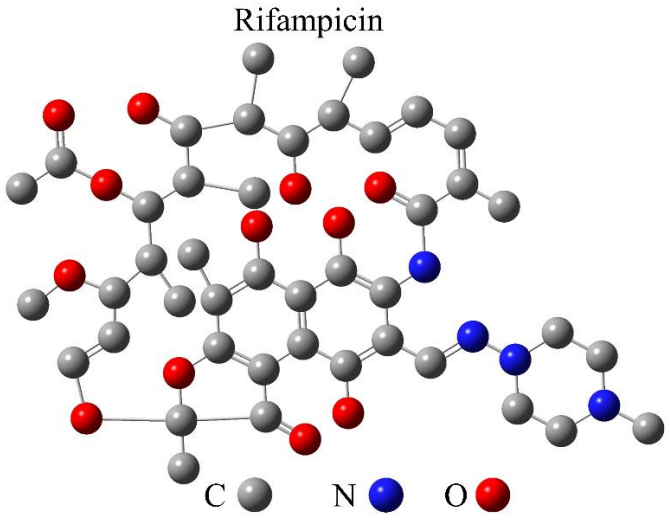

Figure 2.9: *The chemical structure of rifampicin, an antibiotic medication that belongs to a class of drugs known as rifamycins.*

Rifampicin is also used to treat infections caused by other mycobacterial species, such as Mycobacterium leprae (the causative agent of leprosy) and certain nontuberculous mycobacteria. It is sometimes used in combination with other antibiotics to treat serious infections caused by MRSA, particularly in cases where the bacteria are resistant to other antibiotics. Rifampicin works by inhibiting the activity of an enzyme called RNA polymerase, which is essential for bacterial RNA synthesis. By blocking this enzyme, rifampin effectively stops the bacteria from producing essential proteins, ultimately leading to their death.

2.2.1.8. Dichlorofluorescein (DCFH): Dichlorofluorescin (DCFH) is a probe (Figure 2.10) that is trapped within cells and is easily oxidized to fluorescent dichlorofluorescein (DCF) [22]. Dichlorofluorescin (DCFH) is non-fluorescent and converts to fluorescent DCF upon oxidation through reacting with reactive

oxygen species (ROS). This quantifies the amount of ROS as well as cellular oxidative stress.

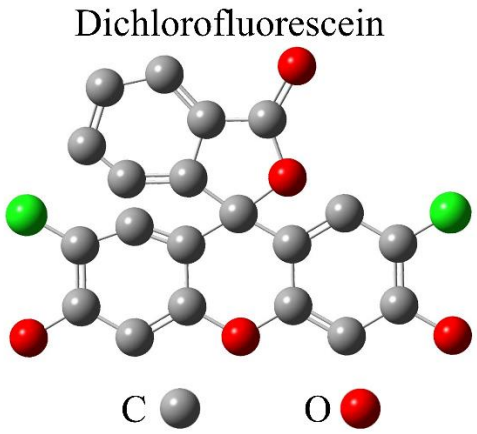

Figure 2.10: *Chemical structure of dichlorofluorescein (DCFH).*

2.2.1.9. 2,2-Diphenyl-1-picrylhydrazyl (DPPH): DPPH (Figure 1.11) is a well-known radical and a trap ("scavenger") for other radicals. Therefore, the reduction rate of a chemical reaction upon the addition of DPPH is used as an indicator of the radical nature of that reaction [23].

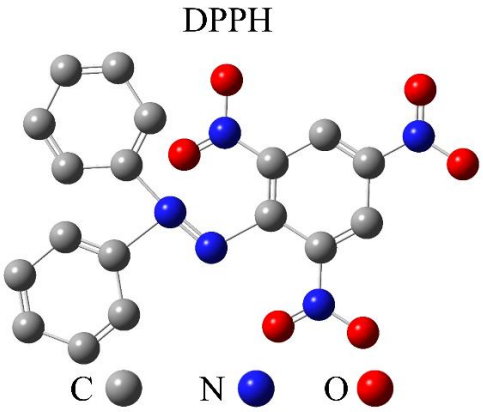

Figure 2.11: *The chemical structure of 2,2-Diphenyl-1-picrylhydrazyl (DPPH).*

Because of a strong absorption band centered at about 520 nm, the DPPH radical has a deep violet color in the solution, and it becomes colorless or pale yellow when neutralized. This property allows visual monitoring of the reaction, and the number of initial radicals can be counted from the change in the optical absorption at 520 nm.

2.2.1.10. Phthalocyanine (PC): PC is very well-known for its widespread applications in the field of optical recording, photodynamic therapy, and solar energy harvesting applications [24-26]. Its structure is given in Figure 2.12. In visible light photocatalysis, sensitizers with extended absorption in the near IR region of the sun emission spectra are paramount, and phthalocyanines are perfectly suited for their integration in light energy conversion systems. They exhibit very high extinction coefficients around 680 nm for efficient photon harvesting [27], as well as reversible redox properties and excellent photoconductivity.

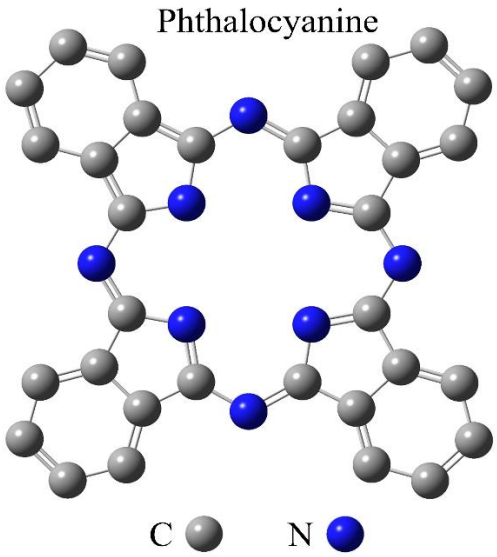

Figure 2.12: *Chemical structure of phthalocyanine with the formula* $(C_8H_4N_2)_4H_2$.

2.2.1.11. Methyl Orange (MO): MO is an azo compound with molecular formula: $C_{14}H_{14}N_3NaO_3S$. It is a model dye which belongs to the class of synthetic organic compounds and is widely used in the textile industry.

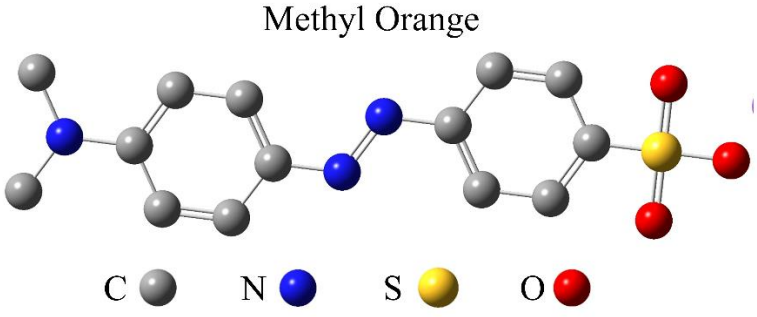

Figure 2.13: *Chemical structure of methyl orange with molecular formula:* $C_{14}H_{14}N_3NaO_3S$.

The removal of these non-biodegradable organic chemicals from the environment is a crucial ecological problem [28]. At room-temperature it appears as a solid, odorless, orange-yellow powder. MO shows orange color in acidic medium and yellow color in basic medium. Its structure is given in Figure 2.13. MO has a strong absorption at λ_{max} = 461 nm [29] which was used for the analysis during decolorization of MO dye.

2.2.1.12. Acridine Orange (AO): AO is an organic dye with molecular formula $C_{17}H_{19}N_3$. AO is widely used as a nucleic acid-selective fluorescent cationic dye which is commonly used to determine cell cycle [30]. AO has strong absorption

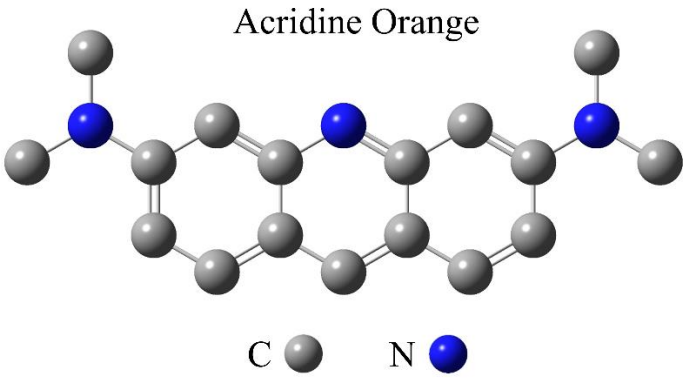

Figure 2.14: *Chemical structure of acridine orange with molecular formula* $C_{17}H_{19}N_3$.

at λ_{max} = ~480 nm [31]. As AO is cell-permeable, it interacts with DNA and RNA by intercalation or electrostatic attractions respectively. When bound to DNA, it is very similar spectrally to fluorescein, with an excitation maximum at 502 nm and an emission maximum at 525 nm (green) [30]. In association with RNA, the excitation maximum of AO shifts to 460 nm (blue), and the emission maximum shifts to 650 nm (red). AO can be used in conjunction with ethidium bromide or propidium iodide to differentiate between viable, apoptotic, and necrotic cells. Additionally, AO may be used to detect nuclear damage or chromatin condensation aiding in clinical diagnosis [32]. Its structure is given in Figure 2.14.

References

[1] H. Spanggaard, F. C. Krebs, A brief history of the development of organic and polymeric photovoltaics, *Sol. Energy Mater. Sol. Cells* 83 (2004) 125.

[2] Y. Shirota, H. Kageyama, Charge carrier transporting molecular materials and their applications in devices, *Chem. Rev.* 107 (2007) 953.

[3] H. B. Gray, J. R. Winkler, Electron tunneling through proteins, *Q. Rev. Biophys.* 36 (2003) 341.

[4] G. McLendon, R. Hake, Interprotein electron transfer, *Chem. Rev.* 92 (1992) 481.

[5] H. Bassler, Charge transport in disordered organic photoconductors: A monte carlo simulation study, *Phys. Status Solidi B* 175 (1993) 15.

[6] V. M. Kenkre, J. D. Andersen, D. H. Dunlap, C. B. Duke, Unified theory of the mobilities of photoinjected electrons in naphthalene, *Phys. Rev. Lett.* 62 (1989) 1165.

[7] J. H. Bang, P. V. Kamat, Quantum dot sensitized solar cells. A tale of two semiconductor nanocrystals: CdSe and CdTe, *ACS Nano* 3 (2009) 1467.

[8] J. R. Lakowicz, Principles of fluorescence spectroscopy, *Springer*, New York, 2006.

[9] D. Banerjee, S. K. Pal, Simultaneous binding of minor groove binder and intercalator to dodecamer DNA: Importance of relative orientation of donor and acceptor in FRET, *J. Phys. Chem. B* 111 (2007) 5047.

[10] M. N. Hasan, A. Bera, T. K. Maji, D. Mukherjee, N. Pan, D. Karmakar, S. K. Pal, Functionalized nano-MOF for NIR induced bacterial remediation: A combined spectroscopic and computational study, *Inorg. Chim. Acta* 532 (2022) 120733.

[11] A. Bera, D. Bagchi, S. K. Pal, Improvement of photostability and NIR activity of cyanine dye through nanohybrid formation: Key information from ultrafast dynamical studies, *J. Phys. Chem. A* 123 (2019) 7550.

[12] N. Xu, Z. Shi, Y. Fan, J. Dong, J. Shi, M. Z.-C. Hu, Effects of particle size of TiO_2 on photocatalytic degradation of methylene blue in aqueous suspensions, *Ind. Eng. Chem. Res.* 38 (1999) 373..

[13] D. Melgoza, A. Hernández-Ramírez, J. M. Peralta-Hernández, Comparative efficiencies of the decolourisation of methylene blue using Fenton's and photo-Fenton's reactions, *Photochem. Photobiol. Sci.* 8 (2009) 596.

[14] M. L. Corrado, W. E. Struble, C. Peter, V. Hoagland, J. Sabbaj, Norfloxacin: Review of safety studies, *Am. J. Med.* 82 (1987) 22.

[15] N. Suwannasom, I. Kao, A. Pruß, R. Georgieva, H. Bäumler, Riboflavin: The health benefits of a forgotten natural vitamin, *Int. J. Mol. Sci.* 21 (2020) 950.

[16] E. Michalova, J. Schlegelova, Tetracyclines in veterinary medicine and bacterial resistance to them, *Vet. Med.* 49 (2004) 79.

[17] J. Kadurugamuwa, T. Beveridge, Natural release of virulence factors in membrane vesicles by *Pseudomonas aeruginosa* and the effect of aminoglycoside antibiotics on their release, *J. Antimicrob. Chemother.* 40 (1997) 615.

[18] M. Koziolek, S. Alcaro, P. Augustijns, A. W. Basit, M. Grimm, B. Hens, C. L. Hoad, P. Jedamzik, C. M. Madla, M. Maliepaard, The mechanisms of pharmacokinetic food-drug interactions–A perspective from the UNGAP group, *Eur. J. Pharm. Sci.* 134 (2019) 31.

[19] K. M. Nelson, J. L. Dahlin, J. Bisson, J. Graham, G. F. Pauli, M. A. Walters, The essential medicinal chemistry of curcumin: Miniperspective, *J. Med. Chem.* 60 (2017) 1620.

[20] S. Wanninger, V. Lorenz, A. Subhan, F. T. Edelmann, Metal complexes of curcumin–synthetic strategies, structures and medicinal applications, *Chem. Soc. Rev.* 44 (2015) 4986.

[21] M. Pröhl, U. S. Schubert, W. Weigand, M. Gottschaldt, Metal complexes of curcumin and curcumin derivatives for molecular imaging and anticancer therapy, *Coord. Chem. Rev.* 307 (2016) 32.

[22] S. Sardar, S. Chaudhuri, P. Kar, S. Sarkar, P. Lemmens, S. K. Pal, Direct observation of key photoinduced dynamics in a potential nano-delivery vehicle of cancer drugs, *Phys. Chem. Chem. Phys.* 17 (2015) 166.

[23] M. Szabo, D. Radu, S. Gavrilas, D. Chambre, C. Iditoiu, Antioxidant and antimicrobial properties of selected spice extracts, *Int. J. Food. Prop* 13 (2010) 535.

[24] A. L. Thomas, Phthalocyanine research and applications, *CRC Press*, 1990.

[25] D. Gu, Q. Chen, X. Tang, F. Gan, S. Shen, K. Liu, H. Xu, Application of phthalocyanine thin films in optical recording, *Opt. Comm.* 121 (1995) 125.

[26] M. A. Loi, P. Denk, H. Hoppe, H. Neugebauer, C. Winder, D. Meissner, C. Brabec, N. S. Sariciftci, A. Gouloumis, P. Vázquez, Long-lived photoinduced charge separation for solar cell applications in phthalocyanine–fulleropyrrolidine dyad thin films, *J. Mater. Chem.* 13 (2003) 700.

[27] D. M. Krichevsky, A. V. Zasedatelev, A. Y. Tolbin, S. Y. Luchkin, A. B. Karpo, V. I. Krasovskii, L. G. Tomilova, Highly transparent low-symmetry zinc phthalocyanine-based monolayers for NO_2 gas detection, *Thin Solid Films* 642 (2017) 295.

[28] Y. Li, X. Li, J. Li, J. Yin, Photocatalytic degradation of methyl orange by TiO_2-coated activated carbon and kinetic study, *Wat. Res.* 40 (2006) 1119.

[29] A. Zyoud, A. Zu'bi, M. H. Helal, D. Park, G. Campet, H. S. Hilal, Optimizing photo-mineralization of aqueous methyl orange by nano-ZnO

catalyst under simulated natural conditions, *J. Environ. Health Sci. Eng.* 13 (2015) 46.

[30] N. Atale, S. Gupta, U. Yadav, V. Rani, Cell-death assessment by fluorescent and nonfluorescent cytosolic and nuclear staining techniques, *J. Microscopy* 255 (2014) 7.

[31] A. Pitchaimani, A. Renganathan, S. Cinthaikinian, K. Premkumar, Photochemotherapeutic effects of UV-C on acridine orange in human breast cancer cells: Potential application in anticancer therapy, *RSC Adv.* 4 (2014) 22123.

[32] E.-E. M. Mohammed, E. Mosad, A. M. Zahran, D. A. Hameed, E. A. Taha, M. A. Mohamed, Acridine orange and flow cytometry: Which is better to measure the effect of varicocele on sperm DNA integrity?, *Adv. Urology* 2015 (2015).

Chapter 3

Instrumentation and Sample Preparation

In this chapter, the instrumental setup and sample preparation techniques used in the thesis work have been described in comprehensive detail. The detailed description of the instrumental setup and sample preparation techniques presented in this chapter aims to provide readers with a comprehensive understanding of the experimental methodology employed in the thesis work. By thoroughly outlining the equipment, procedures, and steps involved, the chapter enables researchers to replicate the experiments accurately and ensures the reproducibility of the study.

3.1. Instrumental Setups:

3.1.1. UV-vis Absorption Spectroscopy: UV-vis absorption spectroscopy is a widely used analytical technique that measures the absorption of light in the ultraviolet (UV) and visible (vis) regions of the electromagnetic spectrum. It provides valuable information about the electronic transitions and the concentration of absorbing species in a sample. In operation, UV-vis absorption spectroscopy is based on the principle that molecules absorb specific wavelengths of light corresponding to the energy differences between their electronic energy levels. When a beam of UV or visible light passes through a sample, some wavelengths are absorbed by the sample, while others are transmitted or reflected. The absorbed light causes electronic transitions within the molecules, leading to an increase in their electronic energy. Components of a UV-vis absorption spectrophotometer, the light source of the spectrophotometer employs a stable and intense light source that emits a broad spectrum of UV and visible light. Common light sources include deuterium lamps for the UV region and tungsten or xenon lamps for the visible region. The monochromator is used to isolate specific wavelengths of light from the source. It consists of a diffraction grating or prism that disperses the incoming

light into its individual wavelengths and allows only the desired wavelength to pass through. The sample holder is designed to hold the sample in a way that the light beam can pass through it. It can be a cuvette, a solid sample holder, or a flow cell, depending on the nature of the sample. The photodetector measures the intensity of the transmitted or reflected light after it has passed through the sample. Commonly used photodetectors include photomultiplier tubes (PMTs) and photodiodes, which convert the light signal into an electrical signal. The data acquisition system records the intensity of the transmitted or reflected light at each selected wavelength. It converts the electrical signal from the photodetector into a digital format and stores the data for further analysis.

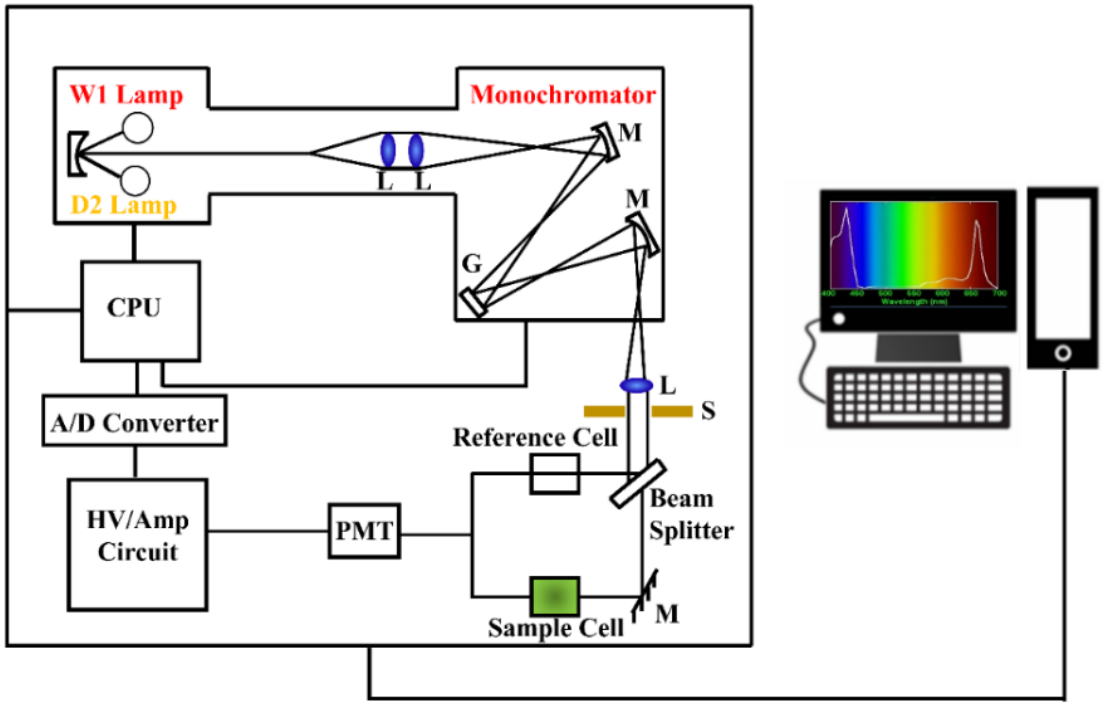

Figure 3.1: *Schematic ray diagram of an absorption spectrophotometer. Tungsten halogen (W1) and deuterium lamps (D2) are used as light sources in the visible and UV regions, respectively. M, G, L, S, PMT designate mirror, grating, lens, shutter, and photomultiplier tube, respectively. CPU, A/D converter and HV/amp indicate central processing unit, analog to digital converter and high-voltage/amplifier circuit, respectively.*

In UV-vis absorption spectroscopy, the sample is placed in the spectrophotometer, and the light beam passes through it. The monochromator selects a specific wavelength of light, which is then directed onto the sample. The intensity of the transmitted or reflected light is measured by the photodetector, and this information is recorded by the data acquisition system.

A reference sample, typically a solvent or blank, is also measured to correct for any contributions from the solvent or instrument background. The absorbance of the sample at a specific wavelength is calculated using the Beer-Lambert Law, which states that absorbance is directly proportional to the concentration of the absorbing species and the path length of the sample.

Steady-state UV-vis absorption spectra were measured with Shimadzu UV-2600 spectrophotometer and Horiba Fluorolog, respectively. Schematic ray diagrams of UV-vis absorption spectroscopy are shown in Figure 3.1. It is a technique that measures the amount of light absorbed by a sample in the ultraviolet and visible regions of the electromagnetic spectrum. In this technique, a beam of light of a specific wavelength is passed through the sample, and the amount of light that is absorbed by the sample is measured. The resulting absorption spectrum can be used to identify the electronic transitions occurring within the sample and provide information about its chemical composition and structure.

3.1.2. Steady-state Emission Spectroscopy: Steady-state emission spectroscopy is a technique used to analyze the emission of light from a sample after excitation. It provides valuable information about the electronic transitions and properties of fluorescent or phosphorescent molecules. This spectroscopic method is commonly employed in various scientific fields, including chemistry, biology, material science, and environmental science. In principle, steady-state emission spectroscopy involves the measurement of the light emitted by a sample after it has been excited by an external energy source. The sample absorbs energy, typically in the form of light or heat, and then emits light of lower energy as it relaxes back to its ground state. The emitted light is detected and analyzed to gather information about the sample's properties.

A typical steady-state emission spectrophotometer utilizes a light source to provide the excitation energy. Depending on the application, the light source can be a xenon or mercury lamp, a laser, or light-emitting diodes (LEDs). The choice of the light source depends on the required excitation wavelength and

intensity. A monochromator or filters are employed to select the desired excitation wavelength or range of wavelengths. These components ensure that only the desired excitation energy reaches the sample, minimizing interference from other wavelengths. The sample holder is designed to securely hold the sample in a way that maximizes the detection of emitted light. It may consist of cuvettes, solid sample holders, or specialized holders for different types of samples. The emitted light from the sample is detected by a photodetector. Commonly used detectors include photomultiplier tubes (PMTs), photodiodes, or charge-coupled devices (CCDs). These detectors convert the light signals into electrical signals that can be further processed and analyzed. The data acquisition system collects and records the emitted light signals detected by the photodetector. It converts the analog signals into digital form, allowing for further analysis and interpretation of the emission spectra.

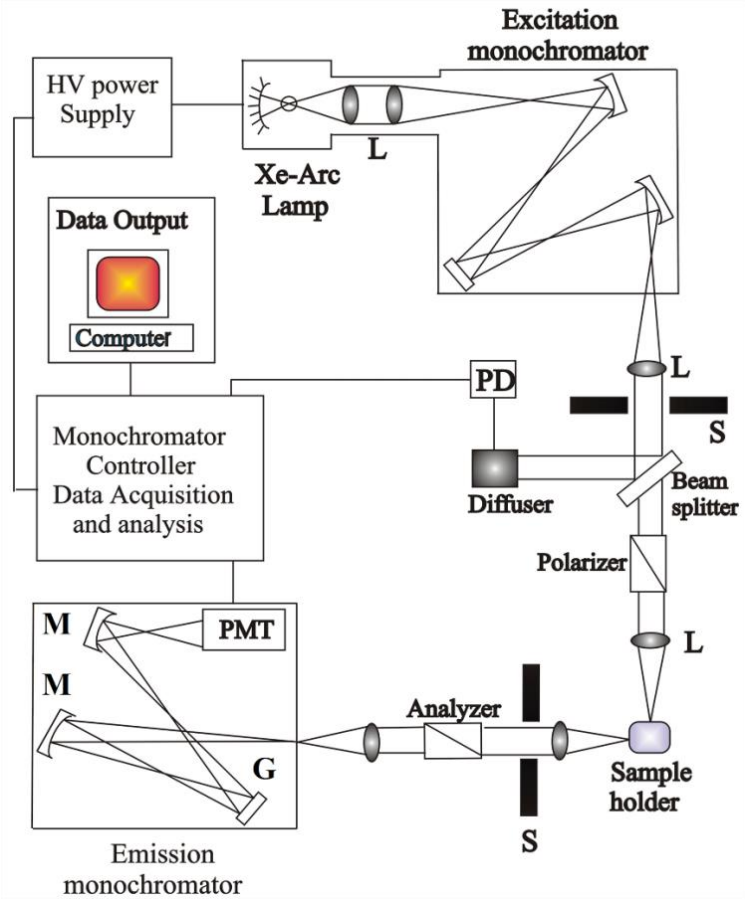

Figure 3.2: *Schematic ray diagram of an emission spectrofluorometer. M, G, L, S, PMT, and PD represent mirror, grating, lens, shutter, and photomultiplier tube and reference photodiode, respectively.*

In steady-state emission spectroscopy, the sample is excited by the light source, which provides the required energy for electronic transitions. The excitation wavelength is selected using a monochromator or filters, ensuring that only the desired energy reaches the sample. Upon excitation, the sample absorbs the energy and enters an excited state. As the excited molecules return to their ground state, they emit light of lower energy. The emitted light is collected by the photodetector and converted into an electrical signal. The data acquisition system records the intensity of the emitted light at different wavelengths to generate an emission spectrum., schematic ray diagrams as shown in Figure 3.2, measures the light emitted by a sample when it is excited by a light source.

3.1.3. Time-correlated Single Photon Counting (TCSPC) Technique: Time-correlated single photon counting (TCSPC) is a powerful technique used to measure the arrival times of individual photons with high precision. It enables the investigation of fluorescence lifetimes, fluorescence decay kinetics, and photon emission dynamics. TCSPC is widely employed in fields such as biophysics, chemistry, and materials science for studying dynamic processes at the molecular level.

The principle behind TCSPC involves the measurement of the time interval between the excitation of a sample and the detection of a single photon emitted from the sample. It relies on the use of ultrafast detectors and timing electronics to achieve accurate time resolution in the picosecond or even sub-picosecond range. A pulsed laser is used as the excitation source. It generates short-duration pulses of light to excite the sample. The sample under investigation contains fluorescent molecules or materials that emit photons upon excitation. These fluorophores may have different fluorescence lifetimes or decay characteristics. A single-photon detector, such as a photomultiplier tube (PMT) or an avalanche photodiode (APD), is used to detect the emitted photons. These detectors can measure the arrival time of individual photons with high sensitivity. The timing electronics provide precise timing signals to measure the time intervals between the excitation pulse and the detected photon. They

include a time-to-amplitude converter (TAC), a time-to-digital converter (TDC), and a clock source. The TAC converts the time interval into an analog voltage, while the TDC converts it into a digital time value. The data acquisition system collects the time-stamped detection events from the TDC and stores them for further analysis. It records the arrival times of the photons and constructs a fluorescence decay curve or histogram. All the picosecond-resolved fluorescence decays were collected using the TCSPC technique. The schematic block diagram of a TCSPC system is shown in Figure 3.3.

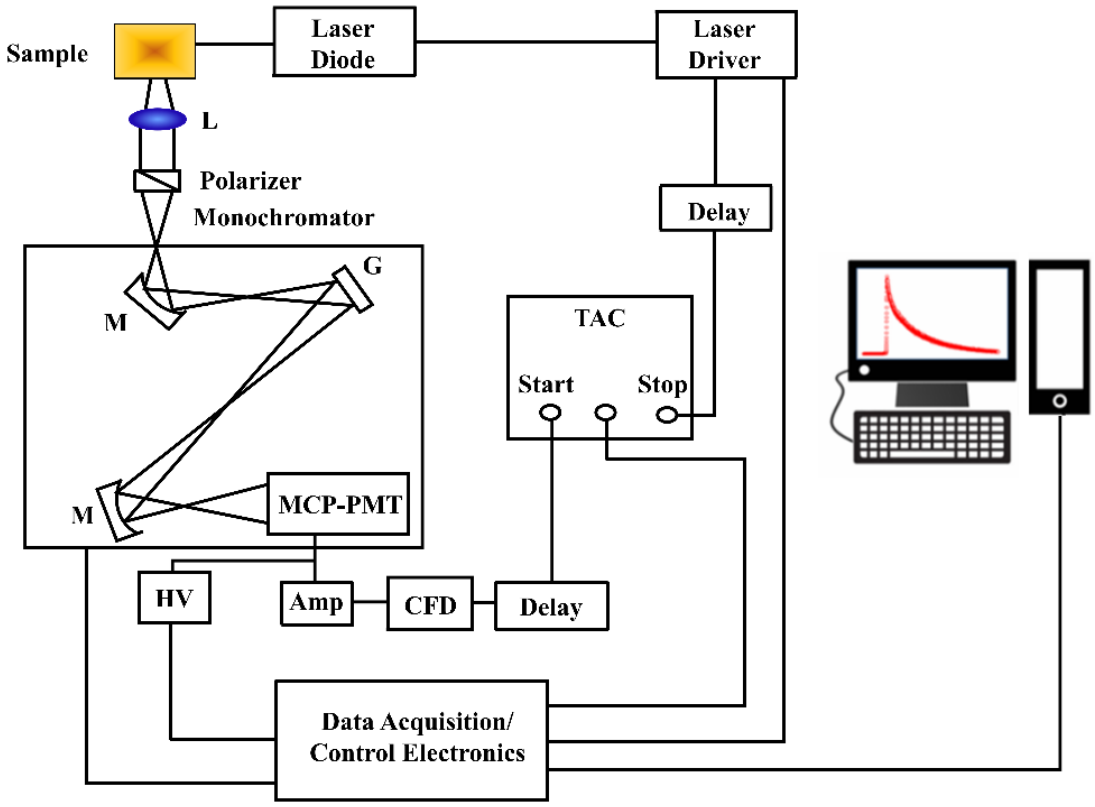

Figure 3.3: *Schematic ray diagram of time-correlated single photon counting (TCSPC). A signal from a microchannel plate photomultiplier tube (MCP-PMT) is amplified (Amp) and connected to the start channel of time to amplitude converter (TAC) via constant fraction discriminator (CFD) and delay. The stop channel of the TAC is connected to the laser driver via a delay line. L, M, G and HV represent lens, mirror, grating and a high voltage source, respectively.*

A commercial TCSPC setup from Edinburgh instruments (U.K.) was used during fluorescence decay acquisitions. The instrument response functions (IRFs) of the laser sources at different excitation wavelengths varied between 70 ps to 90 ps. The fluorescence from the sample was detected by a

photomultiplier after dispersion through a grating monochromator [1]. For all excited state lifetime measurement experiments, the polarizer in the emission side was adjusted to be at 54.7° (magic angle) to the polarization axis of the excitation beam.

3.1.4. Femtosecond Resolved Fluorescence Upconversion Technique: The femtosecond resolved fluorescence spectroscopy was carried out using a femtosecond upconversion setup (FOG 100, CDP) in which the sample was excited at 400 nm, using the second harmonic of a mode-locked Ti-sapphire laser with 80 MHz repetition rate (Tsunami, Spectra Physics), pumped by 10 W Millennia (Spectra Physics).

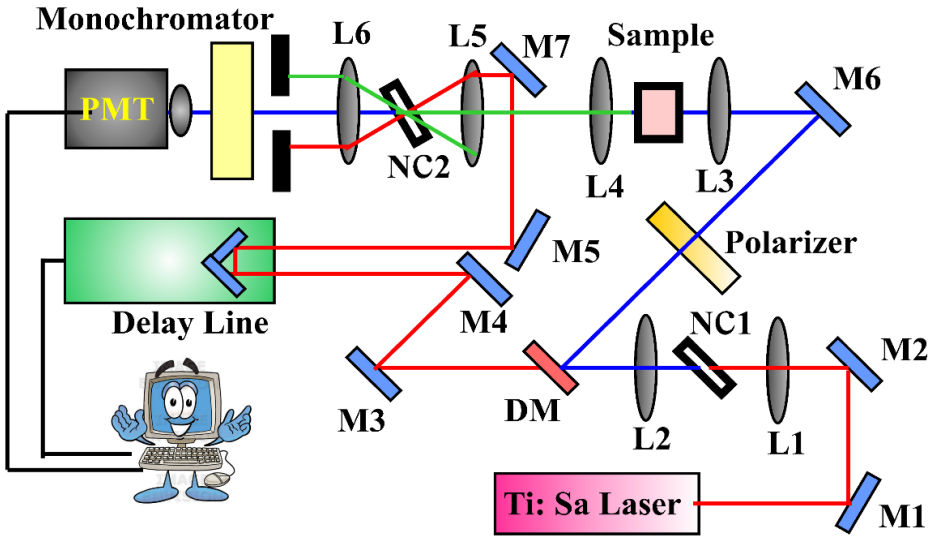

Figure 3.4: *Schematic diagram of a femtosecond fluorescence upconversion experimental setup. A BBO crystal (NC1) is used for the second harmonic generation, which provides a pump beam in the UV region. Another BBO crystal (NC2) generates the upconversion signal of the pump and probe beams. L and M indicate lenses and mirrors, respectively. M1, M2, M3, M4, M5, and M7 are IR mirrors whereas M6 is a UV mirror. DM is a dichroic mirror, and P is the periscope.*

The fundamental beam was passed through a periscopic arrangement (P) (Figure 3.4) before getting frequency-doubled in a nonlinear crystal, NC1 (1 mm BBO (β-barium borate), θ = 25°, ϕ = 90°). This beam was then sent into a rotating circular cell of 1 mm thickness containing the sample *via* a dichroic mirror (DM), a polarizer, and a mirror (M6). The resulting fluorescence emission was collected, refocused with a pair of lenses (L4 and L5) and mixed

with the fundamental beam (770 nm) coming through a delay line to yield an upconverted photon signal in a nonlinear crystal, NC2 (0.5 mm BBO, $\theta = 10°$, $\phi = 90°$). The upconverted light was dispersed in a double monochromator and detected using photon-counting electronics. A cross-correlation function obtained using the Raman scattering from water displayed a full width at half maximum (FWHM) of 195 fs. The femtosecond fluorescence decays were fitted using a Gaussian shape for the exciting pulse.

3.1.5. Femtosecond Resolved Fluorescence Measurements Using Streak Camera Images: Femtosecond-resolved fluorescence lifetime decay measurements were also carried out by capturing the streak camera images in a custom-made steak camera-based setup. The customized streak camera system consists of 3.5 ps FWHM. Laser source (Mai Tai HP 1040S from Spectra Physics, Mode-Locked Ti-sapphire Laser, 2.5 W, repetition rate 80 MHz, working temperature 20–25 °C), sample compartment, monochromator (SpectraPro HRS-300, scan range 0–1500 nm, 300 mm triple grating, grating change repeatability 0.2 nm), streak sweep unit, along with a charge coupled device (CCD) camera (Optronics OPTOSCOPE SC-10). The fluorescence light from the exit slit of the monochromator is guided to the photocathode of the streak camera to produce a horizontal linear spectral image. The schematic diagram of working principle of a streak camera is shown in Figure 3.5.

The produced photoelectrons are then accelerated further by the electrical field and biased in the vertical direction under a variable electrical field through a streak sweep unit. These photoelectrons impinge on the multichannel plate (MCP) inside the streak camera and make multiple electrons that give a single spot on the target phosphor screen. The field scan and the laser pulse flashing are synchronized. These spots are then recorded by CCD and the corresponding pixel information is transferred to a computer for further data processing. The streak camera produces two-dimensional (2D) spectrum-time images (290 ps time along the x-axis for a 15 ps/mm sweep rate span and a 150 nm wavelength span along the y-axis). A streak image helps detect both

wavelength and time from the same laser pulse shot. This experiment effectively captures nearly all photons of various wavelengths and times without producing artifacts from spectrum or decay changes during lengthy measurements. The decay of the fluorescence intensity in the excited state could be represented as $I(t) = I_0 e^{-t/\tau}$, where $I(t)$ is the recorded intensity, I_0 is the initial intensity, and τ is the fluorescence lifetime.

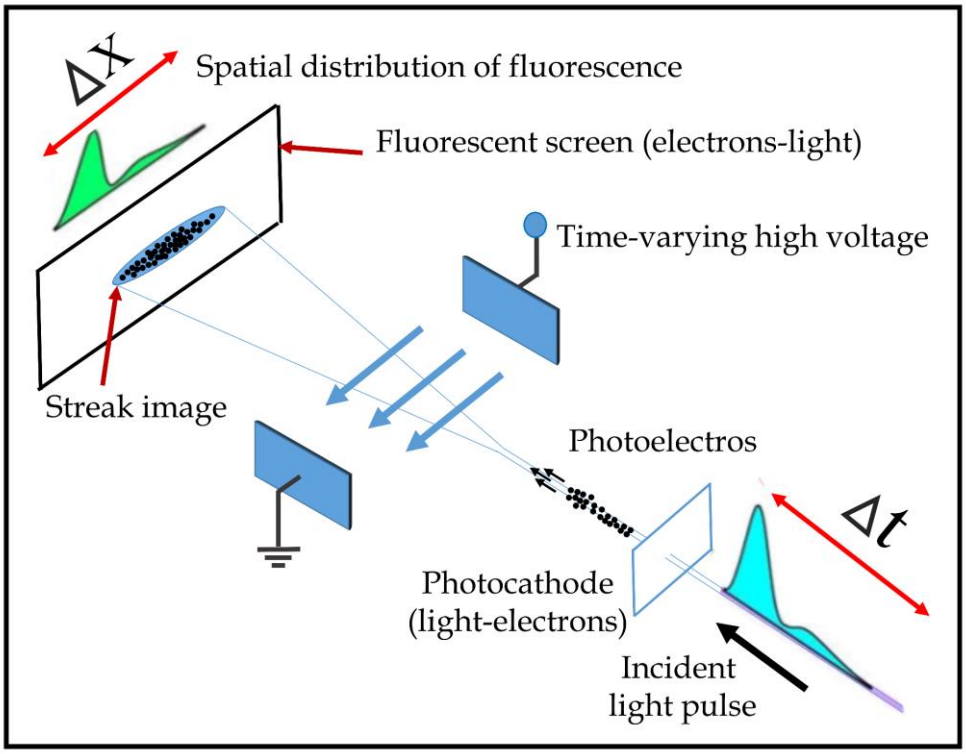

Figure 3.5: *Schematic diagram of working principle of a streak camera for measuring the variation in a pulse of light's intensity with time.*

3.1.6. Near Infrared (NIR) TCSPC: The block diagram of the customized NIR TCSPC system is shown in Figure 3.6. The sample was mounted on the stage lead of a vertically placed microscope compatible cryo stage of Linkam Scientific Instruments (LTS420E-PB4). The temperature controller software LKS10043 is able to tune the temperature from -196 °C to 400 °C. The software controlled liquid nitrogen flow around the stage lead is used for cooling. On the other hand, electrical heating issued to increase the temperature of the stage and that too is controlled by the same software. There is a temperature sensor which senses the accurate temperature of the stage and gives the feedback to the software. According to the difference between the target temperature and

the present temperature of the stage, the software interfaces either the nitrogen flow to the stage or electrical heating. The minimum step of temperature is 0.01 °C for the stage. The details of the stage can be found in the website of Linkam Scientific Instruments as well. There were four pin probes within the stage to provide electrical bias to the sample.

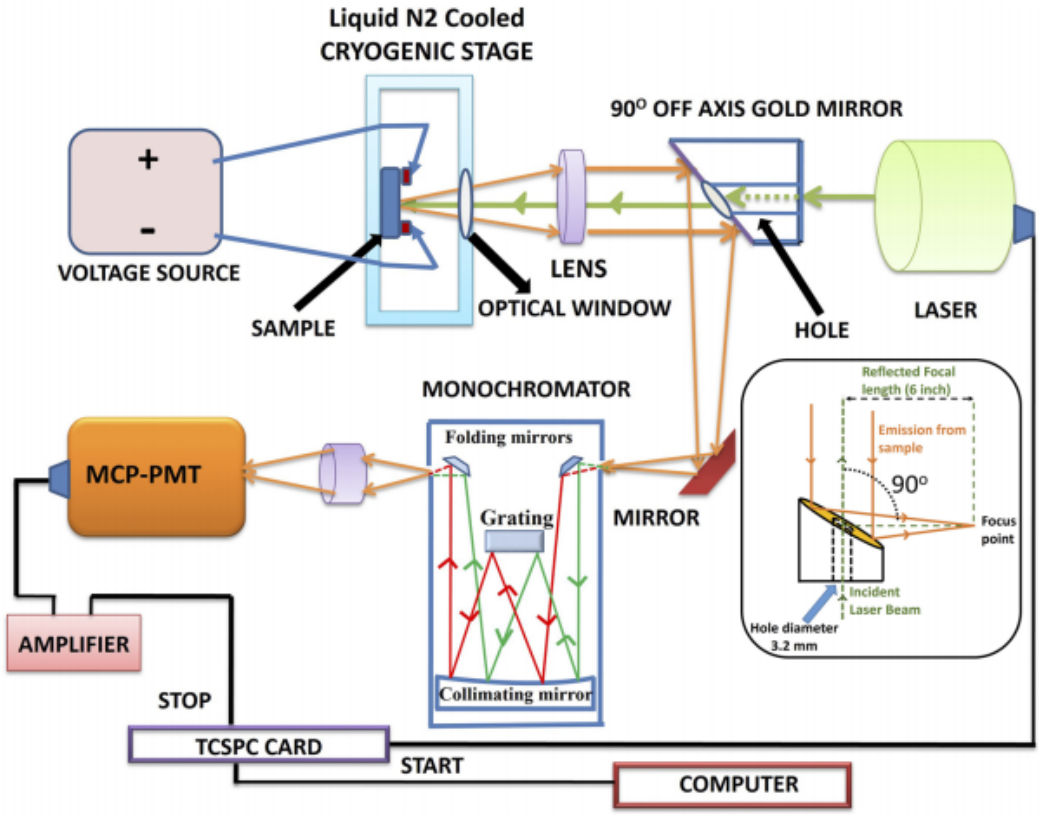

Figure 3.6. *Box diagram of the custom made cryo assisted NIR TCSPC experimental set up along with external voltage source for device sample. The inset shows the ray diagram of the 90° off axis gold mirror.*

The pin probes were connected to a tunable DC voltage source using external cables. The excitation laser of 2 mm beam diameter was passed through the central hole (3.2 mm diameter) of a 90° off axis gold coated parabolic mirror and focused on the sample using a plano-convex lens of 25.4 mm focal length at a spot size of 10 micron. The diverged emission was then collected through an optical window on the stage and has been collimated by the same planoconvex lens. Then, the collimated light was focused on the entry slit of a monochromator using a 90° off axis gold coated parabolic mirror (Thorlab, model number MPD269V_M01) and another reflecting mirror in the optical

path. Parabolic mirrors are able to focus collimated light without any spherical aberration on the axis of incident collimated light. Off-axis parabolic mirror is the side section of a parent parabolic mirror. Collimated light incident to an off-axis parabolic mirror is focused to a particular point at a specific angle with respect to the incident light. For an 90° off-axis parabolic mirror, the angle between the collimated beam and the reflected converging light is 90°. The ray diagram of the 90° off axis gold coated mirror is represented at the inset of Figure 3.6 and the details can be found at the website of Thorlab as well. The diverging light coming from the exit slit was again focused on the detector using a set of coupled plano-convex lens. All optical components (lenses and mirrors) including the 90° off axis gold coated mirror were purchased from Thorlab. The monochromator used in the signal collection path was purchased from Optometrics (Model 05) which has a blazing wavelength at 1.2 micrometer. For the detection of the signal a Hamamatsu Microchannel Plate Photomultiplier Tube (MCP-PMT) with a model number of R3809U-69 has been used. The wavelength response range of the detector is from 900 nm to 1700 nm. The TCSPC card used in the system is SPC-130 module of Becker & Hickl and the transient photoluminescence data was fitted using Micromath Scientist software using the deconvolution by iterative reconvolution method.

3.1.7. Transmission Electron Microscope (TEM): A Transmission Electron Microscope (TEM) is a powerful microscopy technique that allows for high-resolution imaging of thin samples, typically in the range of a few nanometers. It is widely used in various scientific disciplines, including materials science, biology, and nanotechnology. A TEM operates on the principle of transmitting a beam of electrons through a specimen to form an image. It uses a high-energy electron beam instead of light, which enables much higher resolution imaging due to the shorter wavelength of electrons. The electron gun in a TEM produces a beam of high-energy electrons. It consists of a filament that emits electrons when heated, an anode, and a series of electromagnetic lenses to focus the electrons into a narrow beam. The condenser lens system focuses and

shapes the electron beam before it passes through the specimen. It helps to control the illumination of the sample. The specimen holder holds the thin sample that is being analyzed. The sample needs to be prepared in a way that it is transparent to electrons. The objective lens is responsible for forming the image of the specimen. It further focuses the electron beam that has passed through the sample onto a fluorescent screen or a detector. The projection lens magnifies and projects the image formed by the objective lens onto a viewing screen or a camera. A TEM operates under high vacuum conditions to prevent the scattering and absorption of electrons by air molecules. The vacuum system maintains a low-pressure environment within the microscope column.

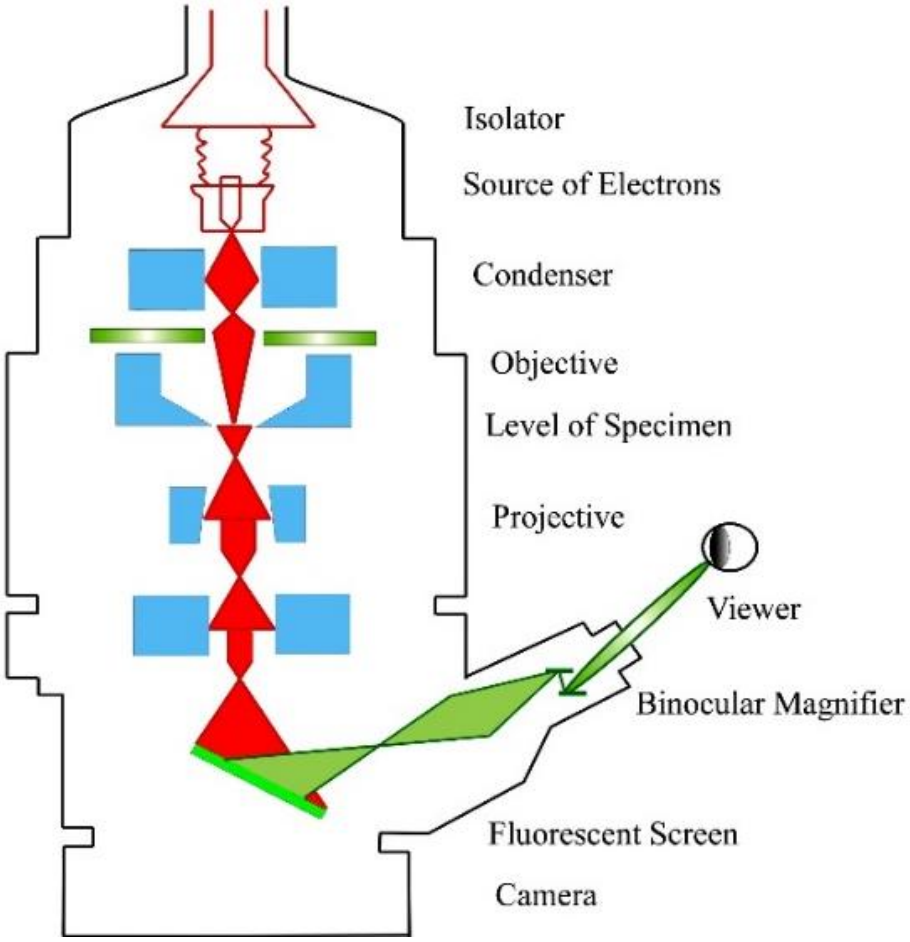

Figure 3.7: *Schematic diagram of a typical transmission electron microscope (TEM). After the transmission of the electron beam through a specimen, the magnified image is formed either in the fluorescent screen or can be detected by a charge-coupled device (CCD) camera.*

In image formation, the electron beam passes through the thin specimen, interacting with its atoms along the way. Some of the electrons are transmitted

through the specimen, while others are scattered or absorbed. The transmitted electrons carry information about the sample's internal structure and interact with a fluorescent screen or a detector to form an image. The resulting image provides detailed information about the sample's morphology, crystal structure, defects, and other properties at atomic or near-atomic scales.

Besides imaging, TEMs can be equipped with various detectors and accessories to perform advanced techniques, such as electron diffraction, energy-dispersive X-ray spectroscopy (EDS), electron energy-loss spectroscopy (EELS), and electron tomography. These techniques provide additional insights into the composition, elemental mapping, crystallography, and electronic properties of the sample. A FEI TecnaiTF-20 field-emission high-resolution TEM (Figure 3.7) equipped with energy dispersive X-ray (EDAX) spectrometer was used to characterize the microscopic structures of samples and to analyze their elemental composition. The sizes of the nanostructures were determined from the TEM images obtained at the 200 kV acceleration voltage of the microscope. Samples for TEM were prepared by placing a drop of the colloidal solution on a carbon-coated copper grid and allowing the film to evaporate overnight at room temperature.

3.1.8. Scanning Electron Microscope (SEM): A Scanning Electron Microscope (SEM) is a powerful imaging technique that uses a focused beam of electrons to create high-resolution, three-dimensional images of the surface of a sample. Unlike the Transmission Electron Microscope (TEM), which transmits electrons through a thin sample, the SEM scans the sample's surface with a beam of electrons and detects the signals emitted from the interaction between the electrons and the sample. The SEM operates on the principle of scanning a finely focused electron beam across the surface of a sample in a raster pattern. As the electron beam interacts with the sample, various signals are generated, which are then collected and used to create an image. The high energy electrons across the sample give rise to secondary electrons. The signal from secondary electrons is detected by the detector and amplified. The ray diagram

of the SEM setup is shown in Figure 3.8. The components of the electron gun in an SEM generates a beam of electrons. It typically uses a heated filament to produce a stream of electrons, which are then accelerated by high voltages towards the sample. The electron lenses in the SEM are responsible for focusing

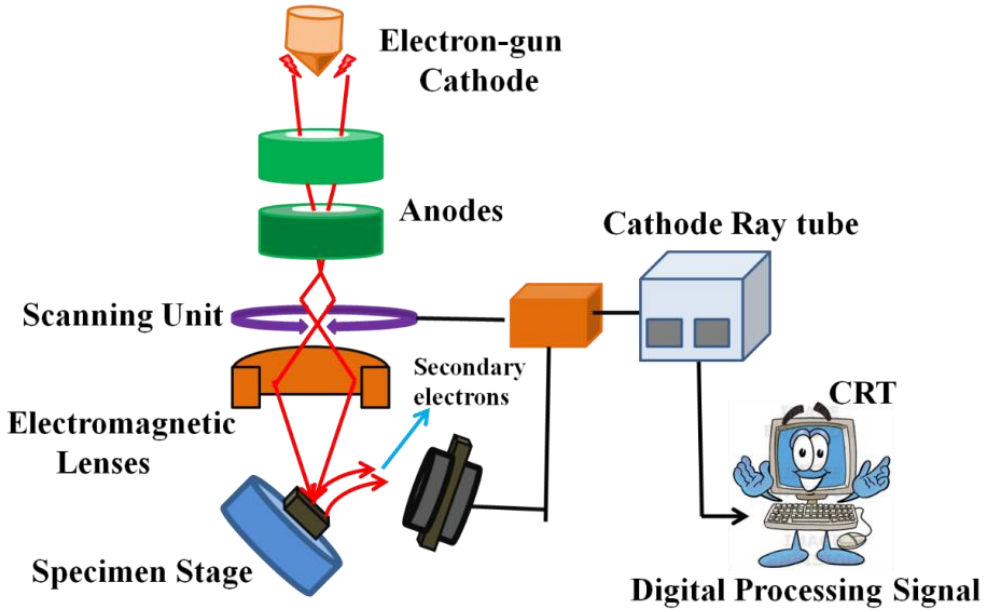

Figure 3.8: *Schematic diagram of a typical scanning electron microscope.*

and shaping the electron beam to a fine spot. They include condenser lenses that focus the beam onto the sample and objective lenses that focus the beam onto the detector. The sample stage holds the specimen and allows for precise positioning and movement of the sample under the electron beam. It may also have heating or cooling capabilities to study sample behavior under different temperature conditions. The scanning coils in the SEM are used to deflect the electron beam in a controlled manner, scanning it across the sample's surface. The scanning motion is typically done in a raster pattern to cover the entire area of interest. Various detectors are used to capture the signals generated by the interaction of the electron beam with the sample. The most common detectors include secondary electron detectors (SE) and backscattered electron detectors (BSE). These detectors measure the electrons that are scattered or emitted from the sample's surface and provide information about the topography and composition of the sample. Like TEMs, SEMs operate under

high vacuum conditions to prevent electron scattering and absorption by air molecules. The vacuum system maintains a low-pressure environment within the microscope chamber. Surface characterization of nano-materials was done by scanning electron microscope, FE (field emission)-SEM; JEOL. Ltd., JSM-6500F. An electron gun is attached to SEM and the electrons from the filament are triggered by 0 kV to 30 kV voltages. Electrons first go through a condenser lens and then through an objective lens, after that through an aperture, and finally, reach the specimen.

3.1.9. Dynamic Light Scattering (DLS): Dynamic light scattering (DLS), also known as photon correlation spectroscopy (PCS) or quasi-elastic light scattering (QELS), is one of the most popular techniques used to determine the hydrodynamic size of the particles.

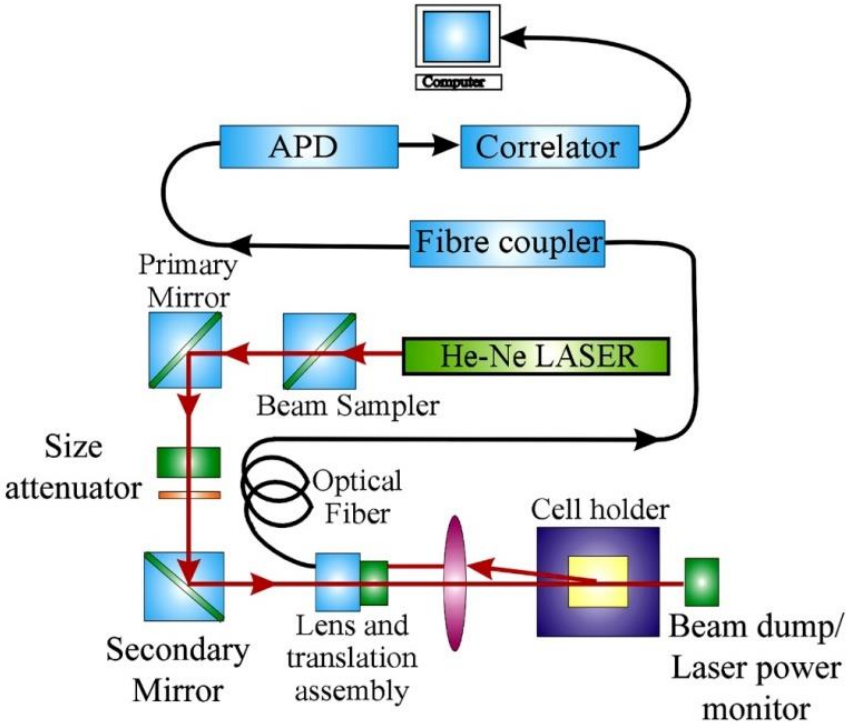

Figure 3.9: *Schematic ray diagram of dynamic light scattering (DLS) instrument. The avalanche photodiode (APD) is connected to the preamplifier/amplifier assembly and finally to the correlator. It has to be noted that lens and translational assembly, laser power monitor, size attenuator and laser are controlled by the computer.*

DLS measurements were performed on a Nano S Malvern instrument (U.K.), employing a 4 mW He-Ne laser (λ= 632.8 nm) and equipped with a

thermostatic sample chamber. The instrument allows DLS measurements in which all the scattered photons are collected at 173° scattering angle. The instrument measures the time-dependent fluctuation in intensity of light scattered from the particles in solution at a fixed scattering angle. The ray diagram of the DLS setup is shown in Figure 3.9. It has been seen that particles in dispersion are in a random Brownian motion and this causes the intensity of scattered light to fluctuate as a function of time. The correlator used in a DLS instrument constructs the intensity autocorrelation function G(τ) of the scattered intensity,

$$G(\tau) = \langle I(t)I(t+\tau)\rangle \tag{3.1}$$

where τ is the time difference (the sample time) of the correlator. For a large number of monodisperse particles in Brownian motion, the correlation function (given the symbol G) is an exponential decay function of the correlator time delay τ,

$$G(\tau) = A[1 + B\exp(-2\Gamma\tau)] \tag{3.2}$$

where A is the baseline of the correlation function, and B is the intercept of the correlation function. Γ is the first cumulant which is related to the translational diffusion coefficient as, $\Gamma = Dq^2$, where q is the scattering vector and its magnitude is defined as,

$$q = \left(\frac{4\pi n}{\lambda_0}\right)\sin\left(\frac{\theta}{2}\right) \tag{3.3}$$

where n is the refractive index of dispersion, λ_0 is the wavelength of the laser, and θ is the scattering angle. For polydisperse samples, the equation can be written as,

$$G(\tau) = A\left[1 + B\left|g^{(1)}(\tau)\right|^2\right] \tag{3.4}$$

where the correlation function $g^{(1)}(\tau)$ is no longer a single exponential decay and can be written as the Laplace transform of a continuous distribution G(Γ) of decay times,

$$g^{(1)}(\tau) = \int_0^\infty G(\Gamma)\exp(-\Gamma\tau)d\Gamma \tag{3.5}$$

The scattering intensity data in DLS are processed using instrumental software to obtain the hydrodynamic diameter (d_H) and the size distribution of the scatterer in each sample. In a typical size distribution graph from the DLS measurement, *X*-axis shows a distribution of size classes in nm, while the *Y*-axis shows the relative intensity of the scattered light. The diffusion coefficient (D) can be calculated using the d_H of the particle from the Stoke-Einstein relation,

$$D = \frac{k_B T}{3\pi\eta d_H} \tag{3.6}$$

where k_B, T, d_H, η are Boltzmann constant, the temperature in Kelvin, hydrodynamic diameter and viscosity, respectively.

3.1.10. X-ray Diffraction (XRD) Measurement: XRD is a popular and powerful technique for determining the crystal structure of crystalline materials. By examining the diffraction pattern, one can identify the crystalline phase of the material. Small-angle scattering is useful for evaluating the average interparticle distance while wide-angle diffraction is useful for refining the atomic structure of nanoclusters. The widths of the diffraction lines are closely related to strain and defect size and distribution in nanocrystals. As the size of the nanocrystals decreases, the line width is broadened due to the loss of long-range order relative to the bulk. This XRD line width can be used to estimate the size of the particle by using the Debye-Scherrer formula 3.7. XRD measurements were performed on a PANalytical XPERT-PRO diffractometer (Figure 3.10) equipped with CuKα radiation (λ = 1.5418 Å at 40 mA, 40 kV).

XRD patterns were obtained by employing a scanning rate of 0.02° s^{-1} in the 2θ range from 10° to 80°.

$$D = \frac{0.9\lambda}{\beta \cos\theta} \tag{3.7}$$

where, D is the nanocrystal diameter, λ is the wavelength of light, β is the full-width half-maximum (FWHM) of the peak in radians, and θ is the Bragg angle.

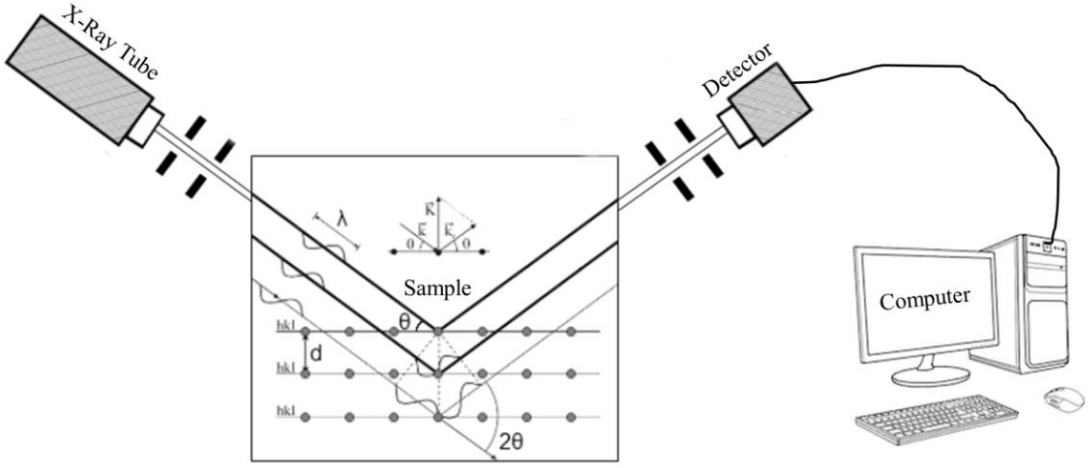

Figure 3.10: *Schematic diagram of an X-ray diffraction (XRD) instrument. By varying the angle θ, the Bragg's law conditions, nλ = 2dsinθ are satisfied by different d-spacings in polycrystalline materials. Plotting the angular positions and intensities of the resultant diffracted peaks of radiation produces a pattern, which is characteristic of the sample.*

3.1.11. Thermogravimetric Differential Thermal Analyzer (TG-DTA): The thermogravimetric (TG) analysis was carried out using a diamond TG-differential thermal analyzer (DTA) from Perkin Elmer. The TG determines the weight change of a sample whereas the DTA measures the change in temperature between a sample and the reference as a function of temperature and/or time. The schematic representation of the TG-DTA setup is shown in Figure 3.11. When a weight change occurs on the sample side, the beam holding the platinum pans is displaced. This movement is detected optically and the driving coil current is changed to return the displacement to zero. The detected driving coil current change is proportional to the sample weight change and the output is the TG signal. The DTA detects the temperature difference between the sample holder and the reference holder using the

electromotive force of thermocouples, which are attached to the holders. This difference is measured as the DTA signal.

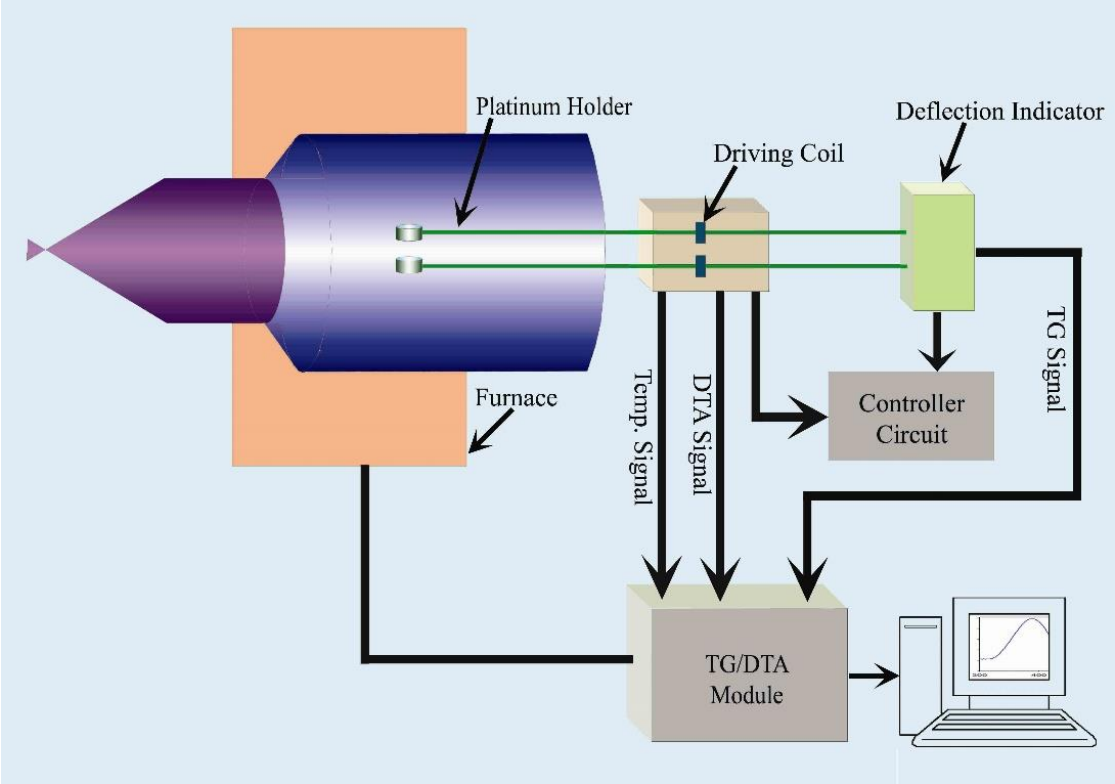

Figure 3.11: *The schematic representation of the TG-DTA setup.*

3.1.12. Fourier Transform Infrared (FTIR) Measurement: FTIR spectroscopy is a technique that can provide very useful information about functional groups in a sample. An infrared spectrum represents the fingerprint of a sample with absorption peaks which correspond to the frequencies of vibrations between the bonds of the atoms making up the material. Because each different material is a unique combination of atoms, no two compounds produce the same infrared spectrum. Therefore, infrared spectroscopy can result in an identification (qualitative analysis) of different kinds of material. Also, the size of the peaks in the spectrum is a direct indication of the amount of material present. The two-beam Michelson interferometer is at the heart of the FTIR spectrometer. It consists of a fixed mirror (M4), a moving mirror (M5), and a beam-splitter (BS1), as illustrated in Figure 3.12. The beam-splitter is a laminate material that reflects and transmits light equally. The collimated IR beam from the source is partially transmitted to the moving mirrors and partially reflected

in the fixed mirror by the beam-splitter. The two IR beams are then reflected in the beam-splitter by the mirrors. The detector then detects the transmitted beam from the fixed mirror and the reflected beam from the moving mirror, simultaneously. The two combined beams interfere constructively or destructively depending on the wavelength of the light (or frequency in wavenumbers) and the optical path difference introduced by the moving mirror. The resulting signal is called an interferogram which has the unique property that each data point (a function of the moving mirror position) which makes up the signal that has information about every infrared frequency which comes from the source. Because the analyst requires a frequency spectrum (a plot of the intensity at each frequency) to make an identification, the measured interferogram signal cannot be interpreted directly.

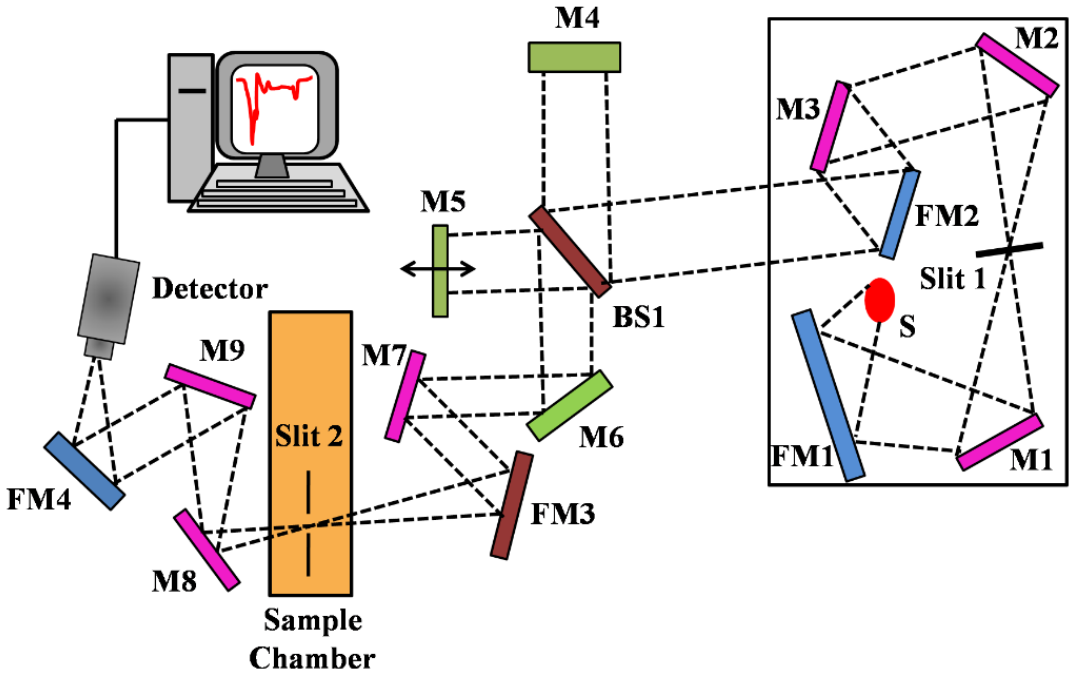

Figure 3.12: *Schematic representation of fourier transform infrared (FTIR) spectrometer. It is a Michelson interferometer in which one of the two fully-reflecting mirrors is movable, allowing a variable delay (in the travel time of the light) to be included in one of the beams. M, FM, and BS1 represent the mirror, focusing mirror and beam splitter, respectively. M5 is a moving mirror.*

A means of "decoding" the individual frequencies is required, which can be accomplished *via* a well-known mathematical technique called the Fourier transformation. This transformation is performed by the computer which then

presents the user with the desired spectral information for analysis. FTIR measurements were performed on a JASCO FTIR-6300 spectrometer (transmission mode). For the FTIR measurements, powdered samples were mixed with KBr powder and pelletized. The background correction was made using a reference blank KBr pellet. Some time Fourier transform infrared spectroscopy (FTIR) of the powder samples are also performed with the attenuated total reflectance (ATR) method using a Vertex 70 V instrument (Bruker, Germany).

3.1.13. Laser Raman Spectroscopy: Raman spectroscopy is a useful technique for the identification of a wide range of substances- solids, liquids, and gases. It is a straightforward, non-destructive technique requiring no sample preparation. Raman spectroscopy involves illuminating a sample with monochromatic light and using a spectrometer to examine light scattered by the sample.

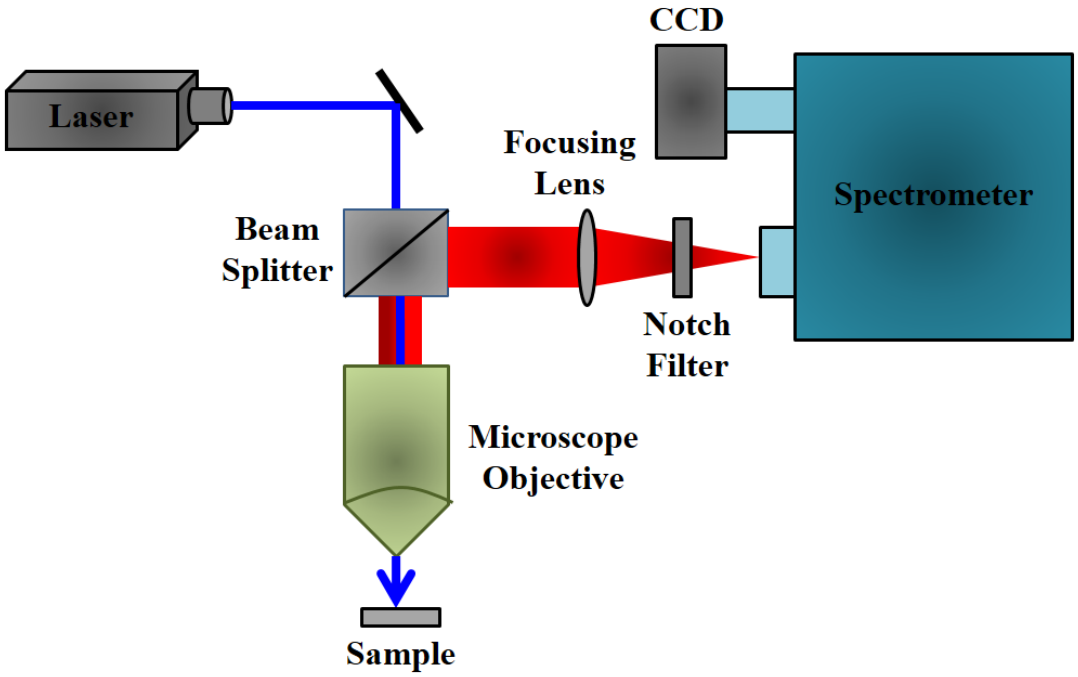

Figure 3.13: *A schematic diagram of a Raman spectrometer.*

At the molecular level photons can interact with matter by absorption or scattering processes. Scattering may occur either elastically, or inelastically. The elastic process is termed Rayleigh scattering, whilst the inelastic process is

termed Raman scattering. The electric field component of the scattering photon perturbs the electron cloud of the molecule and may be regarded as exciting the system to a 'virtual' state. Raman scattering occurs when the system exchanges energy with the photon and the system subsequently decays to vibrational energy levels above or below that of the initial state. The frequency shift corresponding to the energy difference between the incident and scattered photon is termed the Raman shift. Depending on whether the system has lost or gained vibrational energy, the Raman shift occurs either as an up or down-shift of the scattered photon frequency relative to that of the incident photon. The down-shifted and up-shifted components are respectively called the Stokes and anti-Stokes lines. A plot of the detected number of photons versus Raman shift from the incident laser energy gives Raman spectrum. Different materials have different vibrational modes, and therefore characteristic Raman spectra. This makes Raman spectroscopy a useful technique for material identification. There is one important distinction to make between the Raman spectra of gases and liquids, and those taken from solids− in particular, crystals. For gases and liquids, it is meaningful to speak of the vibrational energy levels of the individual molecules which make up the material. Crystals do not behave as if composed of molecules with specific vibrational energy levels; instead, the crystal lattice undergoes vibration. These macroscopic vibrational modes are called phonons. In modern Raman spectrometers (Horiba LabRAM setup), lasers are used as a photon source due to their highly monochromatic nature, and high beam fluxes (Figure 3.13). This is necessary as the Raman effect is weak, typically the Stokes lines are ~10^5 times weaker than the Rayleigh scattered component. In the visible spectral range, Raman spectrometers use notch filters to cut out the signal from a very narrow range centered on the frequency corresponding to the laser radiation. Most Raman spectrometers for material characterization use a microscope to focus the laser beam to a small spot (<1−100 μm diameter). Light from the sample passes back through the microscope optics into the spectrometer. Raman-shifted radiation is detected with a CCD detector and a computer is used for data acquisition and curve

fitting. These factors have helped Raman spectroscopy to become a very sensitive and accurate technique.

3.1.14. Fluorescence Microscope: Commercially available fluorescence microscope (Leica digital inverted microscopes DMI8.) was used in our study.

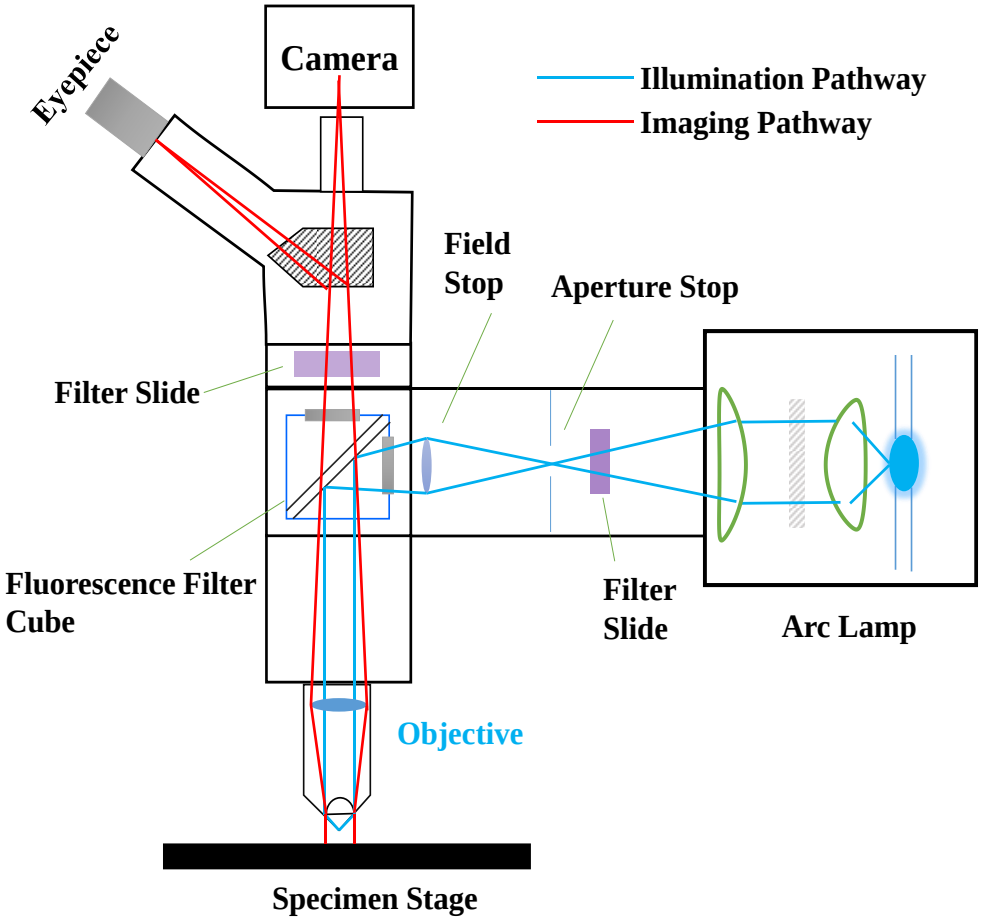

Figure 3.14. *Schematic presentation of the fluorescence microscope.*

The light source is usually a mercury-vapor lamp. For bright field, Tungsten-halogen lamp was used. In particular, an inverted setup with a mercury-vapor lamp as light source is shown in Figure 3.14. The dichroic mirror, excitation and emission filter are joined together within the filter cube (Figure 3.14). Since mercury-vapor lamps emit light over the whole optical spectrum as well as in the ultraviolet range, an optical excitation filter is used to isolate one specific wavelength. Due to the Stokes shift, it is possible to separate excitation and emission light in the same light path optically via a dichroic mirror. This way,

only the emission light is collected by the objective. An emission filter helps to suppress unwanted background light.

3.1.15. Hydrothermal Technique: The hydrothermal technique has been the most popular one, gathering interest from scientists and technologists of different disciplines, for the synthesis of different nanomaterials. The hydrothermal reaction is defined as any heterogeneous chemical reaction in the presence of a solvent (whether aqueous or non-aqueous) above room temperature and a pressure greater than 1 atm in a closed system.

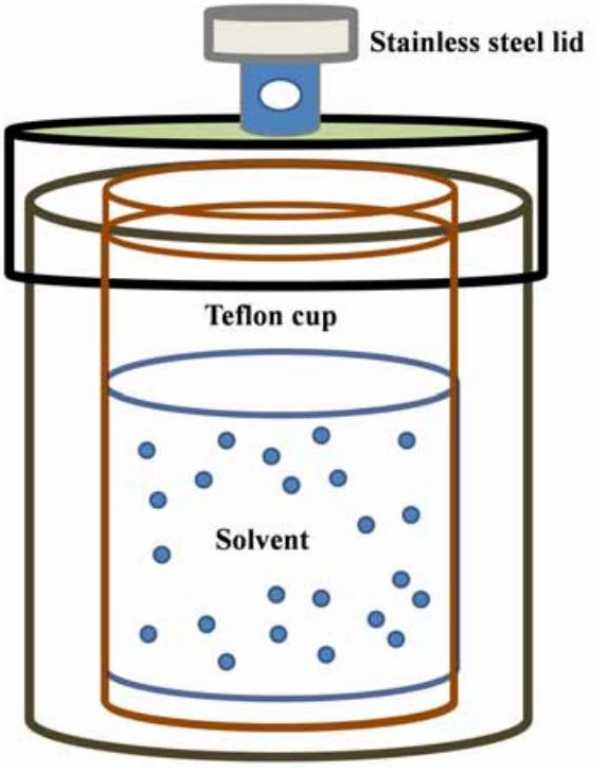

Figure 3.15: *Schematic representation of an lined stainless steel autoclave.*

Crystal growth under hydrothermal conditions requires a reaction vessel called an autoclave. The autoclave must be capable of sustaining highly corrosive salt, which is used to synthesize inorganic materials at high temperatures and pressure for a longer duration of time. For selecting a suitable autoclave, the first and foremost parameter is the experimental temperature and pressure conditions, and the corrosion resistance in that pressure-temperature range in a given solvent or hydrothermal fluid. To avoid corrosion of autoclave material it

should be coated with non-reactive material called Teflon from inside. Due to the larger coefficient of thermal expansion of Teflon versus metal, the Teflon will expand and contract much more upon heating and cooling cycles than its enclosure material. For the synthesis of nanomaterials, we have used the Teflon-lined stainless steel autoclave of 30 mL capacity (Figure 3.15). The autoclave was rested at the desired temperature under autogenous pressure for the desired time.

3.1.16. Electrochemical Impedance Spectroscopy (EIS): Electrochemical Impedance Spectroscopy (EIS) is a powerful technique to investigate the electronic and ionic processes in photovoltaic devices. Electrochemical impedance is usually measured by applying an AC potential to an electrochemical cell and then measuring the current through the cell.

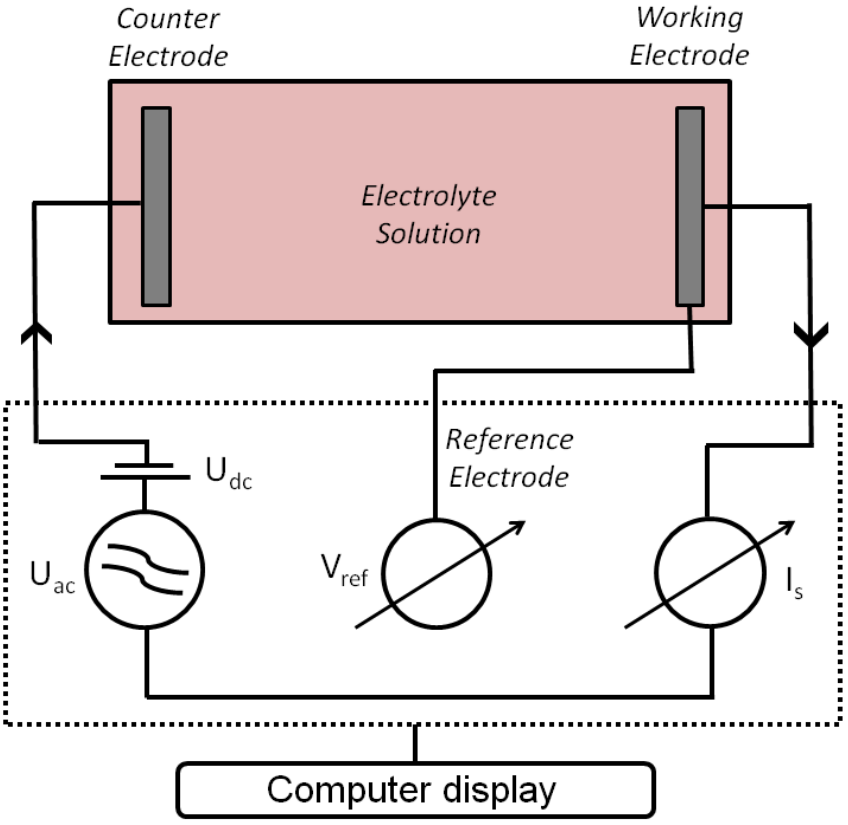

Figure 3.16. *Schematic diagram of a simplified measurement circuit for performing Electrochemical Impedance Spectroscopy (EIS).*

An important advantage of EIS over other techniques is the possibility of using tiny AC voltage amplitudes exerting a very small perturbation on the system.

A Nyquist plot can be made by plotting the real part of the transfer function on the X-axis and the imaginary part on the Y-axis. The Nyquist diagram features typically three semicircles that in the order of increasing frequency are attributed to the Nernst diffusion within the electrolyte, the electron transfer at the oxide/electrolyte interface and the redox reaction at the platinum counter electrode. From applying appropriate equivalent circuits, the transport rate and lifetime of the electron in the mesoscopic film are derived. Electrochemical impedance spectroscopy (EIS) were performed on an electrochemical workstation CHI650E (CH instruments) with a frequency range from 100 kHz to 0.1 Hz in the open circuit condition. The schematic presentation of the EIS set up is shown in Figure 3.16. All impedance measurements were carried out under a bias illumination of 100mW/cm^2. The obtained spectra were fitted using the CHI650E software in terms of appropriate equivalent circuits.

The system containing thin films were used as a working electrode with a 0.27 cm^2 geometric area exposed to the electrolyte solution under light irradiation. The experiments were performed in a conventional three-electrode cell using Ag/AgCl (3.5 M KCl) used as a reference electrode, Pt-foil as counter electrode and the sample coated film as the working electrode. The photo-electrochemical measurement was executed in 0.1 M Na_2SO_3 with 0.1 M Na_2SO_4 solution for SO_3^{2-} (sacrificial) oxidation reaction within the potential range from 0.1 to 0.6 V using a CHI650E potentiostat (CH Instrument, Austin, TX) at a scan rate of 10 mV/s. The water oxidation reaction was carried out in 0.1 M Na_2SO_4 solution in PBS (pH 7) using a similar experimental set up within the range from 0.0 to 1.0 V [2]. The EIS measurements were performed using a similar experimental setup with 0.1 M Na_2SO_4 (in pH 7 PBS) solution employing Autolab 302N PG-stat with a frequency response analyzer (FRA). In the Nyquist plot, the variation of real and imaginary parts of the impedance at different frequencies within the range of 100 kHz to 20 MHz was obtained under UV- visible illumination at an applied potential of 0.8 V. The stability of the system undergoing a water oxidation reaction was examined through

chronoamperometry using the same reaction condition under constant illumination of 100 W/cm^2 at an applied potential of 0.8 V for 30 min [2].

The classical definition of external quantum efficiency (EQE) is the ratio between the numbers of molecules degraded by the number of incident photons involved in the catalysis process [3-5]. The EQE is denoted by the below equation –

$$\text{EQE} = \frac{<reaction\ rate(mol/sec)>}{<photon\ rate(einstein/sec)>} \times 100\% \quad (3.8)$$

EQE of the semiconductor is also calculated from the photo-induced current measurement process. Incident Photon to Charge Carrier Efficiency (IPCE) was calculated by determining the power of the incidental beam of light at a specified wavelength, using the following equation

$$\text{IPCE}\ (\%) = (1240/\lambda) \times (I_{Ph}/P_{in}) \times 100\ \% \quad (3.9)$$

where λ is the wavelength of the incident light, I_{Ph} is the measured photocurrent of the system (in mA/cm^2) and P_{in} is the power of incident beam (in mW/cm^2) [6].

3.1.17. Electrode Preparation for Photocurrent Measurement: 100 mg of NPs were suspended in 5 ml EG and the mixtures were kept in an ultra-sonication bath for ~1 hr. Then 400 µl of the mixture was dropped cast onto a clean ITO coated rectangular size glass plate of dimension 1.5 × 1.5 cm^2 to prepare thin films of samples. The NP coated thin films were annealed in air at ~350 °C for 6 hr. with a ramping rate of 1°C per min. followed by soaking for 3 hr. to obtain uniform, well-adhered thin films.

3.1.18. Light Source Used to Illuminate Samples: For UV light-mediated experiment a homemade UV light source of 360 nm – 500 nm was used to irradiate samples under UV-blue range. For visible light-driven experiments, a readymade light source (λ = ~400 nm to 560 nm and power = 3 mW/cm^2) has been used. For NIR light source a tungsten-halogen light with a 650 nm high-pass filter has been used. A 300 W Xe-lamp (Excelitas USA) with 100 mW/cm^2

illumination was utilized as the light source for the photo-electrochemical measurements.

3.1.19. Photostability Measurement: To characterize the photostability of ZIF8-IR820 nano-MOF, we used the ZIF8-IR820 nano-MOF and IR820 in ethanol solvent. The concentration of IR820 in the ZIF8-IR820 nano-MOF was 1.6 µM and the same concentration of pristine IR820 was used for the measurement. The optical density (OD) measurements were collected at 819 nm in 3 minutes intervals of time under a white LED lamp of power 12 watts and wavelength range 400 nm to 800 nm [7].

3.1.20. Aqueous Stability Measurement: To check the water stability of all the ZIF samples, we have synthesized ZIFs using methanol as the suitable solvent. For all the solution phase experiments, we used dimethyl sulphoxide (DMSO) as the solvent. The solid samples are poured into water for a certain time and then it was collected using multiple centrifugation steps. Finally, the water treated solids are heated at 60 °C for 3 hr for drying before the XRD analysis. The water stability experiments are performed using solid ZIF samples. 2 mg of each of the samples are dissolved in DMSO and 100 µL of the solution is mixed with 2 mL of distilled water. The absorbance at 595 nm is measured at a 1 minute time interval. Moreover, the solid samples are kept in water for 10 days at room temperature, dried and XRD is recorded. The morphology of the ZIFs is analyzed using scanning electron microscopy (Quanta FEG 250: FEG source; accelerating voltage, 200 V to 30 kV; resolution).

3.1.21. pH-responsive Dissolution: To investigate the dissolution pattern of $Zn_{50}Co_{50}$-ZIF, 2 mg sample is dissolved in DMSO and 100 µL of the solution is mixed separately with 2 mL of phosphate buffer (pH = 7.4) and acetate buffer (pH = 5.5). The absorbance at 595 nm is monitored at an hour interval of time.

3.1.22. Drug Loading Capability: The RF drug loading capability (DLC) was measured in an ethanol solution of RF. The absorption peak of RF was collected before and after loading onto ZIF8 sample and by relating the absorption peak

intensity at 480 nm DLC (in percentage) was calculated as per the below equation:

$$\frac{\text{The amount of drug loaded}}{\text{The amount of ZIF8 sample}} \times 100 \quad (3.10)$$

3.1.23. Photocatalytic Measurements: The photocatalytic measurements of the systems have been carried out using photocatalytic degradation of dyes at ambient temperature. The sample was taken in a quartz cuvette (1 mg in 2 ml aqueous medium) and toxic dye (TD) was added to it to get an absorption peak height of 0.6 a.u. The total suspension was then exposed to a light source and absorbance data were collected at 10 minutes interval of time. The percentage degradation (% DE) of TD was determined using the following equation,

$$\% DE = \frac{I_0 - I(t)}{I_0} \times 100 \quad (3.11)$$

For photocatalysis using stainless steel mesh (SSM), a 1 cm^2 mesh has been taken for the experiment. Initially, sample has been decorated on the mesh using the hydrothermal method described above. The nanoparticle decorated mesh is placed into a beaker containing 5 mL of water. The whole system is exposed to light for 4 hrs and data has been collected at 20 minutes time interval. The photocatalytic activity of the mixed ZIF under visible light illumination was performed for photo-decomposition of methylene blue (MB), a model pollutant in an aqueous solution. The photodegradation of MB was examined in a quartz cell (1 cm optical path) containing 3 mL of the solution (1 gL^{-1}) of ZIF. The suspension was irradiated under visible light using a standard white LED light source of 6-watt power and date were taken out at certain time intervals.

3.1.24. DPPH Assay for *In Vitro* Antioxidant Activity Study: UV-vis assisted DPPH assay was performed to study the antioxidant activity of the samples using the reported methodology [8]. The degradation kinetics of 2, 2-diphenyl-1-picrylhydrazyl (DPPH) was observed and monitored by measuring the

decrease in this characteristic absorption peak of DPPH at 520 nm as a function of time. The assay was performed in the dark as well as in the presence of light irradiation and the time interval between two consecutive data was 5 minutes.

3.1.25. Preparation of DCFH for Extracellular ROS Generation Study: DCFH was prepared by the de-esterification reaction of DCFH-DA at room temperature [8]. DCFH was prepared by the composition of 0.5 ml of 1.0 mM DCFH-DA in methanol solvent with 2.0 ml of 0.01 N aqueous NaOH for 30 minutes at room temperature. The mixture was neutralized to pH = 7.4 by 10 ml of 25 mM NaH_2PO_4 solution [9]. The final solution was stored on ice in dark condition. In this assay, DCFH oxidation leads to the formation of a fluorescent DCF, which can be taken upon excitation at the wavelength of 488 nm, using steady-state fluorescence emissions. The extends in the fluorescence intensity at around 520 nm reflects the generation of ROS. For recyclability assay, fresh DCFH is added to the system after 1 hr and the assay is continued for consecutive three cycles. The standard white light source of wavelength 400 nm to 700 nm is used to irradiate the samples.

In order to investigate the DCFH oxidation experiment of Au_ZnO and Au_ZnO-TC, we have used concentration of TC (1.4 μM), ZnO-TC hybrid (the concentration of TC in the nanohybrid is 1.4 μM) and Au_ZnO and Au_ZnO-TC were checked from optical density (OD). The concentration-dependent ROS activity of tri-hybrid is also performed for different concentrations (C1, 5.2 μM; C2, 7.8 μM, C3, 10.4 μM and C4, 13.0 μM) of Au_ZnO-TC tri-hybrid. The room temperature steady-state fluorescence emissions were collected at 525 nm upon an excitation wavelength of 485 nm. The ROS experiments were performed in dark followed by irradiation of white light of wavelength 400 nm to 700 nm. To measure the ROS production capability of ZIF8-IR820, the concentration of the samples was confirmed from OD measurement. We used 1 μM concentration of only IR820 dye and the same concentration of IR820 was fixed in ZIF8-IR820 by maintaining a similar OD at 819 nm. The concentration of ZIF-8 was maintained by keeping the same OD of ZIF-8 with the ZIF8-IR820 nano-MOF

which contains 1 μM of IR820. The pH-dependent ROS measurement was performed in PBS buffer media of two different pH values (pH = 5.5 and pH = 7.4). The concentration dependent ROS studies were measured for four different concentrations (C1, 0.1 OD; C2, 0.15 OD; C3, 0.2 OD and C4, 0.25 OD) of ZIF8-IR820 nano-MOF. The ROS experiment was completed in dark initially for 15 minutes and then under treatment of red light irradiation of wavelength 640 nm for 25 minutes.

3.1.26. *In Vitro* Photodynamic Therapy (PDT): The antibacterial assays of $Zn_{50}Co_{50}$-ZIF have been performed using antibiotic-resistant bacterial strains of gram-positive methicillin-resistant *S. aureus* (MRSA). To perform the growth performance of bacteria under different treatment conditions, bacterial culture of 12 hrs is diluted 20 times and different samples are added. The samples were incubated for 2 hrs followed by light irradiation of 30 minutes. The absorbance at 540 nm is monitored with 30 minutes intervals. Only bacterial culture is considered as negative control. The absorbance is plotted against time and the nature of the plot suggests the relative effectiveness of the ZIF samples as an antibacterial agent. For colony forming unit assay, we have chosen 1 mg/mL concentration of the sample. MRSA culture was incubated with the requisite sample for 3 hrs under dark conditions followed by 30 minutes of white light irradiation followed by plating of the cultures. The plates were incubated overnight at 37 °C and well-grown colonies were counted for estimation of the antibacterial effect of the $Zn_{50}Co_{50}$-ZIF sample.

The bacterial culture of ZIF8-RF was evaluated using MRSA (strain 1692) as the typical culture. The MRSA bacteria growth in Luria Broth (LB) media was performed in a shaker incubator at 37 °C. The colony forming unit (CFU) assay was performed on MRSA bacterial cells. Once the optical density (OD) reached ~0.6 in the absorbance band, the MRSA bacterial culture was diluted 10^3 times. The culture was treated by ZIF8-RF (for four different concentrations C1: 0.25 mg/mL sample, C2: 0.50 mg/mL sample, C3: 0.75 mg/mL sample and C4: 1.00 mg/mL sample of ZIF8-RF) and RF (maintaining the OD at 480 nm similar to

the ZIF8-RF nanohybrid) for 3 hrs. 100 µl from each of the treated samples were spread on agar plates and incubated at 37 °C overnight. The CFU were counted after incubation and the triplicate of the experiment was carried out, and the results were expressed with proper statistical P value less than equal to 0.05.

The antibacterial culture of ZnO-NF has been performed with *E. Coli* cells following a reported method [10]. To observe the bacterial growth analysis under different treatment conditions, bacteria cells were cultured at 37 °C in Luria Broth (LB) medium for 12 hrs, diluted 1000 times and different samples are added. The bacterial assay experiment has been cultured in different cuvettes containing 30 nm ZnO-NF nanohybrids (0.5 mg/mL sample of nanohybrids which contains 0.5 µM NF), 30 nm ZnO nanoparticles (maintaining the O.D. at 369 nm similar to the 30 nm ZnO nanohybrid), NF (concentration of NF used on the basis of NF loading on the surface of ZnO nanoparticles) and DMSO. The samples were incubated at 37 °C after irradiation of UV light (wavelength 375 nm) for 30 minutes. In order to verify the reduction effect of drugs, absorbance was taken in 1 hr interval of time and it has been performed up to ~25 hrs. Finally, the absorbance of all the samples has been performed and plotted with respect to time. The nature of the plot suggests the relative effectiveness of the ZnO-NF samples as antibacterial drugs.

The antimicrobial activity of ZIF8-IR820 samples was investigated against *Staphylococcus hominis* as the model bacteria. *Staphylococcus hominis* were cultured in an incubator shaker of temperature at 37 °C in LB medium for 24 hrs. The experiments proceeded with freshly grown *Staphylococcus hominis* culture, diluted 10^5 times and the samples were added on it. Initially, the dark toxicity was checked for four different concentrations (1 mg/ml, 0.75 mg/ml, 0.5 mg/ml, 0.25 mg/ml and 0.125 mg/ml) of the ZIF8-IR820 nano-MOF. The treatment of white light was introduced on the optimized concentration (0.125 mg/ml) of ZIF8-IR820 nano-MOF. The bacterial cells were incubated for 2.5 hrs followed by 25 minutes irradiation of red light. Then cultures were spread

uniformly on LB agar plates, then it is incubated at 37 °C for 24 hrs to get the number of viable cells. The photo-dose dependent antibacterial action of 0.125 mg/ml ZIF8-IR820 nano-MOF was performed under red light illumination in 5 minutes interval of time.

The antibacterial action of Au_ZnO-TC tri-hybrids has been performed against *S. hominis* bacteria. The fresh bacteria of *S. hominis* has cultured in a shaker incubator at a temperature of 37 °C for 16 hrs. The freshly grown *S. hominis* culture was diluted 10^5 times. Treatment of bacteria has been performed by the samples. The experiment was done on LB agar plates by the colony forming unit (CFU) assays method. Initially, the dark toxicity was optimized by performing concentration dependent antibacterial activity (0.125 mg/ml, 0.25 mg/ml, 0.5 mg/ml, 0.75 mg/ml and 1 mg/ml sample) of the Au_ZnO-TC tri-hybrids. The treatment of light was performed with an optimized concentration of Au_ZnO-TC tri-hybrid which is 0.25 mg/ml. The *S. hominis* cells were incubated for 2.5 hrs at 37 °C followed by 25 minutes illumination of white light. Then the treated bacteria were spread uniformly on agar plates.

3.1.27. Bacterial Biofilm Development Technique: The biofilms of MRSA bacteria were prepared in LB media on 60 mm antiseptic polycarbonate Petri plates. These cells were uniformly spread over the Petri plate and then incubated for 2 days at 37 °C temperature [11]. Crystal violet (CV; 0.1% (w/v)) assay analysis was used to measure the biofilms. After then it was solubilized in 95% ethanol. The level of biofilm arrangement was assessed using the UV-vis absorbance band at 588 nm. The biofilms have also been cultured by the ZIF8-RF sample (concentration C3) with respect to control MRSA and the morphological variations of the biofilms were obtained using SEM setup.

3.2. Chemicals Used:

The chemicals and spectroscopic probes were procured from the following sources. Analytical-grade chemicals were used for synthesis without further purification. Deionized (DI) water obtained from Millipore, was used to

prepare all aqueous solutions. Different solvents including Methanol, Ethanol, DMSO, and Ethylene Glycol were purchased from Sigma-Aldrich. Polyethylene glycol (PEG) (M_w = 1000) was brought from Fluka. The probes methylene blue (Carlo Erba), methyl orange (Sigma-Aldrich), 2,2-Diphenyl-1-picrylhydrazyl (DPPH) (Sigma-Aldrich), the dyes protoporphyrin IX (Sigma-Aldrich), curcumin (Cur) (Sigma-Aldrich), phthalocyanine (Sigma-Aldrich), anhydrous iron(III) chloride ($FeCl_3$), norfloxzcin (Sigma-Aldrich), rifampicin (Sigma-Aldrich), Tetracyclin (Sigma-Aldrich), 2-methyl imidazolate (Sigma-Aldrich), $Zn(NO_3)_2 \cdot 6H_2O$ (Sigma-Aldrich), $CoCl_2$ (Sigma-Aldrich), indocyanine green IR820 (Sigma-Aldrich), Na_2CO_3 (Sigma- Aldrich), NaOH (Sigma-Aldrich), silver nitrate ($AgNO_3$) (Sigma- Aldrich), tri-sodium citrate (Sigma-Aldrich), $NaBH_4$ (Sigma- Aldrich), ZnO nanoparticles (Sigma- Aldrich), Gold(III) chloride $HAuCl_4 \cdot 3H2O$ (Sigma- Aldrich) were purchased for experimental work. The solution of chromium chloride hexahydrate salt ($CrCl_3 \cdot 6H_2O$), ammonium hydroxide (NH_4OH), Dichlorofluorescin (DCFH) (Sigma- Aldrich), Na_2HPO_4, crystal violet, phthalocyanine and zinc acetate dehydrate ($Zn(CH_3CO_2)_2 \cdot 2H_2O$) (Sigma-Aldrich) were also purchased from Sigma-Aldrich.

3.3. Sample Preparation:

In this section, all the sample preparation methods have been discussed.

3.3.1. Synthesis of $Zn_{50}Co_{50}$ Systems: $Zn_{50}Co_{50}$ nanocrystals have been prepared by employing Zn, Co and Hmim (2-methyl imidazolate) ligand ratio as 1:1:8. The concentration of metals and ligand are chosen based on the previously reported results of mixed ZIF synthesis [10]. The synthesis has been carried out through an easy and facile route following a one-pot procedure [12]. In a typical synthesis of ZIF, metal and ligand solutions are prepared individually in the same volume of methanol 5 mL methanolic solution has been prepared using 50 mM of each of the metal salt. Ligand solution is prepared by dissolving 292 mg Hmim in 5mL methanol. The two solutions are

mixed under stirring conditions at room temperature and kept undisturbed for 24 hrs. The resultant solid products are collected by centrifuging (at 5000 rpm, 5 minutes), washed thrice with methanol to remove excess Hmim and then dried overnight at room temperature. ZIF-8 and ZIF-67 are synthesized following the reported strategy using $Zn(NO_3)$ and $CoCl_2$ as precursors respectively.

3.3.2. Synthesis of ZIF-8 Framework: The room temperature sol-gel method was applied for the synthesis of ZIF-8 nano-MOF [13]. Initially, 7.33 mg of ($Zn(NO_3)_2 \cdot 6H_2O$) and 16.22 mg of Hmim were solubilized in 5 mL of methanol solution individually. Once the solutions dissolved, the 5 mL of Hmim solution was mixed with 5 mL of metal ion dropwise under constant magnetic stirring conditions. The mixer solution started precipitating within a few minutes. The final solution was kept at room temperature for 2 hrs and precipitates were collected after washing with methanol and dried under 50 °C.

3.3.3. Synthesis of ZIF8-IR820 Nano-MOF: 20 mg of ZIF-8 was mixed in 10 mL, 0.2 mM of IR820 solution in methanol under constant magnetic stirring and kept for 12 hrs. The final solution was washed 5 times with pure methanol by centrifugation methods. Finally, the precipitates of ZIF8-IR820 were collected and dried at 50 °C [13].

3.3.4. Synthesis of Fe-Cur Composite: The Fe-Cur compound was prepared by mixing curcumin with iron(III) chloride at a molar ratio of 1:1 in a methanolic solution [8, 14]. First, 50 mL of 2 mM curcumin in methanol was heated at 60 °C for dissolution. Iron(III) chloride (2 mM) was dissolved in 100 mL methanol by heating and added into the curcumin solution. A brown colour solid precipitate was formed immediately and it was refluxed for 2.5 hrs [15]. The brown product was filtered and washed firstly with cold methanol and then with water to eliminate the remaining reactants. The purified product was dried in a vacuum overnight at 60 °C and the final appearance of the product was brown.

3.3.5. Synthesis of Zn(II)–Cur Compound: The compound Zn(II)-Cur was synthesized at a molar ratio of 1:1 [8, 14]. 50 mL of 2 mM solution of Cur in methanol was heated at 60 °C for suspension. 2 mM zinc acetate dihydrate was dissolved in 100 mL of methanol by heating. It was added into the Cur and the solution was refluxed for 2.5 hrs [15]. The red solid sample was filtered and washed to eliminate the remaining reactants. The purified sample was dried in a vacuum overnight at 60 °C and the final product was red in colour [14].

3.3.6. Synthesis of Fe_2O_3 Nanoparticles: Fe_2O_3 nanoparticles were prepared following a method described in reference [16]. Typically 203 mg $FeCl_3$ was dissolved in 5 ml ethylene glycol by vigorous stirring. After 30 minutes of stirring 15 ml, 0.25M NaOH was added drop-wise to the solution. Then the solution is vigorously mixed for 2 hrs after which the brown-colored precipitation was transferred into a teflon lined stainless-steel autoclave. The sealed device is kept at a constant temperature of 150 °C for 18 hrs. Under the solvothermal conditions, the complete nucleation process takes place.

3.3.7. Synthesis of Fe_2O_3-PC Nanohybrids: The nanohybrids were prepared using a mechanical attachment process. 30 mg Fe_2O_3 nanoparticles were taken in 30 mL DMSO-water mixture. The pH of the system is slightly adjusted to basic by adding two drops of 0.25 M NaOH. Then 0.2 mM PC solution was added and mixed at room temperature and shaken for 24 hrs to obtain PC attached Fe_2O_3 nanohybrid. The system is then washed several times using Millipore water to remove unattached PC. Finally, as synthesized nanohybrid was dried in an oven and put in the dark until further use.

3.3.8. Synthesis of ZnO Nanoparticles: ZnO nanoparticles of size ~5 nm were prepared in the ethanolic medium following the method as described in reference [17]. 20 mL 4 mM zinc acetate dihydrate $(CH_3COO)_2Zn \cdot 2H_2O$ was heated at 60 °C around 30 minutes [18]. 20 mL 4mM sodium hydroxide solution in ethanol was added in the solution. The mixture was vigorously stirred for 2 hrs at 60 °C. The resulting solution was cooled at room temperature and stored at 4 °C until further use. ZnO nanoparticles of size ~30

nm were synthesized by the precipitation method [19]. Firstly, PEG (10% V/V) was taken in a three-naked flux. Next, 0.05 M zinc acetate and 0.1 M Na_2CO_3 were added simultaneously into the PEG solution. The system was stirred vigorously for 2 hrs. Then the precipitate was washed with double distilled water, ammonia solution (pH = 9), and ethanol. It was dried at room temperature. The precipitate was calcined in a muffle furnace at 450 °C for 3 hr. Finally, ZnO nanoparticle of size ~25 - 30 nm were prepared.

3.3.9. Preparation of ZnO-NF Nanohybrids: The surface 30 nm of ZnO nanoparticles were functionalized by NF by adding 15 mg of 30 nm ZnO nanoparticles to 15 ml of NF solution (0.25 mM solution in DMSO) with regular stirring at room temperature for 15 hrs [18]. After 15 hrs the solution was then centrifuged for 30 minutes. Then the nanohybrid was washed with DMSO three times to remove free dyes. After washing, the nanohybrid was then dried in an oven for 8 hrs under 140 °C. Similarly, the surface of ~5 nm ZnO nanoparticles were functionalized with NF (0.25 mM solution in ethanol) by adding 15 mL of ZnO (5 nm) nanoparticles with continuous stirring at room temperature, for 15 hrs.

3.3.10. Synthesis of Silver Nanoparticles: Citrate functionalized Ag nanoparticle was synthesized at 0 °C temperature in an aqueous solution (pH = 6.5) by following the synthesis technique described below [20]. In a typical synthesis process, 1 mL 5 mM aqueous solution of $AgNO_3$ was added to 16 mL 1 mM aqueous solution of sodium citrate. The solution was then put under continuous stirring conditions in an ice bath at 0 °C for 2 hrs. 150 mL 5mM aqueous $NaBH_4$ solution was added to that solution dropwise. The color of the solution turned yellow and the synthesized nanoparticle was kept at 4 °C temperature until further use.

3.3.11. Synthesis of ZnO-TC Nanohybrids: The synthesis of ZnO-TC nanohybrids were performed under continuous stirring conditions at room temperature. Initially, 12 mg of ZnO nanoparticles were added into 0.2 mM 10 ml of TC solution. After 12 hrs of continuous magnetic stirring, the solution

was taken out and washed with ethanol three times by using centrifuged to remove excess TC from the solution. The ZnO-TC hybrid was then dried in the oven at 75 °C for 5 hrs.

3.3.12. Synthesis of Au_ZnO Nanohybrids: The synthesis of Au nanoparticle decorated ZnO nanohybrids were performed by in situ reaction process [21]. 12 mg of commercial ZnO nanoparticles was taken in an aqueous solution with 5 ml of 1 mM $HAuCl_4 \cdot 3H2O$. The mixer has been put on constant magnetic stirring at room temperature for 30 minutes. Then 5 ml of 5 mM $NaBH_4$ solution was added drop-wise. The solution of ZnO+$HAuCl_4 \cdot 3H2O$ turns purple from light yellow due to the reduction of the Au^{3+} to Au nanoparticles on the surface ZnO.

3.3.13. Synthesis of Au_ZnO-TC Tri-hybrids: The Au_ZnO-TC tri-hybrids were prepared as follows [21]. 12 mg of synthesized Au_ZnO hybrid was added into 10 ml of 0.2 mM TC under constant magnetic stirring at room temperature. After 24 hrs, the solution was washed with ethanol solvent to remove an excess amount of TC. The synthesized Au_ZnO-TC tri-hybrids were then dried in the oven at 75 °C for 5 hrs.

3.3.14. Synthesis of Au_Al_2O_3 Nanohybrids: The synthesis of Au nanoparticle decorated Al_2O_3 nanohybrids were performed by in situ reaction process [21]. 12 mg of commercial Al_2O_3 nanoparticles was taken in an aqueous solution with 5 ml of 1 mM $HAuCl_4 \cdot 3H2O$. The mixer has been put on constant magnetic stirring at room temperature for 30 minutes. Then 5 ml of 5 mM $NaBH_4$ solution was added drop-wise. The solution of Al_2O_3+$HAuCl_4 \cdot 3H2O$ turns purple from light yellow due to the reduction of the Au^{3+} to Au nanoparticles on the surface Al_2O_3.

3.3.15. Synthesis of Au_Al_2O_3-TC Tri-hybrids: Au_Al_2O_3-TC tri-hybrids were fabricated by adding 12 mg of as prepared Au_Al_2O_3 to the TC solution in ethanol of concentration 0.2 mM under constant magnetic stirring at room temperature [21]. After 24 hrs, the solution was washed with ethanol solvent to

remove an excess amount of TC. The synthesized Au_Al_2O_3-TC tri-hybrids were then dried in the oven at 75 °C for 5 hrs.

3.3.16. Synthesis of ZIF8-RF: ZIF8 nanoparticles were produced following the previously described sol−gel method [22]. 10 mg of synthesized ZIF8 sample was added with 0.5 mM of RF solution in DMSO solvent in a constant stirring condition overnight and the ZIF8-RF sample is collected by washing with DMSO and then with distilled water, and dried at 90 °C.

3.3.17. Synthesis of Cr_2O_3 Nanoparticles: Chromium oxide (Cr_2O_3) nanoparticles have been prepared by sol-gel precipitation route. About (2 g, 7.5 mmol) of chromium chloride hexahydrate salt ($CrCl_3 \cdot 6H_2O$) was dissolved in (50 ml) of ethanol. The prepared solution was stirred on the magnetic stirrer for 30 minutes in a container, the solution converts to green. After that, ammonium hydroxide solution (NH_4OH), was added as drop by burette about 2 drops per minute to the prepared solution until the pH of the solution become ~8. After 10 minutes solution was filtered by using a centrifuge, then release the upper solution and washed the precipitate with a small amount of distilled water (repeat step twice). The precipitate was dried at 90 °C for 2 hrs. The green-dark precipitate powder of chromium oxide was obtained (weight 1.5 g, 70% yield). The process can be typed by the following equations:

$$CrCl_3 \cdot 6H2O + 3NH_4OH \rightarrow Cr(OH)_3 + 3NH_4Cl + 6H_2O \quad (3.12)$$

$$2Cr(OH)_3 \rightarrow Cr_2O_3 + 3H_2O \quad (3.13)$$

$$O\ (2CrCl_3 \cdot 2H_2O + 3NH_4OH \rightarrow Cr_2O_3 + 3NH_4Cl + 9H_2 \quad (3.14)$$

The precipitate was annealed at 400 °C for 120 minutes.

3.3.18. Synthesis of Citrate Functionalized Cr_2O_3 Nanoparticles: As prepared Cr_2O_3 nanoparticles were added to 0.5 M aqueous citrate ligand (~20 mg Cr_2O_3 nanoparticles/ml) solution of pH = 7.4 and kept for vigorous stirring for 24 hrs in a cyclomixer. A syringe filter of 0.22 µm diameter was used to eliminate the nonfunctionalized bigger-sized nanoparticles.

References

[1] D. V. O'Conner, D. Philips, Time correlated single photon counting, *Academic Press*, London, 1984.

[2] H. Mandal, S. Shyamal, P. Hajra, B. Samanta, P. Fageria, S. Pande, C. Bhattacharya, Improved photoelectrochemical water oxidation using wurtzite ZnO semiconductors synthesized through simple chemical bath reaction, *Electrochim. Acta* 141 (2014) 294.

[3] N. Serpone, Relative photonic efficiencies and quantum yields in heterogeneous photocatalysis, *J. Photochem. Photobiol. A* 104 (1997) 1.

[4] N. Serpone, A. Salinaro, Terminology, Relative photonic efficiencies and quantum yields in heterogeneous photocatalysis. Part I: Suggested protocol, in: Pure Appl. Chem., 1999, pp. 303.

[5] M. J. Muñoz-Batista, A. Kubacka, A. B. Hungría, M. Fernández-García, Heterogeneous photocatalysis: Light-matter interaction and chemical effects in quantum efficiency calculations, *J. Catal.* 330 (2015) 154.

[6] S. Cho, J.-W. Jang, S.-H. Lim, H. J. Kang, S.-W. Rhee, J. S. Lee, K.-H. Lee, Solution-based fabrication of ZnO/ZnSe heterostructure nanowire arrays for solar energy conversion, *J. Mater. Chem.* 21 (2011) 17816.

[7] A. Chatterjee, P. Kar, D. Wulferding, P. Lemmens, S. K. Pal, Flower-like BiOI microspheres decorated with plasmonic gold nanoparticles for dual detoxification of organic and inorganic water pollutants, *ACS Appl. Nano Mater.* 3 (2020) 2733.

[8] D. Bagchi, S. Chaudhuri, S. Sardar, S. Choudhury, N. Polley, P. Lemmens, S. K. Pal, Modulation of stability and functionality of a phyto-antioxidant by weakly interacting metal ions: Curcumin in aqueous solution, *RSC Adv.* 5 (2015) 102516.

[9] S. Chaudhuri, S. Sardar, D. Bagchi, S. Dutta, S. Debnath, P. Saha, P. Lemmens, S. K. Pal, Photoinduced dynamics and toxicity of a cancer drug in proximity of inorganic nanoparticles under visible light, *ChemPhysChem* 17 (2016) 270.

[10] S. A. Ahmed, D. Bagchi, H. A. Katouah, M. N. Hasan, H. M. Altass, S. K. Pal, Enhanced water stability and photoresponsivity in metal-organic framework (MOF): A potential tool to combat drug-resistant bacteria, *Sci. Rep.* 9 (2019) 19372.

[11] D. Bagchi, S. Dutta, P. Singh, S. Chaudhuri, S. K. Pal, Essential dynamics of an effective phototherapeutic drug in a nanoscopic delivery vehicle: Psoralen in ethosomes for biofilm treatment, *ACS Omega* 2 (2017) 1850.

[12] W. Guo, W. Xia, K. Cai, Y. Wu, B. Qiu, Z. Liang, C. Qu, R. Zou, Kinetic-controlled formation of bimetallic metal–organic framework hybrid structures, *Small* 13 (2017) 1702049.

[13] M. N. Hasan, A. Bera, T. K. Maji, D. Mukherjee, N. Pan, D. Karmakar, S. K. Pal, Functionalized nano-MOF for NIR induced bacterial remediation: A combined spectroscopic and computational study, *Inorg. Chim. Acta* 532 (2022) 120733.

[14] X.-Z. Zhao, T. Jiang, L. Wang, H. Yang, S. Zhang, P. Zhou, Interaction of curcumin with Zn(II) and Cu(II) ions based on experiment and theoretical calculation, *J. Mol. Struct.* 984 (2010) 316.

[15] R. Hariharan, S. Senthilkumar, A. Suganthi, M. Rajarajan, Photodynamic action of curcumin derived polymer modified ZnO nanocomposites, *Mater. Res. Bull.* 47 (2012) 3090.

[16] R. Nandi, S. Mishra, T. K. Maji, K. Manna, P. Kar, S. Banerjee, S. Dutta, S. Sharma, P. Lemmens, K. D. Saha, A novel nanohybrid for cancer theranostics: Folate sensitized Fe_2O_3 nanoparticles for colorectal cancer diagnosis and photodynamic therapy, *J. Mater. Chem. B* 5 (2017) 3927.

[17] S. Sardar, P. Kar, S. Sarkar, P. Lemmens, S. Pal, Interfacial carrier dynamics in PbS-ZnO light harvesting assemblies and their potential implication in photovoltaic/photocatalysis application, *Sol. Energ. Mat. Sol.* 134 (2015) 400.

[18] M. N. Hasan, T. K. Maji, U. Pal, A. Bera, D. Bagchi, A. Halder, S. A. Ahmed, J. H. Al-Fahemi, T. M. Bawazeer, T. Saha-Dasgupta, S. K. Pal, Wide bandgap semiconductor-based novel nanohybrid for potential antibacterial activity: Ultrafast spectroscopy and computational studies, *RSC Adv.* 10 (2020) 38890.

[19] R. Hong, J. Li, L. Chen, D. Liu, H. Li, Y. Zheng, J. Ding, Synthesis, surface modification and photocatalytic property of ZnO nanoparticles, *Powder Technol.* 189 (2009) 426.

[20] D. Paramelle, A. Sadovoy, S. Gorelik, P. Free, J. Hobley, D. G. Fernig, A rapid method to estimate the concentration of citrate capped silver nanoparticles from UV-visible light spectra, *Analyst* 139 (2014) 4855.

[21] S. A. Ahmed, M. N. Hasan, H. M. Altass, A. Bera, R. I. Alsantali, N. Pan, A. Y. A. Alzahrani, D. Bagchi, J. H. Al-Fahemi, A. S. Khder, S. K. Pal, Tetracycline encapsulated in Au nanoparticle-decorated ZnO nanohybrids for enhanced antibacterial activity, *ACS Appl. Nano Mater.* 5 (2022) 4484.

[22] C.-Y. Sun, C. Qin, X.-L. Wang, G.-S. Yang, K.-Z. Shao, Y.-Q. Lan, Z.-M. Su, P. Huang, C.-G. Wang, E.-B. Wang, Zeolitic imidazolate framework-8 as efficient pH-sensitive drug delivery vehicle, *Dalton Trans.* 41 (2012) 6906.

Chapter 4

Computational Techniques and Details of Calculations

4.1. Introduction:

In condensed matter physics, computational techniques refer to the methods and tools used to simulate and analyze complex systems or phenomena using computer models to understand and predict the behavior of materials at the atomic and molecular scale. There are several computational techniques in condensed matter physics, e.g. Molecular Dynamics (MD), Monte Carlo (MC), Density Functional Theory (DFT), Monte Carlo Renormalization Group (MCRG), Quantum Monte Carlo (QMC) and Time-Dependent Density Functional Theory (TDDFT). These computational techniques have revolutionized the field of condensed matter physics, chemistry and materials science, allowing researchers to study and understand complex materials and phenomena that are difficult or impossible to study experimentally.

Computational DFT is the implementation of the theoretical concepts and mathematical tools into computer programs. These programs are used to simulate the behavior and properties of molecules, materials, and solids. DFT is a single-particle derived technique based on the Kohn-Sham equation. In computational DFT, the electronic structure of the system is calculated by solving the Schrödinger equation using the exchange-correlation functional, which is typically chosen from a set of available functionals that have been developed and tested by the scientific community. Except exchange-correlation, there are several terms in the DFT functional. The most common type of computational DFT is based on the plane-wave basis set and pseudopotentials, which are used to approximate the electronic structure of the system. Other

methods, such as the localized basis set and the real-space grid methods, are also used. Computational DFT has many advantages over experimental techniques, such as being able to simulate the behavior and properties of complex systems, being less expensive and time-consuming, and providing insights into the underlying properties of the system. Overall, computational DFT has become a powerful and widely used tool in many fields of science, such as chemistry, physics, materials science, and biology, and has contributed to the development of new materials and technologies.

Time-dependent DFT is an extension of DFT that enables the study of electronic excitations and dynamics in molecules and materials. TDDFT provides a theoretical framework for calculating the excited state properties of systems, such as electronic transitions, optical spectra, and photochemistry. In TDDFT, the electronic density is not static but evolves due to external perturbations or internal dynamics. The TDDFT equations describe the time-dependent behavior of the electronic density and the exchange-correlation functional. The excitation energies and transition probabilities of a system can be calculated from the TDDFT response function, which describes the system's response to an external electromagnetic field. It is used to calculate the electronic excited states and optical spectra of molecules and materials, to design new materials with desired electronic properties, and to study the dynamics of photochemical reactions. It has become a widely used tool in computational chemistry and materials science, and it has contributed to the understanding of the electronic structure and dynamics of a wide range of systems.

In this chapter, we have included a brief discussion of different methods and techniques used in our investigation of the electronic, magnetic, and optical properties of our systems. Depending upon the physical property of the system under study, we have chosen either the *ab-initio* DFT method or TDDFT. Although the approach of various methods is different, the main objective of those methods is to solve the many-body Hamiltonian which is the fundamental Hamiltonian describing atoms, molecules, clusters, and bulk systems.

4.2. Approach of Various Methods:

4.2.1. The Many Body Hamiltonian: The many-body Hamiltonian is a mathematical operator that describes the behavior of a system composed of many interacting particles. It is used in quantum mechanics to calculate the energy and other properties of such systems. In the many-body Hamiltonian, the total energy of the system is given by the sum of the kinetic and potential energies of all the particles in the system. The potential energy term describes the interactions between the particles, which can be either pairwise or more complex interactions. The many-body Hamiltonian is usually written in terms of the positions and momenta of the particles. The many-body Hamiltonian is important in many areas of physics and chemistry, including condensed matter physics, nuclear physics, and molecular physics. It is used to study the behavior of materials, the properties of atomic nuclei, and the electronic structure of molecules. Materials of different forms are made up of interacting atoms. The properties of matter are a combined result of different interactions between atoms. So, the microscopic properties of the matter are a complex problem. However, the regular periodicity of the atom leads to simplification to investigate the properties of the materials. According to quantum mechanical theory, the microscopic behavior of a collection of the interacting atom can be represented by an ensemble of electrons and nuclei, the fundamental element of an atom, interacting through electrostatic (Coulombic) forces. In principle, the energy may be computed by the solution of the Schrödinger equation which, in the time-independent, nonrelativistic, Born-Oppenheimer approximation is:

$$\boldsymbol{H}\psi\,(R,r) = E\psi\,(R,r) \tag{4.1}$$

The exact Hamiltonian for many body systems can be written in a generalized form as:

$$H = -\sum_{I=1}^{P}\frac{\hbar^2}{2M_1}\nabla_I^2 - \sum_{i=1}^{N}\frac{\hbar^2}{2m_i}\nabla_i^2 + \frac{e^2}{2}\sum_{I=1}^{P}\sum_{J\neq 1}^{P}\frac{Z_I Z_J}{|\boldsymbol{R_I}-\boldsymbol{R_I}|} + \frac{e^2}{2}\sum_{i=1}^{N}\sum_{j\neq 1}^{N}\frac{1}{|\boldsymbol{r_i}-\boldsymbol{r_j}|} - \frac{e^2}{2}\sum_{I=1}^{P}\sum_{i=1}^{N}\frac{Z_I}{|\boldsymbol{R_I}-\boldsymbol{r_j}|} \tag{4.2}$$

where $\boldsymbol{R} = \{\boldsymbol{RI}\}$, I = 1, …P, are the set of P nuclear coordinate and $\mathbf{r} = \{\mathbf{r}_i\}$, i= 1,….N, are the set of N electronic coordinates. Z_I and M_I are the P nuclear charges and masses respectively. m_i is the N electronic masses each of charge e. The first two terms in the right-hand side of the equation describe the kinetic energies of the nuclei and electrons respectively. The last three terms denote the Coulomb interaction between nucleus-nucleus, different electrons, and nucleus-electron respectively. Despite its simplicity, the exact solution of Schrödinger's equation is very challenging as it contains a coupled electron-electron Coulomb interaction term. In practice, solving Schrödinger's equation either in the analytical method or numerical method, requires 3N+3P number of degrees of freedom which makes the equation very difficult to exactly solve beyond the hydrogen atom.

One of the crucial works of computational material science is to solve the many-body Hamiltonian equation with sufficient accuracy and provide a reliable result that can explain the diverse physical property of a broad range of materials. Thus usually one resorts to some sensible approximations. In this matter, there are two most commonly known approximations; a) Born-Oppenheimer approximation and b) Classical Nuclei approximation.

4.2.2. The Born-Oppenheimer Approximation: The Born-Oppenheimer approximation [1] is a fundamental concept in molecular physics and chemistry that allows the separation of electronic and nuclear motion in molecules. The basic idea behind the approximation is that the electronic motion is much faster than the nuclear motion so the electronic motion can be treated as instantaneous relative to the nuclear motion. The approximation assumes that the total wave function of a molecule can be written as a product of an electronic wave function and a nuclear wave function. The electronic wave function describes the motion of the electrons, and the nuclear wave function describes the motion of the nuclei. Using the Born-Oppenheimer approximation, the electronic wave function can be calculated independently of the nuclear wave function, since the electronic motion is assumed to be much faster than the nuclear motion. Thus

one can assume the nuclei to be stationary to electrons that move around it. This allows us to decouple the electron and nuclear degrees of freedom. So, the many-body Hamiltonian can be written as:

$$\Psi(\boldsymbol{R}, \boldsymbol{r}, t) = \theta_m(\boldsymbol{R}, t)\varphi(\boldsymbol{R}, \boldsymbol{r}) \tag{4.3}$$

$$\boldsymbol{H} = \boldsymbol{H}_{electron} + \boldsymbol{H}_{nuclei} \tag{4.4}$$

$$= [\boldsymbol{T}_e + \boldsymbol{V}_{ee} + \boldsymbol{V}_{ne}] + [\boldsymbol{T}_{nn} + \boldsymbol{V}_{nn}] \tag{4.5}$$

where $\mathbf{T}_{nn}$ and $\mathbf{V}_{nn}$ are the nuclear kinetic and potential operators respectively, $\mathbf{T}_e$ and $\mathbf{V}_{ee}$ are the same for the electronic case, and $\mathbf{V}_{ne}$ is the potential energy operator for the electronic and nuclear interaction. As the nuclei are assumed to be fixed, the $\mathbf{T}_{nn}$ term can be ignored, while the $\mathbf{V}_{nn}$ term can be assumed to be constant, this constant nuclear potential energy is called Madelung energy and can be calculated classically.

Thus by solving the electronic part of the Schrödinger equation, it is possible to obtain electron energy $E_{electron}$ and electron wavefunction $\Psi_{electron}$ which explicitly depends on the electron coordinates. Thus the total energy of the system can be written as the sum of electron energy and constant nuclear energy:

$$E_{total} = E_{electron} + E_{nuclei} \tag{4.6}$$

This is a useful tool for understanding the structure and behavior of molecules, and is widely used in theoretical and computational chemistry. However, it is important to note that the approximation is only valid in certain cases, and may break down in situations where the electronic and nuclear motion are strongly coupled.

4.2.3. The Independent Electron Approximation: Now the primary problem in the structure of matter is reduced to solve the Schrödinger equation for a system of N interacting electrons in the Coulombic field generated by a collection of atomic nuclei. Even after the simplification of the Born-Oppenheimer equation, the solution of Eq. (4.3) remains difficult as there are still too many parameters, which makes it difficult to solve the problem. It is possible to get an exact

solution only in the case of uniform electron gas or atom with a small electron number.

In the independent electron approximation approach, the electron-electron interaction in the system is not considered, this approximation allows us to map the problem of many interacting electron systems onto a system of a non-interacting electron moving in an effective potential due to all other electrons. However, to achieve this mapping one can follow two different formulations (a) the wave function-based approaches of Hartree , Hartree-Fock [2] formalism, and (b) the DFT-based approaches [3, 4]. The wave function-based approach is computationally heavy, and it is difficult to solve using the wave function approach for the bigger system. On the other hand, DFT is relatively simpler and computationally controllable compared to the wave function-based approach. In DFT, the many-electron wave-function is completely bypassed in favor of the electron density. This is the reason why DFT becomes the most important conceptual and practical advance in solving many-electron problems in physics and chemistry. The following discussions attempt to explain both the conceptual structure and some of the formalism of DFT.

4.2.4. Density Functional Theory: The term density functional theory refers to all methods that express the ground-state energy as a function of the electronic density ρ(r). The DFT is presently the most successful (and also the most promising) approach to computing the electronic structure of matter. Its applicability ranges from atoms, molecules, and solids to nuclei and quantum and classical fluids. The idea of DFT can be attributed to the Thomas-Fermi theory of electron density concept [5], where In this way, a function of the 3N variable, where N is the number of electrons, can be reduced to a lower dimension. According to that model, the electron density can be written as eq. (4.7). The Thomas-Fermi model, however, was too crude, because the approximation used for the kinetic energy of the electrons as well as errors in the

$$\rho(\boldsymbol{r}) = N \int \psi(r_1, r_2, \dots, r_N)\psi^*(r_1, r_2, \dots, r_N)dr_1 dr_2 \dots dr_N \qquad (4.7)$$

exchange energy was unable to sustain bound states. Nevertheless, it had shown the pathway for the development of DFT by Hohenberg and Kohn in [6] to deal with many-electron problems more efficiently. In 1964, Hohenberg and Kohn put forth two crucial theorems [3] that provided a practical approach for reducing the many-electron problems to an effective one-electron problem. These two theorems are considered the backbone for electronic structure calculations in condensed matter physics.

The primary advantages of taking electronic density as the basic variable are: (i) it is a function of 3 variables, unlike the wave-function which is a function of 3N variables and is simpler to tabulate and plot, (ii) it is a function in 3D space in which we live, and it provides better visualization, (iii) it is an experimental variable. In the next section, we discuss the mathematical formulation of the density of states briefly.

4.2.5. The Hohenberg-Kohn Theorem: The Hohenberg-Kohn theorem is a fundamental theorem in DFT that establishes a one-to-one correspondence between the ground-state electron density and the external potential of a system. The theorem was first proposed by P. Hohenberg and W. Kohn in 1964. The theorem states that the ground-state electron density uniquely determines the external potential of a system, and vice versa. In other words, if two systems have the same ground-state electron density, they must have the same external potential, and therefore the same total energy. The Hohenberg-Kohn theorem provides a theoretical basis for the use of electron density as the fundamental variable in DFT calculations. In practical terms, this means that the total energy of a system can be expressed as a functional of the electron density, rather than being explicitly calculated from the wave function of the system.

4.2.5.1. First Theorem: The electron density $\rho(\mathbf{r})$ determines the external potential (to within an additive constant).

Corollary: Electron density $\rho(\mathbf{r})$ uniquely determines the Hamiltonian operator which can be obtained by solving the full many-body Schrödinger's equation.

Proof: Let the ground state of two N-electron systems be characterized by two different external potentials (differing by more than an additive constant) $v_1(\mathbf{r})$ and $v_2(\mathbf{r})$. Let us further assume that, the corresponding two wave functions ψ_1 and ψ_2 yields the same ground-state electron charge density $\rho_0(\mathbf{r})$. Thus the corresponding Hamiltonians and Schrödinger's equation for the two N-electron systems is given by:

$$\begin{aligned} H_1\psi_1 &= E_1\psi_1 \\ H_2\psi_2 &= E_2\psi_2 \end{aligned} \tag{4.8}$$

One may use the variational principle and write the energy expression as,

$$E_1 = \langle\psi_1|H_1|\psi_1\rangle < \langle\psi_2|H_2|\psi_2\rangle \tag{4.9}$$

$$= \langle\psi_2|H_2|\psi_2\rangle + \langle\psi_2|H_1 - H_2|\psi_2\rangle \tag{4.10}$$

$$< E_2 + \int dr\rho(\boldsymbol{r})\,[v_1(\boldsymbol{r}) - v_2(\boldsymbol{r})] \tag{4.11}$$

On interchanging the suffices, we can write:

$$E_2 < E_1 + \int dr\rho(\boldsymbol{r})\,[v_2(\boldsymbol{r}) - v_1(\boldsymbol{r})] \tag{4.12}$$

Summation of the two inequality leads to a contradiction:

$$E_1 + E_2 < E_2 + E_1 \tag{4.13}$$

Thus, the theorem has been proven by *reductio ad absurdum.* Thus one may conclude that the assumption of identical density arising from two different external potentials is wrong. Hence a given $\rho(\mathbf{r})$ corresponds to only one $v(\mathbf{r})$ and since $v(\mathbf{r})$ is fixed, the Hamiltonian and hence the ground state expectation value of any observable is unique functional of the ground state electron charge density.

4.2.5.2. Second Theorem: For any positive definite trial density ρ_t, such that $\int \rho_t(\mathbf{r})d\mathbf{r} = N$ then $(\rho_t) \geq E_0[\rho_t]$.

Corollary: The functional $E[\rho]$ alone is sufficient to determine the exact ground state energy and density. In general excited states of the electrons must be deter-

mined by other processes.

Proof: The proof of this theorem is very much straightforward. Let us consider, the many-body Hamiltonian $\mathbf{H} = \mathbf{T} + \mathbf{V} + \mathbf{V_{ext}}$ where T is the kinetic energy, V is the electron-electron interaction and $\mathbf{V_{ext}}$ is the external potential. For a given electron charge density $\rho(\mathbf{r})$ total energy can be expressed as:

$$E(\rho) = \langle \psi[\rho] | H | \psi[\rho] \rangle \tag{4.14}$$

$$= \langle \psi[\rho] | T + V | \psi[\rho] \rangle + \langle \psi[\rho] | V_{ext} | \psi[\rho] \rangle \tag{4.15}$$

$$= F(\rho) + \int \rho(r) V_{ext}(\boldsymbol{r}) d\boldsymbol{r} \tag{4.16}$$

Now using Rayleigh-Ritz variational principle to electron charge density we can obtain that:

$$F(\rho) + \int \rho(r) V_{ext}(\boldsymbol{r}) d\boldsymbol{r} = E[\rho(\boldsymbol{r})] \geq E_0[\rho_0(\boldsymbol{r})] = \langle \psi | H | \psi \rangle \tag{4.17}$$

This implies a remarkable fact that the ground state properties of an interacting N electron system can be completely determined by the electron charge density $\rho(\mathbf{r})$. So, the problem is reduced to find $\rho(\mathbf{r})$ which minimizes the energy functional $E[\rho(\mathbf{r})]$.

Now, to determine $E[\rho(\mathbf{r})]$ one need to know the exact analytical form of $F(\rho)$ which contains all the many-body effect. The kinetic and electron-electron functionals are unknown. If good approximations to these functionals could be found direct minimization of the energy would be possible. It was Kohn and Sham who specifically proposed a new approximation that can solve this shortcoming. The Hohenberg-Kohn theorem has had a significant impact on the development of modern theoretical and computational chemistry and has been the basis for many important advances in the field. However, it should be noted that the theorem is limited to ground-state properties, and does not apply to excited states or time-dependent phenomena.

4.2.6. The Kohn-Sham Equation: The Kohn-Sham equation is a fundamental equation in DFT that provides a way to calculate the electronic structure of a

system. The equation is named after Walter Kohn and Lu Jeu Sham, who developed it in 1965 [4]. The weakest part of the Thomas-Fermi theory [6] was the treatment of kinetic energy functionals, which was taken care of by Kohn-Sahm equations based on the Hohenberg-Kohn theorem. It is based on the idea of mapping a many-electron system onto a system of non-interacting electrons in an effective potential. The effective potential is constructed so that the electron density of the non-interacting system matches the electron density of the real system. The effective potential is also chosen so that it can be easily calculated, typically by solving a set of self-consistent equations for the wave functions of the non-interacting electrons in the effective potential. The equations are similar in form to the Schrödinger equation, but with an additional term that accounts for the exchange-correlation energy, which is a measure of the interaction between the electrons. Solving the Kohn-Sham equation involves iteratively adjusting the effective potential until self-consistency is achieved, meaning that the electron density of the non-interacting system matches the electron density of the real system. Once the self-consistent solution is obtained, the total energy and other properties of the system can be calculated.

This equation provided an approximation of kinetic energy functional T(ρ) for the interacting electron system in terms of a non-interacting electron system having the same ground-state charge density ρ(**r**).

The total energy functional for the N interacting electron system can be written in terms of density and has thus the generalized form:

$$E[\rho(\boldsymbol{r})] = F(\rho) + \int \rho(r) V_{ext}(\boldsymbol{r}) d\boldsymbol{r} \tag{4.18}$$

where F[ρ] is a universal function of density.

Kohn-Shan separated this function into three different terms as eq. (4.19). Where T(ρ) is the kinetic energy of the interacting electron and $V_H(\rho)$ is the electrostatic

$$F(\rho) = T(\rho) + V_H(\rho) + E_{xc}^{total}[\rho] \tag{4.19}$$

Coulomb energy of electrons and $E_{xc}^{total}[\rho]$ contains all the exchange and correlation effects. Within the Kohn-Sham formulation, the exact kinetic energy is replaced by the kinetic energy of a system of non-interacting particles having the same charge density with a new effective exchange-correlation term which is in general called the exchange-correlation (XC) energy functional $E_{XC}[\rho]$:

$$E_{xc}(\rho) = E_{XC}^{total}[\rho] + T[\rho] - T_s[\rho] \tag{4.20}$$

where $T_s[\rho]$ represents the kinetic energy of non-interacting electrons. This approximation allows us to map many interacting electron systems onto an exactly equivalent system of non-interacting electrons living under an effective potential contributed by all other electrons and having the same ground-state charge density $\rho(\mathbf{r})$. Thus the interacting many-electron problem is reduced to solving a set of self-consistent non-interacting one-electron equations known as Kohn-Sham equations.

For a system of N non-interacting electrons, the ground state charge density can be represented as a sum over one-electron orbitals φ_i as follows:

$$\rho(r) = \sum |\varphi_i|^2 \tag{4.21}$$

and henceforth the total energy functional for this non-interacting system may be evaluated as:

$$E_{KS}[\rho] = T_s[\rho(\boldsymbol{r})] + \int \boldsymbol{V}_{ext}(\boldsymbol{r})\rho(\boldsymbol{r})d\boldsymbol{r} + \frac{1}{2}\frac{e^2}{4\pi\epsilon_o}\iint \frac{\rho(\boldsymbol{r})\rho(\boldsymbol{r}')}{|\boldsymbol{r}-\boldsymbol{r}'|}d\boldsymbol{r}d\boldsymbol{r}' + E_{xc}[\rho(\boldsymbol{r})] \tag{4.22}$$

and the corresponding Hamiltonian is given by:

$$\boldsymbol{H}_{KS} = -\frac{\hbar^2}{2m}\boldsymbol{\nabla}^2 + V_{eff}(\boldsymbol{r}) \tag{4.23}$$

$$V_{eff}(\boldsymbol{r}) = V_{ext}(\boldsymbol{r}) + \frac{1}{2}\frac{E^2}{4\pi\epsilon_0}\int \frac{\rho(\boldsymbol{r}')}{|r-\boldsymbol{r}'|}dr' + \frac{\delta E_{xc}}{\delta\rho(\boldsymbol{r})} = V_{ext}(\boldsymbol{r}) + V_{Hartree}(\boldsymbol{r}) + V_{xc}(\boldsymbol{r}) \tag{4.24}$$

Thus using Eq. (4.21), (4.22), (4.23), and (4.24) one can find the one-electron orbitals φ_i which minimize the energy and satisfy the following set of one-electron Schrödinger-like equations:

$$\left[-\frac{\hbar^2}{2m}\boldsymbol{\nabla}^2 + V_{eff}(\boldsymbol{r},\boldsymbol{\rho})\right]\varphi(\boldsymbol{r}) = \epsilon_i\varphi_i \tag{4.25}$$

From Eq. (4.25) it should be noted that the above set of one-electron equations can be solved if the effective potential V_{eff} is known. However, to know V_{eff} we have to know the charge density ρ(**r**). Now, ρ(**r**) depends on Kohn-Sham orbitals φ_i, which again depends on V_{ext}(**r**). So, the Kohn-Sham equations can't be solved straightforwardly. Thus the Kohn-Sham equations need to be solved self-consistently by applying iterative methods as follows:

1. Start with an initial guess for the charge density ρ(**r**).
2. Calculate the corresponding *Veff* (**r**,ρ) and solve the Eq. (4.24) with appropriate boundary conditions to obtain the total energy ε_i and the one-electron orbitals φ_i.
3. From the φ_i, calculate the new charge density and repeat the iterative process until convergence is reached. The convergence is self-consistently achieved when the output charge density differs from the input charge density by a preassigned small value.

A flowchart summarizing the above steps is given in Figure 4.1.

The Kohn-Sham equation has become a cornerstone of modern theoretical and computational chemistry and is widely used in the design of new materials, drugs, and catalysts. However, it is important to note that the accuracy of DFT calculations depends on the choice of exchange-correlation functional, which is not well-known in general.

4.2.7. Exchange Correlation Functional: The exchange-correlation (XC) functional is a key component of DFT calculations. It is a mathematical function that accounts for the effects of electron exchange and electron correlation, which are not explicitly included in the Kohn-Sham equation. The XC functional is used

to calculate the exchange-correlation energy, which is a measure of the interaction between the electrons in a system. The exchange energy arises from the antisymmetry of the wave function of a system of indistinguishable particles. It describes the energy change when two electrons exchange places, and it can be calculated exactly for some simple systems.

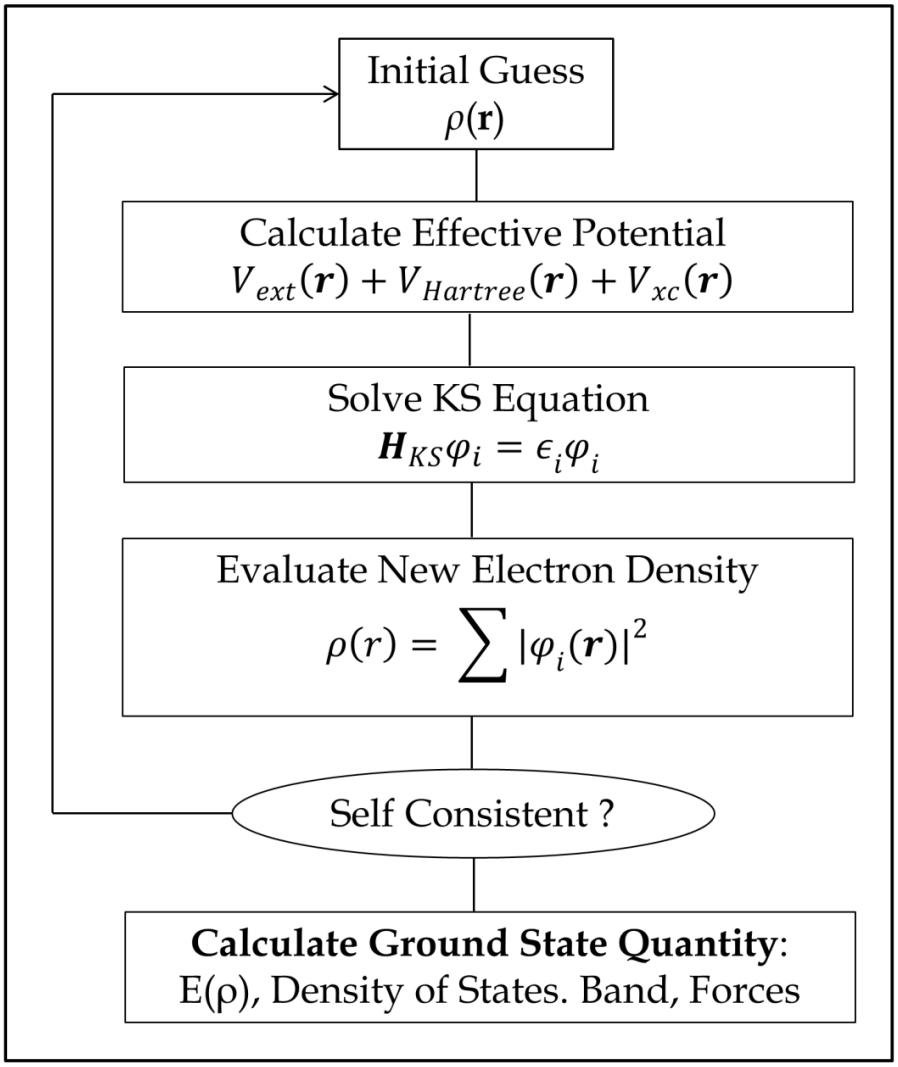

Figure 4.1: *Flowchart illustrating the iterative procedure to solve the Kohn-sham equations.*

However, for more complex systems, the exact exchange energy is not known, and an approximation must be used. The correlation energy arises from the fact that electrons repel each other due to their Coulombic interactions. This repulsion leads to a reduction in the energy of the system, known as the correlation energy. Like the exchange energy, the exact correlation energy is not

known for most systems and must be approximated. Many different forms of XC functionals have been developed, ranging from simple local approximations to more complex non-local functionals that include the effects of electron density gradients. The choice of XC is functional depends on the properties of the system being studied and the accuracy required for the calculations.

Although DFT is accurate in principle, the main drawback of the Kohn-Sham formulation comes due to its inexplicit exchange-correlation term. The exact expression of the E_{XC} is complex and unknown. So, to solve the equation one needs to choose a good approximation of the exchange-correlation function. In practice, the utility of the theory lies in the approximations used for E_{XC}. Even though the exact formulation of E_{XC} is very complex, great progress has been made with a remarkably simple approximation to encounter the problem. the various approximation formulas, the local density approximation (LDA) and generalized gradient approximation (GGA) are the most commonly used approximation methods. The development of more accurate and efficient XC functionals is an active area of research in computational chemistry and materials science. The goal is to develop functionals that can accurately predict the properties of complex systems with reasonable computational costs. The different approximate functionals for exchange-correlation are discussed next section.

4.2.7.1. Local Density Approximation (LDA): The Local Density Approximation (LDA) is a widely used theoretical framework in condensed matter physics, materials science, and related fields for calculating the electronic structure of solids. In the LDA, the energy of the system is expressed as a functional of the electron density, which is the probability density of finding an electron at a given point in space. The electron density is calculated self-consistently by solving the Kohn-Sham equations, which are a set of partial differential equations that describe the behavior of non-interacting electrons in an external potential. This approximation is based on the idea that the electronic structure of a solid is determined by the local environment around each atom, rather than the global

structure of the crystal. It was first introduced by Kohn and Sham in 1965, but the basic idea existed in the theory by Thomas-Fermi-Dirac. Under the LDA approximation, it is assumed that the charge density varies very slowly at any point **r** in space so that the electron gas in a small volume element $d^3\mathbf{r}$ could be considered locally uniform.

LDA postulates that the exchange-correlation functional has the following form:

$$E_{XC}[\rho(r)] = \int \epsilon_{XC}^{LDA}[\rho(\boldsymbol{r})]\rho(\boldsymbol{r})d\boldsymbol{r} \tag{4.26}$$

Under the LDA formalism, an obvious choice is to take ϵ_{XC}^{LDA} to be the exchange and correlation energy density of the homogeneous electron gas of density ρ(**r**). This term can be further written as a sum of the exchange and correlation contributions,

$$\epsilon_{XC}^{LDA}[\rho(\boldsymbol{r})] = \epsilon_{X}^{LDA}[\rho(\boldsymbol{r})] + \epsilon_{C}^{LDA}[\rho(\boldsymbol{r})] \tag{4.27}$$

for any homogeneous electron gas, the exchange energy $\epsilon_{X}^{LDA}[\rho(\boldsymbol{r})]$ part can be formulated by Dirac equation:

$$\epsilon_{X}^{LDA}[\rho(\boldsymbol{r})] = -\frac{3}{4}\left(\frac{3}{\pi}\right)^{\frac{1}{3}}\rho^{\frac{1}{3}} = -\frac{3}{4}\left(\frac{9}{4\pi^2}\right)^{\frac{1}{3}}\frac{1}{r_s} = -\frac{0.058}{r_s} \tag{4.28}$$

where $r_s = (3/4\pi\rho)^{1/3}$ is the mean inter-electron distance.

On the other hand, the functional form of correlation energy density $\epsilon_{C}^{LDA}[\rho(\boldsymbol{r})]$ is unknown and in 1980, Ceperley and Adler [7] provided an accurate estimate of $\epsilon_{C}^{LDA}[\rho(\boldsymbol{r})]$ for the homogeneous electron gas by numerical quantum Monte-Carlo simulations which yield essentially exact results with numerical accuracy. The resultant XC functional was later on parameterized by Perdew and Zunger [8], Perdew and Wang [9], etc. and are now known as LDA functionals.

The LDA approximation is expected to work well for systems in which the electronic charge density is varying slowly, but surprisingly it yields good results even in the case where the density is not slowly varying, for which this approximation hardly looks appropriate [10]. This can be attributed to two facts.

First, the LDA underestimates the exchange energy and overestimates the correlation energy which leads to the cancellation of errors. Secondly, the electron-electron interaction is dependent only on the spherical average of the exchange-correlation hole and not on its detailed shape.

However, while the LDA approximation provides reasonable results for metallic systems, for the semiconductor system, the bandgap is underestimated by a factor of 1/2 to 2/3 factors. The properties of insulators, particularly Mott insulators, are not described well using this formalism. Moreover, it cannot accurately predict activation energy barriers and is known to overestimate the binding energies. Intense efforts are going on to resolve the backlogs of this theory. We shall briefly describe the next step toward the improvement of LDA XC.

4.2.7.2. Generalized Gradient Approximation (GGA): We have seen that the LDA was derived by assuming that the electron density varies very slowly in space. Thus, it was argued that LDA could be improved if we expanded the exchange-correlation functional in terms of the gradient of the density in the Taylor series and truncated it to some order. Such an approximation is known as generalized gradient expansion approximation and was implemented by Herman et al. (1969) [11]. While GGA retains the core features of LDA, it also takes into account the spatial variations in the charge density which are important. The exchange-correlation energy within the GGA approximation can be written as:

$$E_{XC}^{GGA} = \int \epsilon_{XC}[\rho(\boldsymbol{r}), |\nabla\rho(\boldsymbol{r})|]\rho(\boldsymbol{r})d\boldsymbol{r} = \int \epsilon_{XC}[\rho(\boldsymbol{r})]F_{XC}[\rho(\boldsymbol{r}), \nabla\rho(\boldsymbol{r})]\rho(\boldsymbol{r})d\boldsymbol{r} \tag{4.29}$$

where the functional F_{XC} is called an enhancement factor. Depending on the choice of the functional form of enhancement factor F_{xc}, there are many forms of GGAs available that are being used over the years. One that has been widely used is by Perdew and Wang, known as PW86 and PW91 [12, 13]. Later on,

Perdew *et al.* (1996) proposed another functional (PBE) [14], which retains important features of PW91. In this thesis, we have mostly used the GGA-PBE exchange-correlation function, which is briefly described below.

In the case of PBE exchange-correlation functional, first, the enhancement factor F_{XC} over the local exchange is defined as:

$$E_{XC}^{PBE} = \int \epsilon_X^{LDA}[\rho(\boldsymbol{r})]F_{XC}(\rho,\zeta,s)\rho(\boldsymbol{r})d\boldsymbol{r} \tag{4.30}$$

where ρ is the local density, ζ is the relative spin-polarization, and $s = \frac{\nabla\rho(r)}{2\hbar_F\rho}$ is the dimensionless density gradient.

$$F_{XC}(s) = 1 + \mathrm{K} - \frac{\mathrm{K}}{1 + \mu s^2/\mathrm{K}} \tag{4.31}$$

where K and μ are empirically fitted to a database of ionization energies.

The correlation contribution to the energy is written as:

$$E_C^{PBE} = \int[\epsilon_c^{LDA}(\rho,\zeta) + H(\rho,\zeta,t)]\rho(\boldsymbol{r})d\boldsymbol{r} \tag{4.32}$$

with,

$$H(\rho,\zeta,t) = \left(\frac{e^2}{a_o}\right)\gamma\phi^2 ln\left\{1 + \frac{\beta\gamma^2}{t}\left[\frac{1+At^2}{1+At^2+At^4}\right]\right\} \tag{4.33}$$

in this equation $t = \frac{|\nabla\rho(\boldsymbol{r})|}{2\phi\hbar_s\rho}$ is the dimensionless density gradient and $\hbar_s = (\frac{4\hbar_F}{\pi a_o})$ is the Thomas Fermi Screening wave number, and, $\phi(\zeta) = \frac{[(1+\zeta)^{2/3}+(1-\zeta)^{2/3}]}{2}$ is a spin scaling factor.

The Function A has the form:

$$A = \frac{\beta}{\gamma}[\frac{exp(-\epsilon_C^{LDA}[\rho])}{\gamma\phi^3(e^2/a_o)} - 1]^{-1} \tag{4.34}$$

This GGA retains the correct features of LDA and combines them with the inhomogeneity features that are energetically most important. Although the

GGA method works much more precisely over LDA in terms of predicting the binding energies, electronic and magnetic properties of the materials, it does have a few drawbacks. The GGA approximation cannot describe the van der Waals (vdW) interaction. It is also known to overestimate the electric polarization for polar materials [15]. Finally, both GGA and LDA fail for strong electron-electron correlated systems and present research is continuing in search of a better functional.

4.2.7.3. LDA + U or GGA + U Method: It has been seen that LDA and GGA fail to give the correct ground state of strongly correlated systems such as transition metal oxides. LDA + U or GGA + U methods have been designed to correct this situation by constructing an orbital-dependent functional. The idea was taken from the Hubbard model [16, 17]. Suppose we have an orbital that already has one electron. If we put another electron in it, it will cost an energy U because of the electron-electron repulsion in that orbital. This idea when incorporated in LDA or GGA produces the LDA + U method. In the LDA + U or GGA + U method, strong on-site Coulomb repulsion (generally term as U) is directly added to strongly localized orbitals such as *d* and *f* orbitals along with the LDA or GGA functional. The magnitude of the added interaction is determined by the parameter U.

Let us consider a system with a fluctuating number of *d* (or *f*) electrons, but the total number of electrons $N = \sum_i n_i$ is constant. Within the LDA + U method, total energy can be written as:

$$E = E^{LDA} + \frac{1}{2} U \sum_{i \neq j} n_i n_j - U \frac{N(N-1)}{2} \tag{4.35}$$

This orbital-dependent functional gives upper and lower Hubbard band separation equal to U and thus correctly describes the physics of Mott insulators. For example, it correctly gives the antiferromagnetic insulating ground states for many transition metal oxides and cuprate superconductors, which turn out to be metallic using LDA or GGA. However, the main problem of the LDA + U

method is the choice of the value of U. Although U can be found *ab initio* by using the constrained DFT approach, it is overestimated by this method. Thus, the common way of finding U is to treat it as an adjustable parameter so that one finds good agreement between some calculated and experimental results.

4.2.7.4. Van der Waals Corrections: Although the results of Kohn-Sham equations are very much robust i.e. it provides reasonably correct predictions for many properties of various systems [18]. However, the main disadvantage of all common GGA functionals, including hybrids is that they are not able to describe long-range electron correlations precisely that are responsible for vdW forces [19, 20]. The vdW interactions between atoms and molecules play a crucial role in many systems in which they maintain a balance with electrostatic and exchange-repulsion interactions. As a result of it, they control many important fundamental properties including the packing of crystals, the structures of DNA and proteins, the orientation of molecules on surfaces or in molecular films, etc. So, it is very important to incorporate the vdW corrections in the DFT calculations.

Total exchange-correlation energy E_{xc} of a system including vdW correction can be written as:

$$E_{xc} = E_X^{GGA/LDA} + E_C^{GGA/LDA} + E_C^{NL} \tag{4.36}$$

where standard exchange and correlation components of LDA or GGA. Moreover, E_C^{NL} represents the nonlocal term describing the dispersion energy. Typically, E_C^{NL} is computed non-self-consistently i.e. it is simply an add-on to the self-consistent field (SCF). Even though this new add-on has very little effect on computed energy, it affects the computational forces calculated during geometry optimization. Grimme finds the empirical dispersion correction term which is written below:

$$E_C^{NL} = -s_6 \sum_{i=1}^{N_{at}-1} \sum_{j=i+1}^{N_{at}} \frac{C_6^{ij}}{R_{ij}^6} f_{dmp}(R_{ij}) \tag{4.37}$$

Here, N_{at} is the number of atoms in the system, C_6^{ij} denotes the dispersion coefficient for atom pair *ij*, s_6 is a global scaling factor which depends only on the density functional used, and Rij is an interatomic distance.

In order to avoid near-singularities for small R, a damping function f_{dmp} has been used, which can be written as:

$$f_{dmp}(R_{ij}) = \frac{1}{1 + e^{-d(R_{ij}/R_r - 1)}} \tag{4.38}$$

where R_r is the sum of atomic vdW radii. The DFT-D2 method is implemented in the VASP software [21].

4.2.8. Basis Set: To solve the Kohn-Sham equations, a choice of an appropriate basis set to expand the one-electron Kohn-Sham orbitals is necessary. The choice of basis set is dependent on the attributes of the system under study. Over the years, various basis-set methods have been developed for the prediction of the electronic properties of solids with reasonable accuracy. Depending on the choice of basis sets, different methods can be broadly classified into two categories:

4.2.8.1. Fixed Basis Set Methods: In this approach, the Kohn-Sham orbitals are expanded in terms of energy-independent basis sets or fixed basis sets as in the tight-binding model using a linear combination of atomic orbitals (LCAO) [22], the orthogonalized plane wave-pseudopotential methods [23, 24], etc. Here one has to solve the following eigenvalue value equation:

$$(H - \epsilon O).C = 0 \tag{4.39}$$

to determine the eigenvalue ε and expansion coefficient C, where O is the overlap matrix. This method is computationally simple but the disadvantage is that the basis depends on the ionic positions, so Pulay corrections have to be added to the Helmann-Feynman forces.

4.2.8.2. Partial Wave Methods: In these methods, the Kohn-Sham orbitals are expanded in a set of energy and potential-dependent all-electron partial wave basis set as in the cellular method, the augmented plane wave method (APW) [25], and the Korrimga-Kohn-Rostoker (KKR) method [26, 27]. Here one has to solve the set of the equation of the following form:

$$M(\epsilon).C = 0 \tag{4.40}$$

This approach is accurate in the band structure calculation but the main shortcomings of this method are due to the complicated non-linear energy dependence of the secular equation, the solution of this kind of equation is computationally very heavy. To overcome this, in 1975 O. K. Andersen first proposed a unified approach considering the positive aspects of a fixed basis set method and that of partial wave basis by linearisation of energy-dependent of partial waves. Linear augmented plane wave (LAPW) [25] and linear muffin-tin orbital (LMTO) [28] methods are the linearized version of the APW and KKR methods respectively.

In this thesis, we have used two types of basis set methods for geometry optimization and electronic structure calculations: (I) Plane-wave basis set pseudopotential method within the projected augmented wave (PAW) scheme. (II) The all-electron linearized augmented plane wave (LAPW) method.

A brief description of those above-mentioned methods is provided below:

4.2.9. Plane Wave Based Pseudopotential Method: The Plane Wave Based Pseudopotential Method (PWPP) is a widely used theoretical approach in computational materials science and condensed matter physics for calculating the electronic structure of solids. In the PWPP method, the wavefunctions of the electrons are expanded in a basis set of plane waves, which are simple periodic functions that can describe any periodic solid with arbitrary precision. The electron-ion interactions are described using pseudopotentials, which are effective potentials that replace the detailed atomic potential near the nuclei with a simpler form that still captures the essential physics.

4.2.9.1. Plane Wave Basis Set: The choice of the plane wave as a basis function to expand the single-particle Kohn-Sham orbitals is one of the common and widely used approaches in many first-principles method calculations due to the following reasons:

(I) The basis set is independent of the atomic position. (II) The Hellmann-Feynman forces acting on the atoms and the stresses on the unit cell can be easily calculated in terms of the expectation value of the Hamiltonian with respect to the ionic coordinates. So no basis set correction to the force is needed. (III) With this basis set, it is easy to change from a real-space representation (where the potential energy V has a diagonal representation) to momentum-space (where kinetic energy has a diagonal representation) *via* a Fast Fourier Transform (FFT).

According to Bloch's theorem, the wave function of an electron moving in a potential generated by a periodic lattice can be written as a product of a plane wave $e^{i\mathbf{k}.\mathbf{r}}$ and a function $u_{\mathbf{k}}(\mathbf{r})$ that has the periodicity of the lattice. Thus we can write:

$$\psi_k(\boldsymbol{r}) = e^{i\boldsymbol{k}.r} u_{\boldsymbol{k}}(\boldsymbol{r}) \tag{4.41}$$

Furthermore, the cell periodic part $u_{\mathbf{k}}(\mathbf{r})$ of the electron wave-function can be expanded using a basis set of plane waves whose wave vectors are the reciprocal lattice vectors of the crystal. So, we can write $u_{\mathbf{k}}(\mathbf{r})$ in the following way:

$$u_{\boldsymbol{k}}(\boldsymbol{r}) = \sum_{\boldsymbol{G}} c_{i,\boldsymbol{G}} e^{i\boldsymbol{G}.r} \tag{4.42}$$

where the reciprocal lattice vectors G are defined by $\mathbf{G}.l = 2\pi m$ for all l where l is a lattice vector and m is an integer. Therefore the full electron wave-function can be written as:

$$\psi_{\boldsymbol{k}}(\boldsymbol{r}) = \sum_{\boldsymbol{G}} c_{i,k+\boldsymbol{G}} e^{i(k+\boldsymbol{G}).r} \tag{4.43}$$

Thus, we can expand the electron wave-function at each **k** as a linear combination of discrete plane waves.

4.2.9.2. Pseudopotential Method: The electronic states of a large number of materials can be separated into two classes, such as core states, which are localized in space and deep in energy and valence or conduction states which are spread out spatially as well as higher in energy. Since the core electrons are tightly bound to the nucleus and rapidly oscillating due to the orthogonality required within the valence state, a large number of plane waves are required to describe the accurate behavior of the core state's wave functions. This is one of the major problems of the plane wave basis. To overcome the problem, in 1940 C. Herring introduced the orthogonalized plane wave method [29], where he described core states by Bloch sums built from localized orbitals and valence states by plane waves, orthogonalized to the core states.

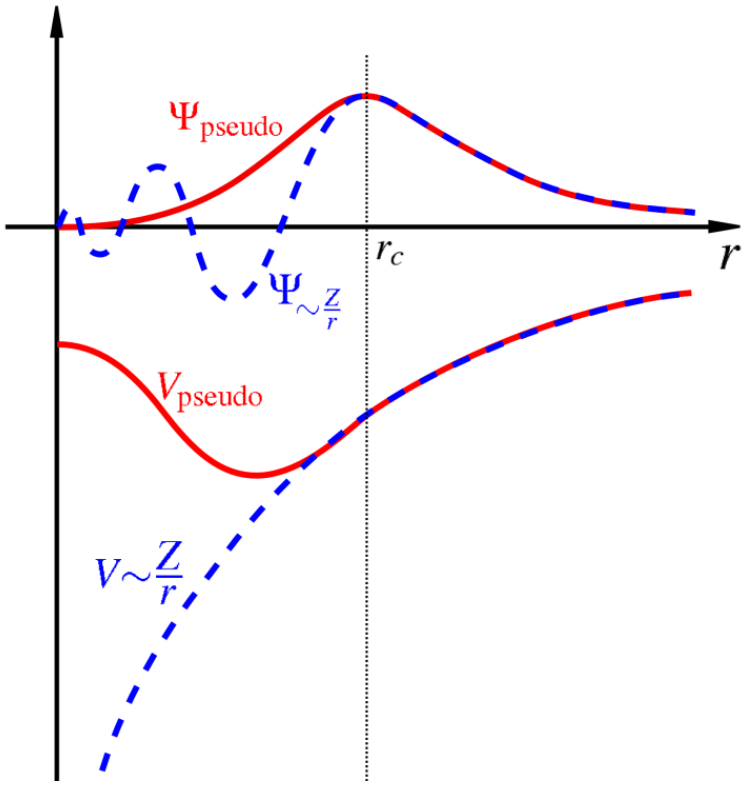

Figure 4.2: *Schematic diagram showing the basic idea of pseudopotential. The figure is taken from web:http://en.wikipedia.org/wiki/Pseudopotential.*

The pseudopotential approximation takes advantage of the fact that electrons in the core state do not play a significant role in determining the physical properties of materials such as chemical bonding, electronic structure, etc. Instead, these electrons partially screen the nucleus and thereby form an inert core along with

the nucleus. Thus the atom can be represented as an ionic core that interacts with the valence electrons *via* a strong ionic potential. This allows separation of the core states and valence states, which is exploited in the pseudopotential approach by removing the core electrons and replacing the strong ionic potential with a weaker effective pseudopotential. The valence electrons are then described by a set of pseudo wave functions which are acted on by the effective pseudopotential. The pseudopotential and pseudo wave functions are constructed in such a way that they are identical to the true potential and true wave function, respectively beyond a certain cut-off radius. The general procedure for obtaining the pseudo-potential is following,

The all-electron (AE) free atom Kohn-Sham radial equation is given by:

$$\left[-\frac{1}{2}\frac{d^2}{dr^2}+\frac{l(l+1)}{2r^2}+V_{eff}^{AE}[\rho^{AE}(\boldsymbol{r})]\right]\boldsymbol{r}R_{nl}^{AE}(\boldsymbol{r})=\in_{nl}^{AE}(\boldsymbol{r})R_{nl}^{AE}(\boldsymbol{r}) \tag{4.44}$$

where R_{nl}^{AE} is the radial part of the all-electron wave-function with angular momentum l. Within the spherical assumption of the Hartree and exchange-correlation potential, the effective potential V_{eff}^{AE} is written as:

$$V_{eff}^{AE}[\rho^{AE}(\boldsymbol{r})]=-\frac{Z}{r}+V_{Hartree}[\rho^{AE}(\boldsymbol{r})]+V_{xc}[\rho^{AE}(\boldsymbol{r})] \tag{4.45}$$

For a given distribution of electrons in the atomic energy levels, the free atom Kohn-Sham radial equation is then solved to obtain the radial wave function R_{nl}^{AE}.

Next, generate a pseudo-wave function R_{nl}^{PS} corresponding to R_{nl}^{AE} imposing the following conditions,

(i) The pseudo wave function should be node-less inside the core region of a certain radius r_c.

(ii) It should coincide exactly with the true all-electrons (AE) wave function beyond a certain cutoff distance i.e $R_{nl}^{PS}=R_{nl}^{AE}$ for $r \geq r_c$.

Knowing the pseudo-wave-function, the pseudo-potential can be obtained by inverting the radial Kohn-Sham equation for the pseudo-wave-function and the valence electronic density, given by:

$$V_{l,scr}^{PS} = \in_l^{PS} - \frac{l(l+1)}{2\boldsymbol{r}^2} + \frac{1}{2rR_l^{PS}(r)}\frac{d^2}{dr^2}[\boldsymbol{r}R_l^{PS}(\boldsymbol{r})] \tag{4.46}$$

The pseudopotential $V_{l,scr}^{PS}$ thus obtained takes into account the screening effect of the valence electrons. Finally to obtain the pseudopotential one has to subtract the Hartree and XC potential calculated only for the valence electrons. Therefore, considering the screening effect the pseudopotential takes the following form:

$$V_l^{PS} = V_{l,scr}^{PS} - V_{Hartree}[\rho^{PS}(\boldsymbol{r})] - V_{xc}[\rho^{PS}(\boldsymbol{r})] \tag{4.47}$$

The basic idea of pseudopotential is depicted in Figure 4.2. The cut-off radius $\mathbf{r}_c$ where pseudo and true wave-functions coincide is not an adjustable pseudopotential parameter. The outermost nodal surface of the true wave-function gives rise to the estimation of the smallest possible value of cut-off radius r_c and the pseudopotential corresponding this cut-off radius close to the minimum, is very realistic and at the same time very strong. If a very large cut-off radius is chosen, the pseudo-potential will be smooth and almost angular momentum independent, and at the same time it will be unrealistic. A smooth potential leads to fast convergence of plane-wave basis calculations. So choosing an optimal cut-off radius is critical to balance between basis-set size and pseudopotential accuracy.

A major drawback of the plane-wave pseudopotential method is that all information on the true wave-function close to the nuclei is lost which can play an important role in determining certain physical properties such as hyperfine splitting, electric field gradients, etc. Within the pseudopotential method, this problem can be addressed by the use of the projected augmented wave (PAW) method proposed by P. Blöchl [30]. A different approach is on the all-electron approach of the linearized augmented plane wave method based on the choice

of partial wave functions as basis sets. Both methods are discussed in the following sections.

4.2.10. Linearized Augmented Plane Wave (LAPW) Formalism: The linearized augmented plane wave (LAPW) is a method for solving the equations of DFT. It was first formulated by Slater in 1937 [31, 32]. Although pseudopotential methods are extremely useful in solving many problems, however, information inherently near the nucleus they are not the method of choice. In such cases, Augmented Plane Wave (APW) basis set can be more useful. LAPW formalism is a modification of the augmented plane wave (APW) method proposed by Slater. Modern implementations allow for several approximations to exchange and correlation (LDA, GGA, and LDA+U, among others) and make no approximations to the shape of the crystal potential, unlike methods employing the atomic sphere approximation (ASA) which assume spherical symmetry around each atom. Like most modern electronic-structure methods, the LAPW method is a variational expansion approach that solves the equations of DFT by approximating solutions as a finite linear combination of basis functions. Electrons that are far away from the nuclei behave as free particles. They can be described by plane waves. In contrast to regions close to the nuclei, the electrons behave in a localized manner at the nuclei site and therefore are more accurately described by atomic-like functions. In the APW method, this allows one to partition the system space into two parts *viz* the 'muffin-tin" (MT) spheres centered at each atom site and the remaining region called interstitial. The MT approximation was widely used in APW codes to elucidate the properties of transition metals and compounds. An MT sphere (S_a) is a sphere of radius R_a constructed around each atom. These MT spheres are chosen in such a way that they do not overlap and fill the space to the maximal extent. The remaining space outside the spheres is called the interstitial region (IS). Within the MT spheres, the potential is approximated to be spherically symmetric while in the interstitial region, it is considered to be constant.

The APW basis functions are then defined as;

$$\phi_G^k(r,\epsilon) = f(x)$$
$$= \begin{cases} \frac{1}{\sqrt{\Omega}} e^{i(k+G).r} & for\ r \in IS \\ \sum_{l,m} A_{lm}^{a,k+G} \varphi_l^a(r,\epsilon) Y_m^l(\theta',\varphi') & for\ r \in S_a \end{cases} \quad (4.48)$$

The position r inside the spheres is given with reference to the center of each sphere. φ_l^a is the solution to the radial Schrödinger equation for an isolated atom to the energy parameter ε. The coefficients $A_{lm}^{a,k+G}$are determined by the requirement that the wave-functions have to be continuous at the boundary of the MT spheres. Thus by matching the plane waves outside the sphere to the function inside the sphere at the boundary the value of $A_{lm}^{a,k+G}$can be obtained. In principle, since the expansion of the plane wave term of Eq. 4.45 contains a series of infinite terms, an infinite number of $A_{lm}^{a,k+G}$ can be found such that two functions can be matched. For practical purposes, however, a truncation at some value of l_{max} is required. A reasonably good condition is given by $R_a G_{max} = l_{max}$ where G_{max} provides the cut-off for the plane wave expansion.

Since, φ_l^a depends on energy, so does the resultant Hamiltonian matrix H. Thus, solving the secular equation to obtain the energy eigenvalues becomes a nonlinear problem that is computationally more expensive and non-trivial. Linearization of the APW method i.e. LAPW [31] helps to get rid of this problem. The linearized version of Augmented Plane Wave basis, following Andersen's linearization approach [33, 34], is expressed as:

$$\phi_G^k(r,\epsilon)$$
$$= \begin{cases} \frac{1}{\sqrt{\Omega}} e^{i(k+G).r} & for\ r \in IS \\ \sum_{l,m} A_{lm}^{a,k+G} \varphi_l^a(r',\in_v) + B_{lm}^{a,k+G} \dot{\varphi}_l^a(r',\in_v) Y_m^l(\theta',\varphi') & for\ r \in S_a \end{cases} \quad (4.49)$$

where the coefficients $A_{lm}^{a,k+G}$ and $B_{lm}^{a,k+G}$can be determined by matching these solutions in magnitude and slope at the sphere boundary. Although adding local orbitals increases the LAPW basis set size, still their number is quite small compared to the typical LAPW basis set the size of a few hundred functions. The

problem with the APW method was the energy dependence of the basis set, which is removed in the LAPW method, however, at the cost of a somewhat larger basis set size.

4.2.11. The Projector-Augmented-Wave (PAW) Formalism: The projector augmented-wave (PAW) method was developed by Blochl in 1994 [30] as a method to accurately and efficiently calculate the electronic structure. The advantage of this formalism is it contains the numerical advantages of pseudopotential calculations while retaining the physics of all-electron calculations including the correct nodal behavior of the valence-electron wave functions and the ability to include upper core states in addition to valence states in the self-consistent iterations. Later Kresse and Joubert modified this PAW method and implemented it within the plane-wave code of the Vienna Ab-initio Simulation Package(VASP) [35, 36]. Within this formalism, the drawback arising due to oscillations of valence-state wave-functions is addressed by transforming the physical wave-functions $\psi_n(\mathbf{r})$ into smooth auxiliary wave-functions $\tilde{\psi}_n(r)$ that can be represented in a plane wave expansion. This is achieved by defining a linear transformation operator $\boldsymbol{T}$ as:

$$T = 1 + \sum_a T^a \tag{4.50}$$

where T^a only acts in the augmentation spheres.

Augmentation spheres are constructs similar to the muffin-tin spheres defined around each atom i and have a radius$|r - R^a| < r_c^a$, where r_c^a is the cut-off radius, a is the atom site index and R_a is the position of the atoms i.

Then transformation **T** maps the smooth auxiliary wave-functions onto the true wave-functions by:

$$\psi_n(r) = \boldsymbol{T}\,\tilde{\psi}_n(r) \tag{4.51}$$

To evaluate the form of the operator **T**, one considers the all-electron partial wave basis functions $|\phi_i^a\rangle$. Let $\left|\tilde{\phi}_i^a\right\rangle$ be the auxiliary partial wave such that

outside the augmentation spheres they are identical to the all-electron partial wave basis functions:

$$|\phi_i^a\rangle = |\tilde{\phi}_i^a\rangle \; \forall |r - R^a| > r_c^a \tag{4.52}$$

Then,

$$|\phi_i^a\rangle = \boldsymbol{T}|\tilde{\phi}_i^a\rangle \tag{4.53}$$

$$|\phi_i^a\rangle = (1 + \sum_{a'} \boldsymbol{T}^{a'})\,|\tilde{\phi}_i^a\rangle \tag{4.54}$$

$$|\phi_i^a\rangle = (1 + \boldsymbol{T}^a)\,|\tilde{\phi}_i^a\rangle \tag{4.55}$$

The above equation implies that:

$$\begin{aligned} \hat{T}^a\,|\tilde{\phi}_i^a\rangle &= |\phi_i^a\rangle - |\tilde{\phi}_i^a\rangle \\ &= \sum_j (|\phi_j^a\rangle - |\tilde{\phi}_j^a\rangle\langle\tilde{p}_j^a|\tilde{\phi}_i^a\rangle) \end{aligned} \tag{4.56}$$

where $\langle\tilde{p}_j^a|$ is the projector operator satisfying the condition $\langle\tilde{p}_j^a|\tilde{\phi}_i^a\rangle = \delta_{i,j}$

So, the operator **T** can be written as:

$$\boldsymbol{T} = 1 + \sum_j (|\phi_j^a\rangle - |\tilde{\phi}_j^a\rangle\langle\tilde{p}_j^a|\tilde{\phi}_i^a\rangle) \tag{4.57}$$

Thus, $\psi_n(r)$ can be reconstructed from $\tilde{\psi}_n(r)$ on operating **T** as:

$$\psi_n(r) = \tilde{\psi}_n(r) + \sum_j (|\phi_j^a\rangle - |\tilde{\phi}_j^a\rangle\langle\tilde{p}_j^a|\tilde{\phi}_i^a\rangle) \tag{4.58}$$

The smooth auxiliary wave-function $\tilde{\psi}_n(r)$ is identical to the all-electron wavefunctions $\psi_n(r)$ outside the augmented spheres. The auxiliary partial waves $|\tilde{\phi}_j^a\rangle$ are chosen such that they form the basis for $\tilde{\psi}_n(r)$ within the augmented sphere. Therefore it can be written as in eq. (4.59). Furthermore, it

can be shown that the all-electron wave function $\psi_n(r)$ can be expanded in terms of all-electron partial waves $|\phi_j^a\rangle$ using the same coefficients C_{ni}^a.

$$\widetilde{\psi}_n(r) = \sum_i C_{ni}^a |\tilde{\phi}_i^a\rangle \tag{4.59}$$

The PAW formalism as implemented within the VASP software by Kresse and Joubert has been primarily used for the work described within this thesis.

4.2.12. Time-Dependent Density Functional Theory: The DFT has been generalized to include time-dependent potentials and is known as TDDFT. This theory can be thought of as a reformulation of the time-dependent quantum mechanics in terms of time-dependent electron density $\rho(\mathbf{r},t)$. This approach has a great advantage over the wave function approach, as the many-body wave function is a function of N positions, where N is the number of electrons while the electron density is a function of one position only.

The main theoretical construction was done by Runge and Gross (1984) who gave a theorem known as the Runge–Gross theorem [37], which is the analog of the Hohenberg–Kohn theorem for the time-dependent electron density $\rho(\mathbf{r},t)$. They showed that DFT can be extended to problems where a time-dependent external perturbation is present, such as the oscillating electric field of a laser. Runge–Gross theorem establishes a one-to-one correspondence between $\rho(\mathbf{r},t)$ and time-dependent external potential $v_{ext}(\mathbf{r},t)$ for a given initial state. Similar to DFT, one can define a fictitious system of non-interacting electrons that has the same density $\rho(\mathbf{r},t)$ of the real system and which moves in a time-dependent effective potential $v_{eff}(\mathbf{r},t)$. This leads to an equation similar to the time-dependent Schrödinger equation, known as the time-dependent KS equation. A noninteracting system is defined in such a way that it reproduces the exact groundstate density of the interacting system. This means that we can calculate the exact density as the sum of squares of single-particle orbitals:

$$\rho(\boldsymbol{r},t) = \sum_{j=1}^{N} |\varphi_j(r)|^2 \tag{4.60}$$

where the orbitals satisfy the following equation:

$$\left[-\frac{\nabla^2}{2} + v_{eff}(\boldsymbol{r}, t)\right]\varphi_j(r) = \varepsilon_j\varphi_j \tag{4.61}$$

This equation is called the time-dependent Kohn Sham equation [38, 39].

Here,

$$v_{eff}(\boldsymbol{r}, t) = v_{ext}(\boldsymbol{r}, t) + v_{XC}(\boldsymbol{r}, t) + \int d^3r' \frac{\rho(\boldsymbol{r}, t)}{|r - r'|} \tag{4.62}$$

Here $v_{XC}(\boldsymbol{r}, t)$ is the time-dependent exchange-correlation potential, and $v_{ext}(\boldsymbol{r}, t)$ is the external time-dependent field. The second term on the right-hand side of Eq. (4.62) is the time-dependent Hartree potential, describing the interaction of classical electronic charge distributions. The exchange-correlation potential $v_{xc}(\boldsymbol{r}, t)$ is an unknown functional of $\rho(\boldsymbol{r}, t)$ which has to be approximated. The functional derivative of exchange-correlation potential $\delta v_{xc}/\delta\rho$ is called the exchange-correlation kernel f_{XC}. The simplest approximation is the adiabatic local density approximation (ALDA) in which the exchange-correlation potential of the homogeneous electron-gas [7] with the instantaneous density is used to evaluate $v_{xc}(\boldsymbol{r}, t)$, that is:

$$v_{XC}^{ALDA}(\boldsymbol{r}, t) = v_{XC}^{unif}(n(\boldsymbol{r}, t)) \tag{4.63}$$

This formalism has been applied to calculate excited-state energies and photo-absorption cross-sections of molecules and clusters. Hence one replaces the inhomogeneous electron system at each point $\boldsymbol{r}$ with a homogeneous electron gas having the density of the inhomogeneous system at $\boldsymbol{r}$. The rationale for this approximation is in the limit of slowly varying density. In practice, however, the macroscopic dielectric function calculated using this kernel has two well-known deficiencies: the quasiparticle gap is too small, and the physics of the bound electron-hole pair is missing. ALDA does not improve on the results obtained within the random phase approximation (RPA) which corresponds to the trivial kernel f_{XC} =0.

4.2.12.1. Exchange Correlation Kernel: The change of electron density in the presence of an external potential requires, in addition to the exchange-correlation potential, the exchange-correlation kernel– the functional derivative of the exchange-correlation potential with respect to the density. The search for improved TDDFT potentials and kernels is hence a subject of increasing interest. There is a large literature dealing with the inclusion of many-body effects into TDDFT kernels, to correctly reproduce excitonic features. In the present thesis, we have used two types of exchange-correlation kernel in order to calculate the excitonic property of systems, these are; a) Bootstrap (BOS) [40] and b) Long Range Contribution (LRC) [41].

4.2.12.2. Bootstrap Method [40]: We have adapted the Bootstrap kernel method as implemented by Gross *et al.* The exact relationship between the dielectric function ε and the kernel f_{xc} for a periodic solid can be written as:

$$\varepsilon^{-1}(\boldsymbol{q},\omega) = 1 + v(\boldsymbol{q})\chi(\boldsymbol{q},\omega)$$

$$= 1 + \chi_0(\boldsymbol{q},\omega)v(\boldsymbol{q})\{1 - [v(\boldsymbol{q}) + f_{xc}(\boldsymbol{q},\omega)]\chi_0(\boldsymbol{q},\omega)\}^{-1} \quad (4.64)$$

In this equation, v is the bare Coulomb potential, χ is the full response function, and χ_0 is the response function of the noninteracting Kohn-Sham system. The frequency-independent approximation for the XC, can be written as:

$$f_{XC}^{boot}(q,\omega) = -\frac{\epsilon^{-1}(q,\omega=0)v(\boldsymbol{q})}{\varepsilon^0_{GG'}(q,\omega=0) - 1} = \frac{\epsilon^{-1}(q,\omega=0)}{\chi^0_{GG'}(q,\omega=0)} \quad (4.65)$$

where $\varepsilon_0 = 1 - v(\boldsymbol{q})\chi_0(\boldsymbol{q},\omega)$ is the dielectric function in RPA formalism [42]. The approximate functional is chosen in such a way that it satisfies two important requirements; a) f_{XC} has the exact long-wavelength behavior *i.e*:

$$f_{XC}(q \to 0) = \alpha_{XC}/q^2 \quad (4.66)$$

In the $\omega \to 0$ limit, the form of f_{XC} should yield static dielectric constants close to the RPA values, which are known to reproduce experiments reasonably well.

These equations are useful when either f_{XC} or ε is unknown. With the addition of the approximation given by Eq. (4.65), however, both f_{XC} and ε can be determined from knowledge of χ_0 exclusively. The *modus operandi* for doing so is to start by setting $f_{XC} = 0$ and then solving Eq. (4.64) to obtain ε^{-1}. This is then ''bootstrapped'' in Eq. (4.65) to find a new f_{XC}, and the procedure repeated until self-consistency between the two equations at ω=0 is achieved.

This Bootstrap kernel has two key advantages: first of all, the computation cost is very minimal, as the most expensive part is the calculation of χ_0, which needs to be calculated only once, and, most importantly no system-dependent external parameter is required.

4.2.12.3. Long Range Method [41]: The long-range component of the exchange-correlation kernel f_{XC} is completely absent from local density or generalized gradient approximations, but it is believed to be present in the "exact" f_{XC}. In the case of solids, the Hartree contribution is not sufficient to yield good absorption spectra (it then just gives rise to the crystal local field effects). In this case, taking into account f_{XC} within Time-Dependent LDA (TDLDA) does not lead to a significant improvement. The reason for this failure can be traced back to the short-range nature of the TDLDA f_{XC}, while the "exact" f_{XC} is believed to be long-ranged, decaying in momentum space as $1/q^2$.

Therefore, when calculating electronic excitations in solids we have the BSE, a precise but computationally demanding method, and at the same time we are using TDDFT, a rather inexpensive method whose applicability is severely limited by the shortcomings of the TDLDA. Several attempts have been made to find a desirable f_{XC} which will be generally applicable. Improvements to the TDLDA might come through the inclusion of dynamical effects and/or long-range nonlocal terms. One of the simplest models used to consider the long-range effect is of the form:

$$f_{XC}^{static}(q) = -\alpha^{static}/q^2 \tag{4.67}$$

where α^{static} is a frequency-independent long-range component of the exchange-correlation kernel. Keeping only this contribution is sufficient to simulate the strong continuum exciton effect in the absorption spectrum. More detailed and accurate formulation involves introducing frequency dependence. In order to improve on this simplest of models, we can follow two paths: a) introduce a more complex spatial behaviour, b) introduce frequency dependence. We have followed the later method in our time-dependent absorption calculations.

The frequency-dependent form of the model kernel is proposed as:

$$f_{xc}^{dyn}(\boldsymbol{q},\omega) = -\frac{1}{q^2}(\alpha + \beta\omega^2) \tag{4.68}$$

the two parameters α and β of Eq. (4.68) can be related to physical quantities, like the dielectric constant and the plasma frequency. This approach is a promising alternative to the use of the significantly more complicated kernels proposed in the literature for the efficient calculation of electronic excitations in complex systems made of semiconductors and insulators.

4.3. Computational Details:

4.3.1. Electronic Structure and Orbital Analysis: The first-principles electronic structure are calculated with the help of plane-wave calculations with norm-conserving projector augmented wave (PAW) pseudopotentials. We have used both the local density approximation (LDA) and generalized gradient approximation (GGA) with Ceperley-Alder (CA) and Perdew-Burke-Ernzerhof (PBE) [43] exchange-correlation functionals respectively, as implemented in the Vienna ab initio simulation program (VASP) [44]. To examine the role of the vdW interactions across the layers, the semi-empirical dispersion potential representing the dipolar interactions is included within the DFT energy functional by using the DFT-D3 method of Grimme [45]. A monkhorst-Pack *k*-grid of dimension 5×5×3 is used for sampling the Brillouin zone and the cut-off for the plane wave expansion is kept at 500 eV. The energy convergences for all

self-consistent field calculations are kept as 10^{-5} eV and the structural optimizations were performed using the conjugate gradient algorithm, till the Hellmann-Feynmann force on each ion is less than 0.01 eV/Å.

4.3.2. Phonon Dispersion Using VASP Phonopy Code: The phonon-dispersion curves are calculated from the VASP-Phonopy code with GGA-PBE exchange-correlation functional after incorporating van der Waal correction. We have employed a combination of the supercell and the finite displacement methods to first generate a 2×2×2 supercell and successively provide a finite displacement to its atoms by an amount of 0.002 Å. The force constants are generated for each supercell by using first-principles VASP calculations and these constants, being a signature of the interatomic potential, are collected after using the Phonopy code to generate the dynamical matrix [46]. Diagonalization of this matrix results in the phonon frequencies and thus produces the phonon dispersion curves along the high-symmetry path of the Brillouin-zone. The plane wave cut-off energy is kept at 500 eV and the criteria for minimization of Hellmann-Feynmann force is kept at 0.001 eV/Å and the criteria for convergence of the electronic energy is kept at 10^{-8} eV.

4.3.3. Hybrid Functional (HSE06) Calculation: We have utilized Heyd Scuseria-Ernzerhof (HSE06) [47] hybrid functional calculations for a precise description of the unoccupied levels and better determination of the band gap of the semiconductor-based system. The energy convergence for all self-consistent field calculations is kept as 10^{-5} eV and the structural optimizations were performed within the conjugate gradient algorithm, till the Hellmann–Feynmann force on each ion is less than 0.01 eV/Å. Band-structure calculation by using HSE06 will complete in two steps. First, HSE SCF: for this copy the input files along with CHGCAR and WAVECAR from GGA-PBE SCF. Put the HSE tags (LHFCALC = .TRUE., HFSCREEN = 0.2, AEXX = 0.25, ALGO = D, TIME = 0.3, LDIAG = .TRUE.) in INCAR file. Second, copy the four input files along with CHGCAR, WAVECAR and IBZKPTS from HSE-SCF. Collect the "k-points in reciprocal lattice" from OUTCAR of GGA-PBE band-structure

calculation and put them at the bottom of IBZKPTS and rename it as KPOINTS. The fourth column of the KPOINTS copied from OUTCAR should be changed to 0.000 and modify the number of automatically generated mesh as per the k-points in reciprocal lattice.

4.3.4. X-ray Spectral Properties: The optimized structures from VASP were taken as input for computing the X-ray spectroscopic properties. The DFT ground state self-consistent solutions are obtained with the GGA potentials, after incorporating the spin-orbit coupling in the fully relativistic manner, as implemented in full potential Linearized Muffin-Tin orbital (FP-LMTO) based RSPt code [48, 49]. To compute the L and M edges, the core-hole is created at the metal-2*p* and 3*p* levels respectively and the corresponding *p*-levels are explicitly included in the single-impurity Anderson model (SIAM) [50, 51]. The Slater-Condon integrals corresponding to the L and M edge X-ray spectroscopy are calculated after considering the corresponding modified basis sets with the core-hole placed at the respective levels. These integrals and the hybridization functions are used in the calculation of the X-ray spectra after solving the SIAM. The double-counting corrections used in this calculation are formulated using the concept of charge-transfer energy [50].

In this approach, the construction of the local Green's function is done with the projection of a single particle Green's function from the lattice momentum to the impurity site. The projection is defined with a particular energy window. The hybridizations of the projected Re-5*d* orbitals with the ligands are calculated from the inversion of the local Green's function in terms of the impurity-bath hopping parameters. The continuous hybridization function is discretized and the resulting bath states are used in the exact diagonalization scheme, as implemented in the impurity model. The SIAM is constructed from the DFT-derived single particle Hamiltonian after combining the Coulomb interaction terms between the impurity 5*d* orbital, relevant bath states and a 2*p* (or 3*p*) core spin-orbital state. The strong spin-orbit coupling of the core states splits the L_3 and L_2 (or M_3 and M_2) edges of the absorption spectrum.

4.3.5. Calculation of Exfoliation Energies: The exfoliation energies are calculated by using formula,

$$\mathrm{E_{ex}(n) = [E_{slab}(n) - E_{bulk}/m]/A} \tag{4.69}$$

Where, $E_{ex}(n)$ is the exfoliation energy of n layers, $E_{slab}(n)$ is the energy of the unit cell of the n-layer slab in a vacuum, E_{bulk} is the energy of the unit cell of the bulk system consisting of m layers, and A is the in-plane area of the bulk unit cell.

4.3.6. DFT + Dynamical Mean-field Theory (DMFT) + Spin Orbit Coupling (SOC): We have used DFT+DMFT+SOC approach to treat the moderately correlated Kagome systems. For strongly correlated systems, the basic task is to find out the actual set of "correlated orbitals" $\{|R, \xi>\}$ with R specifying the Bravais lattice site corresponding to the correlated atom and ξ is the orbital index within the unit cell. In the presence of correlation, the total Hamiltonian of the system can be written after incorporating the Hubbard interaction, explicitly describing the local Coulomb repulsion U as the Local-density approximations (LDA) + U Hamiltonian:

$$H = H_{LDA} + \frac{1}{2}\sum_R \sum_{\xi_1 \ldots \xi_4} U_{\xi_1 \ldots \xi_4} c^{\dagger}_{R,\xi_1} c^{\dagger}_{R,\xi_2} c_{R,\xi_3} c_{R,\xi_4} \tag{4.70}$$

with the atomic-like correlated orbitals, the Coulomb parameter $U_{\xi_1 \ldots \xi_4}$ can be expressed in terms of the Slater integrals F^n as:

$$U_{\xi_1 \ldots \xi_4} = \sum_{n=0}^{2l} a_n(\xi_1 \ldots \xi_4) F_n \tag{4.71}$$

with

$$a_n(\xi_1 \ldots \ldots \xi_4) = \frac{4\pi}{2n+1} \sum_{q=-n}^{n} \langle \xi_1 | Y_{nq} | \xi_3 \rangle \langle \xi_2 | Y^*_{nq} | \xi_4 \rangle \tag{4.72}$$

where $\langle \xi_1 | Y_{nq} | \xi_3 \rangle$ and $\langle \xi_2 | Y^*_{nq} | \xi_4 \rangle$ are the integrals over the products of three spherical harmonics.

The LDA+U Hamiltonian represent an effective Hubbard model, the solution of which requires treating a many-body problem. In spectral DFT, after specifying the main observable quantity, we map the original system into one with lesser

degrees of freedom in such a way that the expectation value of the observable is kept intact. In DFT, we define the main observable as the charge density $\rho(r)$ and the one electron Green's function

$$\hat{G}(z) = \left[(z-\mu)\mathbb{I} - \hat{h}_{LDA} - \hat{\Sigma}(z)\right]^{-1} \tag{4.73}$$

here z is the energy in the complex plane, μ is the chemical potential, $\hat{h}_{LDA}$ is the unperturbed Hamiltonian consisting of the hopping term and $\hat{\Sigma}(z)$ is the self-energy operator, being a many-body representative of the electron interactions. In spectral DFT, the main observable is the local Green's function at the site R:

$$\hat{G}_R(z) = \hat{P}_R \hat{G}(z) \hat{P}_R \tag{4.74}$$

where, $\hat{P}_R = \sum_\xi |R,\xi\rangle\langle R,\xi|$ is the projection operator in the correlation subspace of $\boldsymbol{R}$. Like LDA or GGA approximations in DFT, the corresponding approximation in spectral DFT is Dynamical mean field theory (DMFT), where the self-energy is assumed to be purely local. This assumption of local self-energy allows us to concentrate only on single site R and the effect of the other sites can be replaced with a self-consistent electronic bath $\mathcal{G}_0^{-1}(R,z)$. Thus, the atomic site is considered to be embedded in a fermionic bath and that whole system is treated as a multiband Anderson impurity model. Without knowing the exact Hamiltonian, one can always represent the effective action as:

$$S = -\iint d\tau d\tau' \sum_{\xi_1\xi_2} c^\dagger_{\xi_1}(\tau')[\mathcal{G}_0^{-1}]_{\xi_1\xi_2}(\tau-\tau') c_{\xi_2}(\tau) + \frac{1}{2}\int d\tau \sum_{\xi_1\ldots\xi_4} c^\dagger_{\xi_1}(\tau) c^\dagger_{\xi_2}(\tau) U_{\xi_1\ldots\xi_4} c_{\xi_4}(\tau) c_{\xi_3}(\tau) \tag{4.75}$$

where τ is the imaginary time for the finite temperature many-body system and the limit of the integral are from 0 to $= \frac{1}{KT}$. So, the problem is now defined and the impurity Green's function $\hat{G}_{imp}(z)$ arises from the dynamics ascribed through the action S. With the help of the inverse Dyson equation, an explicit expression for the self-energy operator is obtained after solving the "impurity" problem:

$$\hat{\Sigma}(R,z) = \mathcal{G}_0^{-1}(R,z) - G_{imp}^{-1}(z) \tag{4.76}$$

The solution of this multiband Anderson impurity problem is obtained with the help of the spin-polarized T-matrix fluctuation-exchange (SPTF) solver [52, 53], which is an efficient and reliable impurity solver for moderately correlated electron systems. Once the effective impurity problem is solved and the updated self-energy is obtained, the number of particles will undergo an effective change and thus the chemical potential will be updated and thus a new Green's function is obtained as per equation (S2.4). Thus, one now obtains a new electronic bath $\mathcal{G}_0^{-1}(R,z)$ by using the inverse Dyson equation:

$$\mathcal{G}_0^{-1}(R,z) = G_R^{-1}(z) + \hat{\Sigma}(R,z) \tag{4.77}$$

This full process is iterated until a convergent self-energy is obtained. In the next step, this couples with the convergence of electronic charge via the full self-consistent cycle to obtain a complete solution of DFT+DMFT.

All of these calculations have been performed using the relativistic spin-polarized toolkit (RSPt) [49, 54, 55], which is based on linearized muffin-tin orbitals.

4.3.7. Calculation of Inter-site Exchange Interactions: The Heisenberg and DM interactions are calculated using the Lichtenstein-Katnelson-Antropov-Gubanov (LKAG) relation [56, 57], where the concerned electronic system is mapped onto a generalized classical Heisenberg model:

$$H = -\sum_{i \neq j} e_i^{\alpha} \hat{J}_{ij}^{\alpha\beta} e_j^{\beta}, \quad \alpha, \beta = x, y, z \tag{4.78}$$

Here the unit vector e_i denotes the local spin direction and the fully relativistic exchange tensor constitutes the interactions like Heisenberg exchange, DM interaction and symmetric anisotropic exchange $\hat{\Gamma}$ by following the relations (for the z-component):

$$D_{ij}^{z} = \frac{1}{2}\left(J_{ij}^{xy} - J_{ij}^{yx}\right) \tag{4.79}$$

$$\Gamma_{ij}^{z} = \frac{1}{2}\left(J_{ij}^{xy} + J_{ij}^{yx}\right) \tag{4.80}$$

Similarly, the x and y components can be calculated.

All these parameters are extracted from a fully self-consistent converged DFT+DMFT calculation.

4.3.8. Superconducting Critical Temperature (T_c) of AV_3Sb_5 (A = Cs, Rb and K): The superconducting critical temperature (T_c) calculations were performed based on an analysis of Eliashberg's theory proposed by Allen and Dynes [58] with the help of an approximate formula:

$$T_c = \frac{f_1 f_2 \omega_{log}}{1.20} \exp\left(-\frac{1.04\,(1+\lambda)}{\lambda - \mu^*(1+0.62\lambda)}\right) \tag{4.81}$$

where f_1 and f_2 are correction factors depend on λ, μ^*, ω_{log} and $\bar{\omega}_2$

$$f_1 = \left[1 + \left\{\frac{\lambda}{2.46(1+3.8\mu^*)}\right\}^{3/2}\right]^{1/3} \tag{4.82}$$

$$f_2 = \left[1 + \frac{\lambda^2\left\{\frac{\bar{\omega}_2}{\omega_{log}} - 1\right\}}{\lambda^2 + \left\{1.82(1+6.3\mu^*)\left(\bar{\omega}_2/\omega_{log}\right)\right\}^2}\right] \tag{4.83}$$

and $$\mu^* = \alpha \frac{N}{(1+N)} \tag{4.84}$$

The value of α is in the range of 0.28 to 0.31. N is the density of states at the Fermi level.

The first inverse moment of $\alpha^2F(\omega)$ gives the frequency-dependent electron-phonon coupling constant parameter λ from the relation,

$$\lambda(\omega) = 2\int_0^\infty d(\omega)\,\alpha^2F(\omega)/\omega. \tag{4.85}$$

The values of λ and ω_{log}, as extracted from a density functional perturbation theory (DFPT) calculation by using the Quantum Espresso code was directly used in the Allen and Dynes equation. Here, ω_2 is the second moment of the normalized weight function and the general form of the moment is

$$\omega_n = \frac{2}{\lambda}\int d\omega\,\alpha^2F(\omega)\omega^{n-1}. \tag{4.86}$$

We have calculated the above integral for $n = 2$ by using $\alpha^2F(\omega)$ for each value of λ. After getting the value of ω_2, we calculate the $\bar{\omega}_2$ as

$$\bar{\omega}_n = (\omega_n)^{1/n} \tag{4.87}$$

4.3.9. Time-dependent DFT (TDDFT) for the Calculation of Interacting and Non-interacting Response: In TDDFT, the time-dependent Schrödinger equation is mapped onto an effective one-electron problem, where the time dependence is incorporated in the approximation of the exchange-correlation kernel as a function of the explicit time dependence of the exchange-correlation potential and electron-density as:

$$f_{xc}(r, r', t - t') = \frac{\partial v_{xc}(r,t)}{\partial \rho(r',t')} \tag{4.88}$$

Calculation of the response function involves a many-body approach towards the solution of the Bethe Saltpeter Equation (BSE) using the one-body Green's function. In BSE, the dielectric function is written in terms of the bare-Coulomb potential and the interacting response function as:

$$\epsilon^{-1}_{GG'}(q, \omega) = \delta_{GG'} + v_{GG'}(q)\chi'(q, \omega)\ , \tag{4.89}$$

where $v(q)$ is the bare Coulomb potential and χ is the full response function, which is related to the response function χ^0 of the non-interacting Kohn-Sham system as:

$$\chi'(q, \omega) = \frac{v_{GG'}(q)\chi^0_{GG'}(q,\omega)}{1-[v_{GG'}(q)+f_{xc}(q,\omega)]\chi^0_{GG'}(q,\omega)} \tag{4.90}$$

The time-dependent exchange correlation is calculated from:

$$f_{xc}^{TDDFT}(q, \omega) = \frac{\epsilon^{-1}(q,\omega)}{\chi^0_{GG'}(q,\omega)} \tag{4.91}$$

The coupled equations (2), (3) and (4) are solved by initially setting $f_{xc}^{TDDFT} = 0$ and then calculating $\chi'(q, \omega)$ and thus $\epsilon^{-1}_{GG'}(q, \omega)$. This value is then utilized in equation (4) to find out the new f_{xc}^{TDDFT}. This procedure is repeated until self-

consistency is obtained at ω = 0. The response functions are computed after taking care of both interband and intraband contributions.

4.4. A First-principles Study for Structure-function Correlation: A Case Study:

4.4.1. Introduction: Strong in-plane anisotropy and the presence of metallic bonds in rhenium dichalcogenides ReX_2 (X = S, Se) promote the formation of the Peierls-distorted Re4-parallelogram array along an in-plane axis [59]. As a consequence, the lack of rotational symmetry incites highly anisotropic optical, vibrational, thermal and electrical responses leading to their utilization for optoelectronic [60], electrical [61], photocatalytic [62] and excitonic [63] devices. Manifestation of in-plane anisotropies on polarized photoluminescence [64], Raman [65, 66], thermal conductivity [67] and carrier mobility [68] brightens their prospects for novel functional usage. The superior environmental stability of ReX_2 enhances the application potential of its directional anisotropy in comparison to the anisotropic but highly degradable black phosphorus [69] and many other 2D materials.

In contrast to the well-established in-plane anisotropies of ReX_2 (X = S, Se), there are many conflicting experimental reports on several other properties of these compounds, which lack a proper theoretical explanation. These conflicts can be listed as follows: (A) There is no consensus on the long-debated issue of whether the bandgaps of these systems are direct or indirect in the bulk and monolayer limit [65, 70-77]. Whereas most experiments suggested an indirect band-gap nature for ReS_2 from monolayer to seven layers [65, 71, 73-78], some also indicated the presence of a direct band-gap [70, 72, 73, 79, 80]. Angle resolved photoemission spectra (ARPES) of ReS_2 have been variously interpreted to suggest the band-gap as being nearly direct [81], marginally indirect [82] and significantly indirect [83]. For $ReSe_2$, high resolution ARPES indicated an indirect band gap in bulk single crystals [84]. Nonetheless, the experimental results mainly indicate an indirect bandgap, GW-BSE calculations for both bulk systems suggested a direct bandgap [73, 79, 80]. In addition to the conflict about the nature of bandgap, the role of orbital contributions at the band edges, controlling the in-plane anisotropy and the nature of bandgap, is not analyzed to any larger detail [75]. (B) The question about the presence of interlayer coupling and the relative contribution of van der Waals (vdW) interaction and electronic hybridizations towards it remains unanswered [83, 85-87]. In

ReS_2, the presence of interlayer coupling was confirmed from the shear and the breathing Raman modes [85, 86, 88, 89] and also from anisotropic photoluminescence [90]. The delocalization of electrons across the vdW gap indicates the contribution of electronic hybridization toward interlayer coupling [83] of ReS_2. For $ReSe_2$, the intimate interplay of the in-plane anisotropy and orbital contribution in tuning the interlayer coupling [91, 92] was demonstrated by ARPES measurements. A lack of understanding of the interlayer coupling in these systems leads to the presence of contradicting experiments of the bandgap crossovers with lowering material thickness [70, 80, 83]. (C) Whether ReS_2 and $ReSe_2$ are isostructural or isoelectronic is still an open question. While polarized Raman measurements indicate them to be isostructural [86], the transmission electron micrograph (TEM) spurs the controversy regarding the presence and absence of Bernal stacking in $ReSe_2$ and ReS_2 respectively [72, 93]. The ambipolarity of $ReSe_2$ and n-type doping in ReS_2 illustrate their difference of orbital contributions at the band-edges [94], emphasizing the fact that these two systems are not isoelectronic. (D) Although pressure-induced metallization in these systems is reported [95, 96] to have negative pressure coefficients for the first direct optical transition, which is anomalous when compared to other dichalcogenides [97], there is still a lack of knowledge on the analysis of pressure-induced metallic transition in the light of orbital decomposition.

Despite numerous existing results, all these conflicting experimental and theoretical results are yet to be analysed in the light of structure-property correlations. In this comprehensive work, with the help of a detailed first-principles electronic structure and phonon calculations, we perform a comparative study of the energetics and electronic properties of all the available structures for both of these systems. After converging upon the lowest energy structures, we point out the effects of structural relaxations and orbital decomposition on the detailed anisotropic electronic structure of these systems to explain the existing conflicts. In addition, with the help of a combined full-potential DFT+MLFT approach, we have constructed a single impurity Anderson Model (SIAM) [50, 51] for the Re-5*d* and 2*p* (3*p*) states and solved it to calculate the X-ray spectra for the ground state structures of ReS_2 and $ReSe_2$ for assessing the role of structural optimization and electronic structure on the chemical environments. The following sections describe the results of this comprehensive study.

4.4.2. Re-dichalcogenides: Resolving Conflicts of their Structure-property Relationship [98]: ReX_2 (X = S, Se) have been discussed to stabilize in the

distorted 1T′ structures belonging to the triclinic symmetry group P-1 [72]. Detailed scrutiny of prior literature leads to two different structures for ReS_2 and $ReSe_2$. The initial structure prediction for ReS_2 was carried out by Murray *et al.* [99] with an unit cell of four formula units and lattice parameters $a = 6.42$ Å, $b = 6.51$ Å and $c = 6.46$ Å.

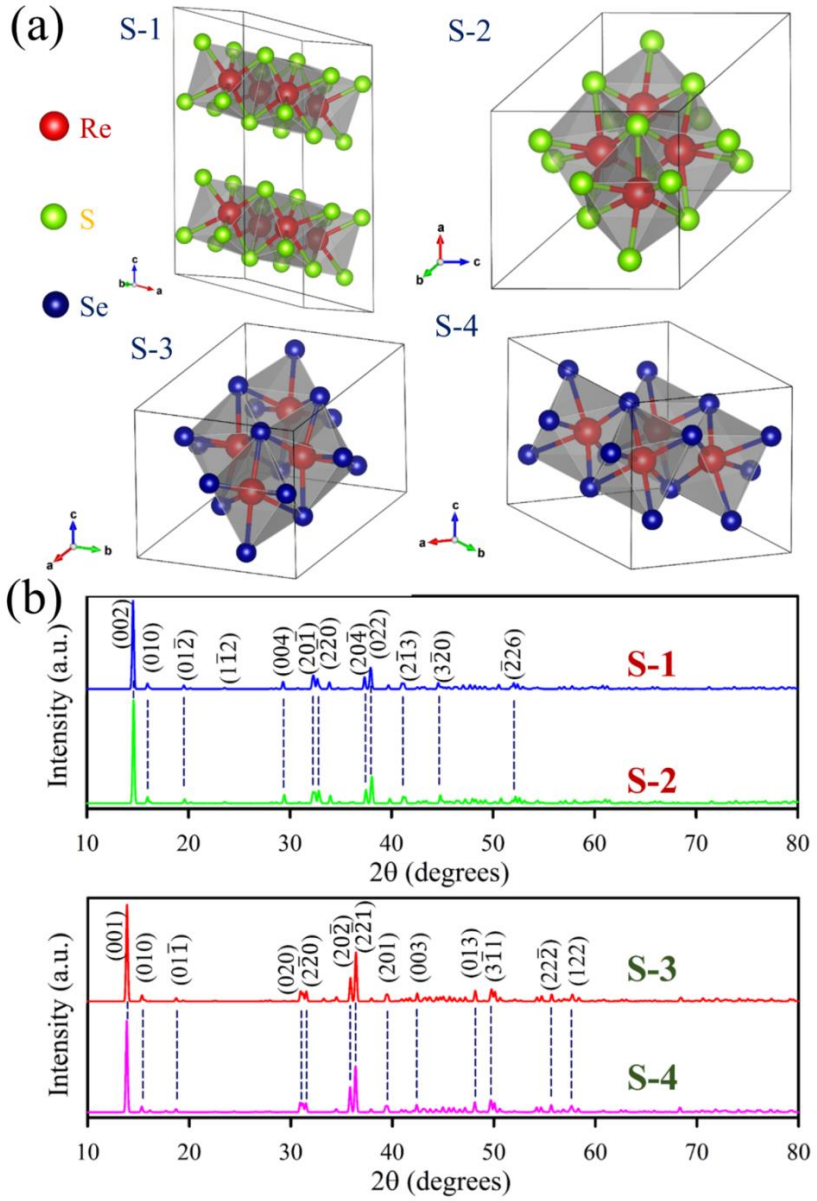

Figure 4.3: *(a) ICSD structure of ReS_2 (S-1), ReS_2 (S-2), $ReSe_2$ (S-3) and $ReSe_2$ (S-4). (b) The simulated XRD spectra for NR structures of S-1, S-2, S-3 and S-4 are presented.*

Later, a flaw in this structure was rectified by Lamfers *et al.* [59] with an unit cell of eight formula units and the modified lattice parameters are $a = 6.35$ Å, $b = 6.45$ Å and $c = 12.78$ Å. Figure 4.3a depicts all the structures of ReS_2, as per

Lamfers *et al.* [59] and Murray *et al.* [99], designated as S-1 and S-2 respectively. Note that, S-1 has four almost coplanar symmetric types for Re due to the presence of the pseudo-inversion centre at (1/4, 0, 0). The repetition of this inversion centre along the *c* axis does not obey the reflection symmetry. This weak reflection asymmetry was ignored in S-2 and thus its c-axis is half of that of S-1.

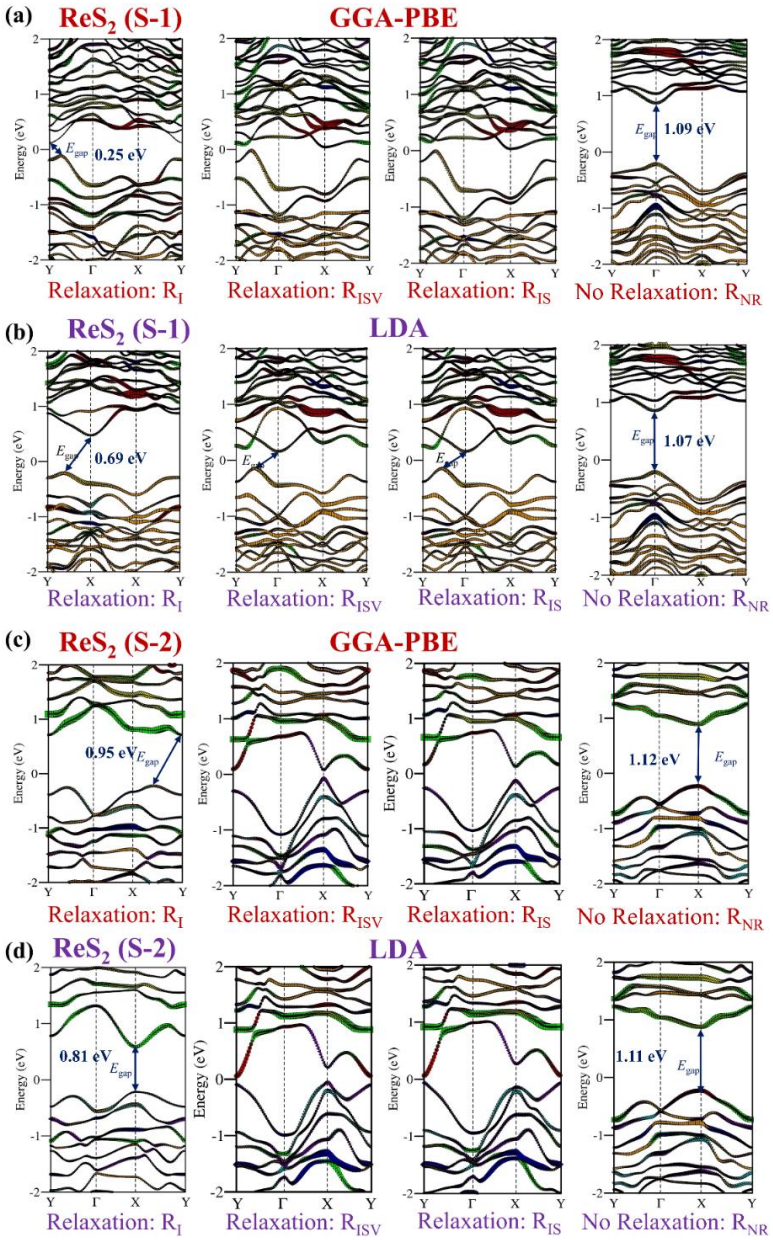

Figure 4.4: *The electronic structures of S-1 (ReS_2 by Lamfers et al.) treated by (a) GGA-PBE and (b) LDA PAW potential. The electronic structures of S-2 (ReS_2 by Murray et al.) treated by (c) GGA-PBE and (d) LDA PAW potential. The calculation has been performed for three different relaxations (R_I, R_{ISV}, R_{IS},) of unit cell and also no relaxation (R_{NR}) after incorporation of spin orbit coupling (SOC).*

Additionally, in S-2, there is a flipping of $c \rightarrow a$ axes in comparison to S-1, leading to an *a*-axis stacking in S-2, in contrast to the *c*-axis stacking in S-1. For $ReSe_2$, the structure defined by Wildervanck *et al.* [100] has lattice parameters $a = 6.71$ Å, $b = 6.60$ Å and $c = 6.73$ Å.

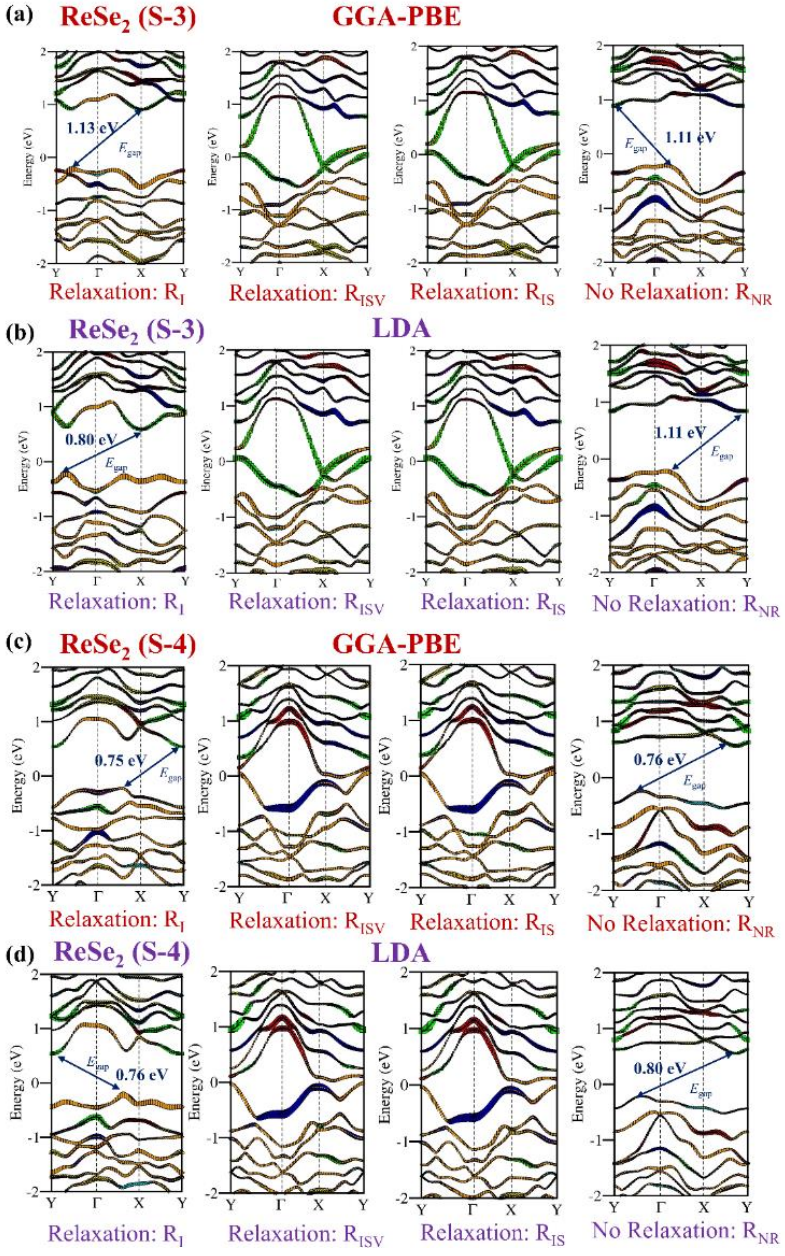

Figure 4.5: *The electronic structures of S-3 ($ReSe_2$ by Lamfers et al.) treated by (a) GGA-PBE and (b) LDA PAW potential. The electronic structures of S-4 (ReS_2 by Wildervanck et al.) treated by (c) GGA-PBE and (d) LDA PAW potential. The calculation has been performed for three different relaxations (R_I, R_{ISV}, R_{IS},) of unit cell and also no relaxation (R_{NR}) after incorporation of spin-orbit coupling (SOC).*

This structure was refined by Lamfers *et al.* [59] with unit cell parameters $a = 6.60$ Å, $b = 6.71$ Å and $c = 6.72$ Å, where there is an interchange of *a* and *b*

lattice parameters. We denote these two structures as S-3 (described by Lamfers *et al.*) and S-4 (described by Wildervanck *et al.*), having four formula units per unit cell. To estimate the impact of structural differences on X-ray diffraction (XRD) patterns, the simulated XRD spectra for all four non-relaxed (NR) structures of ReS_2 and $ReSe_2$ are plotted in Figure 4.3b. The Miller indices of the reflecting planes corresponding to the most significant peaks are marked and these peak positions resemble the experimental data presented in reference [72]. It is evident that the XRD patterns of S-1 and S-2 are indistinguishable and the same is true for S-3 and S-4. Therefore, by mere comparison of the XRD, the subtle differences between the NR structures are untraceable. Since the XRD spectra of the NR structures could not detect the differences between the structures S-1 to S-2 and S-3 to S-4, we have carried out different types of structural relaxations to estimate the impact of relaxation on the XRD spectra.

We have used three different modes of structural relaxations using DFT within the realm of conjugate gradient algorithm. In the first one, designated as R_I, the ionic positions (I) are optimized and the cell volume (V) and shape (S) are intact. The next one is named R_{ISV}, where all these three parameters I, S and V are optimized. For R_{IS}, the ionic positions and the cell shapes are varied. The non-relaxed cases are described as R_{NR}.

Table 4.1: *Electronic structure properties of S-1, S-2, S-3 and S-4 using LDA-CA and GGA-PBE exchange-correlation functional respectively. The bandgaps are calculated using GGA-PBE (with vdW) and LDA-CA (without vdW) functional with PAW potentials after incorporating SOC. Summaries are listed for three different relaxations (R_I, R_{ISV} and R_{IS}) and non-relaxed (R_{NR}) cases.*

System	Potential LDA/GGA	Bandgap (Indirect/Direct)			
		$\mathbf{R_I}$	$\mathbf{R_{ISV}}$	$\mathbf{R_{IS}}$	$\mathbf{R_{NR}}$
ReS_2 (S-1)	LDA	Indirect E_g = 0.69 eV	Indirect E_g = 0.30 eV	Indirect E_g = 0.31 eV	Direct E_g = 1.07 eV
	GGA	Indirect E_g = 0.25 eV	Indirect E_g = 0.12 eV	Indirect E_g = 0.06 eV	Direct E_g = 1.09 eV

ReS_2 (S-2)	LDA	Direct E_g = 0.81 eV	Direct E_g = 0.16 eV	Direct E_g = 0.11 eV	Direct E_g = 1.11 eV
	GGA	Indirect E_g = 0.95 eV	Direct E_g = 0.17 eV	Direct E_g = 0.26 eV	Direct E_g = 1.12 eV
$ReSe_2$ (S-3)	LDA	Indirect E_g = 0.80 eV	Metallic		Indirect E_g = 1.11 eV
	GGA	Indirect E_g = 1.13 eV			Indirect E_g = 1.11 eV
$ReSe_2$ (S-4)	LDA	Indirect E_g = 0.75 eV			Indirect E_g = 0.76 eV
	GGA	Indirect E_g = 0.76 eV			Indirect E_g = 0.80 eV

Table 4.2: *The total energy values corresponding to different modes of structural relaxations (R_I, R_{ISV} and R_{IS}).*

Bulk System	Formation energy per atom (eV)			
	with vdW		without vdW	
	R_{NR}	R_I	R_{NR}	R_I
ReS_2 (S-1)	-5.40	-5.31	-5.16	-4.89
ReS_2 (S-2)	-3.09	-3.13	-2.90	-2.75
$ReSe_2$ (S-3)	-5.00	-5.09	-4.71	-4.61
$ReSe_2$ (S-4)	-4.89	-5.04	-4.61	-4.57

We have used the LDA Ceperley-Alder (LDA-CA) and GGA Perdew-Burke-Ernzerhof (GGA-PBE) calculations with vdW correction after including spin-orbit coupling (SOC) for structures S-1 to S-4 and investigated the types and magnitudes of the bandgaps. The key results of all of these calculations are listed in Table 4.1. For R_{NR}, we find that ReS_2 is a direct band-gap system for both S-1 and S-2, whereas the band-gap of $ReSe_2$ is indirect with both S-3 and S-4. The

incorporation of structural optimization is seen to introduce drastic changes in the electronic structure, especially at the band edges. For R_{ISV} and R_{IS}, the bandgaps in ReS_2 are highly reduced with a change of bandgap from direct to indirect.

Table 4.3: *Calculated formation energies of S-1, S-2, S-3 and S-4 using GGA-PBE and DFT-D3 vdW corrections.*

System	R_I	R_{ISV}	R_{IS}
ReS_2 (S-1)	-186.9436	-184.9797	-184.9745
ReS_2 (S-2)	-92.4122	-91.5381	-91.6497
$ReSe_2$ (S-3)	-87.0059	-84.1383	-84.1205
$ReSe_2$ (S-4)	-86.5089	-84.1738	-84.8164

In S-2, the nature of bandgap varies from LDA to GGA for R_I. In $ReSe_2$, both R_{ISV} and R_{IS} result in a metallic state for S-3 and S-4. For R_I, the GGA potentials abruptly reduce the indirect band-gap for ReS_2, but retain the NR values for both S-3 and S-4. However, the use of hybrid functionals [47] for the exchange-correlation energy enables the rectification of the gap-values for the R_I cases, as will be seen in the next section. This survey indicates that ReX_2 (X = S, Se) are capable of producing widely different results depending on the types of relaxation, approximations used for the energy functional and the input crystal structures. Since both R_{ISV} and R_{IS} are leading to almost metallic behaviour for the bulk systems, we continue with the R_I and R_{NR} schemes to compare the electronic properties. A comparison of the total energies corresponding to these aforementioned modes of structural relaxations indicates that the relaxed systems generated after using the mode R_I provide the lowest energy configuration for each structural system, as can be seen in Table 4.2. The summaries of this full survey of all the structures and methods are presented in Figures 4.4 and 4.5. From this elaborate study, it is seen that the GGA-PBE exchange functional and the relaxation mode R_I is the most effective to generate

the lowest energy configurations. Next, we have compared the formation energies per atom of the bulk structures of ReS_2 and $ReSe_2$ both with and without vdW for R_I and R_{NR}, and the results are presented in Table 4.3.

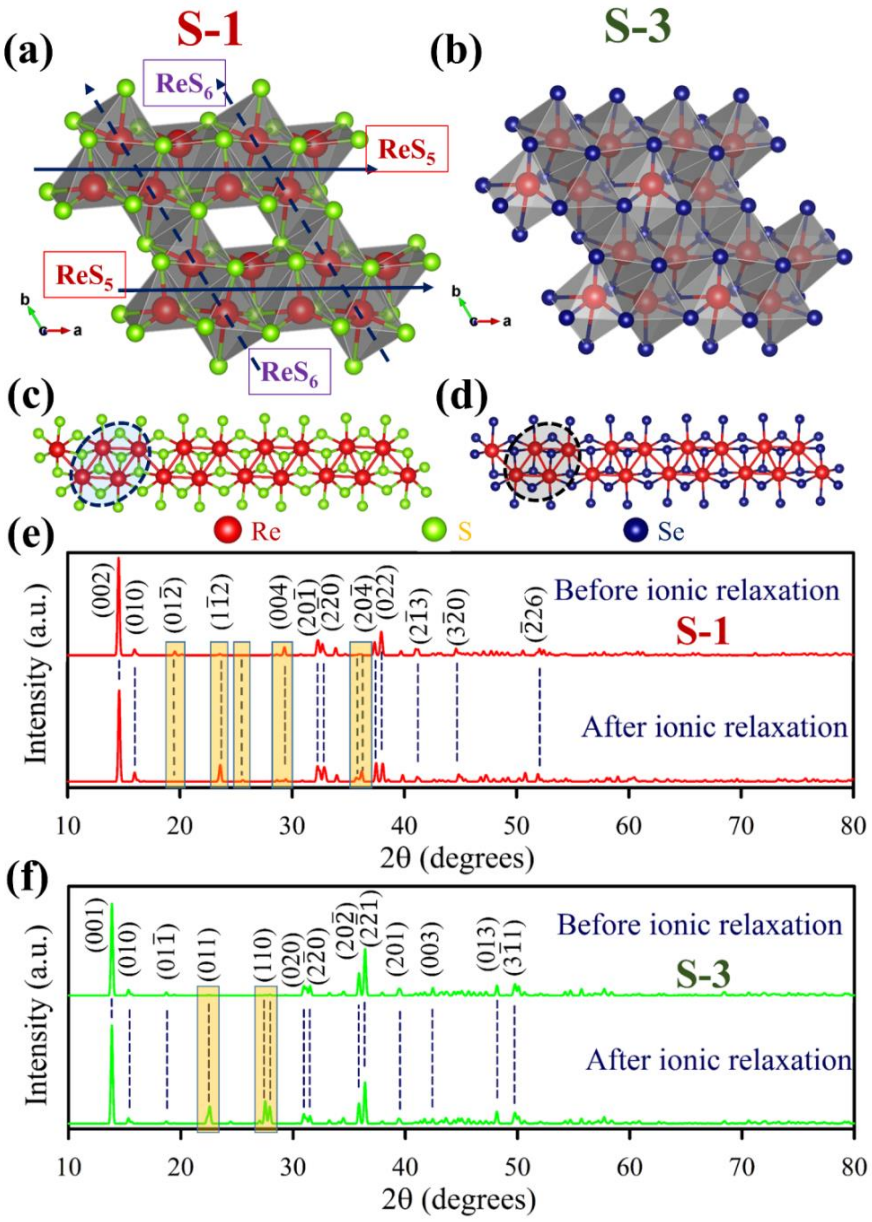

Figure 4.6: *Polyhedral coordinations for (a) S-1 and (b) S-3. Re-Re metallic bonds make up the Re4 parallelogram array along a-direction for (c) ReS_2 and (d) $ReSe_2$. (e) Simulated XRD spectra of S-1 (for R_{NR} and R_I) and (f) S-3. The differences in the XRD peaks are highlighted.*

The comparison of the formation energies implies that for both of these schemes, S-1 and S-3 are the lowest energy structural configurations for ReS_2 and $ReSe_2$ respectively. For ReS_2 in particular, the energy difference between S-1 and S-2 is quite large. Therefore, from here onwards, we shall discuss the results only for

the structures S-1 (for ReS_2) and S-3 (for $ReSe_2$) mostly for the relaxation mode R_I. As inferred from the energetics, ReS_2 and $ReSe_2$ belong to two different structures.

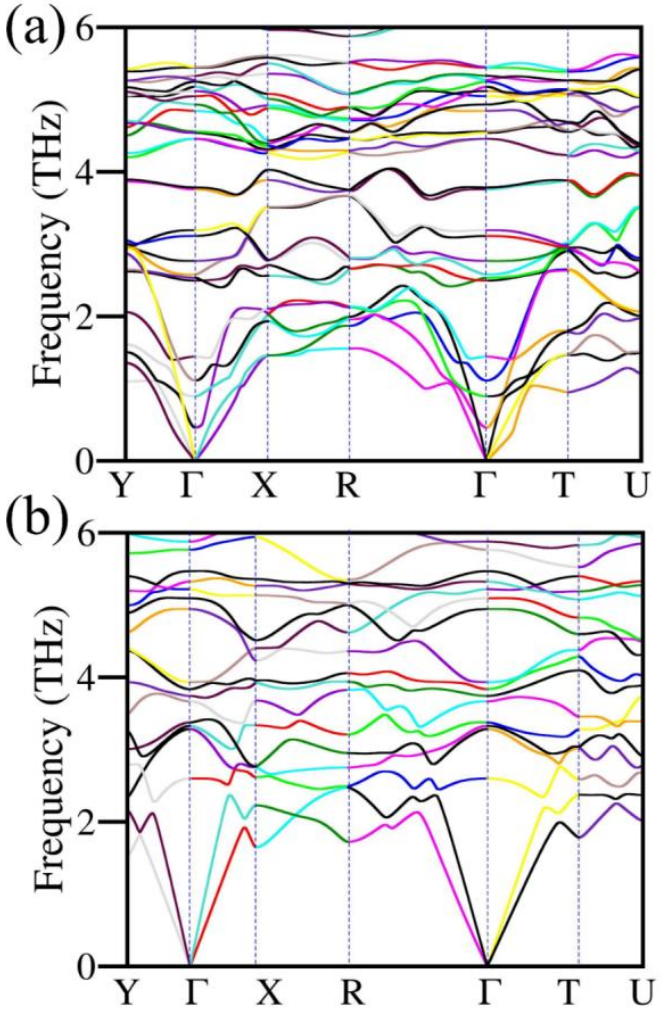

Figure 4.7: *Phonon dispersion curves for (a) ReS_2 (S-1) and (b) $ReSe_2$ (S-3) bulk crystal structure. Different colours signify the projections corresponding to different eigenvectors.*

This non-isostructural nature of these two compounds becomes more evident if we scrutinize the polyhedral coordination of the relaxed structures. Figure 4.6a depicts the polyhedral coordination of ReS_2, which indicates that the in-plane structure consists of the edge-shared ReS_6 octahedral array along the *b*-axis. These arrays are bridged by two face-shared ReS_5 square pyramids along the *a*-axis. This in-plane structure consists of voids surrounded by the bridge and the array. In relaxed ReS_2 (S-1), due to the reflection asymmetry along the *c*-axis, there is no Bernal stacking. $ReSe_2$, on the other hand, consists of only $ReSe_6$

distorted octahedral coordination (Figure 4.6b). The *a-b* plane of $ReSe_2$ is space-filled with face-shared distorted $ReSe_6$ octahedron and reflection symmetry of this plane along *c*-axis confirms the presence of Bernal stacking.

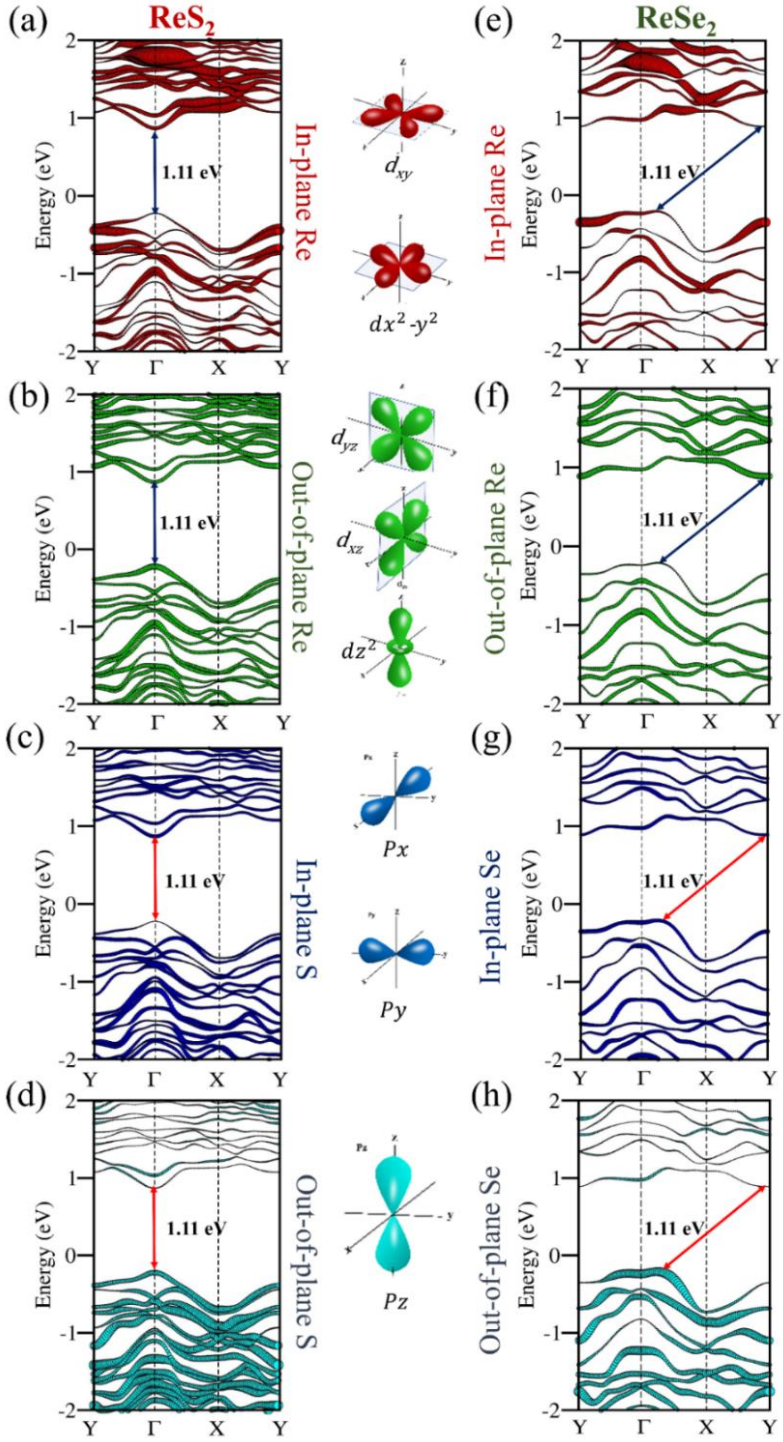

Figure 4.8: *(a) In-plane Re (d_{xy} and $d_{x^2-y^2}$), (b) out-of-plane Re (d_{yz}, d_{xz} and d_{z^2}), (c) In-plane S (p_x and p_y) and (d) out-of-plane S (p_z) orbitally-projected GGA-PBE + SOC bands for R_{NR} of S-1. (e) In-plane Re, (f) out-of-plane Re, (g) in-plane Se and (h) out-of-plane Se orbitally projected GGA-PBE bands for R_{NR} of S-3.*

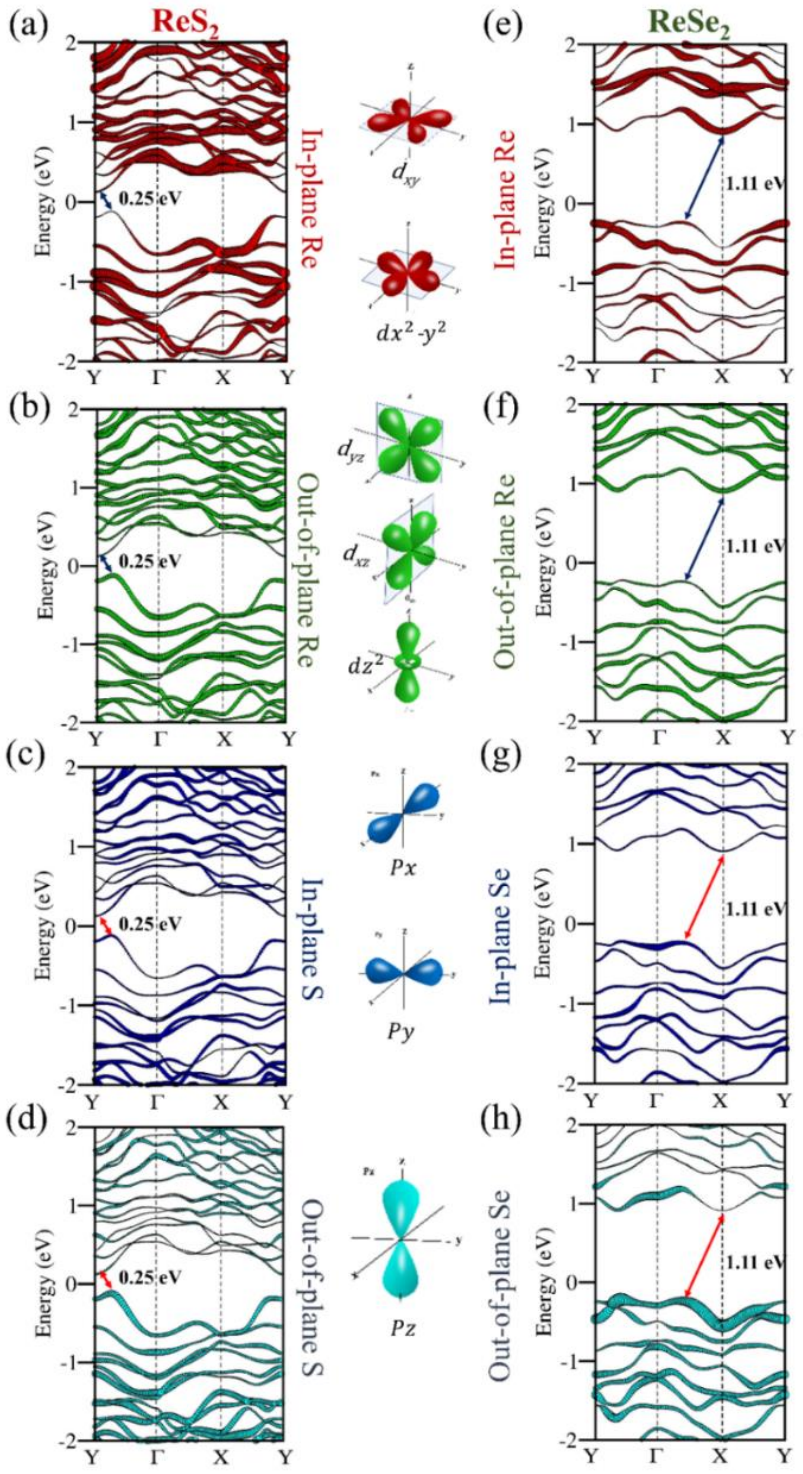

Figure 4.9: *(a) In-plane Re (d_{xy} and $d_{x^2-y^2}$), (b) out-of-plane Re (d_{yz}, d_{xz} and d_{z^2}), (c) in-plane S (p_x and p_y) and (d) out-of-plane S (p_z) bands of structure ReS_2 (S-1) after ionic relaxation. (e) In-plane Re (d_{xy} and $d_{x^2-y^2}$), (f) out-of-plane Re (d_{yz}, d_{xz} and d_{z^2}), (g) in-plane Se (p_x and p_y) and (h) out-of-plane Se (p_z) bands of structure $ReSe_2$ (S-3) after ionic relaxation. The calculations are performed using GGA-PBE with PAW potentials after including SOC.*

This difference in stacking was also pointed out by the TEM experiments [69, 72, 101] and the calculated optimized structures are capable of reproducing this

observation. Both of these systems contain the Re4 parallelogram array along *a*-axis, as seen in Figures 4.6c and d. In Figure 4.6e, we present a comparison of the simulated XRD spectra of ReS_2 and $ReSe_2$ both with and without R_I, highlighting the differences with the rectangular boxes, where the appearance or absence of peaks are indicated.

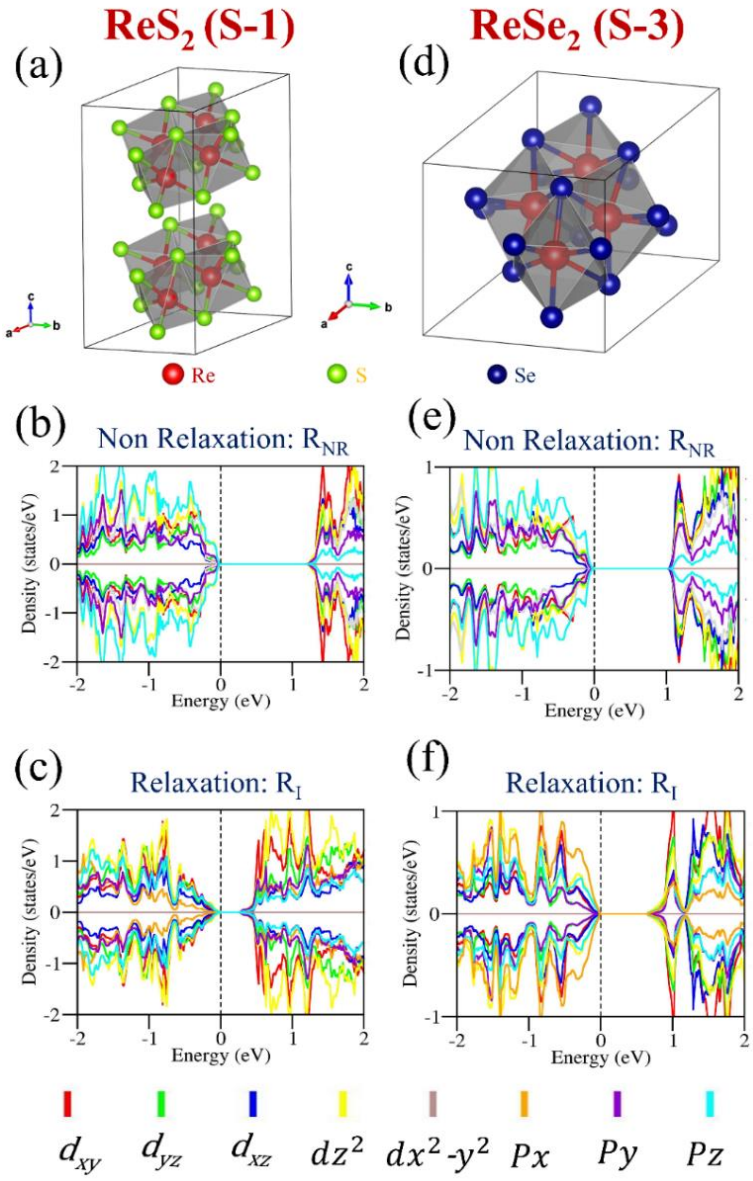

Figure 4.10: *(a) The ionic optimized crystal structure of ReS_2 (S-1) and $ReSe_2$ (S-3), (b) and (c) OPDOS of ReS_2 (S-1) for R_{NR} and R_I respectively. (d) Ionic optimized crystal structure of $ReSe_2$ (S-3), (e) and (f) OPDOS of $ReSe_2$ (S-3) for R_{NR} and R_I respectively. The calculations are performed using GGA-PBE with PAW potentials after including SOC.*

This comparison connotes that with incorporation of structural relaxation, the subtle structural differences between the non-relaxed and relaxed structures

lead to theoretically distinguishable XRD spectra, albeit the significant peaks remain similar to the reference [72]. The significance of choosing an appropriate mode of structural relaxation in reproducing the experimental results becomes evident from this comparison.

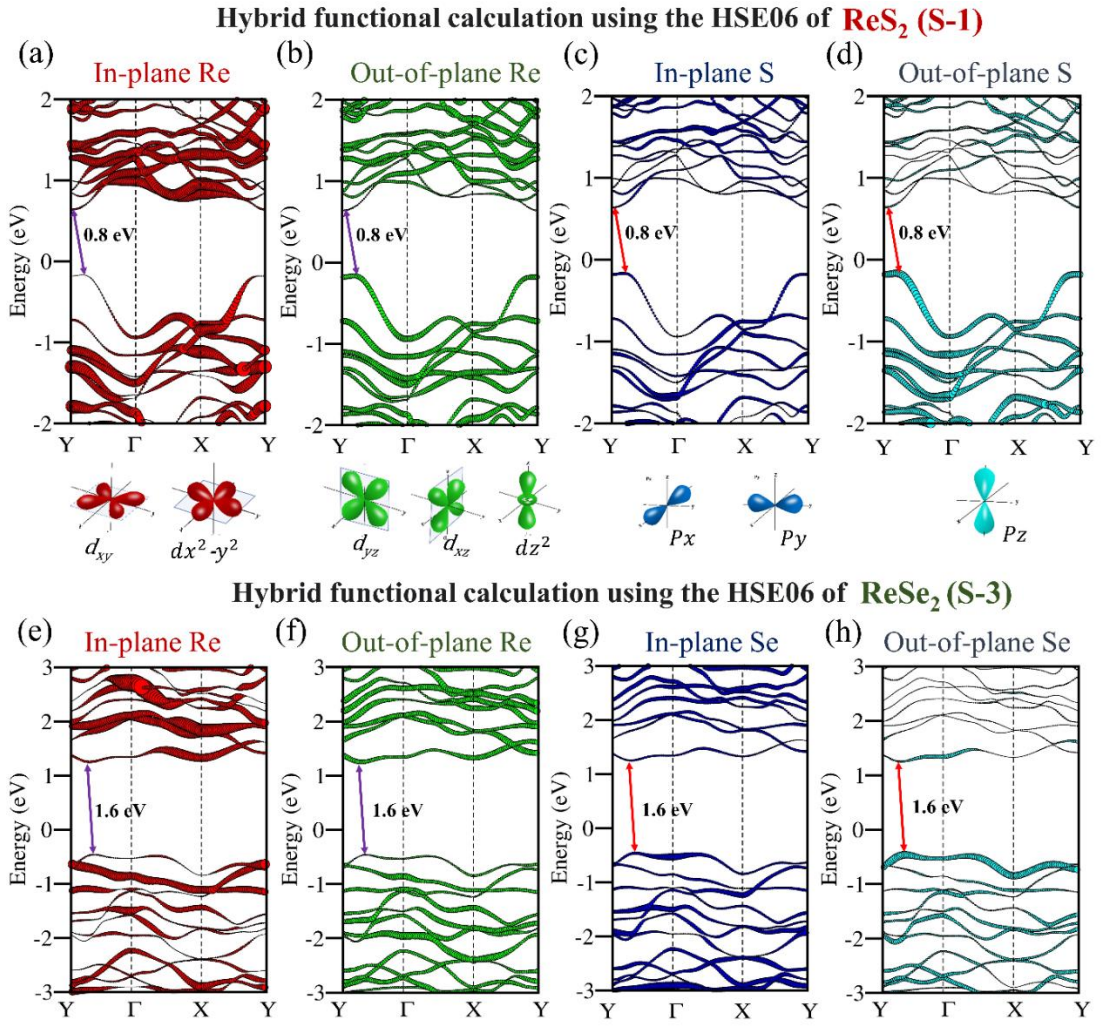

Figure 4.11: *(a) In-plane Re (d_{xy} and $d_{x^2-y^2}$), (b) out-of-plane Re (d_{yz}, d_{xz} and d_{z^2}), (c) in-plane S (p_x and p_y) and (d) out-of-plane S (p_z) orbital-projected HSE06 bands of ReS_2 (S-1) for R_I. (e) In-plane Re, (f) out-of-plane Re, (g) in-plane Se and (h) out-of-plane Se orbital-projected HSE06 bands of $ReSe_2$ (S-3) for R_I.*

For further confirmation of structural stability, we have calculated the phonon dispersions of the bulk structures of S-1 and S-3, corresponding to the R_I mode of structural relaxation, as presented in Figures 4.7a and b. The absence of any imaginary modes confirms that there is no dynamical instability near room temperature. Near the Γ point, the phonon band-dispersions of ReS_2 have a non-

linear *q*-dependence, originating from the out-of-plane ZA-like acoustic modes. On the contrary, the phonon dispersions in $ReSe_2$ are mostly linear near the Γ point, implying a lesser contribution from out-of-plane vibrations. Thus, the phonon dispersions confirm the structural stability of S-1 and S-3. Next, we analyze the orbital contributions from the Re-5*d*, S-*3p* and Se-*4p* orbitals at the valence band maximum (VBM) and conduction band minimum (CBM) to assess the compatibility of these structures to reproduce the experimental ARPES data.

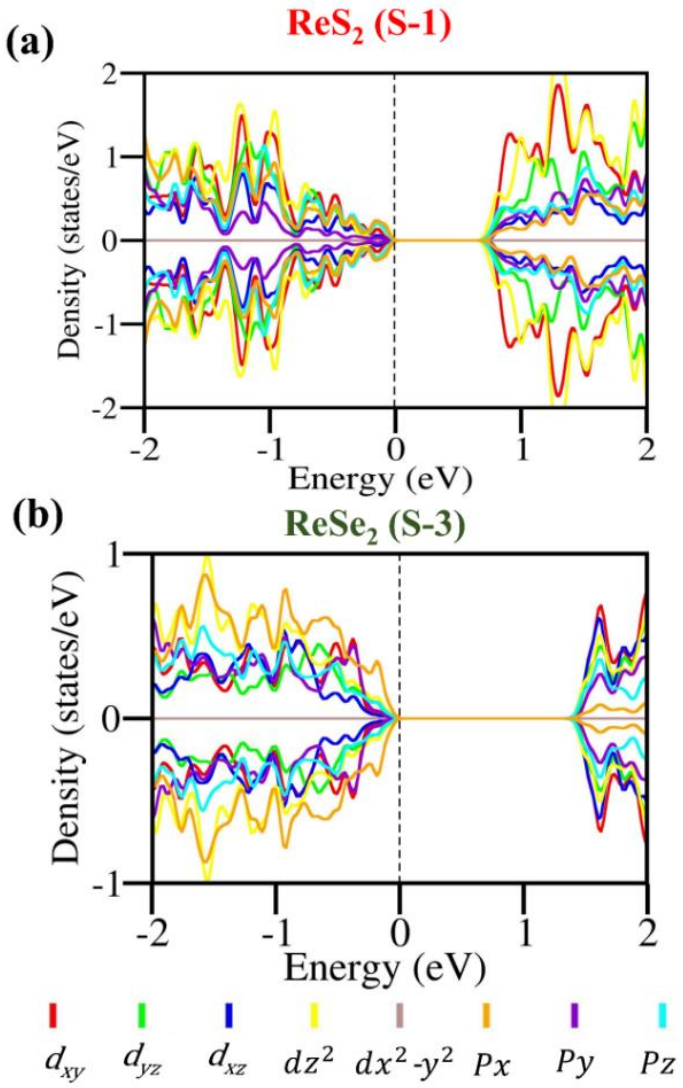

Figure 4.12: *OPDOS of bulk (a) ReS_2 (S-1) and (b) $ReSe_2$ (S-3) by using spin polarised GGA-PBE with HSE06 hybrid functional calculations after ionic relaxation (R_l).*

The in-plane (d_{xy} and $d_{x^2-y^2}$) and out of plane (d_{yz}, d_{xz}, d_{z^2}) orbital contributions of Re-5*d* orbitals and the respective in-plane (p_x and p_y) and out-of-plane (p_z) orbital contributions of S and Se-*p* orbitals at the band edges represent their low-energy

electronic structure. The orbital projection of the band-structures, as calculated with the GGA-PBE+vdW functional after incorporating SOC, for the in-plane and out-of-plane orbitals of bulk S-1 and S-3 for R_{NR} are presented in Figure 4.8.

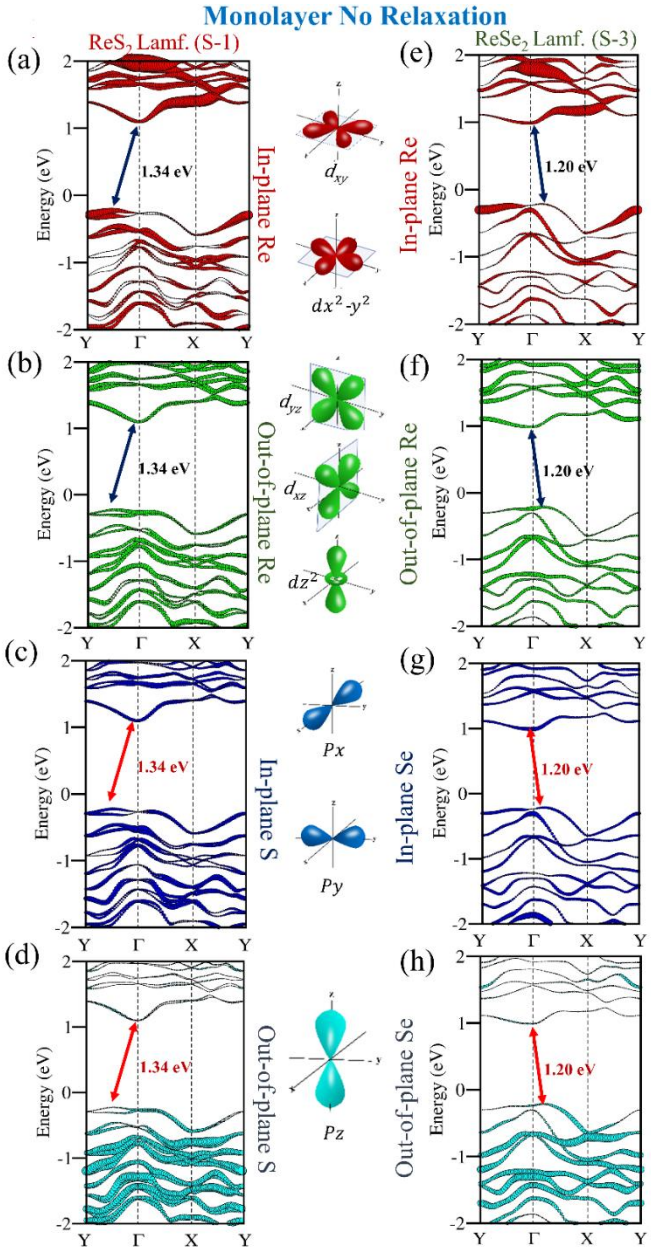

Figure 4.13: *(a) In-plane Re (d_{xy} and $d_{x^2-y^2}$), (b) out-of-plane Re (d_{yz}, d_{xz} and d_{z^2}), (c) In-plane S (p_x and p_y) and (d) out-of-plane S (p_z) orbitally-projected GGA-PBE bands for R_{NR} of monolayer of S-1. (e) In-plane Re, (f) out-of-plane Re, (g) In-plane Se and (h) out-of-plane Se orbitally projected GGA-PBE bands for R_{NR} of monolayer of S-3. All the calculations are done after incorporating SOC.*

For R_{NR}, ReS_2 has a direct bandgap of magnitude 1.21 eV at the Γ-point and $ReSe_2$ is an indirect bandgap system of magnitude 1.11 eV with flat bands at the VBM and CBM. The orbital contributions of the in-plane and out-of-plane

orbitals are mixed at the band-edges for both systems, as can be seen from Figures 4.8a-h. Interestingly, this distribution of the in-plane and out-of-plane orbital contributions undergoes a change for R_I. Figure 4.9 presents the orbital projected band-structure for R_I with GGA-PBE+vdW functional after incorporating SOC. For ReS_2, there is a drastic reduction of the bandgap to 0.25 eV. However, $ReSe_2$ retains its indirect bandgap of 1.11 eV with a shift of the edge of the CBM from Y to X. Unlike the other TMDC systems, the effects of SOC is not very prominent for the S-1 and S-3 bulk structures of ReS_2 and $ReSe_2$, as was also seen in prior studies [79, 80]. We have compared the effects of SOC on the electronic structure of these two systems. The orbital-projected density of states (OPDOS) corresponding to the R_I and R_{NR} are presented in Figure 4.10. The reduction of the bandgap for relaxed systems can be circumvented by using the HSE06 hybrid functional for the exchange correlations, where the overestimation of the electron delocalization for Re-5*d* levels by semi-local GGA-PBE functional is avoided [47]. Figures 4.11a–d represents the orbital projections for S-1 using HSE06, where ReS_2 is an indirect band gap system having a bandgap ~ 0.8 eV. There is a very close direct bandgap transition at Γ, within a few hundred of meV of the indirect transition, which resembles the ARPES valence-band maps as presented in reference [82].

The contribution of both Re and S out-of-plane orbitals are higher at VBM due to a sigma-bonding-like inter-plane charge-overlap of Re-5d_{z^2} and S-3p_z orbitals, matching closely with the ARPES results as presented in reference [81]. The in-plane orbitals contribute more at the CBM. For S-3, as seen from Figures 4.11e-h, the system possesses an indirect bandgap of ~1.6 eV. Whereas the CBM has more contributions from the out-of-plane Re-*5d* and Se-*4p* orbitals, the VBM is constituted of both in-plane and out-of-plane Se-4*p* orbitals, which is very similar to the ARPES results presented in the literature [92]. The corresponding OPDOS are presented in Figure 4.12. While investigating the monolayers, we have first calculated the formation energies per atom for the monolayers of S-1 and S-3 and their negative (Table 4.4) values confirm their stability. The exfoliation energies

for the monolayers of S-1 and S-3 are calculated to be 30.48 and 5.25 meV/Å^2 respectively, as presented in Table 4.4.

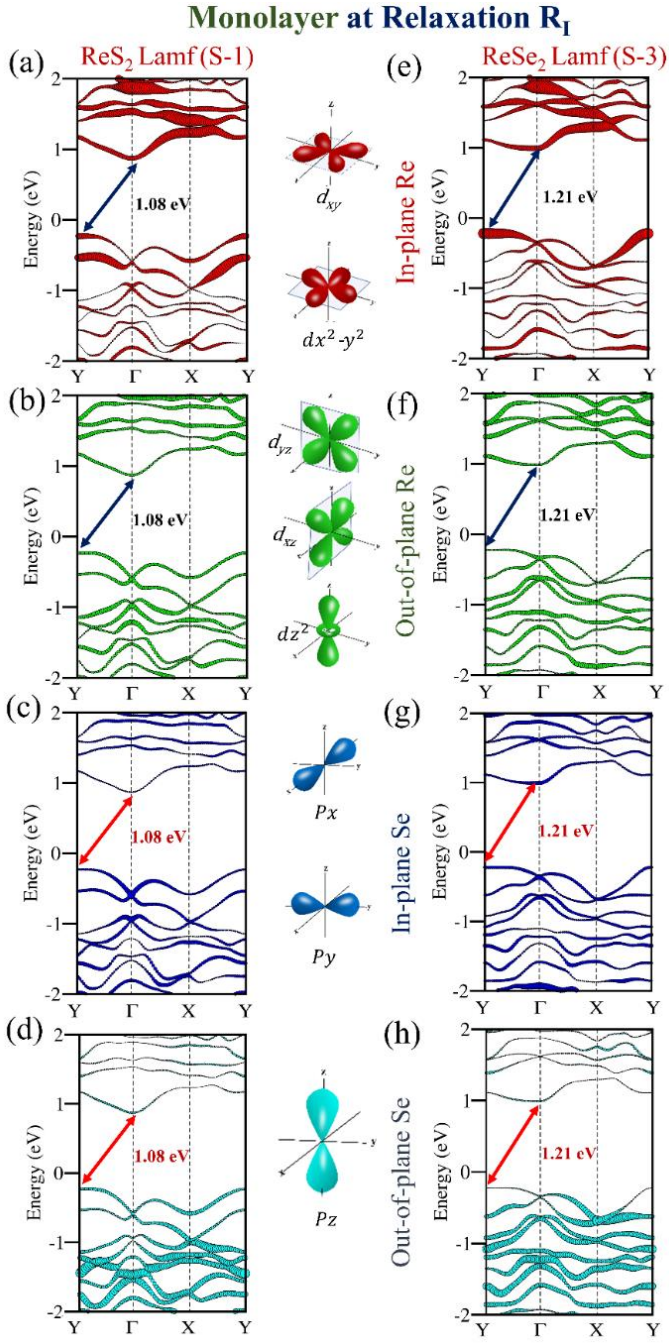

Figure 4.14: *(a) In-plane Re (d_{xy} and $d_{x^2-y^2}$), (b) out-of-plane Re (d_{yz}, d_{xz} and d_{z^2}), (c) in-plane S (p_x and p_y) and (d) out-of-plane S (p_z) bands of monolayer ReS_2 (S-1) structure after ionic relaxation. (e) In-plane Re, (f) out-of-plane Re, (g) in-plane Se and (h) out-of-plane Se, bands of $ReSe_2$ (S-3) structure after ionic relaxation. The calculations are performed using GGA-PBE with potentials after incorporating SOC.*

The exfoliation energy of monolayers of ReS_2 is higher because of the contribution of electronic hybridization to the interlayer coupling in addition to

the vdW interaction. Figure 4.13 depicts the orbital-projection for the R_{NR} monolayers of S-1 and S-3 with the GGA-PBE+vdW functional. Both of the non-relaxed monolayers are displaying indirect band-gaps of magnitudes 1.34 and 1.20 eV respectively for S-1 and S-3. From Figures 4.13a–d, the homogeneous contributions of the in-plane and out-of-plane orbitals at both VBM and CBM are evident. For S-3, as in Figures 4.13e–h, the out-of-plane contributions are more than the in-plane ones at the VBM and the reverse occurs for CBM. A close comparison of NR bulk and monolayers implies the effects of vdW interactions in obtaining a shift in the band-edges while lowering the thickness of the system. Figure 4.14 represents the orbital projections for the relaxed monolayers with the GGA-PBE+vdW functional after incorporating SOC. The effect of SOC is negligible for monolayers, except for splitting of band-crossing at the Γ-point (Figure 4.15), as also seen in a prior study [80]. Unlike bulk systems, the monolayers do not exhibit the drastic reduction of the bandgaps under relaxation, albeit a shift of the band-edges. The anisotropy of the orbitals is not very evident from both R_{NR} and R_I band structures with GGA-PBE functional.

Table 4.4: *Formation energy and exfoliation energy of ReS_2 and $ReSe_2$ monolayers using GGA-PBE method.*

Monolayer System	Formation Energy Per atom (eV)	Exfoliation Energy (meV/Å²)
ReS_2 (S-1)	-5.30	30.48
$ReSe_2$ (S-3)	- 4.91	5.25

Table 4.5: *The electronic band-gaps of S-1 and S-3 after R_I using HSE06 functional.*

System	Bulk/Monolayer	Bandgap (eV)	
		Theoretical	Experimental
ReS_2 (S-1)	Bulk	0.8	1.32 - 1.50 [65, 77, 102, 103]
	Monolayer	1.8	1.58 - 1.85 [102, 103]
$ReSe_2$ (S-3)	Bulk	1.6	1.19 - 1.29 [77, 78, 104, 105]
	Monolayer	1.9	1.47 - 1.52 [104, 105]

The bandgaps are much closer to the experimental values after using a HSE06 calculation, having the magnitudes of 1.8 eV and 1.9 eV for S-1 and S-3 after retaining the indirect bandgap nature, as can be seen from Figure 4.16 [65, 71, 79]. Remarkably, the in-plane versus out-of-plane orbital anisotropy is more prominent in monolayers at VBM for both S-1 and S-3, as seen in Figure 4.16a-h. The CBM has similar contributions from the Re-*5d* in-plane and out-of-plane orbitals. As expected, the out-of-plane S-3p_z and Se-4p_z contributions are less for both VBM and CBM for the monolayers due to the lack of inter-plane charge overlap with the Re-5d_{z^2} orbitals from the next layer. Figure 4.17 presents the OPDOS of monolayers for R_{NR}, R_I and HSE063 Table 4.5 presents a comparison of the theoretical and experimental bandgaps with appropriate references. It has been observed that the R_I mode of structural relaxation is capable of producing the theoretical results resembling close to the experiments. Although, there is experimental evidence of semiconductor to metal transitions for both ReS_2 and $ReSe_2$, as per our knowledge, the theoretical studies dealt with the structures S-2 [99] and S-4 [100].

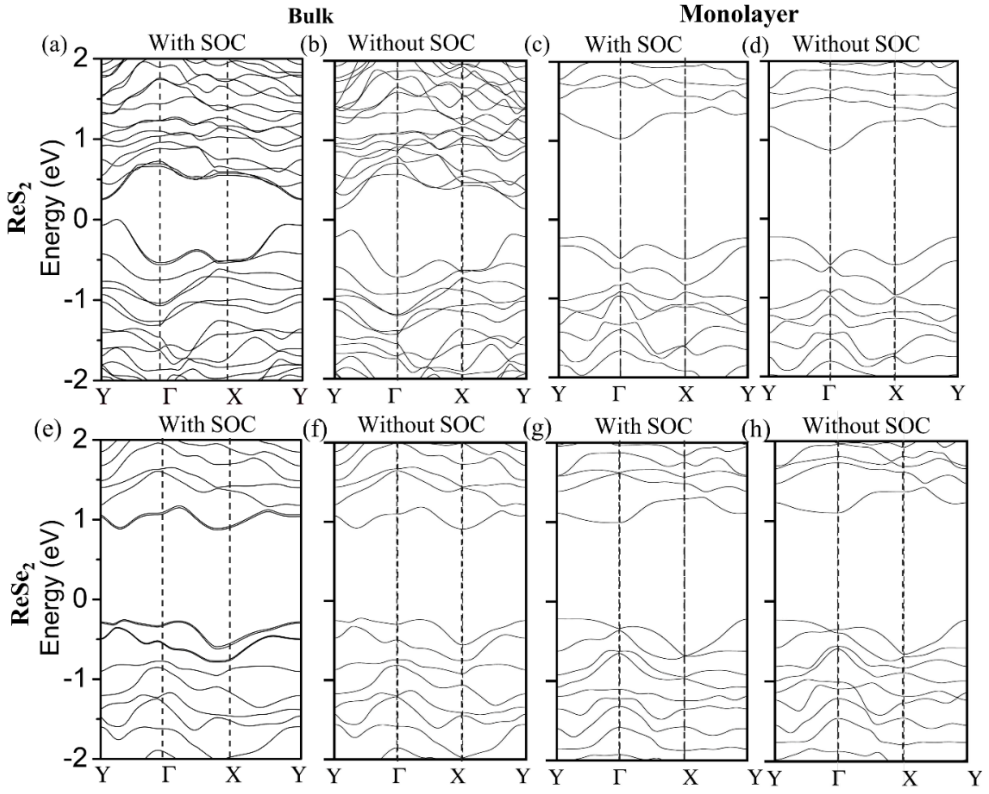

Figure 4.15: *The electronic band structures of (a,b) bulk ReS_2, (c,d) monolayer ReS_2, (e,f) bulk $ReSe_2$ and (g,h) monolayer $ReSe_2$ for both with and without SOC.*

For structures S-1 and S-3, there is no theoretical study to investigate the effects of high pressure. We have explored the high-pressure effects on both of these systems with the help of GGA-PBE+vdW functional. Figure 4.18a presents the evolution of the band structures for S-1 with respect to an isotropic reduction of volume upto 4.6%, where the system undergoes a metallic transition with a closure of the bandgap at the Y point with an increase of the band-flatness for a large region of the Brillouin zone.

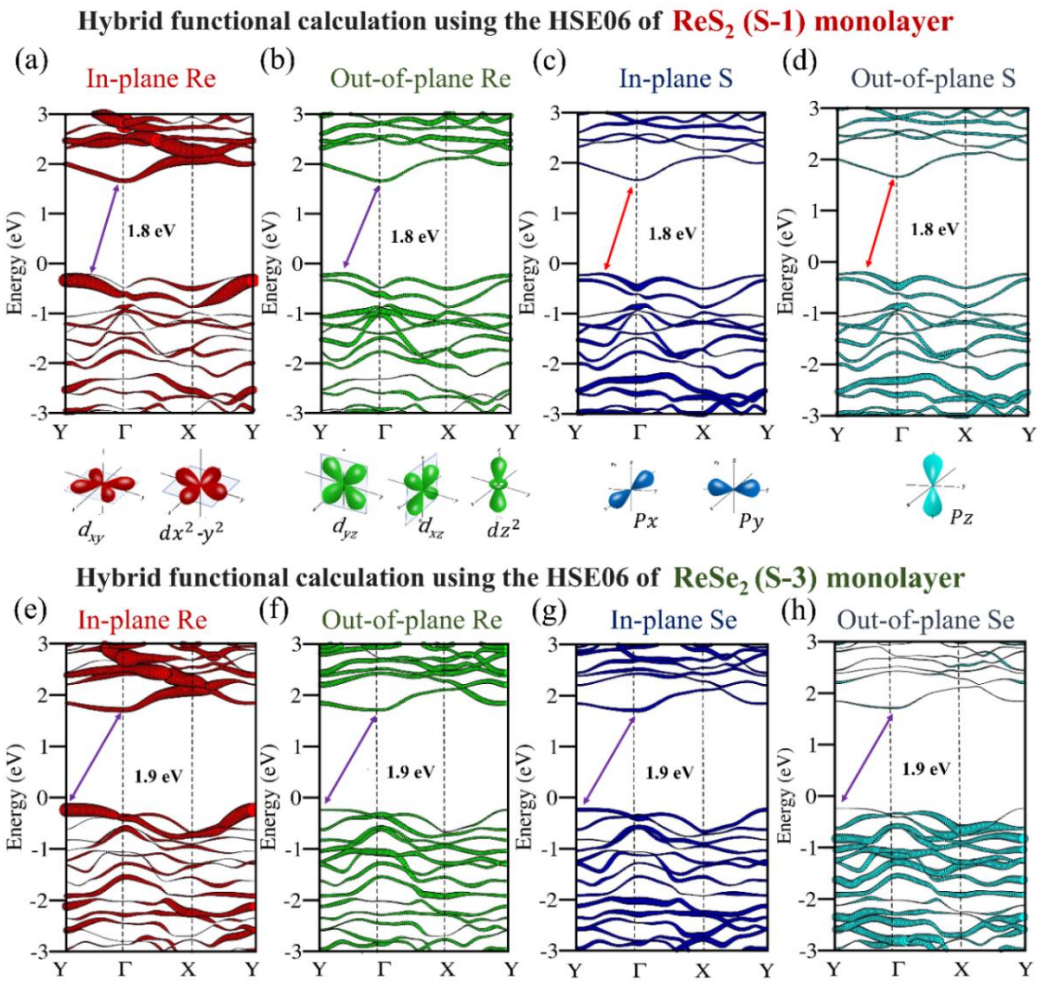

Figure 4.16: *(a) In-plane Re (d_{xy} and $d_{x^2-y^2}$), (b) out-of-plane Re (d_{yz}, d_{xz} and d_{z^2}), (c) in-plane S (p_x and p_y) and (d) out-of-plane S (p_z) orbital-projected HSE06 bands of monolayer ReS_2 (S-1) for R_I. (e) In-plane Re, (f) out-of-plane Re, (g) in-plane Se and (h) out-of-plane Se orbital-projected HSE06 bands of monolayer ReS_2 (S-3) for R_I.*

For S-3, the system is less compressible and the metallic transition occurs after 18.2% volume reduction. The corresponding pressures required to induce a metallic transition are 3.4 GPa and 10.7 GPa for ReS_2 and $ReSe_2$ respectively. The

metallicity appears to be extremely located around the Y point, as can be seen from Figure 4.18b. In Figures 4.18c and d, we have plotted the variation of the total energy versus the volume of the unit cell for ReS_2 and $ReSe_2$, which shows the usual equation of state behavior to be fitted with the Birch-Murnaghan equation (5.1) as:

$$E(V) = E_0 + \frac{9V_0B_0}{16}\left\{\left[\left(\frac{V_0}{V}\right)^{\frac{2}{3}} - 1\right]^3 B_0' + \left[\left(\frac{V_0}{V}\right)^{\frac{2}{3}} - 1\right]^2 \left[6 - 4\left(\frac{V_0}{V}\right)^{\frac{2}{3}}\right]\right\} \quad (4.92)$$

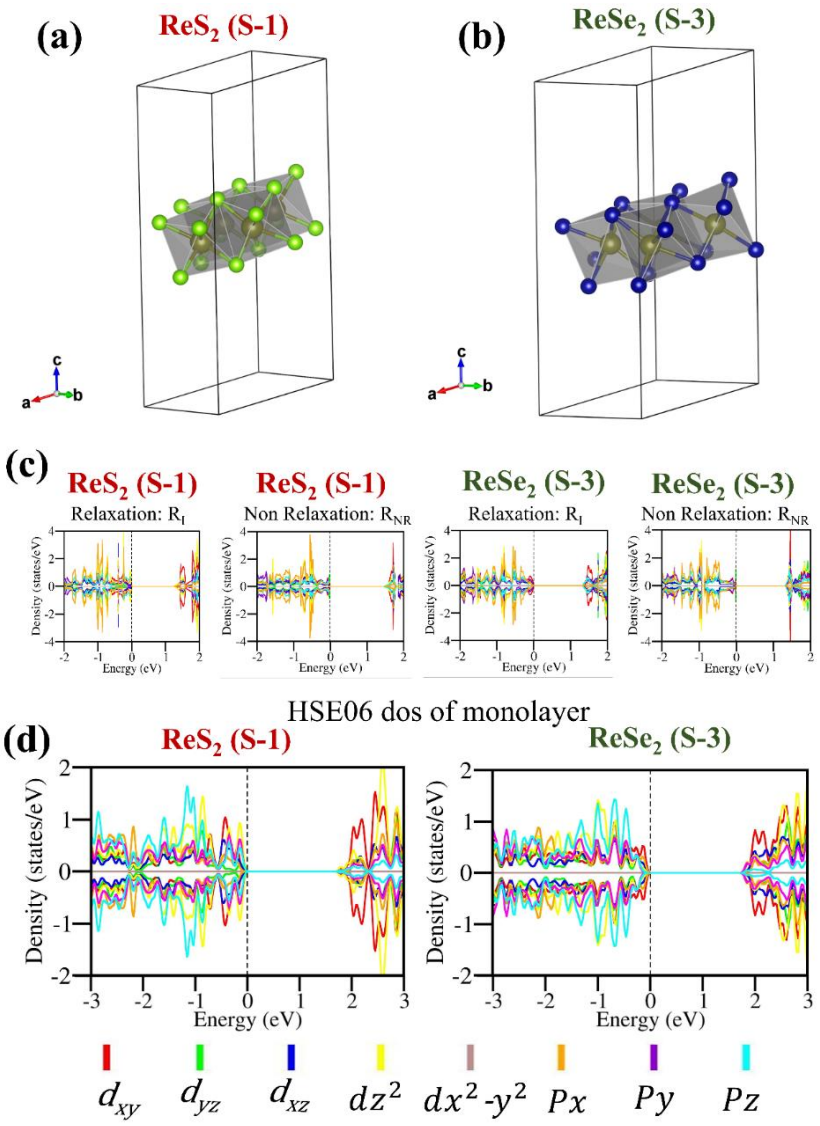

Figure 4.17: *The ionic optimized monolayer structures of (a) ReS_2 (S-1) and (b) $ReSe_2$ (S-3) by using spin polarised GGA-PBE and PAW potential. (c) OPDOS before and after ionic relaxation of ReS_2 (S-1) and $ReSe_2$ (S-3) using spin polarised GGA-PBE and PAW potential after incorporating SOC. (d) OPDOS after ionic relaxation of ReS_2 (S-1) and $ReSe_2$ (S-3) using spin polarised GGA-PBE with HSE06 hybrid functional calculations after ionic relaxation (R_I).*

In this expression, B_0 is the bulk modulus at ambient conditions and B_0' is the pressure derivative of B_0. After fitting the equation of state, the values of the bulk moduli for S-1 and S-3 are calculated to be 73.4 and 53.4 GPa respectively (Table 4.6).

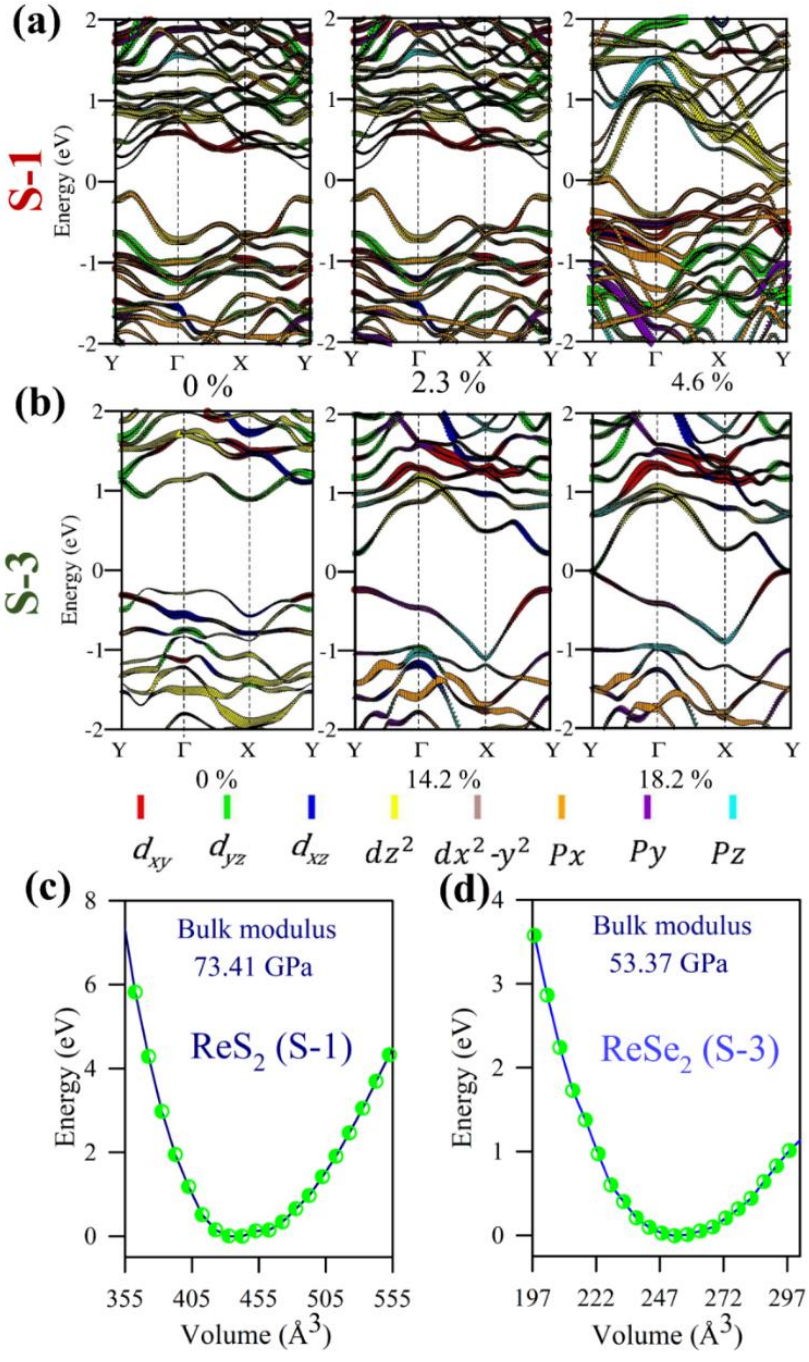

Figure 4.18: *Band structures of (a) ReS_2 (S-1) and (b) $ReSe_2$ (S-3) for different percentages of volume compression. A metallic transition occurs after 4.6% and 18.2% volume compression respectively. Birch-Murnaghan equation of state curve for (c) ReS_2 (S-1) and (d) $ReSe_2$ (S-3) respectively. The energy scale has been normalized so that zero represents the energy minimum.*

In S-3, on the verge of metallic transition, the in-plane contribution is larger than the out-of-plane contribution. Such behavior can be attributed to the fact that S-3 contains only a single layer in the bulk unit cell, which is in contrast to the double-layer per unit cell behavior of S-1.

Table 4.6: *Fitting parameters from Birch-Murnaghan equation of state for both of ReS_2 (S-1) and $ReSe_2$ (S-3).*

System	Eq. volume (Å³)	Bulk modulus (GPa)	Derivative of Bulk modulus (GPa)
S-1	451.78	73.41	3.69
S-3	253.99	53.37	5.14

Next, we used a combined DFT+MLFT approach to calculate the X-ray spectra of S-1 and S-3 for both R_{NR} and R_I structures. First, DFT provides a description of the ground state and the Kohn-Sham eigenvalues have no physical interpretation in terms of the quasi particle excitations.

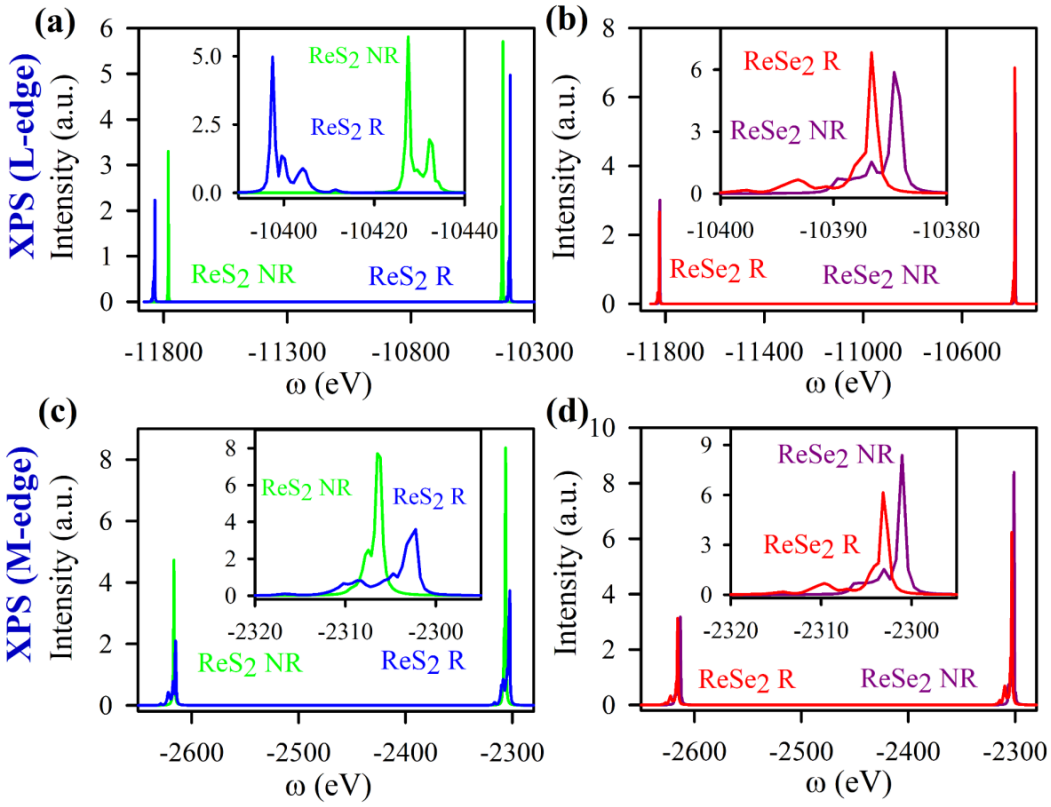

Figure 4.19: *XPS $L_{2,3}$-edge spectra of (a) ReS_2 (S-1) and (b) $ReSe_2$ (S-3). XPS $M_{2,3}$-edge spectra of (c) ReS_2 (S-1) and (d) $ReSe_2$ (S-3). Insets show the single edge of the corresponding spectra.*

Second, the single particle description of the potential and the exchange correlation functional is insufficient to analyze the excitation process. In MLFT, the electron-electron interaction is treated in a many-body approach, wherein one can construct a single-impurity Anderson Model (SIAM) and then solve it with an exact diagonalization scheme to obtain the excitation spectra [50, 51]. The onsite Coulomb repulsions among the 5*d* electrons and the Coulomb interaction between the 2*p* or 3*p* semi-core-hole with the 5*d* electrons are calculated in terms of the Slater-Condon integrals from a converged DFT calculation. A standard screening term is multiplied by each Slater-Condon integral to account for the screening by the itinerant electron. The double counting correction is subtracted from the DFT Hamiltonian by following the charge-transfer formalism, as used in MLFT [50].

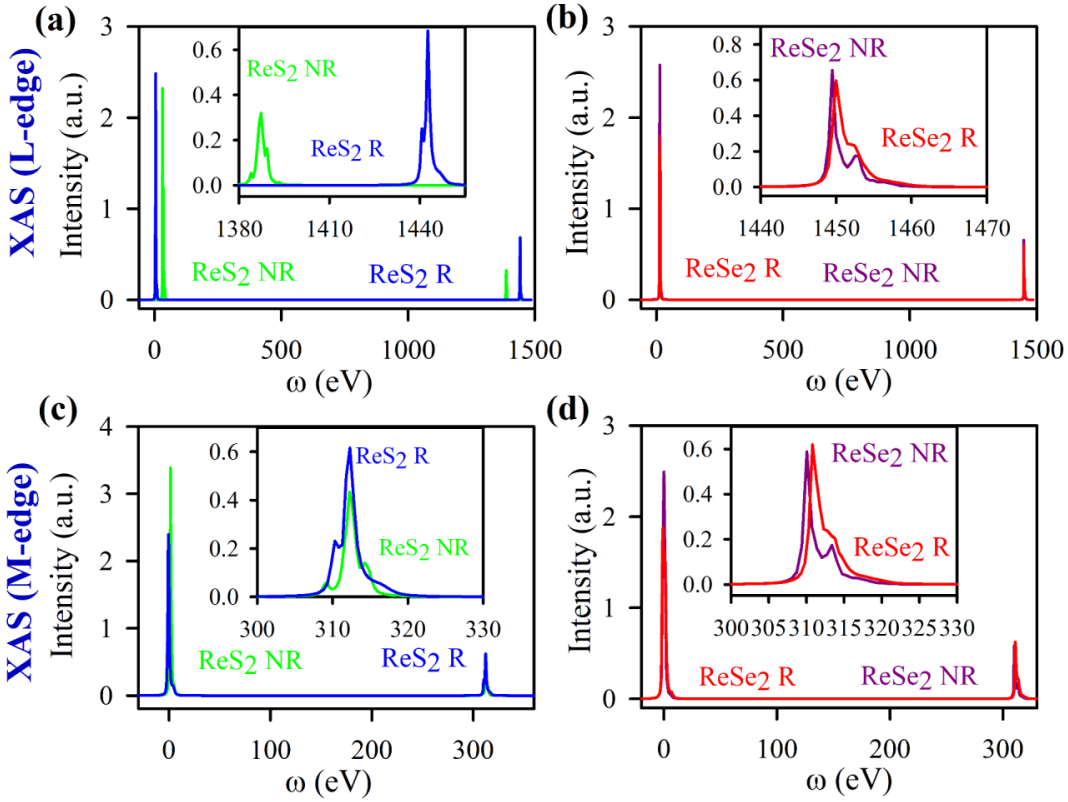

Figure 4.20: *XAS $L_{2,3}$-edge spectra of (a) ReS_2 (S-1) and (b) $ReSe_2$ (S-3). XAS $M_{2,3}$-edge spectra of (c) ReS_2 (S-1) and (d) $ReSe_2$ (S-3). The energy scale has been set to be zero at the threshold energy. Insets show plot of a single edge of the corresponding spectra.*

The fully-relativistic full-potential LMTO calculations are performed for the R_{NR} and R_I of S-1 and S-3. From this solution, a SIAM is constructed with MLFT and

is then solved to calculate the spectral intensities as a function of the energies of the incident photons for the X-ray photo-electron (XPS), X-ray absorption spectroscopy (XAS), valence-band photoemission (PS) and the resonant inelastic X-ray scattering (RIXS) spectra. We have computed both $L_{2,3}$ and $M_{2,3}$ edges of the spectra, where the X-ray photon excites an electron from the Re-2*p* and 3*p* core states respectively to its 5*d* valence states. Figures 4.19a-d present the $L_{2,3}$ and $M_{2,3}$ spectra for the XPS.

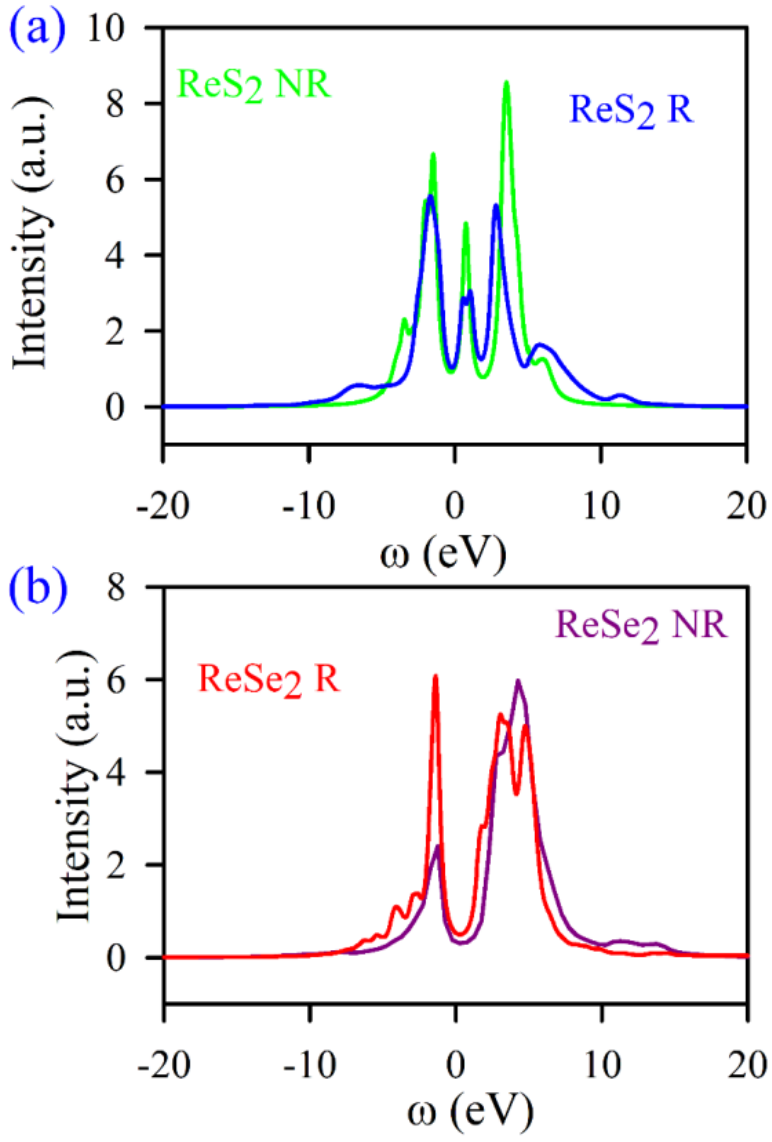

Figure 4.21: *Valence electron PS spectra of (a) ReS_2 (S-1) and (b) $ReSe_2$ (S-3) for R_{NR} and R_I. Zero on the energy scale corresponds to the Fermi energy.*

The differences between the two peak positions signify the large spin-orbit splitting corresponding to the 2*p* and 3*p* core states. The inset focuses on a single

edge for each case. It will be evident that for each spectral plot the peak positions, numbers and types of satellite peaks and their intensities differ substantially from the relaxed to non-relaxed systems. A comparison of the single edges also implies that the peak positions are significantly different between S-1 and S-3.

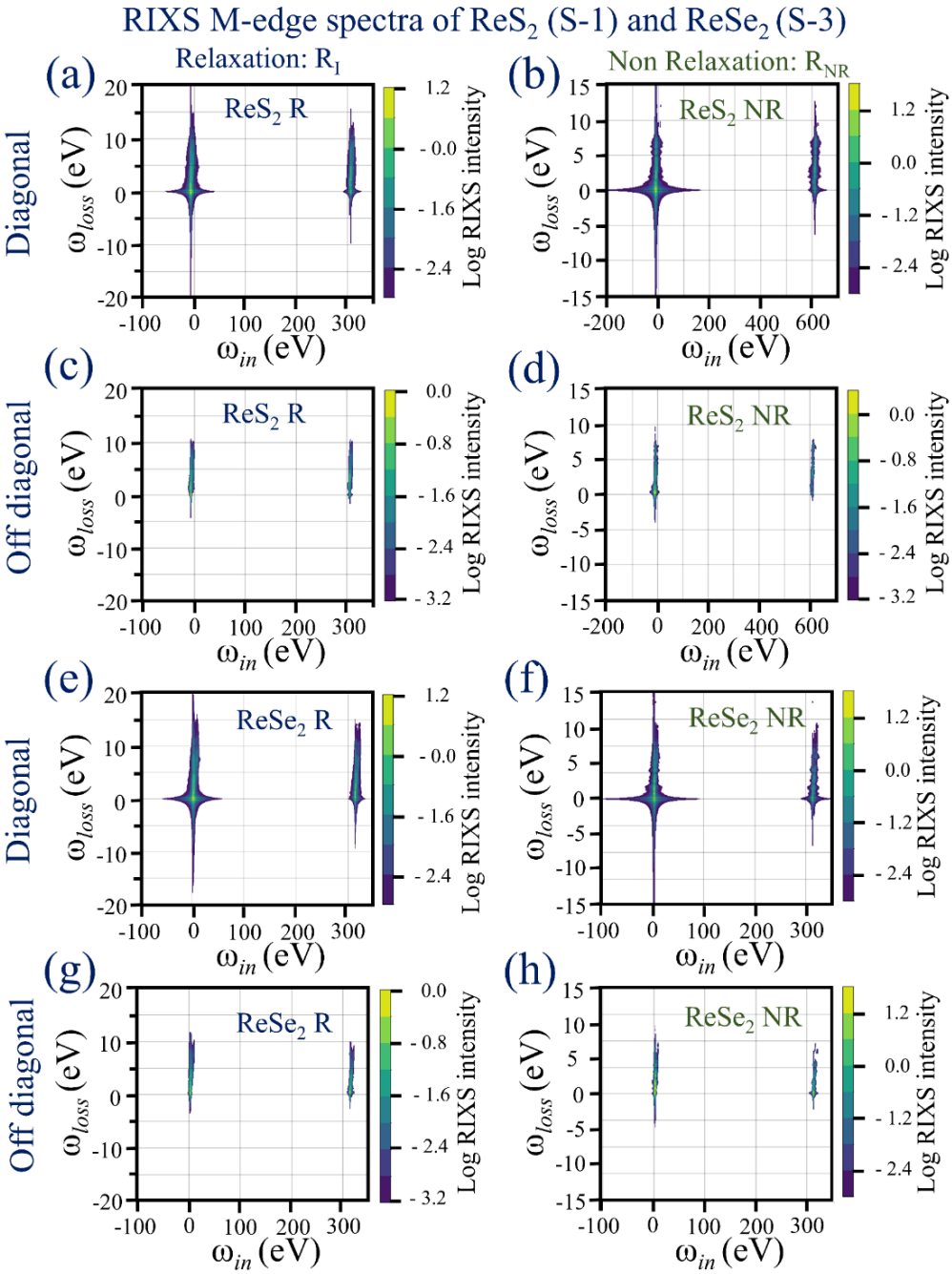

Figure 4.22: *Diagonal components of the RIXS M-edge spectra for (a) ReS_2 (S-1) relaxed and (b) ReS_2 (S-1) NR. Off diagonal components of the RIXS M-edge spectra of (c) ReS_2 (S-1) relaxed and (d) ReS_2 (S-1) NR. Diagonal components of the RIXS M-edge spectra of (e) $ReSe_2$ (S-3) relaxed and (f) $ReSe_2$ (S-3) NR. Off diagonal components of the RIXS M-edge spectra of (g) $ReSe_2$ (S-3) relaxed and (h) $ReSe_2$ (S-3) NR.*

Figures 4.20a-d represent the $L_{2,3}$ and $M_{2,3}$ spectra of XAS for S-1 and S-3 for R_{NR} and R_I. Apart from the differences in the XAS peak positions for the R_{NR} and R_I, the XAS intensity for the NR structure is always higher than the relaxed structure of S-1. For S-3, the difference in the peak-positions and intensities are both marginal, revealing that the effects of relaxations are not so high for $ReSe_2$.

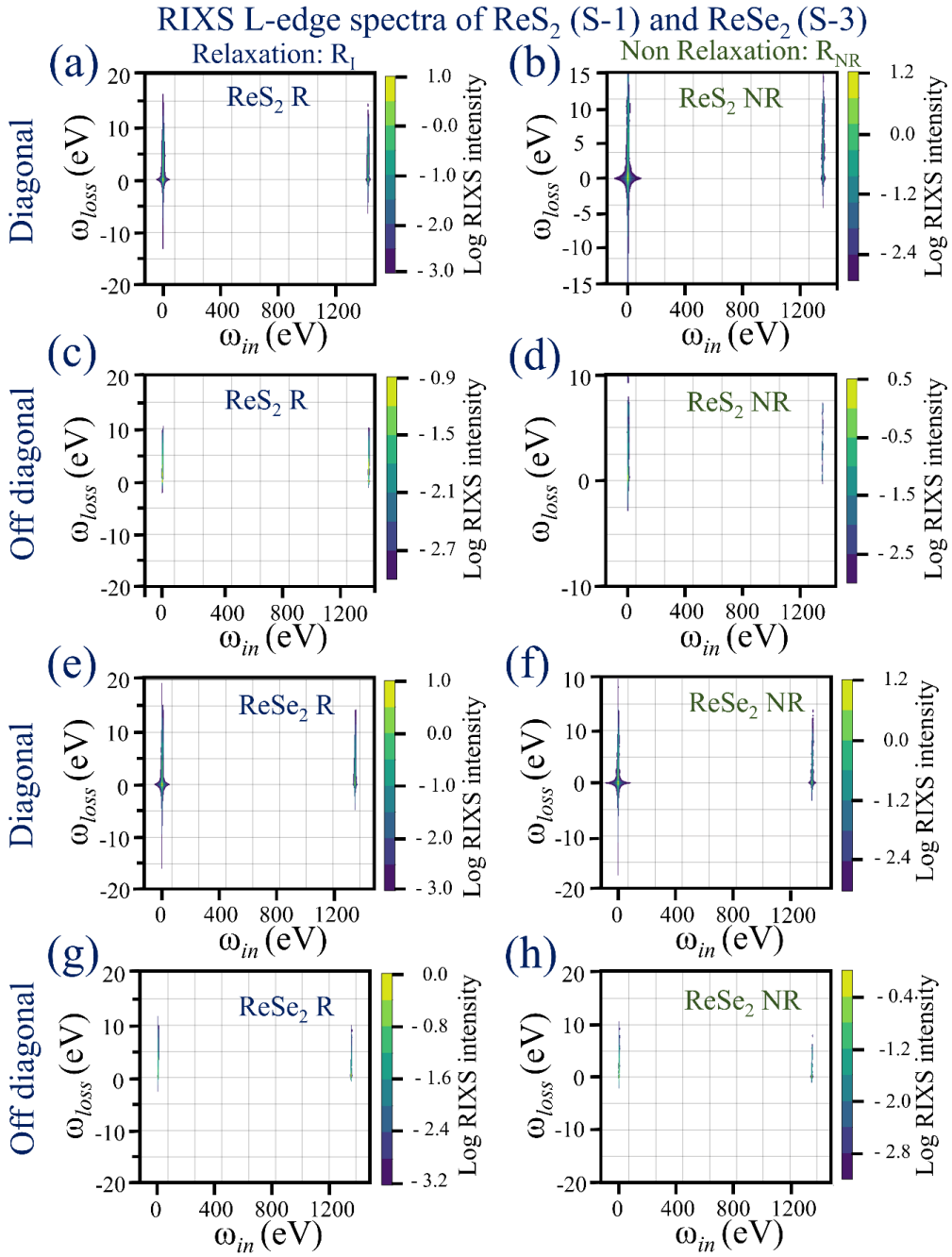

Figure 4.23: *Diagonal RIXS L-edge spectra of (a) ReS_2 relaxed and (b) ReS_2 NR. Off diagonal RIXS M-edge spectra of (c) ReS_2 relaxed and (d) ReS_2 NR. Diagonal RIXS L-edge spectra of (e) $ReSe_2$ relaxed and (f) $ReSe_2$ NR. Off diagonal RIXS L-edge spectra of (g) $ReSe_2$ relaxed and (h) $ReSe_2$ NR.*

Figures 4.21a and b depict the PS for ReS_2 and $ReSe_2$, where the gapped nature of ReS_2 in NR case is smeared out for the relaxed structure. In $ReSe_2$, the value of the band-gap is modified after relaxation, after keeping the upper- and lower-Hubbard nature of the peaks. ReS_2 has a typical three-peak structure, constituting the upper-, lower-Hubbard and the quasiparticle peak around the Fermi level like the metallic systems. Figures 4.22a–h presents the RIXS electron energy loss versus the incident energy plots for the diagonal and off-diagonal components of the dipole matrix corresponding to the $M_{2,3}$ edge. The corresponding RIXS responses of the $L_{2,3}$ edge are presented in Figures 4.23a-h. Thus, for the lowest energy structures of both S-1 and S-3, we have computed the X-ray spectroscopic properties with the help of DFT+MLFT. As per our knowledge, the experimental data corresponding to these calculations are still not available in the literature. These calculations will be helpful to plan future experiments using high-energy X-ray beams.

4.4.3. Conclusion:

In this comprehensive study, we have investigated all the available structures in the contemporary literature for ReS_2 and $ReSe_2$ and then converged upon the lowest energy ones to investigate the details of their electronic structures and shed light upon the existing disputes. Our study indicates the importance of structural relaxations in calculating the electronic structure to obtain a resemblance with the existing experimental data. The anisotropic orbital contributions at the band edges and the controversies about the direct or indirect bandgap nature for the bulk or monolayer can be resolved with these new structures. High-pressure-induced metallic transitions were predicted and the corresponding bulk moduli were calculated for the bulk structures. The X-ray spectral properties were investigated by using the DFT+MLFT methods for the relaxed and non-relaxed systems, which could be of use to plan the future high-energy X-ray experiments on these systems. This study indicates that the structure as well as the electronic properties of these two systems ReS_2 and $ReSe_2$ is quite different.

References

[1] M. Born, R. Oppenheimer, Zur quantentheorie der molekeln, *Annalen der physik* 389 (1927) 457.

[2] V. Fock, Näherungsmethode zur Lösung des quantenmechanischen Mehrkörperproblems, *Z. Physik* 61 (1930) 126.

[3] P. Hohenberg, W. Kohn, Inhomogeneous electron gas, *Phys. Rev.* 136 (1964) B864.

[4] W. Kohn, L. J. Sham, Self-consistent equations including exchange and correlation effects, *Phys. Rev.* 140 (1965) A1133.

[5] E. Fermi, Un metodo statistico per la determinazione di alcune priorieta dell'atome, *Rend. Accad. Naz. Lincei.* 6 (1927) 32.

[6] E. H. Lieb, B. Simon, The Thomas-Fermi theory of atoms, molecules and solids, *Adv. Math.* 23 (1977) 22.

[7] D. M. Ceperley, B. J. Alder, Ground state of the electron gas by a stochastic method, *Phys. Rev. Lett.* 45 (1980) 566.

[8] J. P. Perdew, A. Zunger, Self-interaction correction to density-functional approximations for many-electron systems, *Phys. Rev. B* 23 (1981) 5048.

[9] J. P. Perdew, Y. Wang, Accurate and simple analytic representation of the electron-gas correlation energy, *Phys. Rev. B* 45 (1992) 13244.

[10] R. O. Jones, O. Gunnarsson, The density functional formalism, its applications and prospects, *Rev. Modern Phys.* 61 (1989) 689.

[11] F. Herman, J. P. Van Dyke, I. B. Ortenburger, Improved statistical exchange approximation for inhomogeneous many-electron systems, *Phys. Rev. Lett.* 22 (1969) 807.

[12] J. P. Perdew, W. Yue, Accurate and simple density functional for the electronic exchange energy: Generalized gradient approximation, *Phys. Rev. B* 33 (1986) 8800.

[13] J. P. Perdew, Y. Wang, Accurate and simple analytic representation of the electron-gas correlation energy, *Phys. Rev. B* 45 (1992) 13244.

[14] J. P. Perdew, K. Burke, M. Ernzerhof, Generalized gradient approximation made simple, *Phys. Rev. Lett.* 77 (1996) 3865.

[15] Y. Umeno, B. Meyer, C. Elsässer, P. Gumbsch, Ab initio study of the critical thickness for ferroelectricity in ultrathin Pt/PbTiO3/Pt films, *Phys. Rev. B* 74 (2006) 060101.

[16] J. Hubbard, B. H. Flowers, Electron correlations in narrow energy bands, *P. Roy. Soc. Lond. Math. Phys. Sci.* 276 (1963) 238.

[17] V. Bach, E. H. Lieb, J. P. Solovej, Generalized Hartree-Fock theory and the Hubbard model, *J. Stat. Phys.* 76 (1994) 3.

[18] W. Koch, M. C. Holthausen, A chemist's guide to density functional theory, *John Wiley & Sons*, 2015.

[19] S. Kristyán, P. Pulay, Can (semi) local density functional theory account for the London dispersion forces?, *Chem. Phys. Lett.* 229 (1994) 175.

[20] P. Hobza, J. šponer, T. Reschel, Density functional theory and molecular clusters, *J. Comput. Chem.* 16 (1995) 1315.

[21] S. Grimme, Semiempirical GGA-type density functional constructed with a long-range dispersion correction, *J. Comp. Chem.* 27 (2006) 1787.

[22] J. C. Slater, G. F. Koster, Simplified LCAO method for the periodic potential problem, *Phys. Rev.* 94 (1954) 1498.

[23] D. Vanderbilt, Soft self-consistent pseudopotentials in a generalized eigenvalue formalism, *Phys. Rev. B* 41 (1990) 7892.

[24] G. Kresse, J. Hafner, Norm-conserving and ultrasoft pseudopotentials for first-row and transition elements, *J. Phys. Cond. Matt.* 6 (1994) 8245.

[25] T. L. Loucks, Augmented plane wave method; a guide to performing electronic structure calculations, *W.A. Benjamin*, New York, 1967.

[26] J. Korringa, On the calculation of the energy of a Bloch wave in a metal, *Physica* 13 (1947) 392.

[27] J. Korringa, Early history of multiple scattering theory for ordered systems, *Phys. Rep.* 238 (1994) 341.

[28] O. K. Andersen, O. Jepsen, Explicit, first-principles tight-binding theory, *Phys. Rev. Lett.* 53 (1984) 2571.

[29] C. Herring, A new method for calculating wave functions in crystals, *Phys. Rev.* 57 (1940) 1169.

[30] P. E. Blöchl, Projector augmented-wave method, *Phys. Rev. B* 50 (1994) 17953.

[31] J. C. Slater, Statistical exchange-correlation in the self-consistent field in Adv. Quant. Chem., *Elsevier*, 1972.

[32] J. C. Slater, Wave functions in a periodic potential, *Phys. Rev.* 51 (1937) 846.

[33] O. K. Andersen, Linear methods in band theory, *Phys. Rev. B* 12 (1975) 3060.

[34] D. D. Koelling, G. O. Arbman, Use of energy derivative of the radial solution in an augmented plane wave method: Application to copper, *J. Phys. F: Met. Phys.* 5 (1975) 2041.

[35] G. Kresse, J. Furthmüller, Efficient iterative schemes for ab initio total-energy calculations using a plane-wave basis set, *Phys. Rev. B* 54 (1996) 11169.

[36] G. Kresse, D. Joubert, From ultrasoft pseudopotentials to the projector augmented-wave method, *Phys. Rev. B* 59 (1999) 1758.

[37] E. Runge, E. K. Gross, Density-functional theory for time-dependent systems, *Phys. Rev. Lett.* 52 (1984) 997.

[38] M. Levy, Electron densities in search of Hamiltonians, *Phys. Rev. A* 26 (1982) 1200.

[39] E. H. Lieb, Density functionals for coulomb systems in in density functional methods in physics, *Springer US*, Boston, 1985.

[40] S. Sharma, J. Dewhurst, A. Sanna, E. Gross, Bootstrap approximation for the exchange-correlation kernel of time-dependent density-functional theory, *Phys. Rev. Lett.* 107 (2011) 186401.

[41] S. Botti, A. Fourreau, F. Nguyen, Y.-O. Renault, F. Sottile, L. Reining, Energy dependence of the exchange-correlation kernel of time-dependent density functional theory: A simple model for solids, *Phys. Rev. B* 72 (2005) 125203.

[42] O. Johns, A consistent RPA formalism, *Z. Physik* 253 (1972) 269.

[43] J. P. Perdew, K. Burke, M. Ernzerhof, Generalized gradient approximation made simple, *Phys. Rev. Lett.* 77 (1996) 3865.

[44] G. Kresse, J. Furthmüller, Efficiency of ab-initio total energy calculations for metals and semiconductors using a plane-wave basis set, *Comput. Mater. Sci.* 6 (1996) 15.

[45] S. Grimme, J. Antony, S. Ehrlich, H. Krieg, A consistent and accurate ab initio parametrization of density functional dispersion correction (DFT-D) for the 94 elements H-Pu, *J. Chem. Phys.* 132 (2010) 154104.

[46] A. Togo, I. Tanaka, First principles phonon calculations in materials science, *Scr. Mater.* 108 (2015) 1.

[47] J. Heyd, G. E. Scuseria, M. Ernzerhof, Hybrid functionals based on a screened Coulomb potential, *J. Chem. Phys.* 118 (2003) 8207.

[48] J. M. Wills, O. Eriksson, P. Andersson, A. Delin, O. Grechnyev, M. Alouani, Full-potential electronic structure method : Energy and force calculations with density functional and dynamical mean field theory, *Springer*, Heidelberg, 2010.

[49] A. Grechnev, I. Di Marco, M. I. Katsnelson, A. I. Lichtenstein, J. Wills, O. Eriksson, Theory of bulk and surface quasiparticle spectra for Fe, Co, and Ni, *Phys. Rev. B* 76 (2007) 035107.

[50] J. Lüder, J. Schött, B. Brena, M. W. Haverkort, P. Thunström, O. Eriksson, B. Sanyal, I. Di Marco, Y. O. Kvashnin, Theory of L-edge spectroscopy of strongly correlated systems, *Phys. Rev. B* 96 (2017) 245131.

[51] M. W. Haverkort, M. Zwierzycki, O. K. Andersen, Multiplet ligand-field theory using Wannier orbitals, *Phys. Rev. B* 85 (2012) 165113.

[52] I. Di Marco, J. Minár, S. Chadov, M. I. Katsnelson, H. Ebert, A. I. Lichtenstein, Correlation effects in the total energy, the bulk modulus, and the lattice constant of a transition metal: Combined local-density approximation and dynamical mean-field theory applied to Ni and Mn, *Phys. Rev. B* 79 (2009) 115111.

[53] M. I. Katsnelson, A. I. Lichtenstein, Electronic structure and magnetic properties of correlated metals, *Eur. Phys. J. B* 30 (2002) 9.

[54] P. Thunström, I. Di Marco, O. Eriksson, Electronic entanglement in late transition metal oxides, *Phys. Rev. Lett.* 109 (2012) 186401.

[55] H. Yamaoka, P. Thunström, I. Jarrige, K. Shimada, N. Tsujii, M. Arita, H. Iwasawa, H. Hayashi, J. Jiang, T. Habuchi, D. Hirayama, H. Namatame, M. Taniguchi, U. Murao, S. Hosoya, A. Tamaki, H. Kitazawa, High-resolution photoelectron spectroscopy study of Kondo metals: $SmSn_3$ and $Sm_{0.9}La_{0.1}Sn_3$, *Phys. Rev. B* 85 (2012) 115120.

[56] A. I. Liechtenstein, M. I. Katsnelson, V. P. Antropov, V. A. Gubanov, Local spin density functional approach to the theory of exchange interactions in ferromagnetic metals and alloys, *Magn. Magn. Mater.* 67 (1987) 65.

[57] C. Etz, L. Bergqvist, A. Bergman, A. Taroni, O. Eriksson, Atomistic spin dynamics and surface magnons, *J. Phys.: Condens. Matter* 27 (2015) 243202.

[58] P. B. Allen, R. C. Dynes, Transition temperature of strong-coupled superconductors reanalyzed, *Phys. Rev. B* 12 (1975) 905.

[59] H. J. Lamfers, A. Meetsma, G. A. Wiegers, J. L. de Boer, The crystal structure of some rhenium and technetium dichalcogenides, *J. Alloys Compd.* 241 (1996) 34.

[60] F. Mooshammer, S. Chae, S. Zhang, Y. Shao, S. Qiu, A. Rajendran, A. J. Sternbach, D. J. Rizzo, X. Zhu, P. J. Schuck, J. C. Hone, D. N. Basov, In-plane anisotropy in biaxial ReS_2 crystals probed by nano-optical imaging of waveguide modes, *ACS Photonics* 9 (2022) 443.

[61] S. Y. Hu, C. H. Liang, K. K. Tiong, Y. S. Huang, Y. C. Lee, Electrical anisotropy of W-doped $ReSe_2$ crystals, *J. Electrochem. Soc.* 153 (2006) J100.

[62] Z. Lai, A. Chaturvedi, Y. Wang, T. H. Tran, X. Liu, C. Tan, Z. Luo, B. Chen, Y. Huang, G.-H. Nam, Z. Zhang, Y. Chen, Z. Hu, B. Li, S. Xi, Q. Zhang, Y. Zong, L. Gu, C. Kloc, Y. Du, H. Zhang, Preparation of 1T′-phase $ReS_{2x}Se_{2(1-x)}$ (x = 0–1) nanodots for highly efficient electrocatalytic hydrogen evolution reaction, *J. Am. Chem. Soc.* 140 (2018) 8563.

[63] S. Sim, D. Lee, A. V. Trifonov, T. Kim, S. Cha, J. H. Sung, S. Cho, W. Shim, M.-H. Jo, H. Choi, Ultrafast quantum beats of anisotropic excitons in atomically thin ReS_2, *Nat. Commun.* 9 (2018) 351.

[64] X. Wang, K. Shinokita, H. E. Lim, N. B. Mohamed, Y. Miyauchi, N. T. Cuong, S. Okada, K. Matsuda, Direct and indirect exciton dynamics in few-layered ReS_2 revealed by photoluminescence and pump-probe spectroscopy, *Adv. Funct. Mater.* 29 (2019) 1806169.

[65] O. B. Aslan, D. A. Chenet, A. M. van der Zande, J. C. Hone, T. F. Heinz, Linearly polarized excitons in single- and few-layer ReS_2 crystals, *ACS Photonics* 3 (2016) 96.

[66] D. A. Chenet, O. B. Aslan, P. Y. Huang, C. Fan, A. M. van der Zande, T. F. Heinz, J. C. Hone, In-plane anisotropy in mono- and few-layer ReS_2 probed by raman spectroscopy and scanning transmission electron microscopy, *Nano Lett.* 15 (2015) 5667.

[67] H. Jang, C. R. Ryder, J. D. Wood, M. C. Hersam, D. G. Cahill, 3D anisotropic thermal conductivity of exfoliated rhenium disulfide, *Adv. Mater.* 29 (2017) 1700650.

[68] D. Ovchinnikov, F. Gargiulo, A. Allain, D. J. Pasquier, D. Dumcenco, C.-H. Ho, O. V. Yazyev, A. Kis, Disorder engineering and conductivity dome in ReS_2 with electrolyte gating, *Nat. Commun.* 7 (2016) 12391.

[69] X. Ling, S. Huang, E. H. Hasdeo, L. Liang, W. M. Parkin, Y. Tatsumi, A. R. T. Nugraha, A. A. Puretzky, P. M. Das, B. G. Sumpter, D. B. Geohegan, J. Kong, R. Saito, M. Drndic, V. Meunier, M. S. Dresselhaus, Anisotropic electron-photon and electron-phonon interactions in black phosphorus, *Nano Lett.* 16 (2016) 2260.

[70] S. Tongay, H. Sahin, C. Ko, A. Luce, W. Fan, K. Liu, J. Zhou, Y.-S. Huang, C.-H. Ho, J. Yan, D. F. Ogletree, S. Aloni, J. Ji, S. Li, J. Li, F. M. Peeters, J. Wu, Monolayer behaviour in bulk ReS_2 due to electronic and vibrational decoupling, *Nat. Commun.* 5 (2014) 3252.

[71] N. B. Mohamed, K. Shinokita, X. Wang, H. E. Lim, D. Tan, Y. Miyauchi, K. Matsuda, Photoluminescence quantum yields for atomically thin-layered ReS_2: Identification of indirect-bandgap semiconductors, *Appl. Phys. Lett.* 113 (2018) 121112.

[72] B. Jariwala, D. Voiry, A. Jindal, B. A. Chalke, R. Bapat, A. Thamizhavel, M. Chhowalla, M. Deshmukh, A. Bhattacharya, Synthesis and characterization of ReS_2 and $ReSe_2$ layered chalcogenide single crystals, *Chem. Mater.* 28 (2016) 3352.

[73] A. Arora, J. Noky, M. Drüppel, B. Jariwala, T. Deilmann, R. Schneider, R. Schmidt, O. Del Pozo-Zamudio, T. Stiehm, A. Bhattacharya, P. Krüger, S. Michaelis de Vasconcellos, M. Rohlfing, R. Bratschitsch, Highly anisotropic in-

plane excitons in atomically thin and bulklike 1T'-$ReSe_2$, *Nano Lett.* 17 (2017) 3202.

[74] S. M. Gunasekera, D. Wolverson, L. S. Hart, M. Mucha-Kruczynski, Electronic band structure of rhenium dichalcogenides, *J. Electron. Mater.* 47 (2018) 4314.

[75] C. H. Ho, Y. S. Huang, J. L. Chen, T. E. Dann, K. K. Tiong, Electronic structure of ReS_2 and $ReSe_2$ from first-principles calculations, photoelectron spectroscopy, and electrolyte electroreflectance, *Phys. Rev. B* 60 (1999) 15766.

[76] I. Gutiérrez-Lezama, B. A. Reddy, N. Ubrig, A. F. Morpurgo, Electroluminescence from indirect band gap semiconductor ReS_2, *2D Mater.* 3 (2016) 045016.

[77] J. V. Marzik, R. Kershaw, K. Dwight, A. Wold, Photoelectronic properties of ReS_2 and $ReSe_2$ single crystals, *J. Solid State Chem.* 51 (1984) 170.

[78] D. Wolverson, S. Crampin, A. S. Kazemi, A. Ilie, S. J. Bending, Raman spectra of monolayer, few-layer, and bulk $ReSe_2$: An anisotropic layered semiconductor, *ACS Nano* 8 (2014) 11154.

[79] H.-X. Zhong, S. Gao, J.-J. Shi, L. Yang, Quasiparticle band gaps, excitonic effects, and anisotropic optical properties of the monolayer distorted 1T diamond-chain structures ReS_2 and $ReSe_2$, *Phys. Rev. B* 92 (2015) 115438.

[80] J. P. Echeverry, I. C. Gerber, Theoretical investigations of the anisotropic optical properties of distorted 1T ReS_2 and $ReSe_2$ monolayers, bilayers, and in the bulk limit, *Phys. Rev. B* 97 (2018) 075123.

[81] D. Biswas, A. M. Ganose, R. Yano, J. M. Riley, L. Bawden, O. J. Clark, J. Feng, L. Collins-Mcintyre, M. T. Sajjad, W. Meevasana, T. K. Kim, M. Hoesch, J. E. Rault, T. Sasagawa, D. O. Scanlon, P. D. C. King, Narrow-band anisotropic electronic structure of ReS_2, *Phys. Rev. B* 96 (2017) 085205.

[82] J. L. Webb, L. S. Hart, D. Wolverson, C. Chen, J. Avila, M. C. Asensio, Electronic band structure of ReS_2 by high-resolution angle-resolved photoemission spectroscopy, *Phys. Rev. B* 96 (2017) 115205.

[83] M. Gehlmann, I. Aguilera, G. Bihlmayer, S. Nemšák, P. Nagler, P. Gospodarič, G. Zamborlini, M. Eschbach, V. Feyer, F. Kronast, E. Młyńczak, T. Korn, L. Plucinski, C. Schüller, S. Blügel, C. M. Schneider, Direct observation of the band gap transition in atomically thin ReS_2, *Nano Lett.* 17 (2017) 5187.

[84] L. S. Hart, J. L. Webb, S. Dale, S. J. Bending, M. Mucha-Kruczynski, D. Wolverson, C. Chen, J. Avila, M. C. Asensio, Electronic bandstructure and van der Waals coupling of $ReSe_2$ revealed by high-resolution angle-resolved photoemission spectroscopy, *Sci. Rep.* 7 (2017) 5145.

[85] R. He, J.-A. Yan, Z. Yin, Z. Ye, G. Ye, J. Cheng, J. Li, C. H. Lui, Coupling and stacking order of ReS_2 atomic layers revealed by ultralow-frequency raman spectroscopy, *Nano Lett.* 16 (2016) 1404.

[86] E. Lorchat, G. Froehlicher, S. Berciaud, Splitting of interlayer shear modes and photon energy dependent anisotropic raman response in N-layer $ReSe_2$ and ReS_2, *ACS Nano* 10 (2016) 2752.

[87] J. R. Gadde, A. Karmakar, T. K. Maji, S. Mukherjee, R. Alexander, A. M. R. Sharma, S. Das, A. Mandal, K. Dasgupta, A. Naik, K. Majumdar, R. Hawaldar, K. V. Adarsh, S. K. Ray, D. Karmakar, Two-dimensional ReS_2: Solution to the unresolved queries on its structure and inter-layer coupling leading to potential optical applications, *Phys. Rev. Materials* 5 (2021) 054006.

[88] L. Liang, J. Zhang, B. G. Sumpter, Q.-H. Tan, P.-H. Tan, V. Meunier, Low-frequency shear and layer-breathing modes in raman scattering of two-dimensional materials, *ACS Nano* 11 (2017) 11777.

[89] P. Nagler, G. Plechinger, C. Schüller, T. Korn, Observation of anisotropic interlayer Raman modes in few-layer ReS_2, *Phys. Status Solidi RRL* 10 (2016) 185.

[90] H. Zhao, J. Wu, H. Zhong, Q. Guo, X. Wang, F. Xia, L. Yang, P. Tan, H. Wang, Interlayer interactions in anisotropic atomically thin rhenium diselenide, *Nano Res.* 8 (2015) 3651.

[91] L. S. Hart, S. M. Gunasekera, M. Mucha-Kruczyński, J. L. Webb, J. Avila, M. C. Asensio, D. Wolverson, Interplay of crystal thickness and in-plane anisotropy and evolution of quasi-one-dimensional electronic character in $ReSe_2$, *Phys. Rev. B* 104 (2021) 035421.

[92] B. K. Choi, S. Ulstrup, S. M. Gunasekera, J. Kim, S. Y. Lim, L. Moreschini, J. S. Oh, S.-H. Chun, C. Jozwiak, A. Bostwick, E. Rotenberg, H. Cheong, I.-W. Lyo, M. Mucha-Kruczynski, Y. J. Chang, Visualizing orbital content of electronic bands in anisotropic 2D semiconducting $ReSe_2$, *ACS Nano* 14 (2020) 7880.

[93] Y. Zhou, N. Maity, A. Rai, R. Juneja, X. Meng, A. Roy, Y. Zhang, X. Xu, J.-F. Lin, S. K. Banerjee, A. K. Singh, Y. Wang, Stacking-order-driven optical properties and carrier dynamics in ReS_2, *Adv. Mater.* 32 (2020) 1908311.

[94] N. R. Pradhan, C. Garcia, B. Isenberg, D. Rhodes, S. Feng, S. Memaran, Y. Xin, A. McCreary, A. R. H. Walker, A. Raeliarijaona, H. Terrones, M. Terrones, S. McGill, L. Balicas, Phase modulators based on high mobility ambipolar $ReSe_2$ field-effect transistors, *Sci. Rep.* 8 (2018) 12745.

[95] G. Ernotte, T. J. Hammond, M. Taucer, A gauge-invariant formulation of interband and intraband currents in solids, *Phys. Rev. B* 98 (2018) 235202.

[96] J. Ibáñez-Insa, T. Woźniak, R. Oliva, C. Popescu, S. Hernández, J. López-Vidrier, Structural and high-pressure properties of rheniite (ReS_2) and $(Re,Mo)S_2$, *Minerals* 11 (2021) 207.

[97] R. Oliva, M. Laurien, F. Dybala, J. Kopaczek, Y. Qin, S. Tongay, O. Rubel, R. Kudrawiec, Pressure dependence of direct optical transitions in ReS_2 and $ReSe_2$, *npj 2D Mater. Appl.* 3 (2019) 20.

[98] M. N. Hasan, F. Sorgenfrei, N. Pan, D. Phuyal, M. Abdel-Hafiez, S. K. Pal, A. Delin, P. Thunstrom, D. D. Sarma, O. Eriksson, D. Karmakar, Re-dichalcogenides: Resolving conflicts of their structure–property relationship, *Adv. Phys. Res.* 1 (2022) 2200010.

[99] H. H. Murray, S. P. Kelty, R. R. Chianelli, C. S. Day, Structure of rhenium disulfide, *Inorg. Chem.* 33 (1994) 4418.

[100] J. C. Wildervanck, F. Jellinek, The dichalcogenides of technetium and rhenium, *J. less-common met.* 24 (1971) 73.

[101] X.-F. Qiao, J.-B. Wu, L. Zhou, J. Qiao, W. Shi, T. Chen, X. Zhang, J. Zhang, W. Ji, P.-H. Tan, Polytypism and unexpected strong interlayer coupling in two-dimensional layered ReS_2, *Nanoscale* 8 (2016) 8324.

[102] K. Dileep, R. Sahu, S. Sarkar, S. C. Peter, R. Datta, Layer specific optical band gap measurement at nanoscale in MoS_2 and ReS_2 van der Waals compounds by high resolution electron energy loss spectroscopy, *J. Appl. Phys.* 119 (2016) 114309.

[103] Z. Yin, H. Li, H. Li, L. Jiang, Y. Shi, Y. Sun, G. Lu, Q. Zhang, X. Chen, H. Zhang, Single-layer MoS_2 phototransistors, *ACS Nano* 6 (2012) 74.

[104] M. Hafeez, L. Gan, A. Saleem Bhatti, T. Zhai, Rhenium dichalcogenides (ReX_2, X = S or Se): An emerging class of TMDs family, *Mater. Chem. Front.* 1 (2017) 1917.

[105] S. Yang, C. Wang, H. Sahin, H. Chen, Y. Li, S.-S. Li, A. Suslu, F. M. Peeters, Q. Liu, J. Li, S. Tongay, Tuning the optical, magnetic, and electrical properties of $ReSe_2$ by nanoscale strain engineering, *Nano Lett.* 15 (2015) 1660.

Chapter 5

Synthesis and Optical Characterization of a Nontoxic Nanohybrid for their Potential Drug Delivery Applications

5.1. Introduction:

Treatment of antibiotic resistant infections is a global hazard to human civilization [1] possesses an open challenge to the contemporary therapeutic research to combat multi-drug resistant bacteria [2]. In this direction, nanomaterials have emerged as a substitute tool to fight multi-drug resistant bacteria [3]. As the nanomaterial-bacteria interaction relies on several physical phenomena namely electrostatic attraction, van der Waals forces and hydrophobic. A profound scientific understanding of the interactions, which may not be unique for all cases provides ultimate insight for designing novel antimicrobial agents [4]. The key factor for the development of new antibiotics using nanomaterials is unique according to its physiochemical properties which essentially offers a versatile platform to develop innovative therapeutic strategies [5]. In general, the therapeutic strategies using nanomaterials can be classified into two categories namely direct and indirect interaction of the nanometals with target microorganisms. The direct strategy involves development of a class of organic-inorganic nanohybrid which either included or directly interacts with the microorganisms till their eradication. For example, in a recent study vancomycin-functionalized gold nanoparticles were synthesized to overcome vancomycin-resistant enterococci (VRE) infection [6, 7]. The improved antibacterial activity of the nanohybrids attributes to the enhanced internalization of the antibiotics inside cells connected to the polyvalent effect of concentrated antibiotics present on the surface of nanomaterials [8]. The mechanism of the bactericidal effect was reported to be disruption of negatively charged cell membrane of the bacteria by the cationic

polymer and eventually release of Ag^+ ions from the AgBr nanoparticles [9]. In addition, biopolymers such as DNA, proteins/antibodies are also used in order to develop nanohybrids with specific recognition properties [10]. Antibacterial activity of DNA stabilized Ag nanoparticles was demonstrated by varying the oligonucleotide sequence [11]. It was concluded that the structure of the DNA used to stabilize the nanoparticles plays a key role in cellular internalization and eventually antimicrobial activity [11].

The indirect antimicrobial effect can be achieved through the use of nanomaterials as antimicrobial delivery vehicles to successfully deliver them to the infection site [12, 13]. In order to qualify as a delivery vehicle, a nanomaterial is essential to have the following properties, which can only be achieved through careful nano-surface engineering. Firstly, solubility in the bloodstream of the nanomaterial assures invisibility in opposition to the body's common defense system as mononuclear phagocytic system can eliminate these nano-vehicles from the bloodstream. Secondly, the ability to cross biological barriers through the process of opsonization. As opsonin proteins in the blood rapidly adhere to nanomaterials, allowing the macrophages from the MPS (mononuclear phagocytic system) to bind and remove the nanomaterial from circulation [14]. Recently, nitrite-loaded silane-hydrogel based composite nanomaterial was developed to attach the antimicrobial activity of nitric oxide (NO) [15]. Among other nanomaterial-based drug delivery vehicles for pH-triggered drug delivery systems, enzyme-sensitive delivery systems, bacterial toxin-triggered drug delivery, the strategy for the stimuli-mediated cargo release is both sophisticated and complex, requiring biocompatible materials that can undergo chemical or structural changes in response to stimuli, e.g. light exposure at infection sites [3]. The acidic microenvironments, chronic infections or wounds with pH value in the range of 4−7 might be exploited to construct pH-sensitive nanotherapeutics [16]. The exceptional dissolution of ZnO (zinc oxide) nanoparticles at lower pH inducted its useful purpose as nanocarriers for drug delivery applications [17]. Recently, ZnO nanoparticles of great biocompatibility loaded with NIR active photosensitizer are shown to provide unprecedented antimicrobial

photodynamic therapeutic efficacy [18]. However, a photo-responsive nano-vehicle for the delivery of conventional drugs, where the delivery vehicle itself shows antibacterial properties to drug-resistant bacteria is sparse in the literature and the development of such multifunctional nano-material is the motive of our work.

Metal-organic frameworks (MOFs) constitute a significant class of hybrid inorganic-organic crystalline porous materials and its structures can be manipulated at the atomic scale by an appropriate choice of metal ions and organic ligands [19, 20]. MOF shows a range of applications in different fields including gas separation, gas storage, catalysis and sensing due to their large surface areas and tunable pore sizes [21-23]. MOFs possess many advantages for the adsorption and release of biomolecules and have a great potential for use as a new-age drug-delivery agent. Recently, it has been reported that porous iron(III)-based MOF (MIL) with engineered cores and surfaces are able to function as exceptional nanocarriers for powerful controlled delivery of challenging anti-tumoral drugs against cancer [24]. However, poor bioavailability (solubility, stability) under aqueous conditions of most of the MOF systems hindered its use as a drug-delivery agent [25].

MOFs encompassing their own antibacterial property are mainly reported in the case of Ag-containing MOF systems. Recently, it has been reported that Ag-containing Zr-based MOFs synthesized *via* a two-step process can kill gram-negative *E. coli* infection [26, 27]. However, stability and expense of silver are a matter of concern. Cobalt based MOFs are suggested as the only alternatives of Ag-MOF. Co-based MOF using tetrakis[(3,5-dicarboxyphenyl)-oxamethyl] methane acid as ligand has depicted its potency toward inactivation of *E. coli* [28]. Moreover, Co-SIM-1 and ZIF 67 are also reported as potential antibacterial agents. The main issue of Co-based MOF is its water stability and solubility [29].

In this chapter, we have employed a mixed metal approach to get both water stability and activity in one single MOF system. ZIF-8 and ZIF-67 are highly compatible due to their iso-reticular structure and similar lattice parameters, and

thus the mixed metal ZIF is synthesized *via* the co-precipitation of zinc and cobalt ions with Hmim. Electron microscopic images suggest that zinc and cobalt ions coexist uniformly in the bimetallic ZIF. The unperturbed crystal structures are confirmed using X-ray diffraction. As a consequence of the metal mixing process, the optical characteristics of mixed ZIF get altered which are evaluated using excited state emission property. The water stability of mixed ZIF has been evaluated both in the short term and for a long period. The pH-responsive dissolution of mixed ZIF is also assessed. The photoinduced reactive oxygen species generation was monitored using DCFH assay. The antibacterial effect of mixed ZIF is evaluated against drug-resistant bacterial strains. The light-induced reactivity of mixed ZIF can be employed for many fold applications including therapy and pollutant degradation. However, the detailed study using variant composition of metal ions is indeed of great importance and we would like to perform these types of experiments in the near future.

Besides, there is an appeal for the improvement by employing stimuli responsive nanohybrids that can be accountable for their multifunction, multiuse and profoundly successful execution [30, 31]. These days, nanoparticles are progressively used to target microorganisms and could fill in as an option to natural antibacterial operators [32]. The viability of antibacterial capability might be expanded by means of nanohybrid that could be powerful to prevent the development of microbial infections in humans [33]. The nanohybrid is probably going to maintain stability against degradation, improving bioavailability, and intracellular transportation [34, 35]. MOFs are types of permeable materials containing metal sites attached through organic bridging ligands forming a frame-like structure. They are appreciated broadly due to their large surface area, tunable hole arrangement and manageable functionalities [36, 37]. ZIF8 is thermally nearly as steady as a covalent bond which makes it an extraordinary nominee for various applications [38]. Past reports have exhibited the utilization of ZIF8 as stimuli responsive targeted delivery framework for typical anticancer treatment doxorubicin [39]. Under some conditions, ZIF8 crystals can course through the circulation system pursued by moderate discharge into intracellular

organelles with lower pH 5−6 portraying its likelihood of usage as pH-sensitive drug delivery [33, 40]. We have shown earlier ZIF8 can effectively deliver phototherapeutic drugs into a bacterial infection site and pronouncedly killed the infection using antimicrobial photodynamic therapeutic strategies [33]. Hence, the attention is right now on improvement for increasing aqueous stability and the bioavailability issues of widely used antibiotics using ZIF8 [41].

Therefore, we have used rifampicin (RF), a compelling antituberculosis drug that has tremendous pharmacological significance [42]. The common anti-microbial RF covers a wide scope of natural action while these investigations propose the use of ZIF8 frameworks for focused targeted drug delivery operators to combat anti-microbial resistance bacterial infections. RF is encapsulated into ZIF8 by a simple synthetic procedure [43]. The addition of RF inside the pores of ZIF8 structure is required to bring down the free dissemination of RF in biological media. The synthesized ZIF8-RF nanohybrids are characterized by electron microscopic methods such as transmission electron microscopy (TEM), scanning electron microscopy (SEM) and X-ray diffraction. We have performed optical spectroscopic experiments such as absorption, emission and picosecond resolved fluorescence spectroscopy to validate the formation of the ZIF8-RF nanohybrid. The drug release profile experiment demonstrates that ZIF8-RF has acidic pH-responsive drug delivery capability which is ideal for targeting bacterial diseases. Most notably, ZIF8-RF provides enormous antibacterial activity against MRSA bacteria and prompts total loss of adherence to robust bacterial biofilms. The overall study depicts detailed physical insight for antibiotic-impregnated ZIF8-RF hybrid with tremendous antimicrobial activity that can be beneficial for manifold biomedical application purposes.

5.2. Results and Discussion:

5.2.1. Enhanced Water Stability and Photoresponsivity in Metal-Organic Framework (MOF): A Potential Tool to Combat Drug-Resistant Bacteria [37]: Bimetallic ZIFs are prepared by reacting Co^{2+} and Zn^{2+} metal ions with 2-

methylimidazolate (Hmim) in methanolic solution as depicted in Figure 5.1a. The mixed-coordination of Hmim with an initial similar molar ratio of Zn^{2+} and Co^{2+} ions used in synthesis has been denoted as $Zn_{50}Co_{50}$-ZIF. Figure 5.1b shows the XRD patterns of all synthesized samples namely ZIF-8 (red), ZIF-67 (black) and $Zn_{50}Co_{50}$-ZIF (blue). All samples exhibit the same peaks at 7.22°, 10.2°, 12.5° and 17.8°, which correspond to the diffraction planes (011), (002), (112) and (222) respectively that agree with reported XRD of ZIF-8 [44].

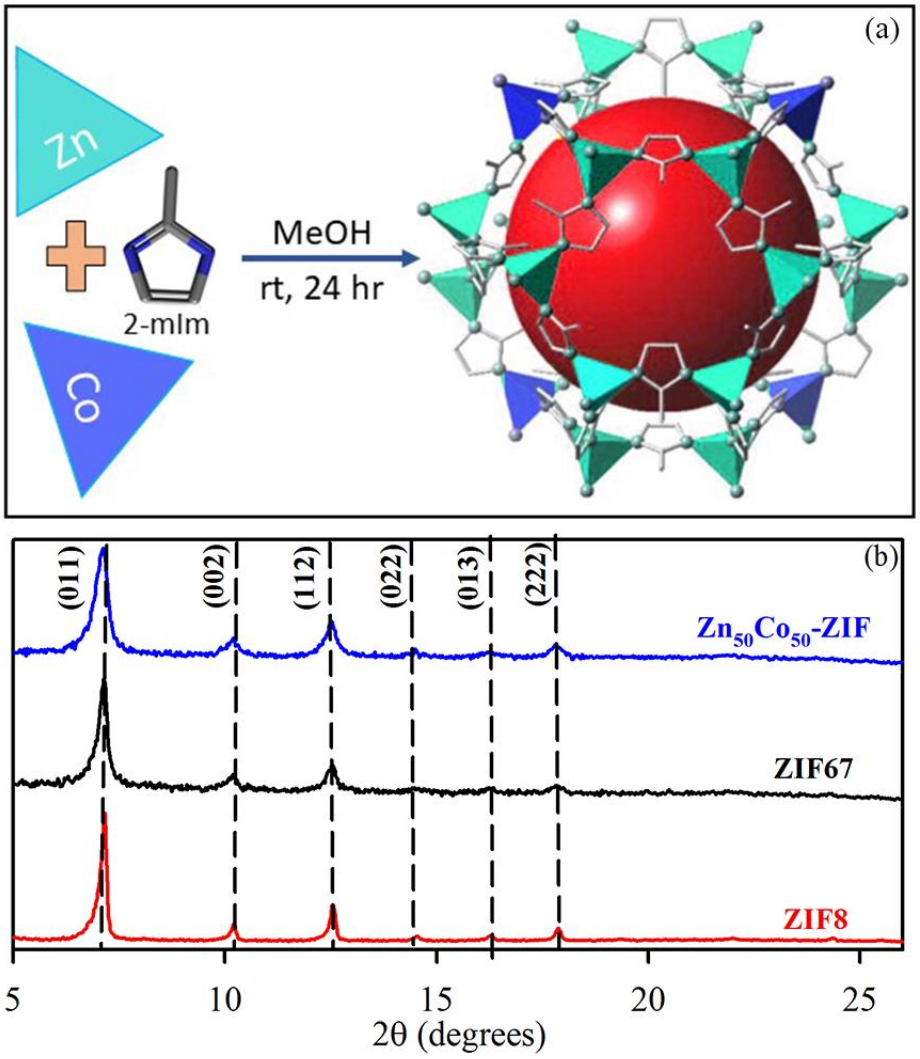

Figure 5.1: *(a) Schematic representation of synthetic strategy for mixed metal zeolitic imidazolate framework (ZIF). (b) XRD patterns of synthesized ZIF-8 (red), ZIF-67 (black) and bimetallic ZIF (blue).*

It indicates that all samples are in pure phases and isostructural with ZIF-8 showing high crystallinity. Also, we have the specific surface areas and porosity properties of this ZIF that are consistent with each other reported in the literature

[45, 46]. Next, we used TEM for the structural characterization of these samples. TEM results revealed the size and morphology of ZIF-8 (Figure 5.2a, b) and ZIF-67 (Figure 5.2d, e) as uniform rhombic dodecahedral-shaped crystals with an average diameter of 150-250 nm. To observe the chemical composition of ZIF systems, we have employed energy filtered TEM (EFTEM) mapping analysis of ZIF-8 (Figure 5.2c) and ZIF-67 (Figure 5.2f). $Zn_{50}Co_{50}$-ZIF crystals are also characterized using TEM analysis. Figure 5.2g depicts the single crystal morphology of the bimetallic ZIF. The average diameter of the crystals is 100 nm. The EFTEM map of a single crystal and multiple crystals of both ZIF-8 and $Zn_{50}Co_{50}$-ZIF depicts (Figure 5.3) the homogeneous distribution of metal ions (Zn^{2+} and Co^{2+}) and ligand atoms (N) throughout the crystal.

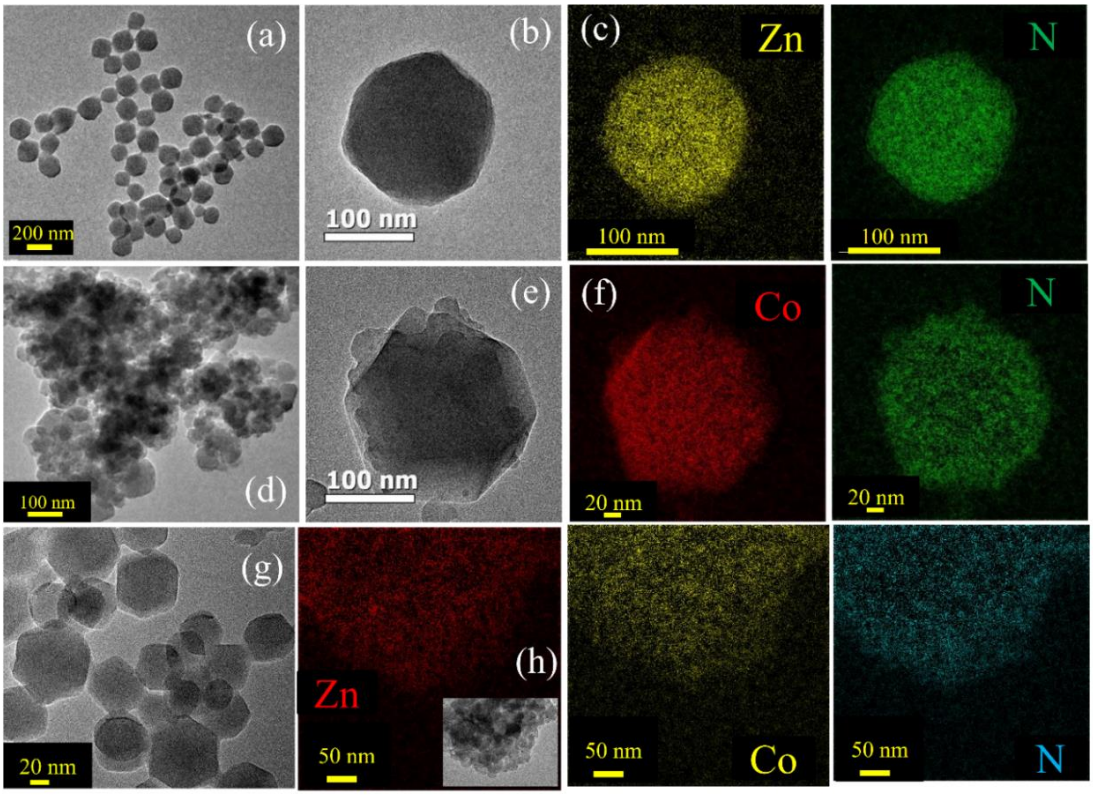

Figure 5.2: *(a) TEM images of ZIF-8 nanoparticles, (b) TEM image of single nanoparticle, (c) EFTEM compositional analysis of ZIF-8 nanoparticles. (d) TEM images of ZIF-67 nanoparticles, (e) TEM image of single nanoparticle, (f) EFTEM compositional analysis of ZIF-67 nanoparticles. (g) TEM images of $Zn_{50}Co_{50}$-ZIF nanoparticles, (h) EFTEM compositional analysis of $Zn_{50}Co_{50}$-ZIF nanoparticles.*

Quantitative analysis of Zn and Co K shell maps collected using the energy dispersive X-ray (EDX) elemental mapping analysis (data not shown) depicts

that the weight percentages of Zn and Co are 11.8% and 10.73% respectively. The observation suggests the similarity between the ratio of Co and Zn used in the synthesis with the metal loaded within the crystal, indicating the formation of actual $Zn_{50}Co_{50}$-ZIF crystals.

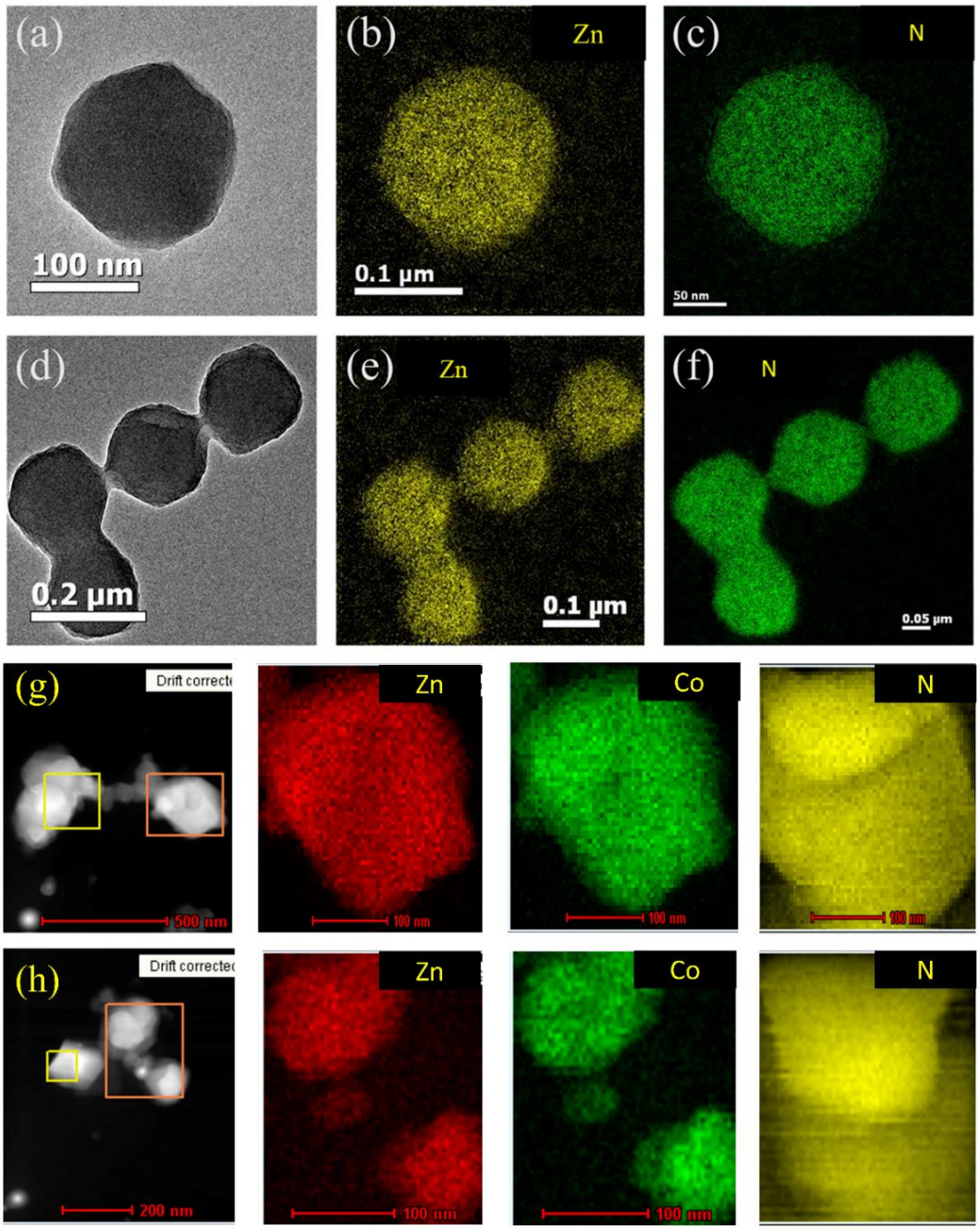

Figure 5.3: *(a) TEM image of single ZIF-8 nanoparticle and (b-c) EFTEM compositional analysis of ZIF-8 nanoparticles. (d) TEM images of ZIF-8 nanoparticles and (e-f) EFTEM compositional analysis of ZIF-8 nanoparticles. (g-h) EFTEM compositional analysis of* $Zn_{50}Co_{50}$*-ZIF nanoparticles.*

After the structural characterizations, the optical absorption spectra of the ZIF systems are evaluated. The absorption spectrum of ZIF-8 is located in the UV region and is virtually featureless in the visible region. ZIF-67 attributes absorption maxima at 588 nm with two shoulder peaks at 565 nm and 537 nm (Figure 5.4a).

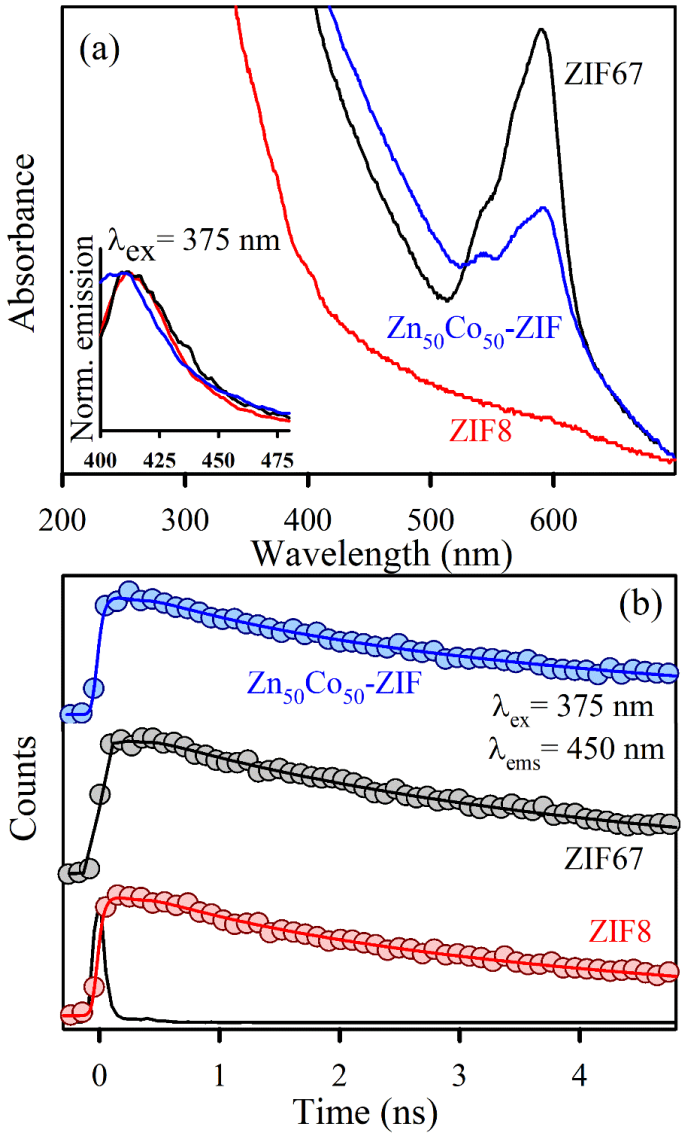

Figure 5.4: *(a) UV-visible absorption spectra of ZIF-8 (red), ZIF-67 (black) and $Zn_{50}Co_{50}$-ZIF (blue). Inset shows the corresponding normalized emission spectra upon excitation at 375 nm. (b) Picosecond resolved fluorescence transients of ZIF-8 (red), ZIF-67 (black) and $Zn_{50}Co_{50}$-ZIF (blue) collected at 450 nm upon excitation at 375 nm.*

These absorption characteristics generate due to the higher-lying [4A2(F) to 4T1(P)] d-d ligand field transitions [47]. The observation also suggests the presence of Co^{2+} in a tetrahedral environment. Following the mixed metal ZIF,

the absorption characteristics are like that of ZIF-67 with a slight red shift in the peak position. The main absorption maximum is at 593 nm with shouldered at 570 nm and 540 nm. All the ZIF systems show broad absorption characteristics in < 400 nm region due to the presence of ligand to metal charge transfer (LMCT) processes. Although the mixed metal ZIF is isostructural with that of ZIF-67, it possesses decreased absorption of Co d−d transitions owing to the dilution of the Co^{2+} chromophores by the non-absorbing Zn^{2+} ions [48]. The evaluation of photoluminescence property of the ZIF systems suggests that all three ZIFs provide an emission maximum of around 450 nm upon excitation at 375 nm (lower inset of Figure 5.4a). The emission band arises mainly due to the association of the linker with the coordinating metal ions and remains at the same position for various metal ions i.e. Zn^{2+} (d^{10}) or Co^{2+} (d^7) [49]. We then performed the excited state photoluminescence experiments to unravel the charge transfer process. The fluorescence decay profiles for ZIF-8, ZIF-67 and $Zn_{50}Co_{50}$-ZIF were obtained upon photoexcitation at 375 nm in ethanol and monitored at 450 nm as shown in Figure 5.4b. The time profile of the fluorescence decay at 450 nm for ZIF-8, ZIF-67 and $Zn_{50}Co_{50}$-ZIF showed bi-exponential decay, with a faster component of ~0.8 ns and a slower component of 4 ns. The lifetime components of the transients are represented in Table 5.1.

Table 5.1: *Picosecond-resolved fluorescence transient lifetime. The emission (monitored at 450 nm) was detected with 375 nm laser excitation. Numbers in parentheses indicate relative contributions.*

System	τ_1 (ps)	τ_2 (ps)	τ_3 (ps)
ZIF-8	847 (17%)	4462 (83%)	3847
ZIF-67	730 (7%)	4212 (93%)	3968
$Zn_{50}Co_{50}$-ZIF	791 (17%)	4440 (83%)	3819

As evident from Table 5.1, time components appear to be similar in all the fluorescence transients indicating superior involvement of ligand for the emission characteristics. The thermal behaviour of the ZIFs is examined *via* thermogravimetric analysis (TGA). Figure 5.5a shows the thermogravimetric

(TG) curves of ZIF-8, ZIF-67 and $Zn_{50}Co_{50}$-ZIF implementing the increasing temperature method. The first weight loss of ZIF-67 occurs from 100°C to 200°C due to the disappearance of guest molecules as well as gas molecules from the cavities. Subsequently, a more weight loss of ZIF-67 occurred in the range of 300 - 450 °C, which could be imposed to the putrefaction of the overall crystal structure.

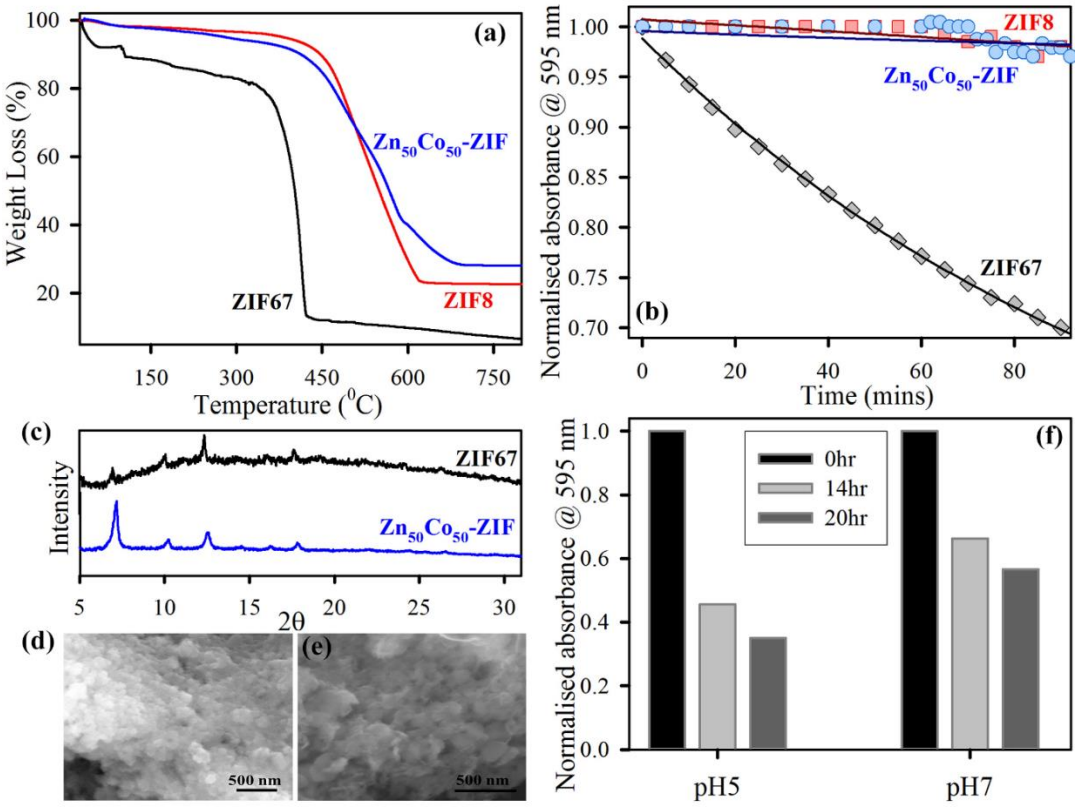

Figure 5.5: *(a) Thermogravimetric profile of ZIF-8 (red), ZIF-67 (black) and $Zn_{50}Co_{50}$-ZIF (blue) monitored under N_2 flow. (b) Aqueous stability of ZIF-8 (red), ZIF-67 (black) and $Zn_{50}Co_{50}$-ZIF (blue) monitored using absorption at 595 nm for 90 minutes time frame. (c) XRD pattern of ZIF-67 (black) and $Zn_{50}Co_{50}$-ZIF (blue) after keeping in water for 10 days at room temperature. SEM images of (d) ZIF-67 and (e) $Zn_{50}Co_{50}$-ZIF, after keeping in water for 10 days at room temperature. (f) Dissolution pattern of $Zn_{50}Co_{50}$-ZIF at two different pH buffer solutions (pH = 5 and 7) over different time intervals as 0 hr (black), 14 hr (light grey), 20 hr (dark grey).*

For ZIF-8 sample, an unchanging weight loss profile is reached with respect to temperatures up to 450 °C, upon which effective weight loss occurs with respect to temperature and suggests the onset of impermanence temperature of the ZIF-8 nanoparticles. After reaching either rottenness temperature, it indicates a steep reduction in weight analogous to a downfall of the ZIF-8 structure and carbonization under extreme thermal stress [50]. The bimetallic ZIF depicts

similar thermal behaviour with ZIF-8 system. There is only one step weight loss associated which is due to the decomposition of the organic linker. It has been observed that $Zn_{50}Co_{50}$-ZIF is quite stable and begins to decompose at 450°C.

The observation suggests that the incorporation of Zn(II) in ZIF-67 crystal improves its thermal stability probably due to that Zn(II) ion has a stronger coordination capability to 2-methylimidazolate than Co(II) ion [51]. As the mixed metallic $Zn_{50}Co_{50}$-ZIF nanoparticles show improvement in thermal stability, so we have assessed its aqueous stability in short time frame as well as in long term. Figure 5.5b shows the change in absorbance at 595 nm (main peak of ZIF systems) with increasing time. It has been observed that ZIF-8 is very stable without unaltered absorbance value after 90 minutes, but ZIF-67 shows ~30% decrease in absorbance value. This suggests that ZIF-67 is not stable in an aqueous environment owing to the spontaneous hydrolysis of ZIF-67 due to breaking of weak Co-Imidazolate bond. $Zn_{50}Co_{50}$-ZIF shows typical stability in water with almost no change in absorbance value at 595 nm. The improved water stability may arise due to lesser possibility of crystal hydrolysis as the Zn-imidazolate bond is much stronger. Further, the long-term water stability of the systems is analyzed using XRD and SEM analysis. XRD pattern of ZIF-67 shows complete perturbation of crystal structure after 10 days of water exposure, whereas the XRD signals remain unchanged for the $Zn_{50}Co_{50}$-ZIF under the same condition (Figure 5.5c). The SEM images of $Zn_{50}Co_{50}$-ZIF and ZIF-67 after 10 days of water exposure are shown in Figures 5.5d and 5.5e respectively. The SEM images also confirm the total structural destruction of ZIF-67 upon long term water exposure which gets improved in case of $Zn_{50}Co_{50}$-ZIF systems [47]. The thermally stable and water steady $Zn_{50}Co_{50}$-ZIF nanoparticles are finally evaluated for their pH-responsive deposition nature. The decrease in the absorbance at 595 nm corresponds to the degree of dissolution of $Zn_{50}Co_{50}$-ZIF. Figure 5.5f shows that there is a ~30% increase in dissolution at acidic pH (pH = 5.5) compare to physiological pH (pH = 7.4). The pH-responsive dissolution trend is mainly because ZIF is a porous network assembled by the coordination interactions within ligand (methylimidazole) linkers and metal ions. The acidic

environment nature will protonate methylimidazole (pKa ~ 7.35) which may decrease the coordination interactions and leads to a damaged network [51]. As it has been already reported that the Zn-N bond in ZIF-8 tends to dissociate in acidic pH, so the trend can be observed in the mixed system also. The enhanced stability (both thermal and aqueous), as well as the pH-responsive dissolution of $Zn_{50}Co_{50}$-ZIF indicate its superior potential for various application purposes. We have chosen and analyze its light-induced effectivity as an alternative antimicrobial agent and a photocatalyst.

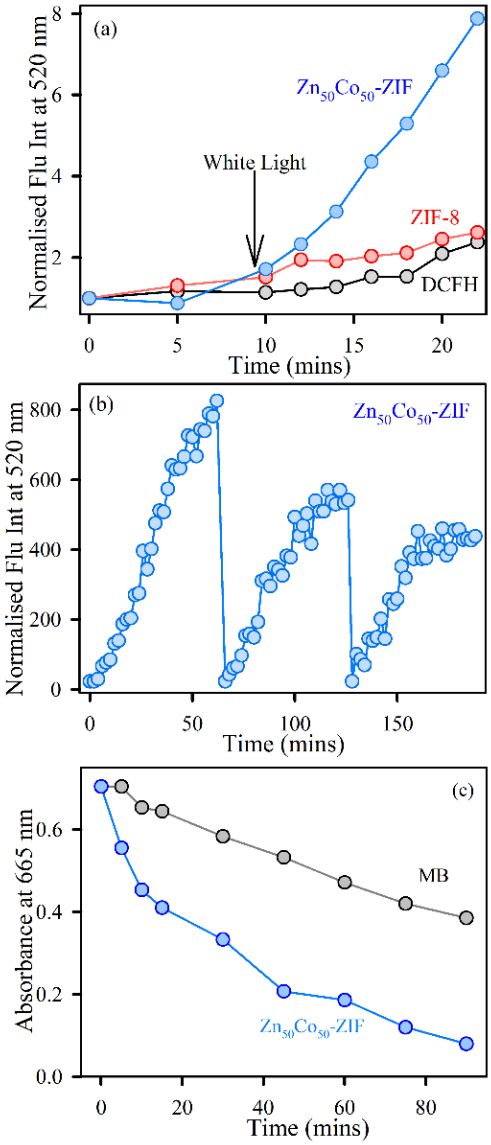

Figure 5.6: *(a) DCFH oxidation with respect to time with addition of ZIF-8 (red), $Zn_{50}Co_{50}$-ZIF (blue) and DCFH control (black) under dark and subsequent white-light irradiation. (b) Recyclability of ROS generation by $Zn_{50}Co_{50}$-ZIF under white light irradiation monitored by DCF fluorescence at 520 nm. (c) Kinetics of methylene blue degradation under white light illumination (control: grey, $Zn_{50}Co_{50}$-ZIF: blue).*

We have evaluated the photoinduced reactive oxygen species generation by $Zn_{50}Co_{50}$-ZIF as the sample possesses broad absorption characteristics, as well as some recent reports, suggest there exists a stable higher energy state in ZIF-67 which can generate reactive species. The increase of DCF emission upon oxidation of DCFH by ROS has been monitored to detect the amount of ROS. $Zn_{50}Co_{50}$-ZIF nanoparticle shows 2.5 times more ROS generation efficiency compare to ZIF-8 under white light illuminated conditions as depicted in Figure 5.6a. The ROS generation capability is also recyclable up to three consecutive cycles (Figure 5.6b). The fitted curve with the exponential rise equation depicts that rate constant for 1st cycle is 186 minutes. Thereafter rate constants for 2nd and 3rd cycles are 48 minutes and 40 minutes respectively. As depicted by transient absorption spectroscopy, there exists a long-lived intermediate excited state in ZIF-67 systems [47]. Thus, we have predicted that mixed ZIF also possesses such stable excited electronic states which contribute to ROS formation ability.

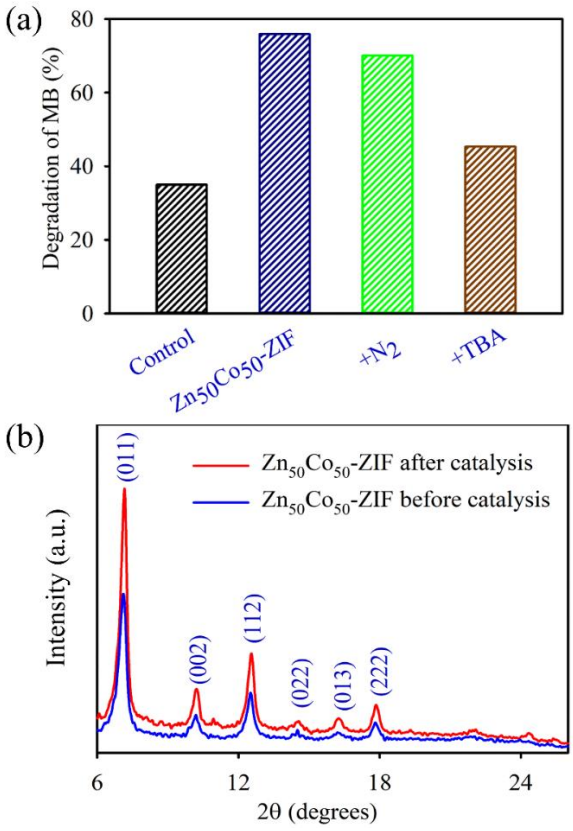

Figure 5.7: *(a) Effect of N_2 and TBA on the photocatalytic activity of $Zn_{50}Co_{50}$-ZIF. (b) XRD experiment of $Zn_{50}Co_{50}$-ZIF before photocatalysis (blue) and after photocatalysis (red).*

We have also performed photocatalysis of model pollutant MB to check the environmental aspect of the mixed ZIF system. Figure 5.6c shows the kinetics of degradation of MB that depicts 75% degradation in 90 minutes. The reactive oxygen species such as ·OH and O_2· are generated in the photocatalytic oxidation process.

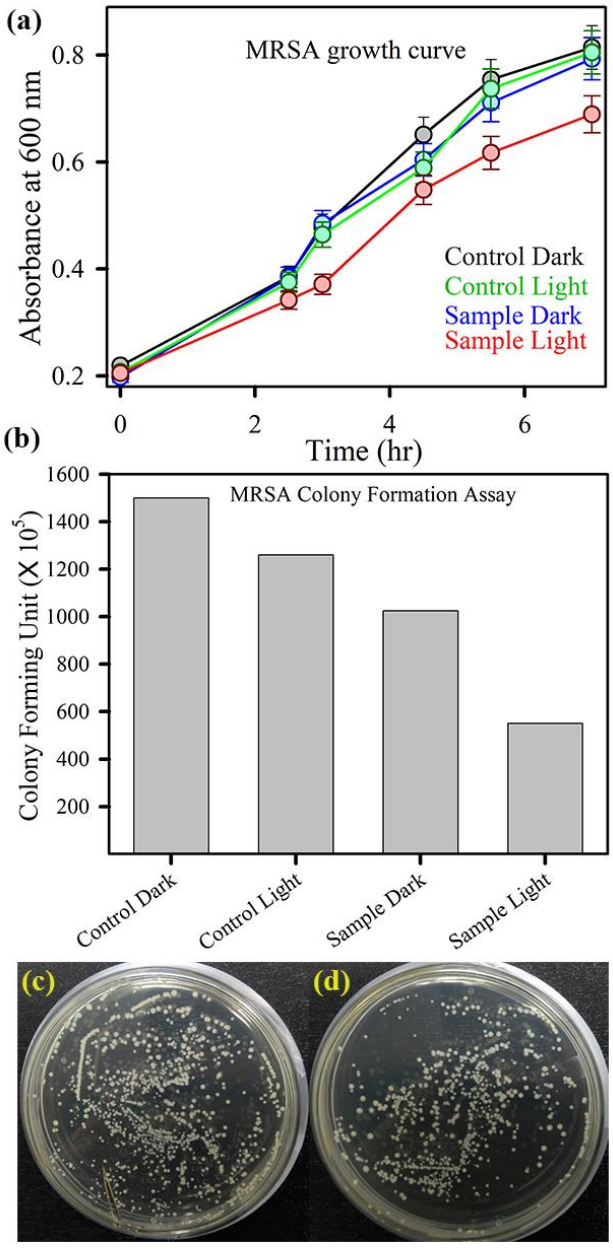

Figure 5.8: *(a) Optical density measurement for Methicillin resistant S. aureus grown in the presence of $Zn_{50}Co_{50}$-ZIF under dark (blue) and white light (red) (control dark is black, and control light is green curve). The error bars represent the standard deviation of three independent measurements. The lines connecting the experimental points are for visual aid. (b) Bacterial viability after treatment with $Zn_{50}Co_{50}$-ZIF in the presence and absence of white light irradiation. (c) shows images of MRSA plates treated with $Zn_{50}Co_{50}$-ZIF, before (left) and after (right) white light irradiation.*

Hence, the effects of radical scavengers on the photo degradation of MB were performed to unravel the reaction process. The scavenger of ·OH, TBA (Tertiary butyl alcohol) was introduced. The degradation efficiency of $Zn_{50}Co_{50}$-ZIF photocatalyst for MB is reduced to 30% after adding TBA and decreased to 5% after adding N_2. Therefore, It can be seen that ·OH has a significant role in the photocatalytic oxidation process of MB, whereas O_2· has a slight effect on this mechanism. We have depicted in Figure 6.7a. Apart from that, in order to confirm the metal leaching during photocatalysis, we performed colorimetric test and EDAX test after photocatalysis of filtered liquid solutions. Also, the XRD experiment of $Zn_{50}Co_{50}$-ZIF has been performed before and after photocatalysis. The XRD peaks of normal $Zn_{50}Co_{50}$-ZIF are exactly similar to the XRD peaks of $Zn_{50}Co_{50}$-ZIF after photocatalysis as shown in Figure 5.7b. The above tests sufficiently justified our conclusion that metal leaching is not happening during photocatalysis.

Finally, we have evaluated the antibacterial action of $Zn_{50}Co_{50}$-ZIF using clinically relevant drug-resistant bacterial strain gram-positive methicillin-resistant *Staphylococcus aureus* (MRSA). Figure 5.8a shows the MRSA growth curve upon treatment with $Zn_{50}Co_{50}$-ZIF. The effect of $Zn_{50}Co_{50}$-ZIF on the bacteria-growth kinetics experiment in LB aqueous media showed a typical antibacterial effect in the presence of visible light. Compared to the growth curve of the control MRSA bacteria, the presence of mixed ZIF samples can slow the growth of MRSA. It is reasonable to determine that the executed high and long-term photodynamic antibacterial activity of $Zn_{50}Co_{50}$-ZIF is due to their higher stability than that of ZIF-67. We have also performed the colony formation assay to check the phototoxicity. As shown in Figure 5.8b, it is observed that $Zn_{50}Co_{50}$-ZIF destroys MRSA colonies around 45% more in the presence of light than in the dark condition. Figures 5.8c and 5.8d show the respective images of plates that show the distinct change in the number of colonies after light treatment. The sustained dissolution at acidic pH following release of metal ions and synergistic effects of dual metal ions uptake by the bacterial cells promotes cell death. Overall, the greater water stability and ROS generation employ a new way for

different types of applications of mixed metallic MOF as $Zn_{50}Co_{50}$-ZIF systems like photodynamic therapy, photocatalysis etc.

5.2.2. Nano MOFs as Targeted Drug Delivery Agents to Combat Antibiotic Resistant Bacterial Infections [52]: The chemical structure of rifampicin (RF) is depicted in Figure 5.9a. Figure 5.9b represents the XRD peaks of synthesized ZIF8 and ZIF8-RF. XRD profiles of both ZIF8 and ZIF8-RF show X-ray diffraction peaks at 2θ = 7.2, 10.3, 12.5, and 17.8° corresponding to diffraction planes (011), (002), (112) and (222).

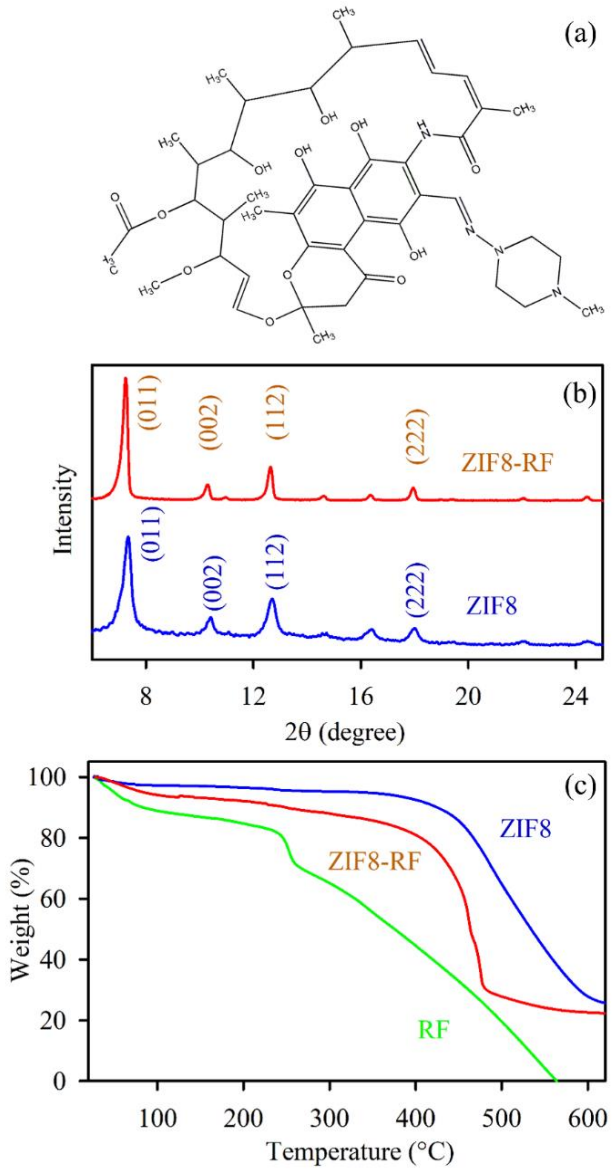

Figure 5.9: *(a) Structure of rifampicin, (b) XRD patterns of ZIF8 (Blue) and ZIF8-RF (Red). (c) Thermogravimetric profile of ZIF8 (blue), RF (green) and ZIF8-RF (red) monitored under N_2 flow.*

The diffraction peaks are in good agreement with reported articles [33] affirming that the synthesized sample has an unadulterated ZIF8 stage before and after the drug encapsulation. In any case, the XRD shape of ZIF8-RF (Figure 5.9b) displays comparative peaks to ZIF8 with minor fluctuation as a tiny widening at lower values of 2θ in ZIF8-RF contrasted with those of ZIF8. The perception shows a reduction in the precise crystal size as indicated by Debye−Scherrer's equation [53]. The RF drug encapsulation into the micro-pores of ZIF8 is answerable for the adjustment in the interplanar distances. The thermal stability of the samples is evaluated utilizing TGA (thermogravimetric analysis), the subsequent bends are shown in Figure 5.9c.

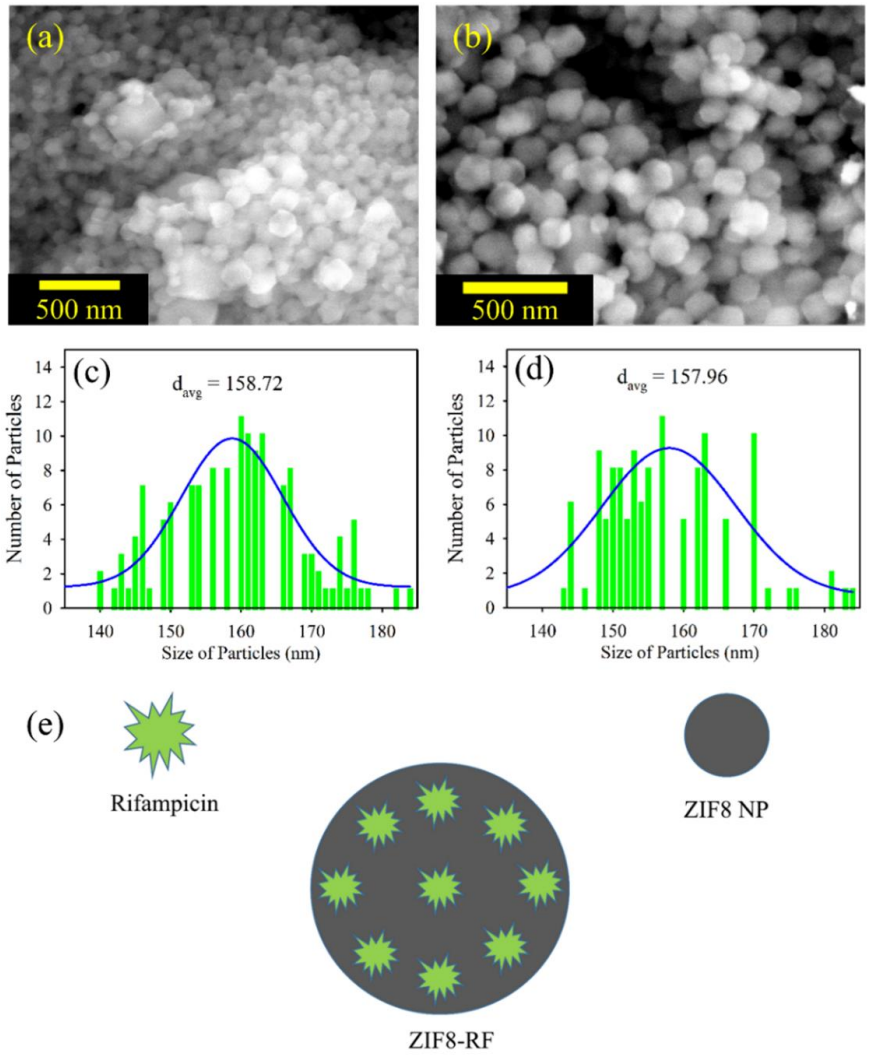

Figure 5.10: *(a) The FESEM image of ZIF8 and (b) FESEM image of ZIF8-RF. (c) Particle distributions of ZIF8 (average particle size 158.72 ± 0.52 nm) and (d) Particle distributions of ZIF8-RF (average particle size 157.96 ± 1.07 nm). (e) Schematic representation of ZIF8-RF nanohybrid.*

The primary weight reduction is around 10% before 450 °C due to the removal of solvent and some guest molecules. A significant difference in around 60% weight reduction after 500 °C suggests the separation of the natural ligand which accounts for the collapse of the system structure. Along these, ZIF8 is thermally steady up to nearly 450 °C. Whereas, for the thermal steadiness of RF, the underlying weight reduction is about 13% happens at around 80 °C, which may resemble the removal of the dissolvable particles. A significant difference in around 40% weight reduction after 250 °C and complete weight reduction happens at around 500 °C as appeared in Figure 5.9c. The thermal stability existence of ZIF8-RF, the underlying weight reduction is about 10% happens at the scope of 300 °C, due to the removal of the dissolvable particles. Moreover, ZIF8-RF starts thermal breakdown at 400 °C, and almost 76% weight reduction happens within 500 °C. The commencement of thermal breakdown at a prior temperature is ascribed to the separation of RF particles encapsulated into the pores of ZIF8 structure [54].

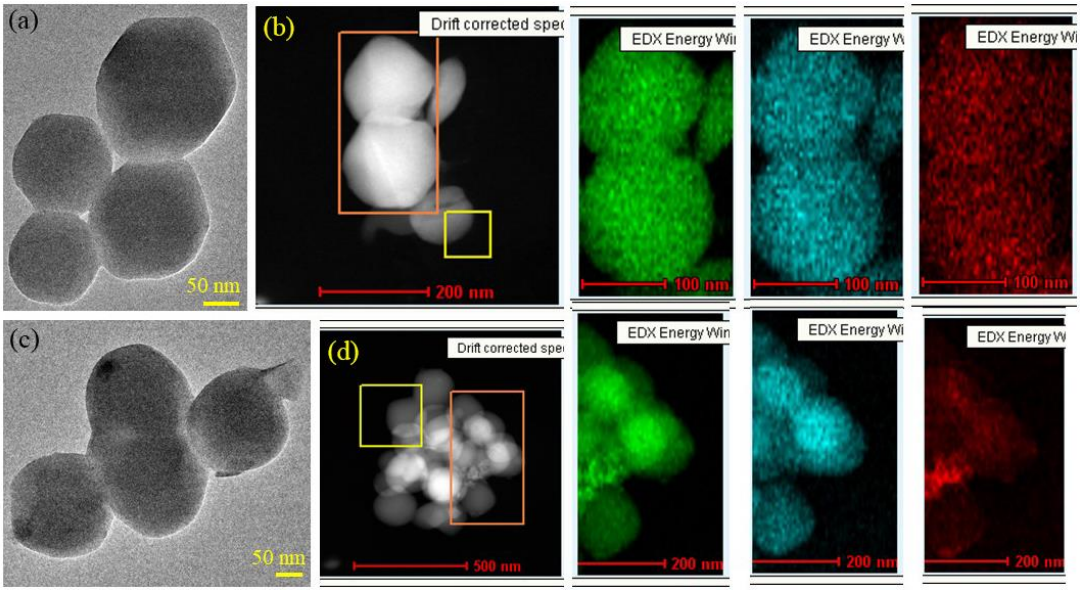

Figure 5.11: *(a) TEM image of ZIF8 and (b) EDAX mapping of ZIF8. (c) TEM image of ZIF8-RF and (d) EDAX mapping of ZIF8-RF. Green dots signify Zn, blue dots signify N, red dots denote O.*

The morphological investigation of the synthesized nanoparticles of ZIF8 and ZIF8-RF is performed using SEM, TEM and EFTEM analysis. SEM image of ZIF8 (Figure 5.10a) represents an unchanging rhombic dodecahedron crystal

structure. The SEM images of ZIF8-RF (Figure 5.10b) outline adjustment in edge thickness contrasted with ZIF8 and shrinkage of crystal size. No clear accumulation or damage in crystal structure is observed by SEM image that confirms RF molecules are encapsulated into the pores or to the outside surface of the synthesized ZIF8 system [55]. Figure 5.10c represents the particle size distribution of ZIF8 (average particle size 158.72 ± 0.52 nm) and Figure 5.10d represents the particle size distribution of ZIF8-RF (average particle size 157.96 ± 1.07 nm). The size of ZIF8 is unchanged before and after drug loading. Figure 5.10e depicts the schematic representation of the formation of ZIF8-RF nanohybrid. The TEM experiment is performed for structural clarification of ZIF8 and ZIF8-RF. It shows uniform size distribution of around 160 nm (Figure 5.11a). The morphology of ZIF8 nanoparticles are depicted as rhombic dodecahedral. To investigate the synthetic structure of ZIF8 frameworks, we have used EFTEM mapping experiment of ZIF8 (Figure 5.11b). The EFTEM mapping of ZIF8 represents the homogeneous distribution of metal (Zn) ions and nitrogen (N) atoms all through the crystal. ZIF8-RF nano-conjugates are also analyzed, Figure 5.11c represents the crystal structures of the ZIF8-RF. It shows a slight reduction in size of the nanoparticle and the EFTEM mapping (Figure 5.11d) shows the homogeneous distribution of ions all through the ZIF8-RF structure. It shows no destruction in the overall crystal structure and depicts that RF molecules are attached into the pores of the ZIF8 structure [55].

To investigate the optical properties of the frameworks, UV-Vis absorption bands are measured for all samples. Figure 5.12a shows the UV-Vis absorption spectra of RF (Green), ZIF8 (Red) and ZIF8-RF (Blue) in DMSO. The characteristic absorbance peaks are observed at 330 nm and 480 nm respectively. After conjugation, the trademark peaks of RF are seen in ZIF8-RF as shown in Figure 5.12a (Blue) which shows the effective complexation among RF and ZIF8 nanoparticles. The room temperature photoluminescence spectra of RF (Green) and ZIF8-RF (Blue) are shown in Figure 5.12b and the room temperature excitation spectra are given in the inset. It is seen that both RF and ZIF8-RF

showed an emission maximum at 425 nm upon excitation at 375 nm. In both cases, after the attachment of RF to the ZIF8 nanoparticles, the steady state emission intensity is decreased which may show the atomic level interaction during the synthesis process. We have investigated Förster Resonance Energy Transfer (FRET) from the ZIF8 surface to the RF because of their significant spectral overlap as appeared in Figure 5.12c. The steady state emission intensity of ZIF8 in the nanohybrid quenched significantly compared to that of free ZIF8, which can be described by the effective nonradiative photo-induced processes from ZIF8 to the RF [56].

Table 5.2: *Picosecond-resolved fluorescence transient lifetime. The emission (monitored at 450 nm) was detected with 375 nm laser excitation. Numbers in parentheses indicate relative contributions.*

System	τ_1 (ps)	τ_2 (ps)	τ_3 (ps)	τ_{avg} (ps)
ZIF8	50 (40%)	608 (40%)	3510 (20%)	965
ZIF8-RF	34 (69%)	320 (20%)	2253 (11%)	335

Thus, we propose FRET from the donor of ZIF8 nanoparticles to RF, the acceptor [57]. The fluorescence decay of the ZIF8 in the presence and absence of the acceptor RF are depicted in Figure 5.12d, upon excitation with 375 nm laser and collected at 450 nm. Detailed information on the fitting parameters of the fluorescence decay is presented in Table 5.2. From FRET formulations, the separation between the donor ZIF8 nanoparticles and acceptor RF is found to be 13.3 Å, and the energy transfer efficiency is calculated to be 65%. The FRET separations confirm the vicinity of the RF to the ZIF8 [57]. From that point, the time-dependent drug release profile experiment of ZIF8-RF is performed at two distinct pH conditions. The drug release profile of ZIF8-RF measured up to 8 hours for the time interval of 2 hours as shown in Figure 5.13a. It is found that there is a significant RF release (69%) with respect to control ZIF8. It has to be noted that if a drug is not been released for a longer period of time (between 5 and 12 h after the administration of a single dose) may be excreted from our body

[58]. As the higher metabolic degrees due to anaerobic fermentation, microbial diseases regularly have acidic situations [59], ZIF8-RF is anticipated to be invested more in the diseased site than ordinary tissues. These outcomes demonstrate that ZIF8-RF carries on as pH-responsive treatment, as the Zn−N coordination in ZIF8 dissociates at pH ~5.0. The Zn−N dissociation makes the pH-responsive drug release and due to this reason, ZIF8 is ideal for targeting bacterial diseases [33, 60].

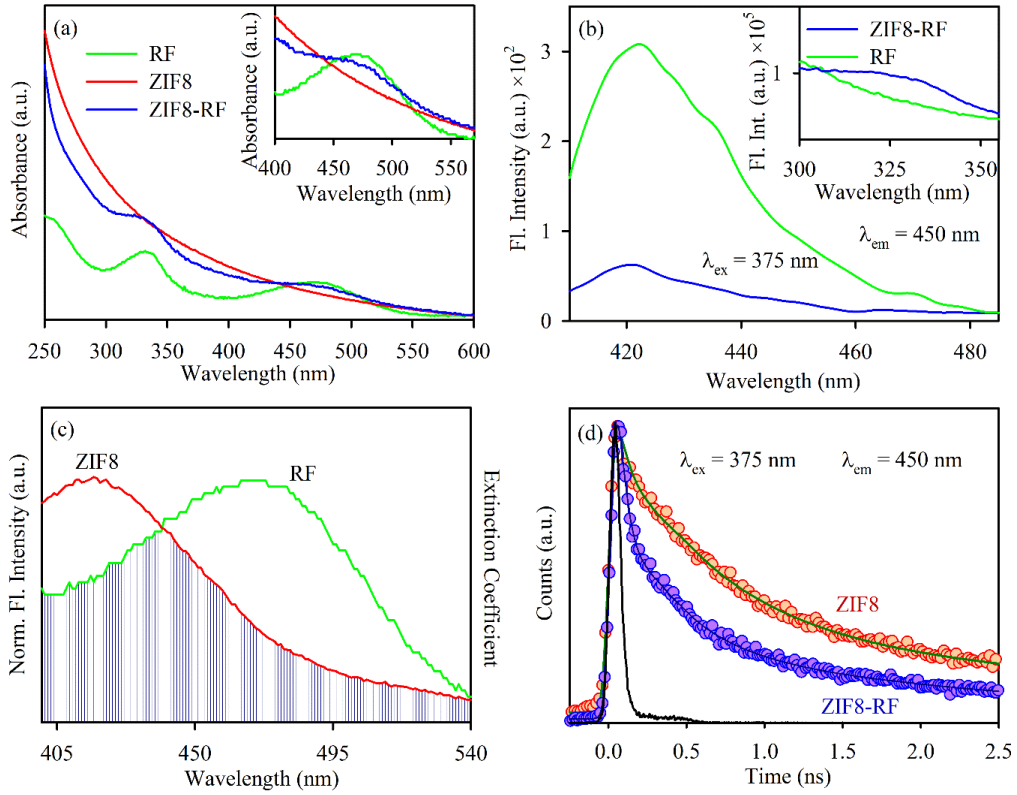

Figure 5.12: *(a) UV-Visible absorbance of ZIF8-RF (Blue), RF (Green) and ZIF8 (Red). (b) Room-temperature PL spectra (excitation at 375 nm) of RF (Green) and ZIF8-RF (Blue). Inset shows steady state excitation spectra of RF (Green) and ZIF8-RF (Blue) at 450 nm. (c) Spectral overlap of ZIF8 (donor) and RF (acceptor). (d) The picosecond resolved fluorescence transient of ZIF8-RF (Blue), RF (Green) and ZIF8 (Red). The excitation wavelength was 375 nm and the collection wavelength was 450 nm.*

Scheme 5.1 depicts the schematic representation of nano MOFs as targeted drug delivery agents to combat antibiotic-resistant bacterial infections. The RF drug loading capacity (DLC) of ZIF8 is calculated by measuring the absorption peak of RF at ~480 nm, which is found to be 42%. Next, we investigated the antimicrobial activity of ZIF8-RF toward MRSA bacteria. We have performed

control experiments using the same amount of ZIF-8 as that of ZIF8-RF with 3 hr incubation time. The pH of LB culture medium reduces with bacterial growth as the cell density increases [61].

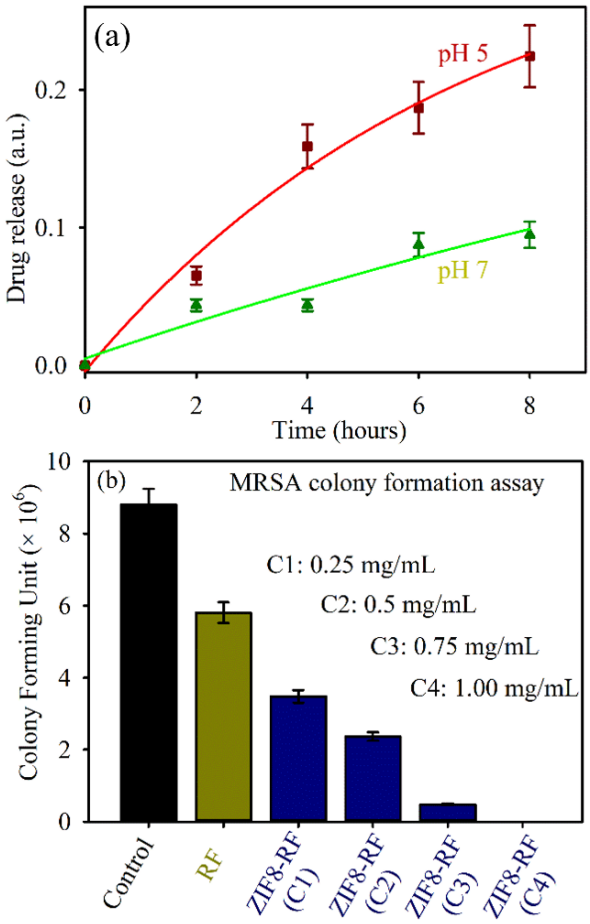

Figure 5.13: *(a) Drug release nature of ZIF8-RF at two different pH conditions. (b) Dose-dependent antibacterial effect of ZIF8-RF at varying concentrations on methicillin-resistant S. aureus.*

The experiments for variable concentrations of ZIF8-RF are analyzed as appeared in Figure 5.13b. For RF (green) treated samples, an extremely less bacterial executing impact is seen. The samples are treated with four different concentrations (C1: 0.25 mg/mL sample, C2: 0.50 mg/mL sample, C3: 0.75 mg/mL sample and C4: 1.00 mg/mL) of ZIF8-RF. The visual distinction in the number of MRSA bacteria has been occurred after treated with ZIF8-RF nano-conjugate. The highest antibacterial impact is found to be ~96% colony reduction for C3 concentration of ZIF8-RF and the MIC is found to be 1 mg/mL (C4). ZIF-8 has not provided any significant change in a number of bacterial colonies

compared to the untreated MRSA. This effect suggests that the delivery of RF plays a significant role in the antibacterial effect of ZIF8-RF composite. Thus, we anticipated the lower pH condition due to bacterial growth, promote the loosening of bonds in porous ZIF8 and consequently improves the delivery of RF.

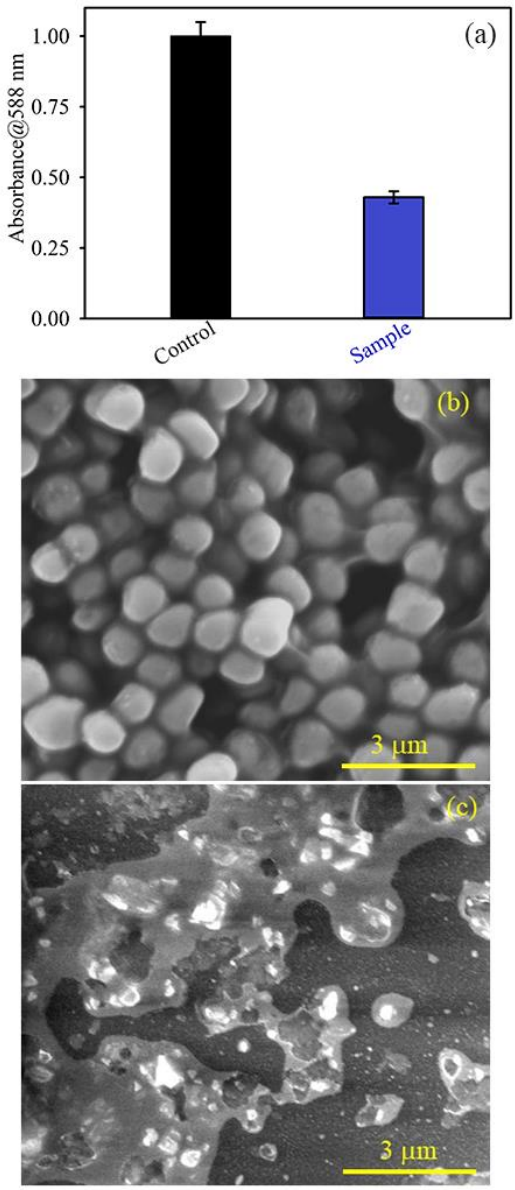

Figure 5.14: *(a) Antibiofilm effects of ZIF8-RF on the MRSA biofilm monitored by the adhesion efficiency of biomass through the crystal violet staining assay. Field emission gun SEM images of (b) MRSA biofilms and (c) MRSA biofilms after ZIF-RF-treated samples. Scale bar is 3 µm.*

The extraordinary antimicrobial viability of ZIF8-RF inspires us to investigate the antibiofilm ability of ZIF8-RF nano-MOF. Biofilms are infectious arrangements of free living microbials connected to a surface or with one another

using EPS (extra polymeric substance), a common organic drug-resistant [62]. To build up that MRSA 1692 can form biofilms, we first accomplished a CV assay on overnight grown bacteria. The CV-stained sample has been stored on the sides of the developed MRSA biofilm. The investigation of the optical density at 588 nm (Figure 5.14a) of solubilized crystal violet stain helped us to observe the effect of ZIF8-RF nano-MOF on MRSA bacteria.

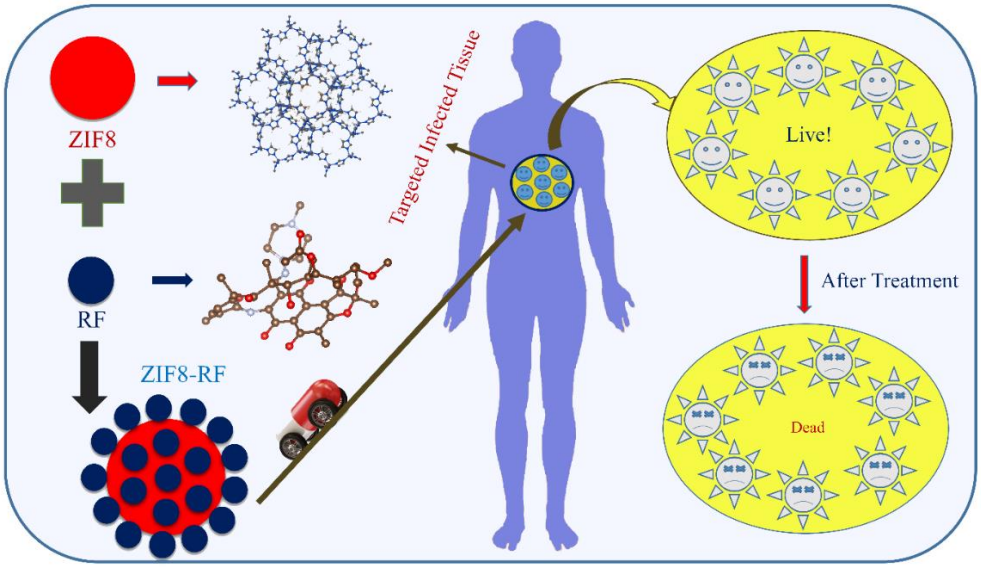

Scheme 5.1: *Schematic representation of nano MOFs as targeted drug delivery agents to combat antibiotic-resistant bacterial infections.*

The intrinsic acidic condition of biofilms encourages us to do further annihilation activity by ZIF8-RF on MRSA bacteria. The morphological changes after treatment of the biofilms are exhibited by SEM images as shown in Figures 5.14b and 5.14c. It shows a drastic change in the MRSA biofilms after being treated with ZIF8-RF nano-MOFs. These observations confirm that ZIF8-RF is exceptionally successful against MRSA bacterial infections. The anti-bacterial effect by ZIF8-RF using bioanalytical techniques is predictable to deliver momentous real-life applicability of the fabricated nano-MOFs.

5.3. Conclusion:

In summary, our work employs a synthesis of novel mixed metal zeolitic imidazolate framework to enhance the applicability of MOF-based systems. The

synthesis follows a solution phase strategy and an equal molar ratio of Zn and Co metal ions are incorporated within the framework using imidazolate as the linker. The $Zn_{50}Co_{50}$-ZIF nanocrystals have been structurally characterized using XRD and TEM. Energy filtered mapping of the crystal suggests homogeneous distribution of Zn and Co ions. The optical absorption spectra confirm that the incorporation of Co improves the visible light absorption property. The photoluminescence analysis suggests that the emission peak at 450 nm in the ZIF system mainly originated from the ligand part and the excited state lifetime is independent of the metal characteristics. The mixed metal shows enhanced thermal stability, water stability and pH-responsive dissolution characteristics. The reason behind the improvement of the properties is mainly the synergistic effect between the two metal ions. Zn is mainly responsible for stability whereas Co improves the activity. The generation of photoinduced reactive oxygen species (ROS) by $Zn_{50}Co_{50}$-ZIF under white light illumination is monitored. The ROS generation is found to be recyclable. $Zn_{50}Co_{50}$-ZIF depicts antibacterial photodynamic therapeutic activity towards drug-resistant bacterial strains. It can also degrade model pollutant MB under white light illumination.

Moreover, the synthesized nanohybrid (ZIF8-RF), drug molecules encapsulated into the well-characterized porous structure of ZIF8, prevents the self-aggregation property of RF. ZIF8-RF nano binding shows FRET from ZIF8 to RF that confirm the proximity of the RF to the ZIF8 with molecular resolution. The immense impact of ZIF8-RF toward MRSA bacteria at particularly lower concentrations proposes its uniqueness and possible outcomes for real applications. The overall investigation implements, the synthesized nanohybrids can be used as potential biomedicine with great biocidal properties and also as a future light-harvesting material for manifold applications.

References

[1] P. S. Jørgensen, D. Wernli, S. P. Carroll, R. R. Dunn, S. Harbarth, S. A. Levin, A. D. So, M. Schlüter, R. Laxminarayan, Use antimicrobials wisely, *Nature* 537 (2016) 159.

[2] R. Laxminarayan, P. Matsoso, S. Pant, C. Brower, J.-A. Røttingen, K. Klugman, S. Davies, Access to effective antimicrobials: A worldwide challenge, *Lancet* 387 (2016) 168.

[3] A. Gupta, S. Mumtaz, C.-H. Li, I. Hussain, V. M. Rotello, Combatting antibiotic-resistant bacteria using nanomaterials, *Chem. Soc. Rev.* 48 (2019) 415.

[4] L. Wang, C. Hu, L. Shao, The antimicrobial activity of nanoparticles: Present situation and prospects for the future, *Int. J. Nanomedicine* 12 (2017) 1227.

[5] Z. Jiang, N. D. Le, A. Gupta, V. M. Rotello, Cell surface-based sensing with metallic nanoparticles, *Chem. Soc. Rev.* 44 (2015) 4264.

[6] H. Gu, P. Ho, E. Tong, L. Wang, B. Xu, Presenting vancomycin on nanoparticles to enhance antimicrobial activities, *Nano Lett.* 3 (2003) 1261.

[7] H. Gu, P.-L. Ho, K. W. Tsang, L. Wang, B. Xu, Using biofunctional magnetic nanoparticles to capture vancomycin-resistant enterococci and other gram-positive bacteria at ultralow concentration, *J. Am. Chem. Soc.* 125 (2003) 15702.

[8] A. M. Fayaz, K. Balaji, M. Girilal, R. Yadav, P. T. Kalaichelvan, R. Venketesan, Biogenic synthesis of silver nanoparticles and their synergistic effect with antibiotics: A study against gram-positive and gram-negative bacteria, *Nanomed.: Nanotechnol. Biol. Med.* 6 (2010) 103.

[9] V. Sambhy, M. M. MacBride, B. R. Peterson, A. Sen, Silver bromide nanoparticle/polymer composites: Dual action tunable antimicrobial materials, *J. Am. Chem. Soc.* 128 (2006) 9798.

[10] E. Katz, I. Willner, Integrated nanoparticle–biomolecule hybrid systems: Synthesis, properties, and applications, *Angew. Chem.* 43 (2004) 6042.

[11] S. Javani, R. Lorca, A. Latorre, C. Flors, A. L. Cortajarena, A. l. Somoza, Antibacterial activity of DNA-stabilized silver nanoclusters tuned by oligonucleotide sequence, *ACS Appl. Mater. Interfaces* 8 (2016) 10147.

[12] L. Chu, H. Gao, T. Cheng, Y. Zhang, J. Liu, F. Huang, C. Yang, L. Shi, J. Liu, A charge-adaptive nanosystem for prolonged and enhanced *in vivo* antibiotic delivery, *Chem. Commun.* 52 (2016) 6265.

[13] A. Gupta, R. F. Landis, V. M. Rotello, Nanoparticle-based antimicrobials: Surface functionality is critical, *F1000Research* 5 (2016) 364.

[14] V. P. Torchilin, Multifunctional, stimuli-sensitive nanoparticulate systems for drug delivery, *Nat. Rev. Drug Discov.* 13 (2014) 813.

[15] R. Y. Pelgrift, A. J. Friedman, Nanotechnology as a therapeutic tool to combat microbial resistance, *Adv. Drug Deliv. Rev.* 65 (2013) 1803.

[16] H. Dong, J. Huang, R. R. Koepsel, P. Ye, A. J. Russell, K. Matyjaszewski, Recyclable antibacterial magnetic nanoparticles grafted with quaternized poly (2-(dimethylamino) ethyl methacrylate) brushes, *Biomacromolecules* 12 (2011) 1305.

[17] D. Bagchi, V. S. Rathnam, P. Lemmens, I. Banerjee, S. K. Pal, NIR-light-active ZnO-based nanohybrids for bacterial biofilm treatment, *ACS omega* 3 (2018) 10877.

[18] D. Bagchi, A. Halder, S. Debnath, P. Saha, S. K. Pal, Exploration of interfacial dynamics in squaraine based nanohybrids for potential photodynamic action, *J. Photochem. Photobiol. A* 380 (2019) 111842.

[19] H.-C. Zhou, J. R. Long, O. M. Yaghi, Introduction to metal–organic frameworks, in, *ACS Publications*, 2012.

[20] Y. Zhao, X.-G. Yang, X.-M. Lu, C.-D. Yang, N.-N. Fan, Z.-T. Yang, L.-Y. Wang, L.-F. Ma, {Zn_6} cluster based metal–organic framework with enhanced room-temperature phosphorescence and optoelectronic performances, *Inorg. Chem.* 58 (2019) 6215.

[21] J. Lee, O. K. Farha, J. Roberts, K. A. Scheidt, S. T. Nguyen, J. T. Hupp, Metal–organic framework materials as catalysts, *Chem. Soc. Rev.* 38 (2009) 1450.

[22] H. Wang, W. Meng, J. Wu, J. Ding, H. Hou, Y. Fan, Crystalline central-metal transformation in metal-organic frameworks, *Coord. Chem. Rev.* 307 (2016) 130.

[23] J.-Q. Liu, Y. Pan, Q. Ding, H. Xu, C. Shi, A. Singh, A. Kumar, A new Zn (II)-based 3D metal–organic framework with uncommon sev topology and its photocatalytic property for the degradation of organic dyes, *CrystEngComm* 21 (2019) 4578.

[24] P. Horcajada, T. Chalati, C. Serre, B. Gillet, C. Sebrie, T. Baati, J. F. Eubank, D. Heurtaux, P. Clayette, C. Kreuz, Porous metal–organic-framework nanoscale carriers as a potential platform for drug delivery and imaging, *Nat. Mater.* 9 (2010) 172.

[25] P. Horcajada, R. Gref, T. Baati, P. K. Allan, G. Maurin, P. Couvreur, G. Ferey, R. E. Morris, C. Serre, Metal–organic frameworks in biomedicine, *Chem. Rev.* 112 (2011) 1232.

[26] B. Mortada, T. A. Matar, A. Sakaya, H. Atallah, Z. Kara Ali, P. Karam, M. Hmadeh, Postmetalated zirconium metal organic frameworks as a highly potent bactericide, *Inorg. Chem.* 56 (2017) 4739.

[27] Y. Han, W. Liu, J. Huang, S. Qiu, H. Zhong, D. Liu, J. Liu, Cyclodextrin-based metal-organic frameworks (CD-MOFs) in pharmaceutics and biomedicine, *Pharmaceutics* 10 (2018) 271.

[28] W. Zhuang, D. Yuan, J. R. Li, Z. Luo, H. C. Zhou, S. Bashir, J. Liu, Highly potent bactericidal activity of porous metal-organic frameworks, *Adv. Healthc. Mater.* 1 (2012) 225.

[29] S. Aguado, J. Quirós, J. Canivet, D. Farrusseng, K. Boltes, R. Rosal, Antimicrobial activity of cobalt imidazolate metal–organic frameworks, *Chemosphere* 113 (2014) 188.

[30] C. M. Courtney, S. M. Goodman, J. A. McDaniel, N. E. Madinger, A. Chatterjee, P. Nagpal, Photoexcited quantum dots for killing multidrug-resistant bacteria, *Nat. Mater.* 15 (2016) 529.

[31] D. Bagchi, S. Dutta, P. Singh, S. Chaudhuri, S. K. Pal, Essential dynamics of an effective phototherapeutic drug in a nanoscopic delivery vehicle: Psoralen in ethosomes for biofilm treatment, *ACS Omega* 2 (2017) 1850.

[32] S. Wang, P. Huang, X. Chen, Stimuli-responsive programmed specific targeting in nanomedicine, *ACS Nano* 10 (2016) 2991.

[33] D. Bagchi, A. Bhattacharya, T. Dutta, S. Nag, D. Wulferding, P. Lemmens, S. K. Pal, Nano MOF entrapping hydrophobic photosensitizer for dual-stimuli-responsive unprecedented therapeutic action against drug-resistant bacteria, *ACS Appl. Bio Mater.* 2 (2019) 1772.

[34] N. Denora, A. Lopedota, M. Perrone, V. Laquintana, R. M. Iacobazzi, A. Milella, E. Fanizza, N. Depalo, A. Cutrignelli, A. Lopalco, Spray-dried mucoadhesives for intravesical drug delivery using N-acetylcysteine-and glutathione-glycol chitosan conjugates, *Acta Biomater.* 43 (2016) 170.

[35] A. Dahan, A. Hoffman, Rationalizing the selection of oral lipid based drug delivery systems by an *in vitro* dynamic lipolysis model for improved oral bioavailability of poorly water soluble drugs, *J. Control. Release* 129 (2008) 1.

[36] T. Dutta, D. Bagchi, S. K. Pal, Bimetallic zeolitic imidazolate framework as an active excipient of curcumin under physiological condition, *Biomed. Phys. Eng. Express.* 4 (2018) 055004.

[37] S. A. Ahmed, D. Bagchi, H. A. Katouah, M. N. Hasan, H. M. Altass, S. K. Pal, Enhanced water stability and photoresponsivity in metal-organic framework (mof): A potential tool to combat drug-resistant bacteria, *Sci. Rep.* 9 (2019) 19372.

[38] X. Liu, Y. Li, Y. Ban, Y. Peng, H. Jin, H. Bux, L. Xu, J. Caro, W. Yang, Improvement of hydrothermal stability of zeolitic imidazolate frameworks, *Chem. Commun.* 49 (2013) 9140.

[39] W. Cai, J. Wang, C. Chu, W. Chen, C. Wu, G. Liu, Metal–organic framework-based stimuli-responsive systems for drug delivery, *Adv. Sci.* 6 (2019) 1801526.

[40] C.-Y. Sun, C. Qin, X.-L. Wang, G.-S. Yang, K.-Z. Shao, Y.-Q. Lan, Z.-M. Su, P. Huang, C.-G. Wang, E.-B. Wang, Zeolitic imidazolate framework-8 as efficient pH-sensitive drug delivery vehicle, *Dalton Trans.* 41 (2012) 6906.

[41] F. Chen, L. Wang, Y. Xing, J. Zhang, Stable photoluminescence of lanthanide complexes in aqueous media through metal-organic frameworks nanoparticles with plugged surface, *J. Colloid Interface Sci.* 527 (2018) 68.

[42] T. Mondol, S. Batabyal, S. K. Pal, Interaction of an antituberculosis drug with nano-sized cationic micelle: Förster resonance energy transfer from dansyl to rifampicin in the microenvironment, *Photochem. Photobiol.* 88 (2012) 328.

[43] J. Cui, L. Wang, Y. Han, W. Liu, Z. Li, Z. Guo, Y. Hu, Z. Chang, Q. Yuan, J. Wang, ZnO nano-cages derived from ZIF-8 with enhanced anti mycobacterium-tuberculosis activities, *J. Alloys Compd.* 766 (2018) 619.

[44] Q. Song, S. Nataraj, M. V. Roussenova, J. C. Tan, D. J. Hughes, W. Li, P. Bourgoin, M. A. Alam, A. K. Cheetham, S. A. Al-Muhtaseb, Zeolitic imidazolate framework (ZIF-8) based polymer nanocomposite membranes for gas separation, *Energy Environ. Sci.* 5 (2012) 8359.

[45] K. Zhou, B. Mousavi, Z. Luo, S. Phatanasri, S. Chaemchuen, F. Verpoort, Characterization and properties of Zn/Co zeolitic imidazolate frameworks *vs.* ZIF-8 and ZIF-67, *J. Mater. Chem. A* 5 (2017) 952.

[46] M. Wang, J. Liu, C. Guo, X. Gao, C. Gong, Y. Wang, B. Liu, X. Li, G. G. Gurzadyan, L. Sun, Metal–organic frameworks (ZIF-67) as efficient cocatalysts for photocatalytic reduction of CO_2: The role of the morphology effect, *J. Mater. Chem. A* 6 (2018) 4768.

[47] B. Pattengale, S. Yang, J. Ludwig, Z. Huang, X. Zhang, J. Huang, Exceptionally long-lived charge separated state in zeolitic imidazolate

framework: Implication for photocatalytic applications, *J. Am. Chem. Soc.* 138 (2016) 8072.

[48] J. K. Zareba, M. Nyk, M. Samoć, Co/ZIF-8 heterometallic nanoparticles: Control of nanocrystal size and properties by a mixed-metal approach, *Cryst. Growth Des.* 16 (2016) 6419.

[49] S. Liu, Z. Xiang, Z. Hu, X. Zheng, D. Cao, Zeolitic imidazolate framework-8 as a luminescent material for the sensing of metal ions and small molecules, *J. Mater. Chem.* 21 (2011) 6649.

[50] J. B. James, Y. Lin, Kinetics of ZIF-8 thermal decomposition in inert, oxidizing, and reducing environments, *J. Phys. Chem. C.* 120 (2016) 14015.

[51] X. Qian, Q. Ren, X. Wu, J. Sun, H. Wu, J. Lei, Enhanced water stability in Zn-doped zeolitic imidazolate framework-67 (ZIF-67) for CO_2 capture applications, *ChemistrySelect* 3 (2018) 657.

[52] S. A. Ahmed, M. N. Hasan, D. Bagchi, H. M. Altass, M. Morad, I. I. Althagafi, A. M. Hameed, A. Sayqal, A. E. R. S. Khder, B. H. Asghar, H. A. Katouah, S. K. Pal, Nano-MOFs as targeted drug delivery agents to combat antibiotic-resistant bacterial infections, *R. Soc. Open Sci.* 7 (2020) 200959.

[53] U. Holzwarth, N. Gibson, The Scherrer equation versus the 'Debye-Scherrer equation', *Nat. Nanotechnol.* 6 (2011) 534.

[54] H. Nabipour, M. H. Sadr, G. R. Bardajee, Synthesis and characterization of nanoscale zeolitic imidazolate frameworks with ciprofloxacin and their applications as antimicrobial agents, *New J. Chem.* 41 (2017) 7364.

[55] A. R. Chowdhuri, B. Das, A. Kumar, S. Tripathy, S. Roy, S. K. Sahu, One-pot synthesis of multifunctional nanoscale metal-organic frameworks as an effective antibacterial agent against multidrug-resistant Staphylococcus aureus, *Nanotechnology* 28 (2017) 095102.

[56] D. Bagchi, T. K. Maji, S. Sardar, P. Lemmens, C. Bhattacharya, D. Karmakar, S. K. Pal, Sensitized ZnO nanorod assemblies to detect heavy metal

contaminated phytomedicines: Spectroscopic and simulation studies, *Phys. Chem. Chem. Phys.* 19 (2017) 2503.

[57] Z. S. Seddigi, S. A. Ahmed, S. Sardar, S. K. Pal, Ultrafast dynamics at the zinc phthalocyanine/zinc oxide nanohybrid interface for efficient solar light harvesting in the near red region, *Sol. Energy Mater. Sol. Cells* 143 (2015) 63.

[58] G. Acocella, V. Pagani, M. Marchetti, G. Baroni, F. Nicolis, Kinetic studies on rifampicin, *Chemotherapy* 16 (1971) 356.

[59] J. L. Smith, The role of gastric acid in preventing foodborne disease and how bacteria overcome acid conditions, *J. Food Prot.* 66 (2003) 1292.

[60] H. Zheng, Y. Zhang, L. Liu, W. Wan, P. Guo, A. M. Nyströ̈m, X. Zou, One-pot synthesis of metal–organic frameworks with encapsulated target molecules and their applications for controlled drug delivery, *J. Am. Chem. Soc.* 138 (2016) 962.

[61] C. Ratzke, J. Gore, Modifying and reacting to the environmental pH can drive bacterial interactions, *PLoS Biol.* 16 (2018) e2004248.

[62] P. S. Stewart, J. W. Costerton, Antibiotic resistance of bacteria in biofilms, *Lancet* 358 (2001) 135.

Chapter 6

A Combined Optical Spectroscopy and Computational Studies on Nanohybrids with Wide Band Semiconductor for Potential Biomedical Applications

6.1. Introduction:

Bacterial infections are one of the most dangerous health problems worldwide that affect almost all age group people [1] that initiate various social and economic complications [2, 3]. Increased infections and outbreaks related to a pathogenic burden, antibiotic infection of bacteria, the emergence of new bacterial mutations, and shortage of applicable vaccines create danger for people's health worldwide, especially in children [4]. These are most generally treated by broad-spectrum antibiotics (Norfloxacin, Ciprofloxacin, Tetracyclin, Meticillin, etc.) [5]. However, they have some limitations like overuse of antibiotics, extended durations of treatment, use of sub-therapeutic dosages, prophylactic use of antibiotics, and misuse of antibiotics for other non-bacterial infections [1, 6, 7]. So it is very much required to develop a new alternative strategy (targeted and stimuli responsive) to overcome bacterial infections.

Implementation of light harvesting nanomaterials (like metallic, inorganic oxide nanoparticles) for numerous targeted biomedical aspects is presently going through a dramatic expansion [8, 9]. In the last few years, photosensitizers (PS) have been broadly used in antibacterial photodynamic therapy (PDT) because of their high molar extinction coefficient, less toxicity, good biocompatibility, etc. [10, 11]. Some reports on their photocatalytic activity are also present [12]. They can generate reactive oxygen species (ROS) from neighboring water and oxygen molecules upon excitation [13]. These ROS are responsible for their antibacterial, antifungal and anticancer activity [14]. However, there are some limitations

associated with photosensitizers that restrict their practical applications [15]. Many PS have poor solubility in polar protic solvents (many dyes undergo aggregation in polar protic solvents), very short circulation time and poor photostability [16, 17]. In order to avoid these limitations for both photosensitizers and inorganic nanoparticles, the formulation of organic-inorganic (unit cell to large crystal) nanohybrid has got key importance in this field [18].

There is a high demand for the development of stimuli responsive nanohybrid just because of multifunction, multiuse and highly effective implementation [19, 20]. Nowadays, nanoparticles are increasingly used to target bacteria and could serve as an alternative to organic antibacterial agents [21, 22]. Efficacy of antibacterial agents may be increased *via* nano-binding which could be effective to obstruct infections in humans and animals as well as to prevent the growth of bacteria in family products [23]. The nanohybrid is likely to keep safety against degradation, develop bioavailability, advancement in intracellular penetration, control delivery of the drug and enhanced efficacy [24-27]. Therefore, the improvement of new antibiotics is necessary to enhance the efficacy. Nonetheless, this kind of attempt has already passed since the late 1980s just because of the relatively low potential recovery on investment and high expenditure on development [28]. Hence, our attention has been focused on newly synthesized, less toxic, low cost and exciting nanoparticle-based light-harvesting hybrid materials with antibacterial activity.

The inappropriate and inconsistent use of these antibacterial agents gives rise to unwholesome or harmful bacteria [29]. Thus, improving novel and light sensitive antibacterial drugs against bacterial strains has become the ultimate demand [30]. The potential toxicology of newly synthesized hybrid materials upon light exposure is mysterious [31]. Such kind of medication could be applied to the affected tissue while surrounding cells remain normal, active and healthy [32]. This requires the drugs or nanohybrid materials to be activated in the targeted organism. Recently, nanotechnology and nanoparticle-based materials

have gained a lot of attention in antibiotics, antimicrobial action against bacteria and more specifically cancer therapy [33]. Therefore, our strategy has been focused on the use of antibiotics as light sensitive moieties. Norfloxacin (NF) has been widely used in the medicinal sector for various diseases including urinary tract infections in chronically catheterized patients [34, 35]. We chose a wide bandgap semiconductor ZnO nanoparticle due to its advantages compared to other nanoparticles such as targeted delivery vehicles, non-toxic, chemically reliable, biodegradable, excellent wide bandgap, greater binding energy (60 MeV), lower cost and abundance in nature [32, 36-38]. We have synthesized NF functionalized nanohybrid using ZnO nanoparticles (~5 nm and ~30 nm) to study the effect of crystal dimension on molecular interactions. We have chosen the fluorescence properties of 5 nm ZnO nanoparticles to confirm the nanohybrid formation and excited state electron transfer dynamics from ZnO to NF. We have used 30 nm ZnO for application purposes as 5 nm ZnO is not stable at room temperature. The newly synthesized nanohybrid has been characterized using various microscopic (HRTEM and XRD) and optical spectroscopic techniques. To represent the optical spectroscopic properties of the systems, we have used UV-visible, steady-state fluorescence and picosecond resolved time correlated single photon counting (TCSPC) studies which demonstrate the efficient electron transfer from NF to ZnO nanoparticle. This enhances the reactive oxygen species (ROS) generation capability of the system. First principles density functional theory (DFT) calculation has been performed using the Vienna Ab initio simulation package (VASP) code to understand the charge separation mechanism of both systems. To explore the electron densities of occupied and unoccupied levels of the ZnO-NF complex, we have investigated the nature of electronic structure for both systems. It is observed that there is a high chance of charge transfer from NF to ZnO which validates the experimental findings. Finally, for the potential applications of the nanohybrid system, *in vitro* bacteria culture has been performed on *E. coli* bacteria. A significant bacterial death has been occurred by the nanohybrid compared to the free NF in the presence of UV light of wavelength 375 nm.

Also, the resistance among several infectious agents to various antimicrobial drugs has originated as a source of a human health threat in the world [39-41]. In each year, more than 35000 deaths have been reported in the United States, in addition, 2.8 million patients have serious illnesses [42, 43]. Some reports conclude 10 million annual deaths will occur from antibiotic-resistant bacteria by 2050 [44] which is more than the deaths initiated by cancer disease. The development of new antibacterial agents is needed to combat bacterial infections as the improvement of antibiotic resistance is predicted to progress more in the upcoming years.

Considering this issue, antimicrobial photodynamic therapy is one of the most encouraging and new approaches to combat bacterial infections [45-48]. This process involves the activation of photosensitizer upon light irradiation to produce ROS which can destroy the infected tissue [49]. In general, the process follows two types of mechanisms (type I and type II) to begin a photochemical course of action. Type I reactions progress through radical production by involving photoinduced triplet state electron transfer processes from photosensitizer to inorganic nanoparticles [50]. In type II, it involves the direct energy transfer process from the triplet excited state of photosensitizer to the ground state of molecular oxygen [51]. However, the chances of happening such a mechanism depend upon the anchoring group present in the photosensitizer as well as the neighbouring environment [52].

Furthermore, the antibacterial efficacy of photosensitizer at the NIR wavelength region (650-900 nm) could contribute more due to higher light penetration into the biological tissue [53-55]. There are numerous advantages of NIR light activated antibacterial applications such as a lesser chance of antibacterial resistance generation due to high light penetration, targeted antibacterial treatment, and negligible side effects for the surrounding healthy cells [55, 56]. However, photosensitizers are mostly hydrophobic that which leads to self-aggregation in aqueous solution. This self-aggregation process is harmful to the efficiency of photodynamic therapy as it reduces the overall ROS production

[57]. In addition to that, cyanine dye such as IR820 has poor photostability as they are degraded by self-generated singlet oxygen under NIR irradiation. Moreover, ineffective delivery of photosensitizer molecules particularly to the infected site leads to demolition action on the neighbouring unaffected tissues.

An encouraging and innovative method to improve the antibacterial activity of photosensitizers is its delivery using nanoparticles into the infected site [58]. Nanomaterials have criteria activated by external stimuli in the bacterial growth environment, preferential for targeted drug delivery [59]. The use of inorganic nanoparticles in biological applications is comparatively new and continuously increasing due to tunable surface properties and ease of functionalization [60]. Nowadays, metal-organic frameworks (MOFs) are considered new kinds of porous frameworks having enormously high porosity, large surface area, and enough pore size to be attached with organic photosensitizers [61-64]. It can easily be functionalized with a huge number of small organic molecules due to its large surface porosity nature [65-67]. In this work, we, aim to fabricate a user-friendly as well as an easy synthetic strategy of nano-MOF which maintains thermal and photostability with ultrahigh drug loading capacity for photo-induced antibacterial applications.

Amongst them, ZIF-8 is a type of MOF made by metal ions Zn^{2+} linked *via* nitrogen atoms of four imidazole rings identically. ZIF-8 nanoparticles have all the properties of MOF with exceptional application in targeted drug delivery under physiological conditions [68-72]. In this work, we have synthesized ZIF-8 nano-MOF having a uniform size of ~50 nm. The ZIF-8 nano-MOFs are functionalized by IR820 a typical cyanine dye. The functionalized ZIF8-IR820 nano-MOFs are characterized using various electron microscopic and optical spectroscopic techniques to confirm the formation of hybrid nanomaterials. It shows improvement in thermal and photostability properties after functionalization. The time-resolved fluorescence transient depicts the excited state charge transfer process from IR820 to ZIF-8 in functionalized nano-MOF. The density of states (DOS) of the hybrid indicates the possibility of ligand-to-

metal charge transfer from IR820 to ZIF-8 and the charge density of the hybrid displays a big charge overlap in the interface of ZIF-8 and IR820. This confirms the mutual charge transfer from IR820 to ZIF-8 in the hybrid system which further supports the experimental findings. It enhanced ROS production capability in a pH-responsive manner upon red light excitation. The antibacterial action of ZIF8-IR820 is investigated against *Staphylococcus hominis* bacteria and it shows efficient NIR-induced antimicrobial activity due to enhanced ROS generation capability. Thus, the study depicts a detailed physical insight into a photosensitizer-encapsulated nano-MOF system which shows efficient NIR light-induced dose-dependent antibacterial activity that would be beneficial for bacterial remediation.

6.2. Results and Discussion:

6.2.1. Wide Bandgap Semiconductor Based Novel Nanohybrid for Potential Antibacterial Activity: Ultrafast Spectroscopy and Computational Studies [73]: Figure 6.1a depicted the structure of NF, it has a carboxylic (-COOH) group which can make bond formation with other material. The powder X-ray Diffraction (XRD) of ZnO nanoparticles displayed many peaks which indicates the presence of many diffraction planes. The XRD patterns of ZnO (blue) and NF-ZnO (red) are depicted in Figure 6.1b. The diffraction peaks are well-indexed using JCPDS Card No. 36-1451, which confirms the wurtzite ZnO. No additional peaks were obtained in the X-ray diffraction patterns which proposed its crystalline impurities. Nanohybrid shows the same nature of diffraction peaks as ZnO, which confirms there is no change of phase during the formation of nanohybrid. The crystalline nature and size of synthesized ~ 5 nm ZnO nanoparticle, ~30 nm ZnO nanoparticle, ~5 nm ZnO-NF nanohybrid and ~30 nm ZnO-NF nanohybrid were analyzed by TEM and HRTEM techniques. Figure 6.1c illustrates the HRTEM image of size ~5 nm ZnO nanoparticles and Figure 6.1d depicts the HRTEM image of synthesized ~5 nm NF functionalized ZnO nanohybrid. Which shows the high crystallinity nature of synthesized ~5 nm ZnO nanoparticles and ~5 nm ZnO nanohybrid. The TEM image (Figure 6.1e) of

nanohybrid shows a sphere-like structure. The overall particle size distribution of nanohybrid is shown in the inset of Figure 6.1e and the average particle size was found to be 29.35 ± 0.68 nm. The inter-planer distance in the lattice fringe was found to be 0.27 nm of a single nanohybrid, which relates to the distance between two (002) planes as shown in Figure 6.1f, depicts the synthesized nanohybrid as polycrystalline [32].

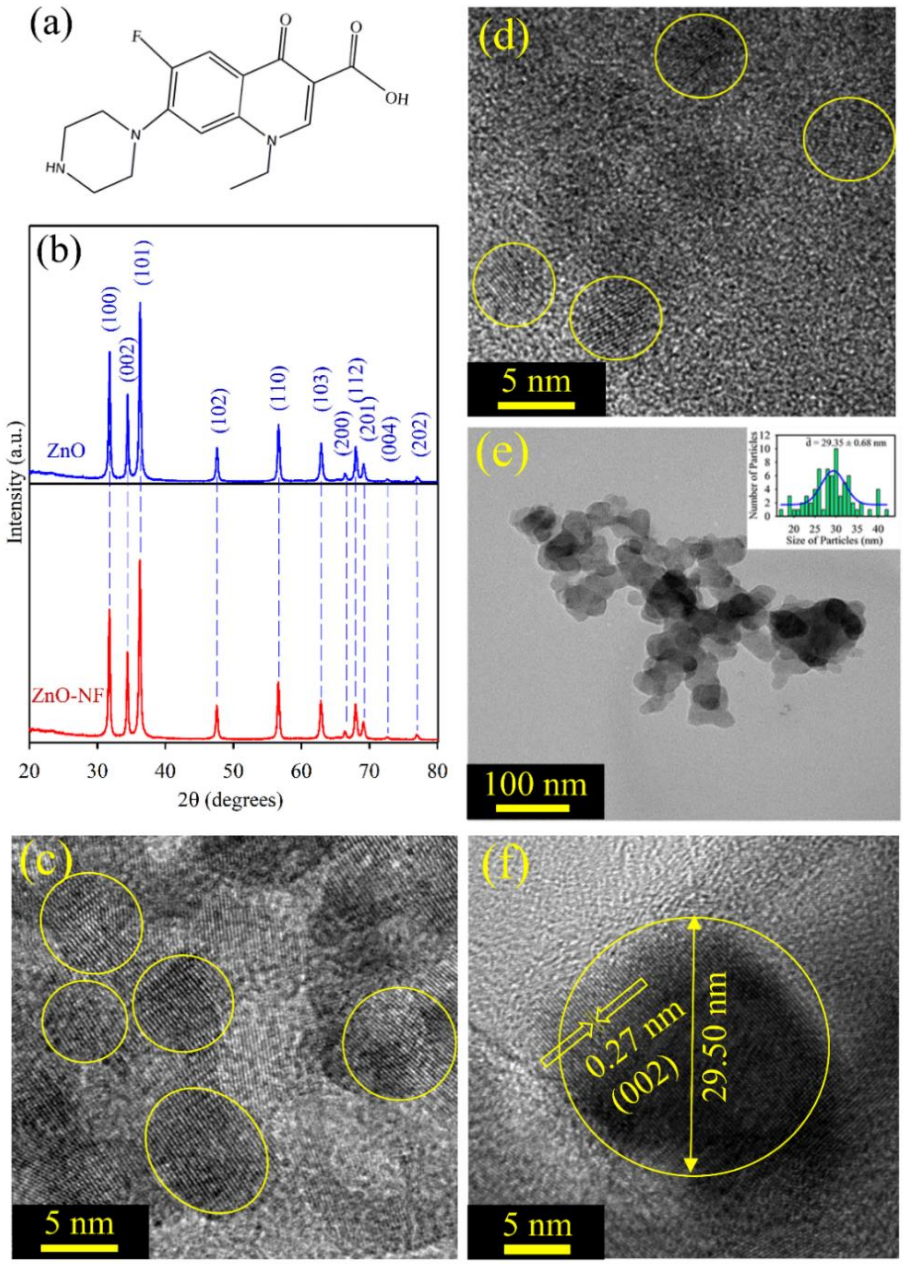

Figure 6.1: *(a) Depicted the structure of norfloxacin (b) XRD patterns of ZnO nanoparticles (Blue) and XRD patterns of ZnO-NF nanohybrid (Red). (c) The HRTEM image of ~5 nm ZnO nanoparticles. (d) The HRTEM image of ~5 nm ZnO-NF nanohybrid. (e) The TEM image of 30 nm ZnO nanohybrid and the inset shows particle distributions (average particle size 29.35±0.68 nm). (f) The HRTEM image of 30 nm ZnO-NF nanohybrid.*

To investigate the optical properties of the systems, UV-Vis absorption spectra were measured for all the samples. Figure 6.2a shows the UV-Vis absorption spectra of NF (Green) and 5 nm ZnO nanoparticle (Blue) in ethanol solvent exhibited the characteristic peaks at 330 nm and 353 nm respectively. After binding 5 nm ZnO nanoparticle to NF, the characteristic peak of NF was seen in nanohybrid with a new peak at 348 nm corresponding to 5nm ZnO nanoparticle, which indicates the sign of complexation between NF and 5 nm ZnO nanoparticles.

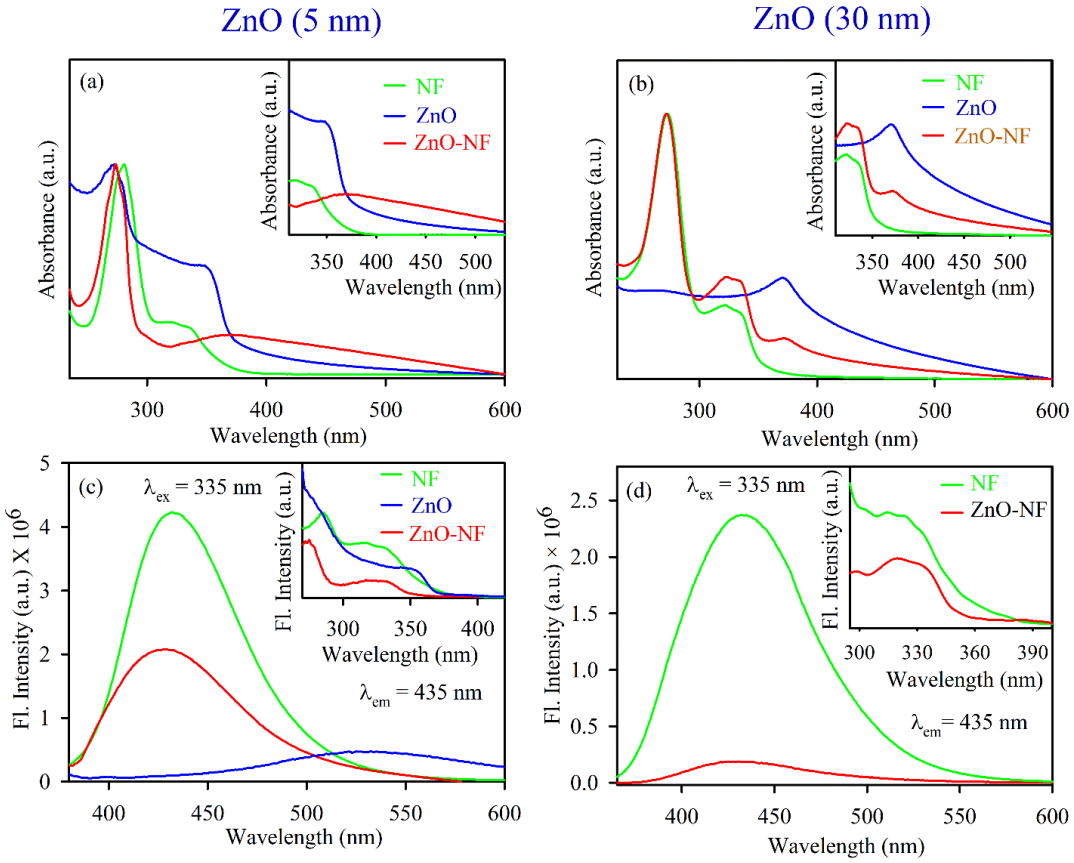

***Figure 6.2**: (a) UV-visible absorbance of 5 nm ZnO nanoparticle (Blue), NF (Green) and 5 nm ZnO-NF nanohybrid (Red), inset shows corresponding absorbance in enlarged wavelength scale. (b) UV-visible absorbance of 30 nm ZnO nanoparticle (Blue), NF (Green) and 30 nm ZnO-NF nanohybrid (Red), inset shows corresponding absorbance in enlarged wavelength scale. (c) Room-temperature PL spectra (excitation at 335 nm) of NF (Green), 5 nm ZnO nanoparticle (Blue) and 5 nm ZnO-NF nanohybrid (Red), inset shows corresponding excitation spectra. (d) Room-temperature PL spectra (excitation at 335 nm) of NF (Green) and 30 nm ZnO-NF nanohybrid (Red), inset shows corresponding excitation spectra.*

Similarly, the absorption of NF (Green) and 30 nm ZnO nanoparticles (Blue) in DMSO, exhibited the characteristic peaks at 330 nm and 370 nm respectively. After binding 30 nm ZnO to NF, the characteristic peak of NF was seen in

nanohybrid (Red) with a new peak at 372 nm corresponding to ZnO nanoparticle as shown in Figure 6.2b, which also indicates the sign of complexation between NF and 30 nm ZnO nanoparticles. The room temperature photoluminescence (PL) spectra of the 5 nm ZnO nanoparticle (blue) in Figure 6.2c shows a large and broad green-yellow emission centered at around 530 nm, which can be attributed to the oxygen vacancy defect states (mostly present at the surface of the nanoparticles) [74]. Here, NF exhibits an emission maximum at 435 nm upon excitation at 335 nm and nanohybrid exhibits (slightly blue shift with respect to NF) emission maxima at 431 nm. The excitation spectra are presented in the inset of Figure 6.2c. On the other hand, 30 nm ZnO has no broad green-yellow room temperature emission centered at around 530 nm due to less oxygen vacancy defects states [75].

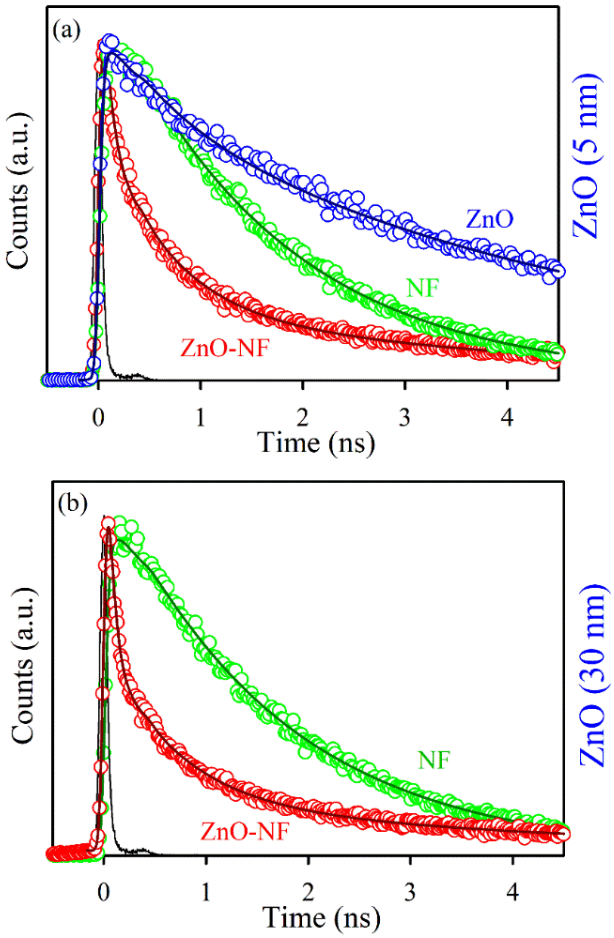

Figure 6.3: *(a) The picosecond-resolved fluorescence transient of 5nm ZnO nanoparticle (Black), NF (Blue) and 5 nm ZnO-NF nanohybrid (Red). The excitation wavelength was 375 nm and the collection wavelength was 440 nm. (b) The picosecond-resolved fluorescence transient of 30 nm ZnO-NF nanohybrid (Red) and NF (Blue).*

The room temperature photoluminescence spectra of NF (Green) and 30 nm ZnO-NF (Red) are shown in Figure 6.2d and the corresponding room temperature excitation spectra are given in the inset. It is observed that both NF and nanohybrid exhibited an emission maximum of 435 nm upon excitation at 335 nm. In both cases, after the attachment of NF to the ZnO nanoparticles, the steady state emission intensity is significantly reduced. This may indicate the molecular level interactions during the synthesis process. The emission quenching in this region may be due to a nonradiative process, which is attributed to charge transfer from the NF to ZnO within the nanohybrid [17]. To understand the electron transfer from NF to ZnO nanoparticles, TCSPC studies have been performed for all the samples. The time resolved fluorescence decay for 5 nm ZnO nanoparticles (Black), free NF and 5 nm ZnO-NF was measured upon excitation with a 375 nm laser and detected at a wavelength of 440 nm as shown in Figure 6.3a. The excited state time resolved decay profile of NF was fitted with exponential decay, the lifetime was found to be 1.6 ns.

Table 6.1: *Picosecond-resolved fluorescence transient lifetime of NF and 30 nm ZnO-NF in DMSO solvent. The emission (monitored at 440 nm) was detected with 375 nm laser excitation. The values in parentheses represent the relative weight percentages of the time components.*

Systems	τ_1 (ns)	τ_2 (ns)	τ_3 (ns)	τ_{avg} (ns)
NF	1.6 (100)	---	---	1.6
ZnO-NF	0.05 (70)	0.7 (22)	3.9 (8)	0.5

The excited state lifetime of NF quenches in nanohybrid with respect to NF. The fitting parameter of the time resolved fluorescence decays are depicted in Table 6.1. On the other hand, 30 nm ZnO has no time resolved fluorescence decay profile due to less oxygen vacancy state, the time resolved fluorescence decays for free NF (Green) and 30 nm ZnO-NF (Red) in the DMSO solvent are measured with a 375 nm laser and emission has been detected at a wavelength of 440 nm as shown in Figure 6.3b. The excited state lifetime of NF quenches in nanohybrid with respect to NF. It has been found that a faster component (50 ps) arises after the attachment of NF on the surface of 30 nm ZnO nanoparticle (Table 6.1) as

well as after the attachment of NF on the surface of 5 nm ZnO nanoparticle (Table 6.2). Here, the potential of energy transfer is eliminated as there is no overlap between NF emission and ZnO absorption spectra. Therefore, a faster component indicates the PET (photoinduced electron transfer) from the highest occupied molecular orbital (HOMO) of NF to the conduction band of the ZnO semiconductor nanoparticles [32]. Thus, the PET interfaced from the HOMO of NF to the CB (conduction band) of ZnO nanoparticle scale down the recombination of electron and hole of the semiconductor. This appreciates the biological antibacterial activity [32], which will be discussed in the later course of the discussion. To investigate the insight of the electron delocalization of occupied and unoccupied levels of the ZnO-NF complex, we have investigated the band decomposed electron densities nature of nanohybrid. It is observed that there is a high possibility of electron transfer from NF to ZnO in the nanohybrid system which validates the experimental findings. Among several different binding modes, bidentate binding of NF through the carboxylic O to the Zn on the nonpolar [$10\bar{1}0$] surface was found to be the most energetically favourable mode of binding.

Table 6.2: *Picosecond-resolved fluorescence transient lifetime of ZnO 5 nm, NF and 5 nm ZnO-NF in ethanol solvent. The emission (monitored at 440 nm) was detected with 375 nm laser excitation. The values in parentheses represent the relative weight percentages of the time components.*

Systems	τ_1 (ns)	τ_2 (ns)	τ_3 (ns)	τ_{avg} (ns)
ZnO	0.6 (23)	4.7 (77)	---	3.7
NF	---	0.9 (46)	2.2 (54)	1.6
ZnO-NF	0.08 (56)	0.6 (31)	4.1 (13)	0.7

The bond distances of Zn and two carboxylic O of the NF are found to be 1.98 Å and 2.01 Å respectively, which is consistent with the computationally estimated covalent bond distances of Zn and O in ZnO (1.98 Å, 1.98 Å, 1.98 Å and 1.99 Å). This indicates the formation of covalent bonds between ZnO and NF. The binding energy of the nanohybrid has been calculated by using the equation

(6.1). The theoretically calculated binding energy of the nanohybrid is found to be -1.9 eV. The negative sign of the binding energy indicates the formation of a stable nanohybrid.

$$E_B = E_{ZnO\text{-}NF} - E_{ZnO} - E_{NF} \tag{6.1}$$

The band decomposed charge density calculations were performed to find out the electronic distribution of the valance band maximum (VBM), and the conduction band minimum (CBM) as shown in Figures 6.2.4a and 6.2.4b respectively. It suggests that in ground state the highest energy electrons remain localized on the O of NF. Given the energy, the electron delocalizes to the CBM of the ZnO nanoparticles, was confirmed by time-resolved fluorescence spectroscopy with 30 nm ZnO nanoparticle. A similar result was observed for the NF complex with $(ZnO)_{12}$ atom cluster as shown in Figures 6.2.4c and 6.2.4d, which validates the experimental findings with 5 nm ZnO nanoparticle.

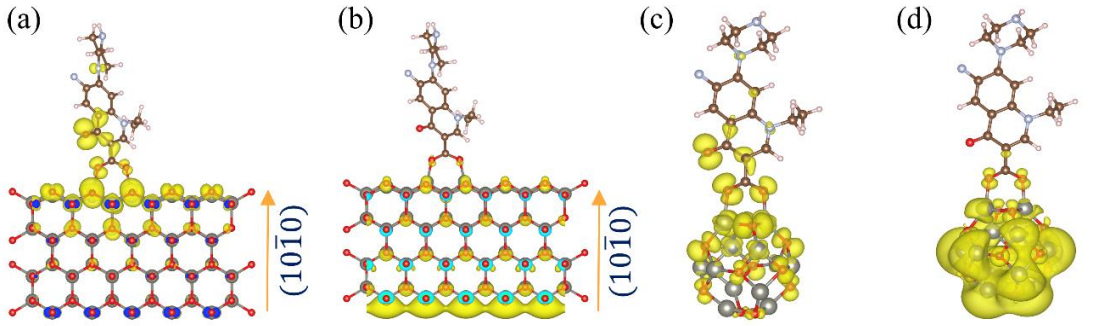

Figure 6.4: *Band decomposed electron densities of ZnO-NF nanohybrids (a) VBM of nanohybrid for the lowest energy binding conformation of NF on the nonpolar zig-zag surface of ZnO wurtzite structure and (b) CBM of nanohybrid for the lowest energy binding conformation of NF on the nonpolar zig-zag surface of ZnO wurtzite structure. (c) HOMO of nanohybrid for the lowest energy binding conformation of NF on $(ZnO)_{12}$ nanocluster. (d) LUMO of nanohybrid for the lowest energy binding conformation of NF on $(ZnO)_{12}$ nanocluster.*

The DOS (density of states) analysis has continued to gain further investigation into the observed effect. We calculated the TDOS (total density of states) of ZnO nanoparticles and the gap between the VB (valence band) and CB (conduction band) of ~0.8 eV has been obtained which is in accordance with the literature data [76] as shown in Figure 6.5c. It shows non-magnetic and semiconducting. The total DOS of NF is also calculated as shown in Figure 6.5b. Changes in the coordination number of atoms affect the banded nature of the material, retaining

the reduction in the hybridization and covalent bond nature of atoms [77]. In the nanohybrid system, the contribution of the DOS near the Fermi level comes from NF. This may indicate the molecular level interactions during the formation of nanohybrid. After investigation of the photoinduced electron transfer dynamics and excited state molecular dynamics, we have continued our research on the antibacterial activity of nanohybrid.

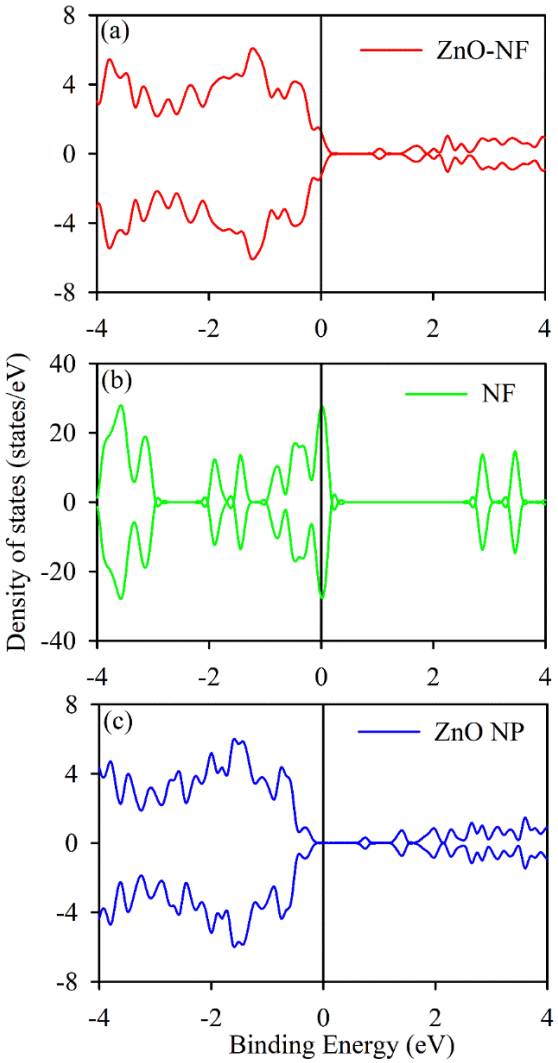

Figure 6.5: *TDOS of (a) ZnO-NF, (b) NF, (c) ZnO nanoparticle surface [10$\bar{1}$0] direction. The black solid line represents Fermi energy (E_F).*

In vitro reactive oxygen species (ROS) generation is performed using a well-known familiar marker dichlorofluorescein (DCFH). DCFH is oxidized to fluorescent DCF in the presence of ROS which shows an emission peak near 520 nm. Thus, the enhancement of ROS during the experiment is monitored at 520 nm. The experiment was performed in the absence of light for 10 minutes and

under irradiation of UV light (wavelength 375 nm) for 30 minutes. The results are depicted in Figure 6.6a. With an increase in the time of light exposure, the enhancement of ROS has been observed for synthesized ZnO-NF nanohybrid as compared to NF and ZnO.

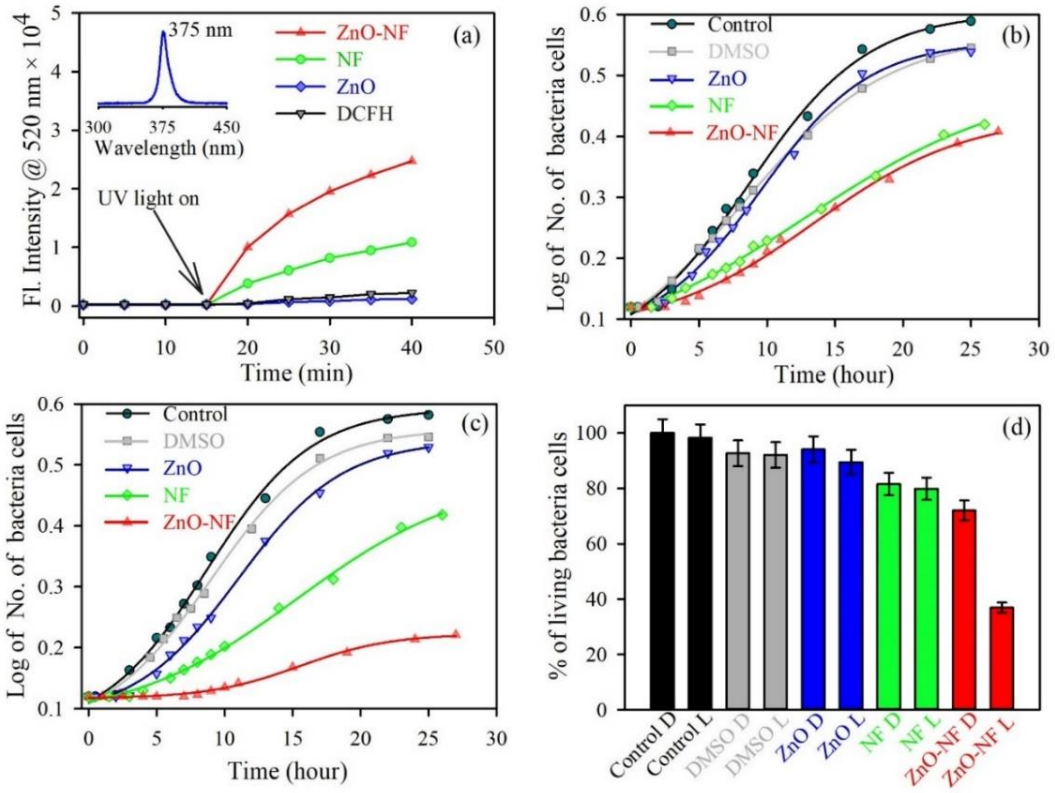

Figure 6.6: *(a) The DCFH oxidation with time in the presence of ZnO nanoparticle (Blue), NF (Green) and ZnO-NF nanohybrid (Red). Growth of cells (b) in the absence of UV light and (c) in the presence of UV light over time control (dark), DMSO (Gray), ZnO nanoparticle (blue), NF (green) and ZnO-NF nanohybrid (red). (d) Percentages of living bacteria cells (D, Dark; L, Light).*

The electron capture (from the HOMO of dye to CB of ZnO) is responsible for the enhancement of ROS generation in the nanohybrid. Mainly, this excited state electron and produced hole generate ROS from the neighbouring H_2O and O_2. The detailed reaction mechanisms are listed below-

$$NF + h\boldsymbol{\nu} = NF\ (e^- + h^+) \tag{6.2}$$

$$NF\ (h^+) + H_2O \rightarrow NF + H^+ + OH^- \tag{6.3}$$

$$NF\ (h^+) + OH^- \rightarrow NF + \dot{0}H \tag{6.4}$$

$$ZnO\ (e^-) + O_2 \rightarrow ZnO + \dot{0}_2^- \tag{6.5}$$

$$\dot{0}_2^- + H^+ \rightarrow H\dot{0}_2^- \tag{6.6}$$

$$H\dot{0}_2^- + H\dot{0}_2^- \rightarrow H_2O_2 + O_2 \quad (6.7)$$

$$ZnO\ (e^-) + H_2O_2 \rightarrow ZnO + \dot{0}H + OH^- \quad (6.8)$$

$$H_2O_2 + \dot{0}_2^- \rightarrow \dot{0}H + OH^- + O_2 \quad (6.9)$$

For a potential application, we have performed *in vitro* bacteria culture. A bacterial culture experiment for the antibacterial activity is conducted on *E. coli*, which is incubated for around 25 hours at 37 °C with the fixed concentrations of ZnO-NF nanohybrid, free NF and ZnO nanoparticles in the absence of light (Figure 6.6b), and in the presence of light (Figure 6.6c) to study the cell growth rate. The enhancement of antibacterial activity is observed by the complex in the presence of light as compared to free NF and ZnO nanoparticles. The percentages of living cells with respect to control are shown in Figure 6.6d. Nanohybrid has significantly higher bacteria death, which is around 65% compared to free NF (20%) and ZnO nanoparticles (11%) for a particular concentration.

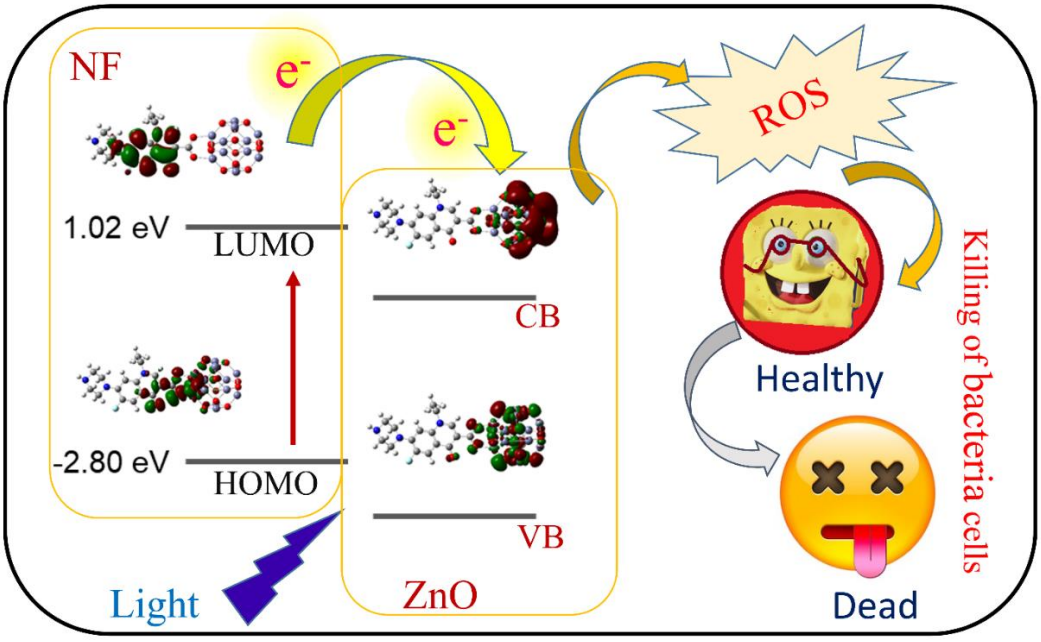

Scheme 6.1: *Schematic representation of electron shuttling in semiconductor ZnO nanostructure leading to antibacterial activity.*

However, the antibacterial application depends on the dose. The bacterial death can be increased by increasing the dose of ZnO-NF [78]. This approach could be applied to other antibiotics that will enhance their potential utilization in a PDT.

6.2.2. Functionalized Nano-MOF for NIR Induced Bacterial Remediation: A Combined Spectroscopic and Computational Study [79]: In this work, we have synthesized ZIF-8 nanoparticles by one-step simple synthetic procedure. Figure 6.7a depicts the schematic representation of the ZIF-8 synthesis procedure. The synthesized nano-MOFs are functionalized by a well-known cyanine dye photosensitizer IR820. Figure 6.7b shows the X-ray diffraction of pure ZIF-8 (red) and ZIF8-IR820 (blue).

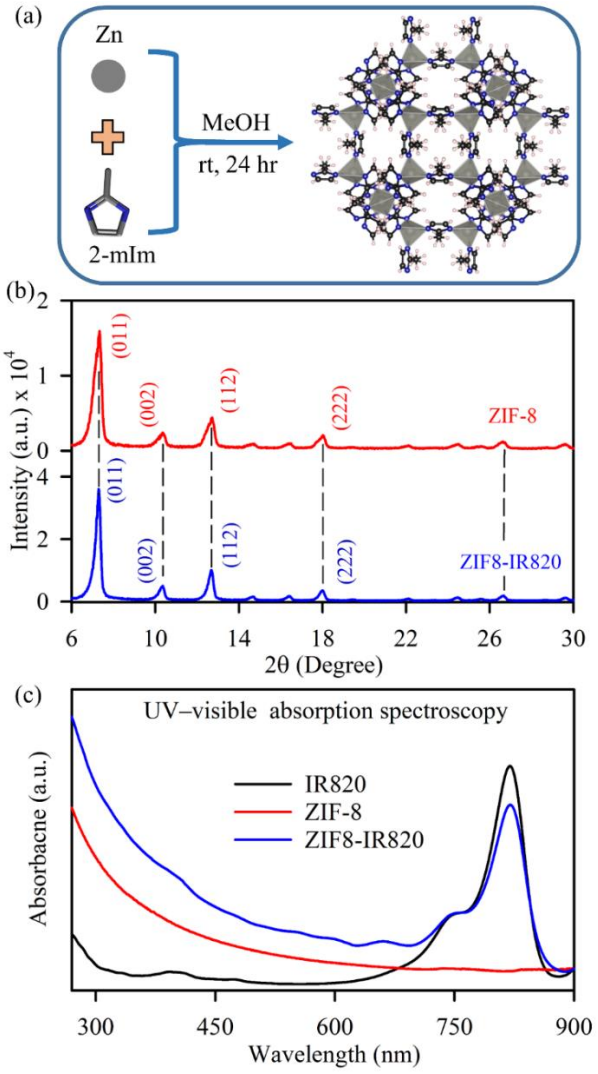

Figure 6.7: *(a) The schematic representation for the preparation of zeolitic imidazolate framework (ZIF-8) nanoparticles. (b) The X-ray Powder Diffraction (XRD) patterns of ZIF-8 nano-MOF (red) and the functionalized nano-MOF (ZIF8-IR820) (blue). (c) Absorption spectra of IR820 (black), ZIF-8 (red) and ZIF8-IR820 (blue) using DMSO as the solvent.*

The X-ray diffraction patterns of both ZIF-8 and ZIF8-IR820 depict the diffraction peaks at 2θ = 7.3, 10.5, 12.6, and 18.1° associated with (011), (002), (112), and (222) diffraction planes of ZIF-8 [68] which confirmed that the sample has pure ZIF-8

phase before and after dye encapsulation. Nevertheless, the diffraction peaks of ZIF8-IR820 (blue line in Figure 6.7b) reveal the same characteristics peaks as ZIF-8 with slight broadening at smaller values of 2θ related to those of ZIF-8. It implies shrinkage in the crystal size, agreeing with Debye−Scherrer's method [80]. The functionalization of dye molecules into pores of ZIF-8 is the prime reason for the size modification of the ZIF-8. To investigate the optical properties of the samples, UV-visible absorption spectra are measured as shown in Figure 6.7c.

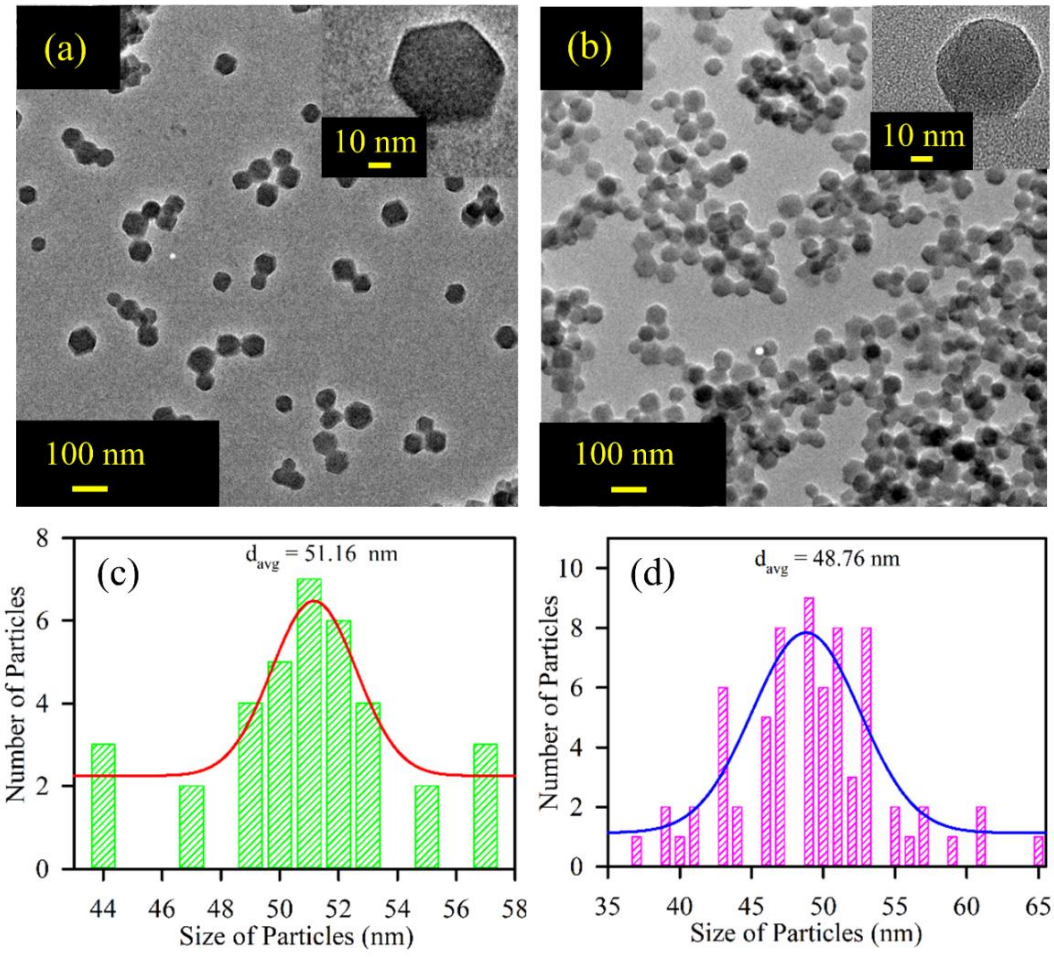

Figure 6.8: *(a) The TEM image of ZIF-8 nanoparticles, inset shows HRTEM image of ZIF-8 nanoparticle. (b) TEM image of ZIF8-IR820 nano-MOF and inset shows HRTEM of ZIF8-IR820 nano-MOF. (c) The average particle distributions of the ZIF-8 nanoparticles. (d) The average particle distributions of the functionalized nano-MOF ZIF8-IR820.*

It depicts the absorption spectra of ZIF-8 (red), NIR dye IR820 (black), and the ZIF8-IR820 nano-MOF (blue) in methanol solvent. The two absorption peaks at 819 nm and with a shoulder at 746 nm are observed for IR820. The absorption

peak of IR820 at 819 nm relates to 0 → 0 transition and a 746 nm corresponds to the 0 →1 vibronic sub-band [81, 82]. In the case of functionalized nano-MOF, absorption peaks of IR820 and the same nature of absorption spectra of ZIF8 are observed simultaneously in ZIF8-IR820. This confirms the formation of the hybrid system.

Further investigation regarding morphological analysis and crystal size distribution of the nano-MOFs are investigated using TEM as shown in Figure 6.8. Figure 6.8a depicts the uniform rhombic dodecahedron crystalline nature of the synthesized framework ZIF-8. The morphological structure of ZIF-8 exhibits sharp edges in nature as shown in the inset of Figure 6.8a. The TEM image of functional nano-MOFs (ZIF8-IR820) is depicted in Figure 6.8b. The encapsulation of IR820 into ZIF-8 alters the sharp crystalline nature as shown in the inset of Figure 6.8b which results in a little shrinkage of crystal size. The particle size distributions are calculated from TEM results to measure the average size of the ZIF-8 nano-MOF before (Figure 6.8c) and after IR820 encapsulation (Figure 6.8d). The average particle size of the ZIF-8 and ZIF8-IR820 nano-MOF are found to be 51.16 nm and 48.76 nm respectively. The incorporation of ligand IR820 inside the micropores of ZIF-8 nano-MOF is responsible to reduce the edge sharpness as well as a decrease in the crystal size. The thermal stability of ZIF-8 and functionalized ZIF8-IR820 nano-MOF is represented in Figure 6.9a. In the case of ZIF-8, the first weight-loss is started at ~500 °C is ~5% which corresponds to the removal of solvent as well as some guest molecules. Thus the thermal stability of ZIF-8 is upto ~525 °C as shown in Figure 6.9a and an intense change has occurred after 525 °C. However, in the case of ZIF8-IR820, the primary weight loss of ~5% occurs within the temperature range of 350 °C which corresponds to the removal of the solvent molecules. In addition to that, ZIF8-IR820 nano-MOF initiates disintegration at 400 ◦C, and approximately 86% weight loss occurs within 515 °C. The beginning of thermal breakdown at an earlier temperature relates to the dissociation of IR820 molecules incorporated into micropores of the framework. The thermal

weight loss before 515 °C recommends the separation of the organic molecules [83]. The percentage of drug loading is calculated from TGA weight loss curves in the temperature range of 120 to 480 °C which is 43%.

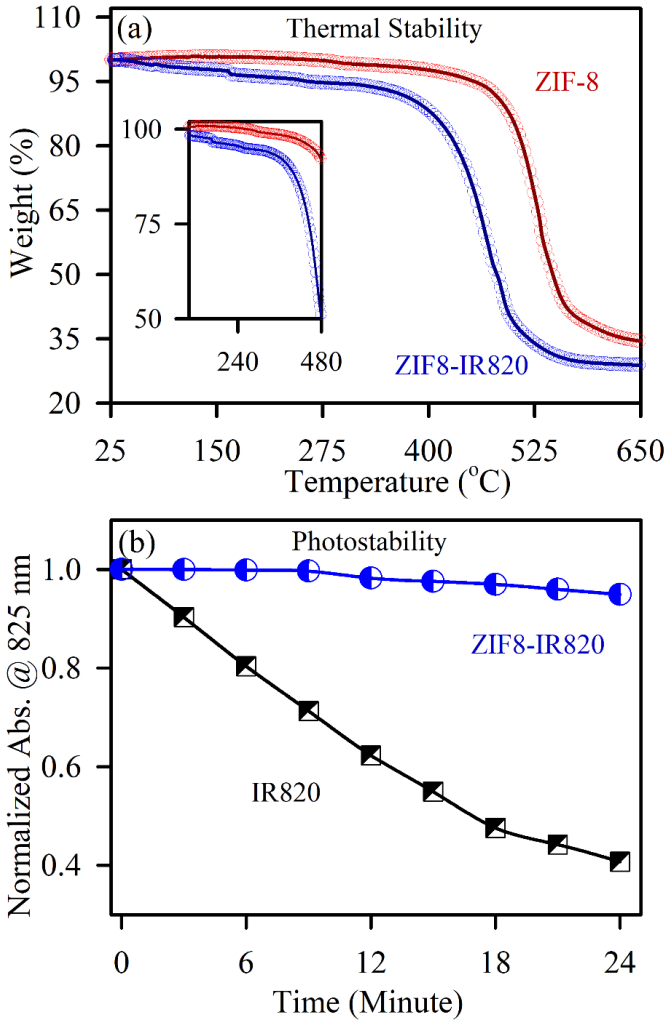

Figure 6.9: *(a) Thermogravimetric profile of ZIF-8 (red) and ZIF8-IR820 (blue) monitored under N_2 flow. (b) Time-dependent photo-degradation of IR820 and ZIF8-IR82.*

Also, the IR820 dye loading capacity was measured in an ethanol solution and by comparing the absorption peak intensity of IR820 at 819 nm before and after loading onto ZIF8 sample (data not shown). The dye loading capacity is found to be 42% which is consistent with TGA analysis. Such high DLC is crucial for therapeutic applications. The efficient drug loading capability of ZIF-8 indicates favourable molecular reorientation of IR820 ligands into micropores of ZIF-8 structure. Figure 6.9b depicts photo-degradation of IR820 and the ZIF8-IR820 nano-MOF with time. The degradation rate of IR820 is much higher as related to

that of the ZIF8-IR820 nano-MOF under white light illumination. The percentage of degradation is found to be ~55% for IR820 with respect to ZIF8-IR820 nano-MOF in 24 minutes of an experimental time. The emission properties of the IR820 and hybrid are depicted in Figure 6.10a. The emission peaks of both IR820 and ZIF8-IR820 are measured at wavelength 820 nm (λ_{ex} = 740 nm) in methanol solvent. There is a significant quenching of steady state emission in the hybrid system which shows the possibility of an excited-state nonradiative process.

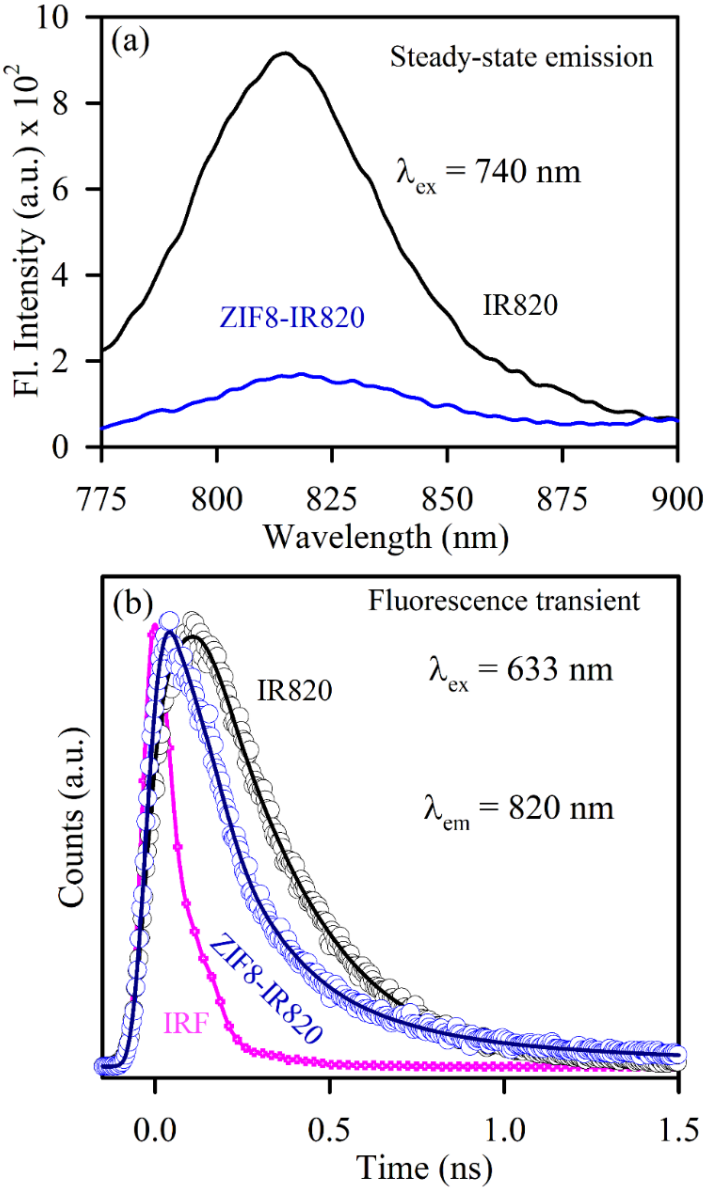

Figure 6.10: *(a) Room-temperature PL spectra of IR820 (black) and ZIF8-IR820 nanohybrid (blue). The excitation wavelength was 633 nm. (b) The picosecond-resolved fluorescence transient of IR820 (black) and ZIF8-IR820 nanohybrid (blue). The excitation wavelength was 633 nm of laser and the collection wavelength was 700 nm.*

In order to investigate the excited state dynamics of IR820 on the surface of ZIF-8, we have performed the picosecond-resolved fluorescence study of IR820 and ZIF8-IR820 upon excitation at 633 nm laser source and detected at 820 nm (Figure 6.10b) using methanol as the solvent. The fitted time parameters (Table 6.3) for the excited-state fluorescence transient of IR820 in methanol show a single time constant of 243 ps. IR820 has the ability to produce heat if it is excited by NIR light [84] and also it produces singlet oxygen by energy transfer from its T_1 state to triplet oxygen [85]. These are the reasons behind the faster lifetime of IR820.In the case of functionalized nano-MOF, the picosecond resolved transient curve is departed from single exponential to bi-exponential with an additional component of 38 ps having a significant contribution of 68%. It suggests charge transfer from HOMO of IR820 dye (the singlet state (S_1) of IR820) to the conduction band (CB) of ZIF-8 [73]. The details of picosecond-resolved fitting parameters are listed in Table 6.3.

Table 6.3: *Picosecond-resolved fluorescence transient lifetime. The emission decay is collected at 820 nm with 633 nm laser excitation. Numbers in parentheses indicate relative contributions.*

System	τ_1 (ps)	τ_2 (ps)	τ_{avg} (ps)
IR820	243 (100%)	0	243
ZIF8-IR820	38 (68%)	188 (32%)	90

We predict that encapsulation of IR820 with ZIF-8 leads to bandgap realignment of the functionalized system which is in favour of photo-induced electron transfer. This electron transfer process decreases the rate of the intersystem crossing process and prevents the electron transfer to the triplet-excited (T_1) state in the photosensitizer dye [86]. Thus, the process of energy transfer from the T_1 state of IR820 to the triplet state of oxygen is arrested by the electron-transfer process which should decrease the production of singlet oxygen by the functionalized nano-MOF [87] and increases its photostability over free IR820.

In order to investigate the electronic property and charge transfer mechanism in the hybrid system, we have performed first principles DFT investigations. We

have optimized all three structures (ZIF-8, IR820 and the nanohybrid) to its ground state. The formation energy of the hybrid system is approximately -0.18 eV/atom, confirming the chemical stability of the nanohybrid. The orbital projected density of states (OPDOS) of the systems are presented in Figure 6.11. ZIF8 shows a bandgap of 4.6 eV which is consistent with the reported literature [88].

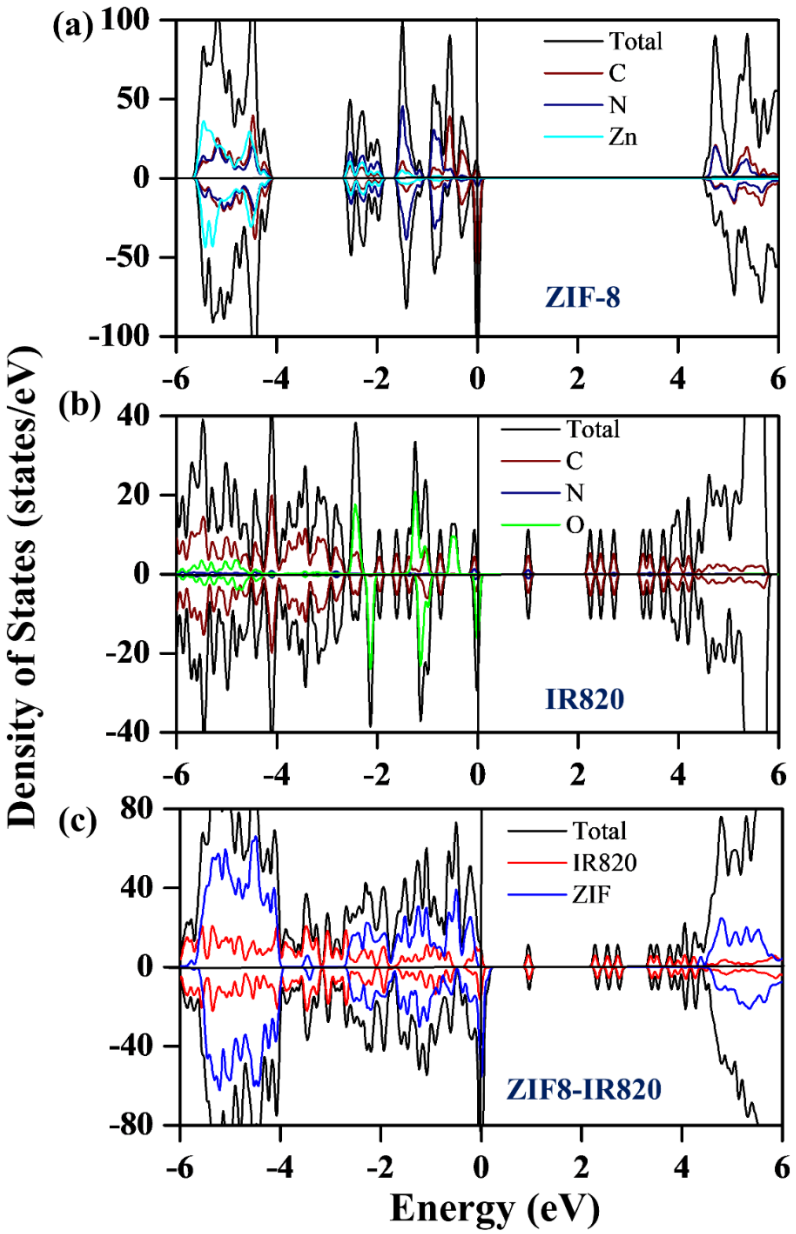

***Figure 6.11**: Density of states of (a) ZIF-8 nano-MOF, (b) IR820 and (c) functionalized ZIF8-IR820 nano-MOF.*

The valance band maxima (VBM) of ZIF8 indicates a strong hybridization of the C-2*p* and N-2*p* states. On the other hand, the VBM of IR820 is mostly populated

with the C-2*p* and O-2*p* states. The OPDOS of the hybrid system implies that the VBM of the combined system is mainly constituted by the C-2*p* and O-2*p* electrons of ZIF-8 and IR820 respectively. On the other hand, the conduction band maxima are mainly consisted of the IR820 levels. There is a significant reduction of the effective bandgap in the hybrid system. The hybrid system indicates *p*-type doping due to the ligand-to-metal charge transfer from IR820 to ZIF-8 as also evidenced experimentally.

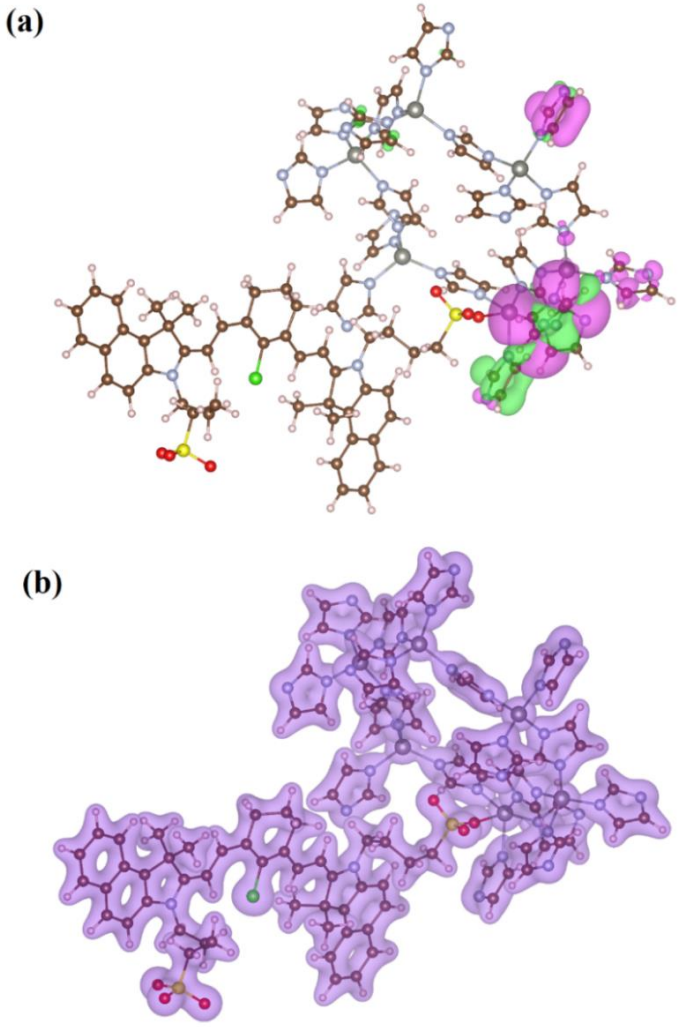

Figure 6.12: *(a) Spin density and (b) charge density plot of the ZIF8-IR820 nanohybrid system.*

The DOS of the hybrid system as plotted in Figure 6.11c reveals a high degree of spin polarization, which is also reflected in the spin density plot of the system as depicted in Figure 6.12a. There is a spin imbalance in the ZIF-8 after the formation of the nanohybrid because of the mutual electronic interaction of the individual systems within the assembled system. The charge density of the

hybrid system is plotted in Figure 6.12b which displays a significant charge overlap between ZIF-8 and IR820 at the interface, confirming the mutual charge transfer from IR820 to ZIF-8 in the hybrid system [89]. The enhanced excited state charge transfer process motivates us to investigate the photoinduced ROS generation ability of ZIF8-IR820 and IR820. It shows an enormous increase in ROS for ZIF8-IR820 nano-MOF under red light as shown in Figure 6.13a. The increment of ROS is observed to be ~12-fold increase in 25 minutes for ZIF8-IR820 compared to only IR820. Nevertheless, the same strategy is used to check the ROS capability of only ZIF-8 which shows no increment of ROS.

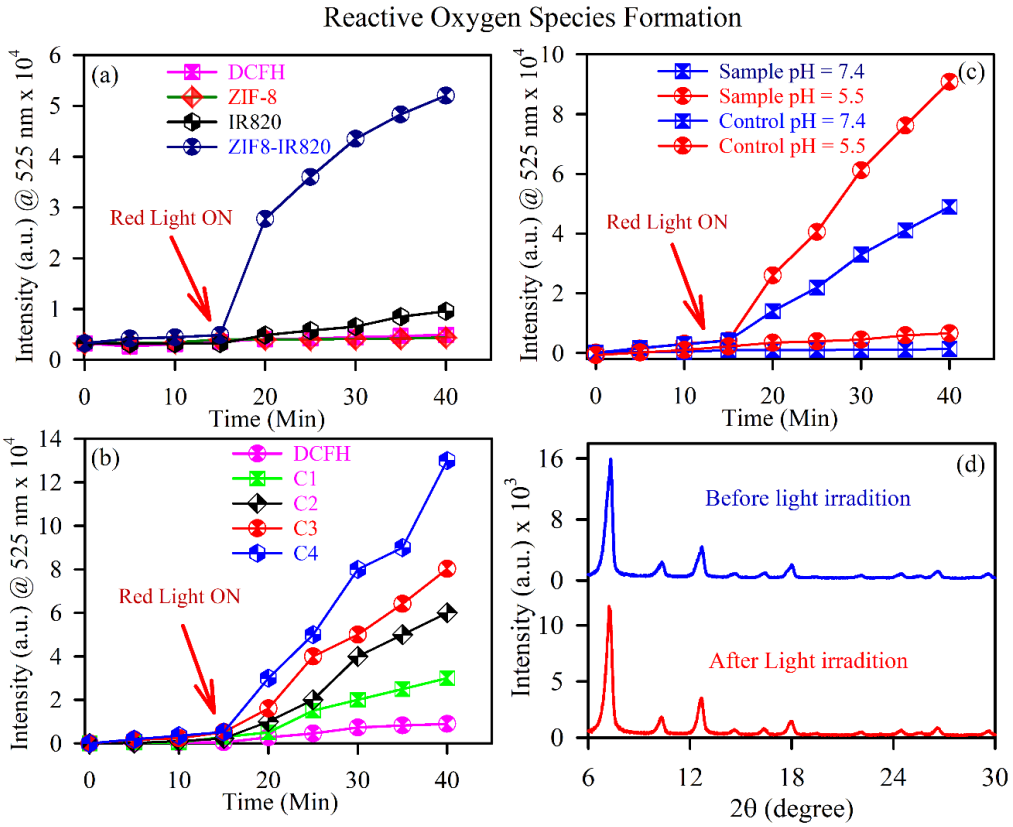

Figure 6.13: *The DCFH oxidation (monitored at 525 nm) with respect to control DCFH (pink), (a) in the presence of ZIF-8 nanoparticles (red), IR820 (black) and ZIF8-IR820 nanohybrid (blue), (b) in the presence of ZIF8-IR820 nanohybrid at variable concentrations (C1, 0.1 OD; C2, 0.15 OD; C3, 0.2 OD and C4, 0.25 OD) and (c) in the presence of ZIF8-IR820 nanohybrid at two different pH values only under dark (15 minutes) and in presence of red light (25 minutes). The excitation wavelength was 484 nm. (d) XRD of nano-MOF before and after light irradiation for 45 minutes.*

The enormous amount of photoinduced ROS motivates us to investigate the concentration-dependent and pH-dependent ROS production capability of ZIF8-IR820. The concentration-dependent DCFH oxidation of nano-MOF is

investigated for four different concentrations (C1, 0.1 OD; C2, 0.15 OD; C3, 0.2 OD and C4, 0.25 OD) of ZIF8-IR820 as shown in Figure 6.13b. Greater ROS production was observed with increasing the concentration of ZIF8-IR820. The higher DCF formation at a higher concentration of ZIF8-IR820 is the reason behind the greater ROS production [90].

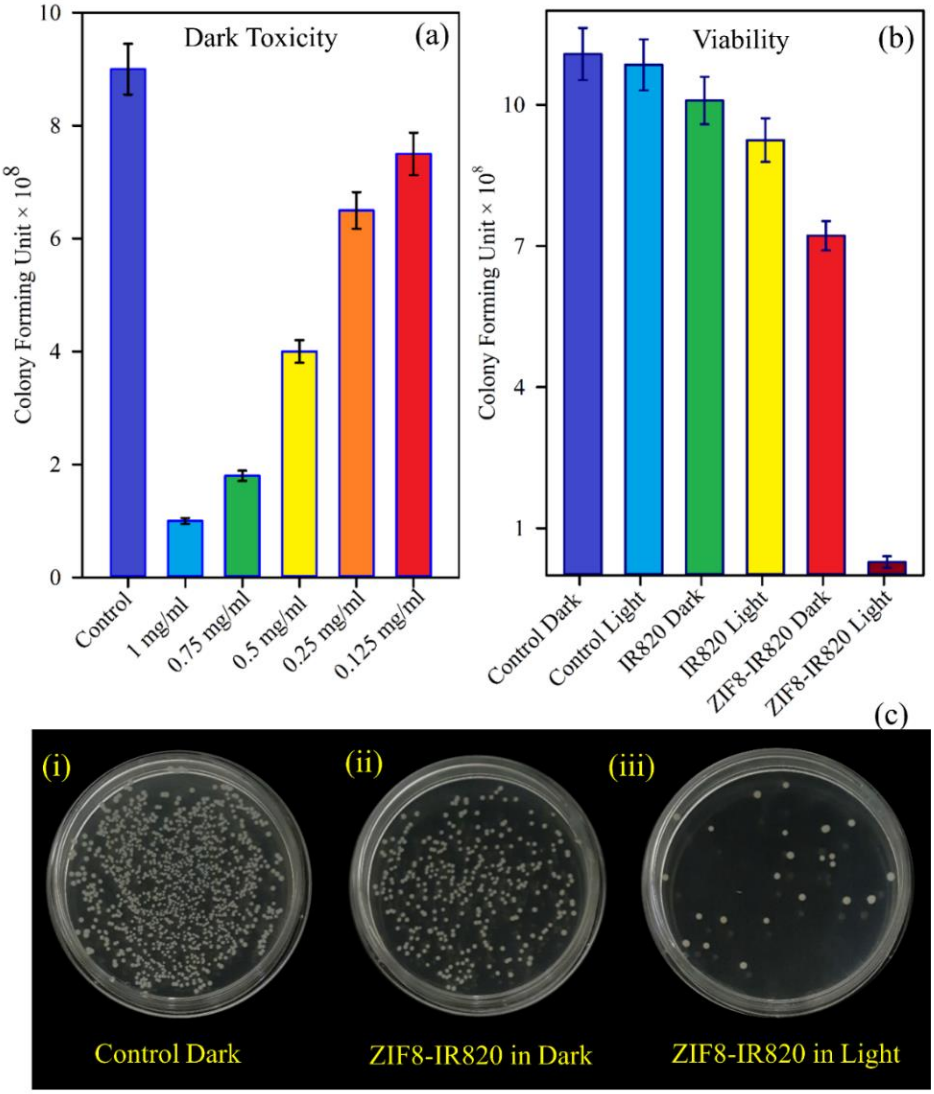

Figure 6.14: *(a) Optimisation of bacterial viability in dark of ZIF8-IR820 for different concentrations of samples with respect to control. (b) The treatment with 0.125 mg/ml ZIF8-IR820 samples in the presence and absence of red light irradiation. (c) The images of Staphylococcus hominis plates treated with ZIF8-IR820, (i) control of Staphylococcus hominis bacteria, (ii) Staphylococcus hominis bacteria treated in the absence of light and (iii) after treated with red light irradiation for 25 minutes.*

Figure 6.13c depicts pH-dependent DCFH oxidation of ZIF8-IR820 at two different pH values. The ROS capability of ZIF8-IR820 is much higher in acidic conditions at pH = 5.5 which is doubled as compared to normal pH = 7.4. The

reactivity of superoxide ion is comparatively prominent at acidic pH due to its protonation which shows better ROS generation at lower pH range [91]. However, only IR820 depicts negligible changes of ROS in acidic pH, which further indicates that functionalized ZIF8-IR820 nano-MOFs are acting as pH-responsive photoinduced ROS generating nanomaterials.

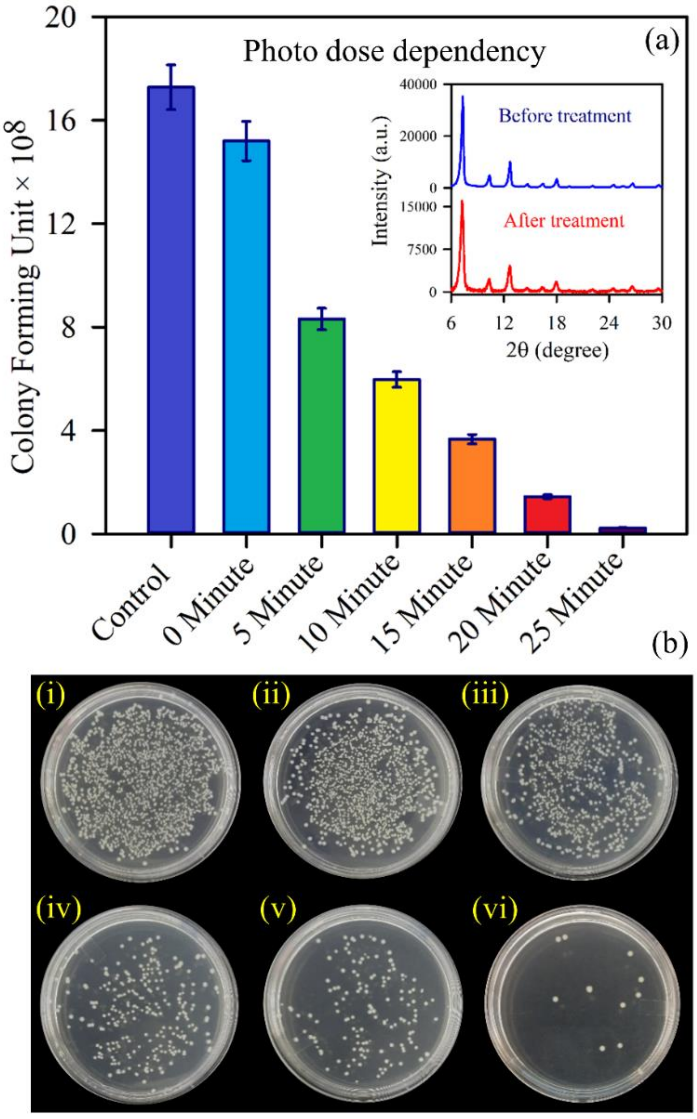

Figure 6.15: *(a) Bacterial viability with varying times of red light irradiation and inset shows the XRD of nano-MOF before and after bacteria treatment. (b) Images of Staphylococcus hominis plates treated by ZIF8-IR820 sample with varying time of red light irradiation, ((i) 0 minute, (ii) 5 minute, (iii), 10 minute, (iv) 15 minute, (v) 20 minute and (vi) 25 minute.*

Moreover, the XRD of ZIF8-IR820 before and after the red light irradiation on the sample is performed to investigate the structural stability after light irradiation (Figure 6.13d.) The XRD peaks of ZIF8-IR820 are similar before and after light treatment on nano-MOF for 45 minutes. It confirms that the structural

nature of nano-MOF remain intact after red light irradiation. The enhanced ROS production in the presence of red light suggests ZIF8-IR820 could be used as a potential NIR-induced antibacterial agent. For the antimicrobial activity study, we have evaluated the antimicrobial action of functionalized nano-MOF toward *Staphylococcus hominis* bacteria under dark and red light illumination. To optimize the dark toxicity nature, we have treated *Staphylococcus hominis* bacteria for different concentrations (1 mg/ml, 0.75 mg/ml, 0.5 mg/ml, 0.25 mg/ml and 0.125 mg/ml) of ZIF8-IR820 nano-MOF (keeping IR820 concentration same) as shown in Figure 6.14a. The very less bacterial killing effect is observed under dark conditions for 0.125 mg/ml concentration of ZIF8-IR820 nano-MOF with respect to control (Figure 6.14a). Then we proceed with red light irradiation viability treatment on *S. hominis* bacteria with the optimized concentration (0.125 mg/ml) of ZIF8-IR820 nano-MOF as shown in Figure 6.14b. The enormous antimicrobial activity of ZIF8-IR820 nano-MOF in the presence of red light of wavelength 650 nm is observed which is around 96% in 25 minutes due to enhanced ROS generation. The control experiments have also been performed keeping the same amount of ZIF-8 in 0.125 mg/ml ZIF8-IR820 nano-MOF. ZIF-8 nano-MOF has negligible antibacterial activity against *S. hominis* bacteria. For IR820 treated samples, negligible antibacterial activity is observed in the absence of light and very less bacterial effect under red light treatment (Figure 6.14b). However, the bacteria-killing efficacy is better at concentrations higher than the concentration used in 0.125 mg/ml ZIF8-IR820 nano-MOF after 25 minutes of red-light exposure. Figure 6.14c depicts the images of colony forming unit (CFU) plates treated by ZIF8-IR820 on *S. hominis* bacteria. The images in Figure 6.14c depict (i) the untreated plate of *S. hominis* bacteria, (ii) *S. hominis* bacteria treated with 0.125 mg/ml ZIF8-IR820 nano-MOF in dark and (iii) *S. hominis* bacteria treated by 0.125 mg/ml ZIF8-IR820 nano-MOF in presence of red light for 25 minutes. The enhanced antimicrobial activity of ZIF8-IR820 nano-MOF in the presence of red light motivates us to investigate the photo-dose dependent action of ZIF8-IR820 nano-MOF against the same bacteria. Figure 6.15a depicts the photo-dose dependent experiment of ZIF8-IR820 nano-MOF. The

experiments are performed by red light irradiation in 5 minutes intervals of time. The antimicrobial activity of ZIF8-IR820 nano-MOF is increased with increasing the time of red light illumination (Figure 6.15a). Moreover, the Powder XRD tests of ZIF-IR820 before and after the antibacterial treatment is also performed to check the stability of nan-MOF as shown in the inset of Figure 6.15a.

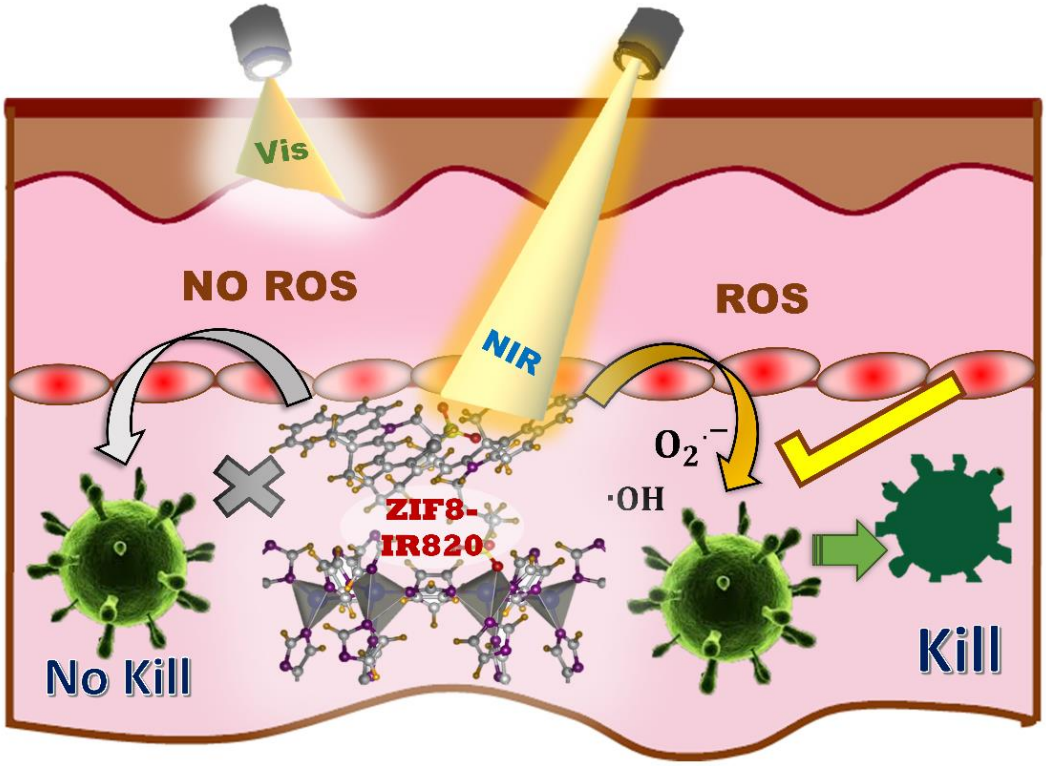

Scheme 6.2: *Schematic representation of nano-MOF to deliver the photosensitizers in the targeted bacterial cells that could be used for photoinduced bacterial remediation.*

The XRD peaks of ZIF8-IR820 are similar before and after antibacterial treatment for 2.5 hours of incubation which confirm the stability of the nano-MOF. The enhancement of ROS with time of ZIF8-IR820 nano-MOF in the presence of red light is the main cause of killing the bacteria. Figure 6.15b shows *S. hominis* plates treated with 0.125 mg/ml ZIF8-IR820 under red light. The difference in CFU number of *S. hominis* bacteria after treatment of light indicates the potential photo-dose dependent antibacterial effect of ZIF8-IR820. The efficiency is measured to be ~96% CFU reduction in 25 minutes and complete bacterial reduction is observed by ZIF8-IR820 nano-MOF after 30 minutes of irradiation of red light. The study confirms that ZIF8-IR820 is highly effective against bacterial infections which can be useful for real-life antibacterial applications.

6.3. Conclusion:

In summary, we have investigated the enhanced antibacterial ability of ZnO-NF nanohybrid over free NF and ZnO nanoparticles using various experiments as well as computational studies. We have established the benefit of NF as the light-stimulated drug. NF is strongly associated with ZnO nanoparticles and the attachment has been confirmed using various spectroscopy mechanisms. The excited state charge transmission process from NF to ZnO semiconductor are confirmed by TCSPC and supported by the first principles DFT-based computational analysis. This charge transfer mechanism shows a greater extent of ROS generation. The antibacterial photodynamic effect on *E. coli* is confirmed using the cell culture experiment, which suggests significant changes after light-stimulated drug treatment. Our results figure out that bacterial cell death has occurred to a high ROS production process. It reveals that the ZnO-NF nanohybrid is much more effective in the antibacterial effect on *E. coli* cells compare to free NF and ZnO nanoparticles. This developed procedure could be applied to other antibiotics that will enhance their ability in PDT. This result provides a new path that has the capability to deliver the NF in the targeted cells, which can be used for disinfection or membrane-based antibacterial applications.

Moreover, we investigate an approach for the fabrication of functionalized nano-MOF (ZIF-8) encapsulating with a well-known cyanine dye IR820 which improves its photodynamic action. The functionalized ZIF8-IR820 nano-MOF provides greater thermal stability and photostability after encapsulation with ZIF-8. The time-resolved fluorescence study of ZIF8-IR820 explains the excited-state charge-transfer dynamics from IR820 to ZIF-8 in the functionalized nano-MOF. The first principles DFT analysis of functionalized nano-MOF illustrates the possibility of ligand to metal charge transfer which is consistent with experimental findings. The excited-state ligand to metal charge transfer in the functionalized nano-MOF is responsible for the production of photoinduced ROS in a pH-responsive manner because of more access of molecular oxygen.

The functionalized nano-MOF shows an enormous antimicrobial effect against *S. hominis* bacteria even at distinctly lower concentrations which recommend its remarkability for real application. Overall, the study demonstrates a detailed physical understanding of photosensitizer encapsulated nano-MOF system which shows efficient NIR light-induced photo-dose dependent antibacterial activity. It provides a new path to deliver the photosensitizers in the targeted bacterial cells that would be used for photoinduced bacterial remediation.

References

[1] P. Karpecki, M. R. Paterno, T. L. Comstock, Limitations of current antibiotics for the treatment of bacterial conjunctivitis, *Optom. Vis. Sci.* 87 (2010) 908.

[2] J. Jose, A. Anas, B. Jose, A. B. Puthirath, S. Athiyanathil, C. Jasmin, M. R. Anantharaman, S. Nair, C. Subrahmanyam, V. Biju, Extinction of antimicrobial resistant pathogens using silver embedded silica nanoparticles and an efflux pump blocker, *ACS Appl. Bio Mater.* 2 (2019) 4681.

[3] M. Haque, M. Sartelli, J. McKimm, M. Abu Bakar, Health care-associated infections - An overview, *Infect. Drug Resist.* 11 (2018) 2321.

[4] P. E. Sheffield, P. J. Landrigan, Global climate change and children's health: Threats and strategies for prevention, *Environ. Health Perspect.* 119 (2010) 291.

[5] I. Chopra, M. Roberts, Tetracycline antibiotics: Mode of action, applications, molecular biology, and epidemiology of bacterial resistance, *Microbiol. Mol. Biol. Rev.* 65 (2001) 232.

[6] W. M. JAME, Prevalence study of antibiotic usage and health care associated infections at near east university hospital in northern cyprus, *Near East University*, Turkey, 2016.

[7] Y. Wang, Z. Zhou, J. Zhu, Y. Tang, T. D. Canady, E. Y. Chi, K. S. Schanze, D. G. Whitten, Dark antimicrobial mechanisms of cationic phenylene ethynylene polymers and oligomers against *Escherichia coli*, *Polymers* 3 (2011) 1199.

[8] J. Shi, A. R. Votruba, O. C. Farokhzad, R. Langer, Nanotechnology in drug delivery and tissue engineering: From discovery to applications, *Nano Lett.* 10 (2010) 3223.

[9] J. Wang, P. Zhao, X. Li, H. Fu, X. Yang, G. Wang, Y. Yang, H. Wei, Z. Zhou, W. Liao, Evaluating the photodynamic biocidal activity and investigating the mechanism of thiazolium cyanine dyes, *ACS Appl. Bio Mater.* (2020).

[10] R. Peng, Y. Luo, Q. Cui, J. Wang, L. Li, Near-infrared conjugated oligomer for effective killing of bacterial through combination of photodynamic and photothermal treatment, *ACS Appl. Bio Mater.* (2020).

[11] M. R. Hamblin, Fullerenes as photosensitizers in photodynamic therapy: Pros and cons, *Photochem. Photobiol. Sci.* 17 (2018) 1515.

[12] X.-J. Wen, C.-G. Niu, D.-W. Huang, L. Zhang, C. Liang, G.-M. Zeng, Study of the photocatalytic degradation pathway of norfloxacin and mineralization activity using a novel ternary Ag/AgCl-CeO_2 photocatalyst, *J. Catal.* 355 (2017) 73.

[13] K. S. Kim, D. Lee, C. G. Song, P. M. Kang, Reactive oxygen species-activated nanomaterials as theranostic agents, *Nanomedicine* 10 (2015) 2709.

[14] A. Abdal Dayem, M. Hossain, S. Lee, K. Kim, S. Saha, G.-M. Yang, H. Choi, S.-G. Cho, The role of reactive oxygen species (ROS) in the biological activities of metallic nanoparticles, *Int. J. Mol. Sci.* 18 (2017) 120.

[15] V. Mohanraj, Y. Chen, Nanoparticles-A review, *Trop. J. Pharm. Res.* 5 (2006) 561.

[16] P. Verma, H. Pal, Aggregation studies of dipolar coumarin-153 dye in polar solvents: A photophysical study, *J. Phys. Chem. A* 118 (2014) 6950.

[17] A. Bera, D. Bagchi, S. K. Pal, Improvement of photostability and NIR activity of cyanine dye through nanohybrid formation: Key information from ultrafast dynamical studies, *J. Phys. Chem. A* (2019).

[18] S. Sreejith, T. T. M. Huong, P. Borah, Y. Zhao, Organic–inorganic nanohybrids for fluorescence, photoacoustic and Raman bioimaging, *Sci. Bull.* 60 (2015) 665.

[19] C. M. Courtney, S. M. Goodman, J. A. McDaniel, N. E. Madinger, A. Chatterjee, P. Nagpal, Photoexcited quantum dots for killing multidrug-resistant bacteria, *Nat. Mater.* 15 (2016) 529.

[20] S. Wang, P. Huang, X. Chen, Stimuli-responsive programmed specific targeting in nanomedicine, *ACS Nano* 10 (2016) 2991.

[21] L. Wang, C. Hu, L. Shao, The antimicrobial activity of nanoparticles: Present situation and prospects for the future, *Int. J. Nanomed.* 12 (2017) 1227.

[22] S. K. Sehmi, S. Noimark, S. D. Pike, J. C. Bear, W. J. Peveler, C. K. Williams, M. S. P. Shaffer, E. Allan, I. P. Parkin, A. J. MacRobert, Enhancing the antibacterial activity of light-activated surfaces containing crystal violet and ZnO nanoparticles: Investigation of nanoparticle size, capping ligand, and dopants, *ACS omega* 1 (2016) 334.

[23] Y. Jia, A. Omri, L. Krishnan, M. J. McCluskie, Potential applications of nanoparticles in cancer immunotherapy, *Hum. Vaccines Immunother.* 13 (2017) 63.

[24] G. Applerot, A. Lipovsky, R. Dror, N. Perkas, Y. Nitzan, R. Lubart, A. Gedanken, Enhanced antibacterial activity of nanocrystalline ZnO due to increased ROS-mediated cell injury, *Adv. Funct. Mater.* 19 (2009) 842.

[25] R. Brayner, R. Ferrari-Iliou, N. Brivois, S. Djediat, M. F. Benedetti, F. Fiévet, Toxicological impact studies based on Escherichia coli bacteria in ultrafine ZnO nanoparticles colloidal medium, *Nano Lett.* 6 (2006) 866.

[26] J. Pasquet, Y. Chevalier, E. Couval, D. Bouvier, G. Noizet, C. Morlière, M.-A. Bolzinger, Antimicrobial activity of zinc oxide particles on five micro-organisms of the challenge tests related to their physicochemical properties, *Int. J. Pharm.* 460 (2014) 92.

[27] K. L. Kotloff, J. P. Winickoff, B. Ivanoff, J. D. Clemens, D. L. Swerdlow, P. J. Sansonetti, G. Adak, M. Levine, Global burden of Shigella infections: Implications for vaccine development and implementation of control strategies, *Bull. World Health Organ.* 77 (1999) 651.

[28] A. Joe, S.-H. Park, D.-J. Kim, Y.-J. Lee, K.-H. Jhee, Y. Sohn, E.-S. Jang, Antimicrobial activity of ZnO nanoplates and its Ag nanocomposites: Insight

into an ROS-mediated antibacterial mechanism under UV light, *J. Solid State Chem.* 267 (2018) 124.

[29] Y. Wang, E. Y. Chi, D. O. Natvig, K. S. Schanze, D. G. Whitten, Antimicrobial activity of cationic conjugated polyelectrolytes and oligomers against saccharomyces cerevisiae vegetative cells and ascospores, *ACS Appl. Mater. Interfaces* 5 (2013) 4555.

[30] M.-H. Oh, S.-H. Paek, G. W. Shin, H.-Y. Kim, G. Y. Jung, S. Oh, Simultaneous identification of seven foodborne pathogens and *Escherichia coli* (pathogenic and nonpathogenic) using capillary electrophoresis–based single-strand conformation polymorphism coupled with multiplex PCR, *J. Food Prot.* 72 (2009) 1262.

[31] A. D. Maynard, D. B. Warheit, M. A. Philbert, The new toxicology of sophisticated materials: Nanotoxicology and beyond, *Toxicol. Sci.* 120 (2010) S109.

[32] D. Bagchi, V. S. Rathnam, P. Lemmens, I. Banerjee, S. K. Pal, NIR-light-active ZnO-based nanohybrids for bacterial biofilm treatment, *ACS omega* 3 (2018) 10877.

[33] N. Beyth, Y. Houri-Haddad, A. Domb, W. Khan, R. Hazan, Alternative antimicrobial approach: Nano-antimicrobial materials, *Evid Based Complement Alternat Med.* 2015 (2015) 246012.

[34] O. Rutschmann, A. Zwahlen, Use of norfloxacin for prevention of symptomatic urinary tract infection in chronically catheterized patients, *Eur. J. Clin. Microbiol. Infect. Dis.* 14 (1995) 441.

[35] S. P. Gopi, S. Ganguly, G. R. Desiraju, A Drug–drug salt hydrate of norfloxacin and sulfathiazole: Enhancement of *in vitro* biological properties *via* improved physicochemical properties, *Mol. Pharm.* 13 (2016) 3590.

[36] Z. L. Wang, Zinc oxide nanostructures: Growth, properties and applications, *J. Phys. Condens. Matter.* 16 (2004) R829.

[37] T. K. Maji, P. K. Sarkar, P. Kar, B. Liu, P. Lemmens, D. Karmakar, S. K. Pal, A combined experimental and computational study on a nanohybrid material for potential application in NIR photocatalysis, *Appl. Catal. A: Gen.* 583 (2019) 117124.

[38] F. Lu, W. Cai, Y. Zhang, ZnO hierarchical micro/nanoarchitectures: Solvothermal synthesis and structurally enhanced photocatalytic performance, *Adv. Funct. Mater.* 18 (2008) 1047.

[39] F. Prestinaci, P. Pezzotti, A. Pantosti, Antimicrobial resistance: A global multifaceted phenomenon, *Pathog. Glob. Health* 109 (2015) 309.

[40] C. Pettinari, R. Pettinari, C. Di Nicola, A. Tombesi, S. Scuri, F. Marchetti, Antimicrobial MOFs, *Coord. Chem. Rev.* 446 (2021) 214121.

[41] E. Peterson, P. Kaur, Antibiotic resistance mechanisms in bacteria: Relationships between resistance determinants of antibiotic producers, environmental bacteria, and clinical pathogens, *Front. Microbiol.* 9 (2018).

[42] R. Rowen, Unholy interlocking of government, corporate, and medical dogma sacri-fices lives-the semmelweis saga resurrected, *J. Infect Dis Epidemiol* 7 (2021) 199.

[43] C. B. Beard, S. N. Visser, L. R. Petersen, The need for a national strategy to address vector-borne disease threats in the united states, *J. Med. Entomol.* 56 (2019) 1199.

[44] M. E. de Kraker, A. J. Stewardson, S. Harbarth, Will 10 million people die a year due to antimicrobial resistance by 2050?, *PLoS Med.* 13 (2016) e1002184.

[45] P. Sen, M. Managa, T. Nyokong, New type of metal-free and Zinc(II), In(III), Ga(III) phthalocyanines carrying biologically active substituents: Synthesis and photophysicochemical properties and photodynamic therapy activity, *Inorg. Chim. Acta* 491 (2019) 1.

[46] C. Mari, R. Rubbiani, G. Gasser, Biological evaluation of nitrile containing Ru(II) polypyridyl complexes as potential photodynamic therapy agents, *Inorg. Chim. Acta* 454 (2017) 21.

[47] Z. Yu, P. Zhou, W. Pan, N. Li, B. Tang, A biomimetic nanoreactor for synergistic chemiexcited photodynamic therapy and starvation therapy against tumor metastasis, *Nat. Commun.* 9 (2018) 1.

[48] B. M. Amos-Tautua, S. P. Songca, O. S. Oluwafemi, Application of porphyrins in antibacterial photodynamic therapy, *Molecules* 24 (2019) 2456.

[49] T. Maisch, Anti-microbial photodynamic therapy: Useful in the future?, *Lasers Med. Sci.* 22 (2007) 83.

[50] H. Shi, L. Du, K. C. Lo, W. Xiong, W. K. Chan, D. L. Phillips, Photoinduced triplet state electron transfer processes from ruthenium containing triblock copolymers to carbon nanotubes, *J. Phys. Chem. C* 121 (2017) 8145.

[51] A. Blázquez-Castro, Direct $^1O_2$ optical excitation: A tool for redox biology, *Redox Biol.* 13 (2017) 39.

[52] T. Maisch, R.-M. Szeimies, G. Jori, C. Abels, Antibacterial photodynamic therapy in dermatology, *Photochem. Photobiol. Sci.* 3 (2004) 907.

[53] T. Dai, Y.-Y. Huang, M. R. Hamblin, Photodynamic therapy for localized infections—State of the art, *Photodiagn. Photodyn. Ther.* 6 (2009) 170.

[54] B. Pucelik, A. Sułek, J. M. Dąbrowski, Bacteriochlorins and their metal complexes as NIR-absorbing photosensitizers: Properties, mechanisms, and applications, *Coord. Chem. Rev.* 416 (2020) 213340.

[55] I. Yoon, J. Z. Li, Y. K. Shim, Advance in photosensitizers and light delivery for photodynamic therapy, *Clin Endosc* 46 (2013) 7.

[56] G. Jori, C. Fabris, M. Soncin, S. Ferro, O. Coppellotti, D. Dei, L. Fantetti, G. Chiti, G. Roncucci, Photodynamic therapy in the treatment of microbial

infections: Basic principles and perspective applications, *Lasers Surg. Med.* 38 (2006) 468.

[57] Y. Feng, L. Liu, J. Zhang, H. Aslan, M. Dong, Photoactive antimicrobial nanomaterials, *J. Mater. Chem. B* 5 (2017) 8631.

[58] W. Gao, Y. Chen, Y. Zhang, Q. Zhang, L. Zhang, Nanoparticle-based local antimicrobial drug delivery, *Adv. Drug Deliv. Rev.* 127 (2018) 46.

[59] C. I. C. Crucho, The attack of the smart particles: Should bacteria be afraid?, *ACS Med. Chem. Lett.* 9 (2018) 2.

[60] J. Jeevanandam, A. Barhoum, Y. S. Chan, A. Dufresne, M. K. Danquah, Review on nanoparticles and nanostructured materials: History, sources, toxicity and regulations, *Beilstein J. Nanotechnol.* 9 (2018) 1050.

[61] M. N. Hasan, A. Bera, T. K. Maji, S. K. Pal, Sensitization of nontoxic MOF for their potential drug delivery application against microbial infection, *Inorg. Chim. Acta* 523 (2021) 120381.

[62] C. Pettinari, F. Marchetti, N. Mosca, G. Tosi, A. Drozdov, Application of metal − organic frameworks, *Polym. Int.* 66 (2017) 731.

[63] M.-X. Wu, Y.-W. Yang, Metal–organic framework (MOF)-based drug/cargo delivery and cancer therapy, *Adv. Mater.* 29 (2017) 1606134.

[64] Y. Wang, J. Yan, N. Wen, H. Xiong, S. Cai, Q. He, Y. Hu, D. Peng, Z. Liu, Y. Liu, Metal-organic frameworks for stimuli-responsive drug delivery, *Biomaterials* 230 (2020) 119619.

[65] J. Zhuang, C.-H. Kuo, L.-Y. Chou, D.-Y. Liu, E. Weerapana, C.-K. Tsung, Optimized metal–organic-framework nanospheres for drug delivery: Evaluation of small-molecule encapsulation, *ACS Nano* 8 (2014) 2812.

[66] Y. Sun, L. Zheng, Y. Yang, X. Qian, T. Fu, X. Li, Z. Yang, H. Yan, C. Cui, W. Tan, Metal–organic framework nanocarriers for drug delivery in biomedical applications, *Nano-Micro Lett.* 12 (2020) 103.

[67] K. K. Gangu, S. Maddila, S. B. Mukkamala, S. B. Jonnalagadda, A review on contemporary metal–organic framework materials, *Inorg. Chim. Acta* 446 (2016) 61.

[68] S. A. Ahmed, M. N. Hasan, D. Bagchi, H. M. Altass, M. Morad, I. I. Althagafi, A. M. Hameed, A. Sayqal, A. E. R. S. Khder, B. H. Asghar, Nano-MOFs as targeted drug delivery agents to combat antibiotic-resistant bacterial infections, *R. Soc. Open Sci.* 7 (2020) 200959.

[69] C.-Y. Sun, C. Qin, X.-L. Wang, G.-S. Yang, K.-Z. Shao, Y.-Q. Lan, Z.-M. Su, P. Huang, C.-G. Wang, E.-B. Wang, Zeolitic imidazolate framework-8 as efficient pH-sensitive drug delivery vehicle, *Dalton Trans.* 41 (2012) 6906.

[70] L. R. de Moura Ferraz, A. É. G. A. Tabosa, D. D. S. da Silva Nascimento, A. S. Ferreira, V. de Albuquerque Wanderley Sales, J. Y. R. Silva, S. A. Júnior, L. A. Rolim, J. J. de Souza Pereira, P. J. Rolim-Neto, ZIF-8 as a promising drug delivery system for benznidazole: Development, characterization, *in vitro* dialysis release and cytotoxicity, *Sci. Rep.* 10 (2020) 16815.

[71] S. Feng, X. Zhang, D. Shi, Z. Wang, Zeolitic imidazolate framework-8 (ZIF-8) for drug delivery: A critical review, *Front. Chem. Sci. Eng.* 15 (2021) 221.

[72] R. Xie, P. Yang, S. Peng, Y. Cao, X. Yao, S. Guo, W. Yang, A phosphorylcholine-based zwitterionic copolymer coated ZIF-8 nanodrug with a long circulation time and charged conversion for enhanced chemotherapy, *J. Mater. Chem. B* 8 (2020) 6128.

[73] M. N. Hasan, T. K. Maji, U. Pal, A. Bera, D. Bagchi, A. Halder, S. A. Ahmed, J. H. Al-Fahemi, T. M. Bawazeer, T. Saha-Dasgupta, S. K. Pal, Wide bandgap semiconductor-based novel nanohybrid for potential antibacterial activity: Ultrafast spectroscopy and computational studies, *RSC Adv.* 10 (2020) 38890.

[74] T. Bora, K. K. Lakshman, S. Sarkar, A. Makhal, S. Sardar, S. K. Pal, J. Dutta, Modulation of defect-mediated energy transfer from ZnO nanoparticles for the photocatalytic degradation of bilirubin, *Beilstein J. Nanotechnol.* 4 (2013) 714.

[75] T. K. Maji, D. Bagchi, P. Kar, D. Karmakar, S. K. Pal, Enhanced charge separation through modulation of defect-state in wide band-gap semiconductor for potential photocatalysis application: Ultrafast spectroscopy and computational studies, *J. Photochem. Photobiol. A: Chem.* 332 (2017) 391.

[76] T. K. Maji, P. Kar, H. Mandal, C. Bhattacharya, D. Karmakar, S. K. Pal, Halide-modulated functionality of wide band gap zinc oxide semiconductor nanoparticle, *ChemistrySelect* 3 (2018) 6382.

[77] S. D. Assa Aravindh, U. Schwingenschloegl, I. S. Roqan, Defect induced d 0 ferromagnetism in a ZnO grain boundary, *J. Chem. Phys.* 143 (2015) 224703.

[78] M. Khatun, S. Choudhury, B. Liu, P. Lemmens, S. K. Pal, S. Mazumder, Resveratrol–ZnO nanohybrid enhanced anti-cancerous effect in ovarian cancer cells through ROS, *RSC Adv.* 6 (2016) 105607.

[79] M. N. Hasan, A. Bera, T. K. Maji, D. Mukherjee, N. Pan, D. Karmakar, S. K. Pal, Functionalized nano-MOF for NIR induced bacterial remediation: A combined spectroscopic and computational study, *Inorg. Chim. Acta* 532 (2022) 120733.

[80] U. Holzwarth, N. Gibson, The Scherrer equation versus the 'Debye-Scherrer equation', *Nat. Nanotechnol* 6 (2011) 534.

[81] H. V. Berlepsch, C. Böttcher, H-aggregates of an indocyanine Cy5 dye: Transition from strong to weak molecular coupling, *J. Phys. Chem. B* 119 (2015) 11900.

[82] H. Mustroph, K. Reiner, J. Mistol, S. Ernst, D. Keil, L. Hennig, Relationship between the molecular structure of cyanine dyes and the vibrational fine structure of their electronic absorption spectra, *ChemPhysChem* 10 (2009) 835.

[83] H. Nabipour, M. H. Sadr, G. R. Bardajee, Synthesis and characterization of nanoscale zeolitic imidazolate frameworks with ciprofloxacin and their applications as antimicrobial agents, *New J. Chem.* 41 (2017) 7364.

[84] P. Kumar, R. Srivastava, IR 820 stabilized multifunctional polycaprolactone glycol chitosan composite nanoparticles for cancer therapy, *RSC Adv.* 5 (2015) 56162.

[85] Q. Zheng, L. D. Lavis, Development of photostable fluorophores for molecular imaging, *Curr. Opin. Chem. Biol.* 39 (2017) 32.

[86] S. Liu, R. G. Parr, Second-order density-functional description of molecules and chemical changes, *J. Chem. Phys.* 106 (1997) 5578.

[87] A. Bera, M. N. Hasan, U. Pal, D. Bagchi, T. K. Maji, T. Saha-Dasgupta, R. Das, S. K. Pal, Fabrication of nanohybrids toward improving therapeutic potential of a NIR photo-sensitizer: An optical spectroscopic and computational study, *J. Photochem. Photobiol. A* 424 (2022) 113610.

[88] A. Baghban, S. Habibzadeh, F. Zokaee Ashtiani, Bandgaps of noble and transition metal/ZIF-8 electro/catalysts: A computational study, *RSC Adv.* 10 (2020) 22929.

[89] T. K. Maji, M. N. Hasan, S. Ghosh, D. Wulferding, C. Bhattacharya, P. Lemmens, D. Karmakar, S. Kumar Pal, Development of a magnetic nanohybrid for multifunctional application: From immobile photocatalysis to efficient photoelectrochemical water splitting: A combined experimental and computational study, *J. Photochem. Photobiol. A* 397 (2020) 112575.

[90] T. Dutta, D. Bagchi, A. Bera, S. Das, T. Adhikari, S. K. Pal, Surface engineered ZnO-humic/citrate interfaces: Photoinduced charge carrier dynamics and potential application for smart and sustained delivery of Zn micronutrient, *ACS Sustainable Chem. Eng.* 7 (2019) 10920.

[91] W. He, Y.-T. Zhou, W. G. Wamer, M. D. Boudreau, J.-J. Yin, Mechanisms of the pH dependent generation of hydroxyl radicals and oxygen induced by Ag nanoparticles, *Biomaterials* 33 (2012) 7547.

Chapter 7

A Combined Spectroscopic and Computational Studies on Tri-hybrid Nanomaterial for Potential Removal of Antibiotic Burden and Bacterial Remediation

7.1. Introduction:

Infections instigated by antibiotic-resistant of bacteria are considered one of the most dangerous health threats in the world [1-3]. The resistance amongst several antimicrobial agents to various antibacterial drugs namely antibiotics has initiated the threat of bacterial infection [4-7]. Several thousand death and a few million serious illnesses of patients have been reported in the United States alone each year due to bacterial infection. Bacterial infection is the second leading cause of death in patients with cancer and it increases at a fast pace in recent years [8, 9]. So, the development of new antimicrobial agents is required to combat diseases caused by bacterial infections.

Bacterial infections are generally treated by wide-spectrum antibiotics (such as tetracycline, ciprofloxacin, norfloxacin, methicillin, and azithromycin) [10-12]. Among them, tetracycline (TC) is well known for its broad range of activity. It acts as an antibiotic in the dark and as a photosensitizer under illumination with visible light [13, 14]. However, the use of antibiotics has many limitations in antibacterial applications including the lack of targeted treatment and mismanagement of antibiotics for non-bacterial diseases. The high doses of antibiotics used progressively lead to the emergence of antibiotic resistance of bacteria [15-17]. A potential approach to developing non-invasive therapeutic strategies for bacterial infections has attracted significant attention [18, 19].

Light harvesting applications of hybrid nanomaterials for targeted theranostics are leading with high interest. In a few years, numerous hybrid materials have

been developed to deliver antibiotics and organic molecules for sustaining therapeutic activities such as Ag-based antibacterial agents, metal oxides (ZnO, CuO, etc.) and also some heterosystems [20-23]. They can produce ROS upon photo-excitation which is responsible for their biomedical action (antifungal, antibacterial, anticancer action, etc.) as ROS has capability to destroy the active substances in the bacterial inner or outer membrane [24-26]. However, to minimize the possible side effects and complications, stimuli responsiveness is necessary. In this regard, ZnO-based hybrids nanomaterials are the most promising and encouraging system for modulation of drug activity, targeted disease site-specific delivery, low cost and less toxicity [27-29].

Implementation of a dual responsive mechanism could be a very useful technique to achieve enhanced efficacy in antibacterial photodynamic therapy (aPDT). The approach is based on the combined effect of excited stated photoelectron transfer process and dipolar coupling of a covalently linked donor to the acceptor, although, the approach has been earlier utilized to increase the efficacy in dye-sensitized solar cells [30-32]. These are expensive for their synthesis and the developed hybrids are not biocompatible. The implementations of dual sensitization are not reported to enhance the antimicrobial activity of the drug molecules.

In this regard, the development of a dual responsive (electron and energy transfer) tri-hybrid system could be an appropriate solution for the enhancement of antimicrobial action and hence is the main motive of our current study. In this work, we report the fabrication of metal hybrid nanomaterials which is Au-decorated ZnO (Au_ZnO). The morphology and composition of the samples were characterized by microscopic, optical spectroscopic and DFT-based computational techniques. We encapsulated an antibacterial agent TC with Au_ZnO system to make a novel Au_ZnO-TC tri-hybrid. The steady state photoluminescence and time-resolved fluorescence transient study demonstrate the FRET from TC to Au as well as charge transfer from TC to ZnO in the Au_ZnO-TC tri-hybrid system. The energy transfer from TC to Au nanoparticle

triggers an enormous electron separation in the Au_ZnO-TC tri-hybrid system which enhanced the production of ROS in the presence of white light. The dual sensitization in the tri-hybrids leads to wide-range antimicrobial activity against gram-positive bacteria due to immense ROS under white light irradiation. Therefore, the developed tri-hybrids show enhanced antibacterial activities due to dual sensitization. Moreover, the Au nanoparticle-decorated ZnO is capable of destroying excess antibiotics which gradually decreases the appearance of drug-resistance bacteria. This study demonstrates a promising aspect that could be beneficial for manifold biological applications.

7.2. Results and Discussion:

7.2.1. Tetracycline Encapsulated in Au Nanoparticle-decorated ZnO Nanohybrids for Enhanced Antibacterial Activity [33]: The schematic representation of the synthesis of Au-decorated ZnO nanohybrid and encapsulation of TC on Au_ZnO is shown in Scheme 7.1. Figure 7.1 depicts the characteristic X-ray diffraction patterns of ZnO, ZnO-TC and Au-ZnO.

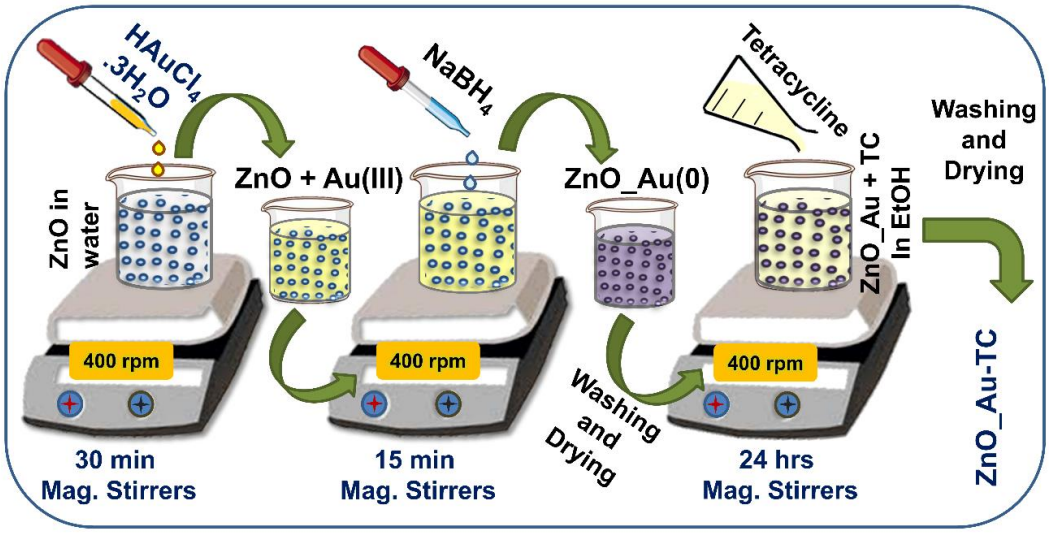

Scheme 7.1: *Schematic Representation for the Synthesis Procedure of Au-decorated ZnO nanohybrid and Au_ZnO-TC tri-hybrid.*

The X-ray diffraction of the ZnO nanoparticles suggests its wurtzite structure with hexagonal type. The decoration of Au nanoparticles into the surface of ZnO nanoparticles retains the same position of diffraction peaks of ZnO. It suggests

that upon the decoration of Au nanoparticles, the structure of pure ZnO nanoparticle crystal remains intact. The presence of some additional characteristic peaks of Au nanoparticles have appeared in the XRD pattern of the Au-ZnO nanohybrids. TC decoration over ZnO crystal does not change their XRD pattern. The value of 2θ of the diffraction peaks of Au nanoparticles are found at 38.15°, 44.31° and 64.54° which correspond to (111), (200) and (220) planes respectively [34].

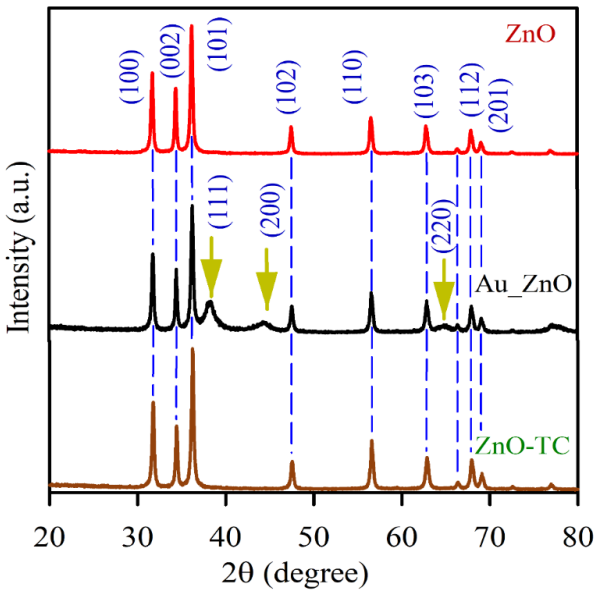

Figure 7.1: *XRD patterns of commercial 30 nm ZnO nanoparticles (red), synthesized Au-ZnO (black) and ZnO-TC (dark red).*

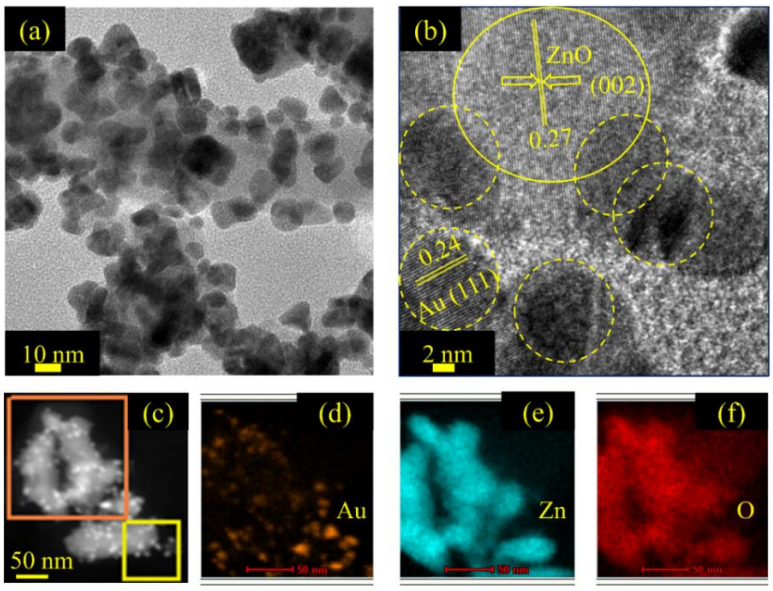

Figure 7.2: *(a) TEM images of Au-ZnO (b) HRTEM image of Au-ZnO. (c-f) EFTEM compositional analysis of Au-ZnO.*

The HR-TEM images of Au-ZnO nanohybrid (Figures 7.2.2a and 7.2.2b) show the decoration of Au nanoparticles on ZnO. The fringes distance for the ZnO nanoparticles of sizes <50 nm is found to be 0.27 nm which signifies the (002) crystal planes of ZnO nanoparticles [29]. The interplanar distance of 0.24 nm for the Au nanoparticles corresponds to the (111) crystal planes [35] which confirms the presence of Au in Au_ZnO nanoparticles, and an average diameter of the Au nanoparticles is found to be ~10 nm. The EFTEM images of Au_ZnO nanoparticles show a composition of Au (gold), Zn (blue) and O (red) as shown in Figure 7.2c-f.

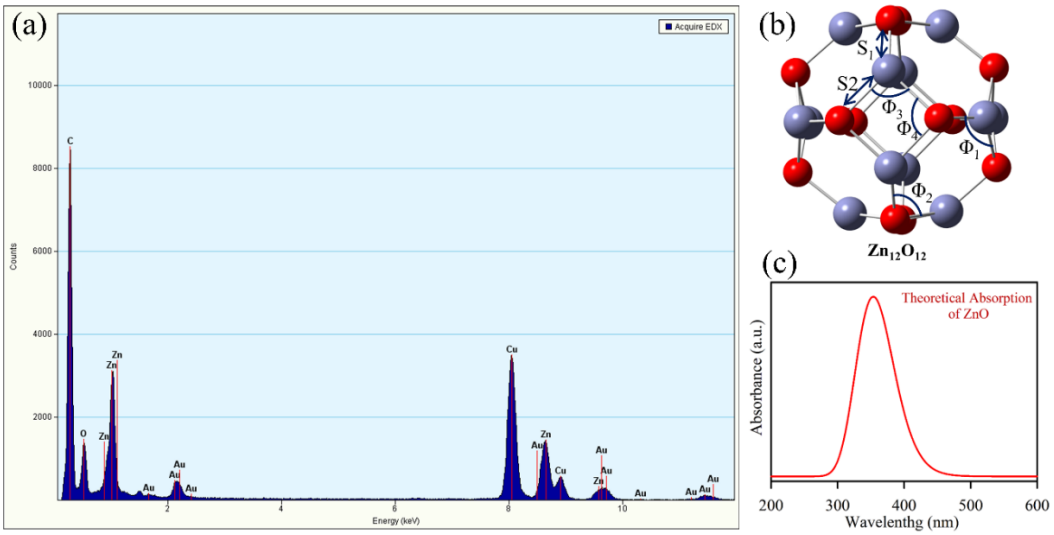

Figure 7.3: *(a) EDAX spectrum extracted from the map visibly and numerically identifies ~8% Au, even though they contain common elements. (b) Optimized structure of $Zn_{12}O_{12}$, calculated average bond lengths of hexagons (S1) and tetragons (S2) are about 1.88 and 1.96 Å respectively. The angles in hexagons (Φ_1, Φ_2) and tetragons (Φ_3, Φ_4) were 126.68°, 112.29°, 91.07° and 87.75° respectively. (c) Theoretical UV-visible absorbance of $Zn_{12}O_{12}$ nanoparticle.*

The composition analysis is also confirmed from EDAX as depicted in Figure 7.3a. The atomic % values of Au, Zn and O are found to be 7.89%, 45.37% and 46.73% respectively which are tabulated in Table 7.1. Therefore, HR-TEM images depict the attachment of Au nanoparticles on ZnO and the EDAX mapping analysis confirms the atomic % of Au nanoparticles which is 7.89% in Au_ZnO nanohybrid. The DFT-based technique is applied to investigate the physical insight of Au_ZnO nanohybrid. First, the structural geometry of pristine $Zn_{12}O_{12}$ is prepared by a combination of eight hexagons of $(ZnO)_3$ and six tetragons of $(ZnO)_2$ rings. The structural geometry of pristine $Zn_{12}O_{12}$ has tetrahedral

rotational and inversion symmetry. The optimized geometry of the $Zn_{12}O_{12}$ nanoparticle is depicted in Figure 7.3b. The calculated average bond distances of hexagons (S1) and tetragons (S2) are about 1.87 and 1.95 Å, and angles in hexagons (Φ_1, Φ_2) and tetragons (Φ_3, Φ_4) are 126.66°, 112.28°, 91.60° and 87.45° respectively.

Table 7.1: *Atomic percentage in Au_ZnO nanohybrid from EDAX spectrum.*

S. No	Elements	Atomic %	Uncert. %
1	O(K)	46.73	0.22
2	Zn(K)	45.37	0.35
3	Au(L)	7.89	0.32

The optimized structure of $Zn_{12}O_{12}$ using DFT/B3LYP exchange-correlation functions showed that the distances S1 and S2 were 1.85 and 1.93 Å respectively. The calculated Φ_1, Φ_2, Φ_3 and Φ_4 angles were found to be 126.41°, 112.37°, 91.97° and 86.92° respectively [36]. From the comparison, we concluded that the results well agree with the calculated data reported in the literature [36, 37]. Absorption spectra of $Zn_{12}O_{12}$ nanocage are calculated by using the same exchange-correlation function as shown in Figure 7.3c. The calculated absorption peak of ZnO is 350 nm which is consistent with our experimental absorption spectra for smaller ZnO nanoparticles [29]. The TDOS of $Zn_{12}O_{12}$ is calculated as shown in Figure 7.4a which shows orbital delocalization in the valence and conduction bands of $Zn_{12}O_{12}$ nanoparticles. The highest occupied molecular orbital (HOMO) and lowest unoccupied molecular orbital (LUMO) of $Zn_{12}O_{12}$ are separated by a bandgap of 3.43 eV which agrees well with previous work [38]. Figure 7.4b depicts the surfaces of the frontier molecular orbitals of $Zn_{12}O_{12}$. The HOMO/LUMO of ZnO are localized on the Zn and O sites, respectively. It indicates that the Zn sites are electrophilic and O sites are nucleophilic in ZnO.

In order to investigate the Au-decoration on ZnO nanoparticles, Au-doped $Zn_{12}O_{12}$ nanoparticles are made with two Au atoms, as shown in Figure 7.4c. The Au-doped $Zn_{12}O_{12}$ structure is optimized B3LYP/6-311++G(d,p)-SDD based

method and the frontier molecular orbitals of Au-doped $Zn_{12}O_{12}$ hybrid are shown in Figure 7.4d. Figure 7.4e shows the TDOS of Au-doped $Zn_{12}O_{12}$ nanoparticles. It depicts some additional states near the Fermi level which indicates charge transfer near the bandgap. Moreover, after the doping process, the LUMO level significantly shifted toward the Fermi level and consequently, the bandgap was considerably narrowed.

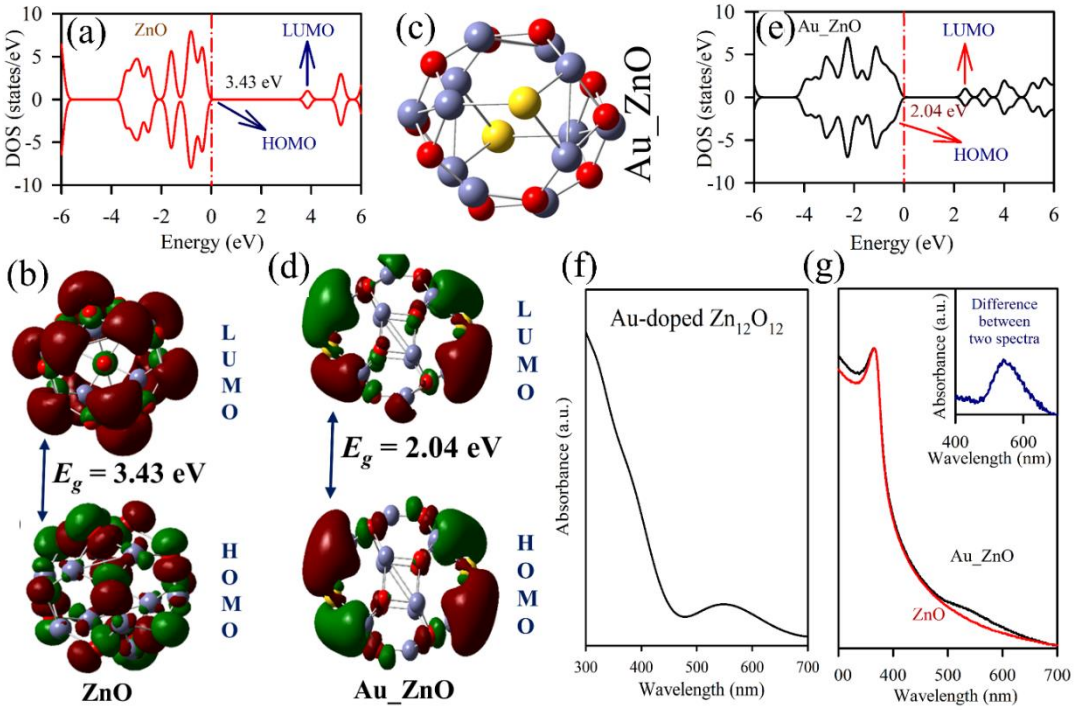

Figure 7.4: *(a) Density of states (DOS) plot and (b) the frontier molecular orbitals LUMO and HOMO of $Zn_{12}O_{12}$ nanoparticle. (c) The optimized structure of Au-doped $Zn_{12}O_{12}$. (d) LUMO and HOMO of Au-doped ZnO nanoparticle. (e) DOS of Au-doped $Zn_{12}O_{12}$ nanoparticle. The energy gap between HOMO and LUMO is 2.04 eV. (f) Theoretically computed UV-Visible absorbance of Au-doped $Zn_{12}O_{12}$. (g) UV-Vis absorption spectra of ZnO (red) and Au-ZnO (black). Inset shows the difference between the two absorbance spectra.*

The bandgap of ZnO significantly decreases to 2.04 eV, which indicates the formation of Au-doped $Zn_{12}O_{12}$ hybrid nanomaterials. So, the theoretical investigation is well-matched with experimental results as seen in HRTEM. The UV-vis absorption of Au-doped $Zn_{12}O_{12}$ is calculated with the most stable geometry of hybrids as shown in Figure 7.4f which is well-matched with our experimental result and also indicates the formation of Au nanoparticle-doped $Zn_{12}O_{12}$ nanohybrid. Figure 7.4g depicts the absorption spectra of ZnO nanoparticles and Au-ZnO nanohybrid. In the case of Au-ZnO nanohybrid, the

peak of ZnO at 370 nm is visible whereas the newly generated peak at 540 nm signifies the presence of a surface plasmon resonance band of Au nanoparticles. The inset shows the difference between the absorption spectra of ZnO and Au_ZnO nanoparticles which depict the absorption spectra of Au nanoparticles. This confirms the presence of Au in Au_ZnO nanoparticles which is also a signature of the formation of Au_ZnO nanohybrid.

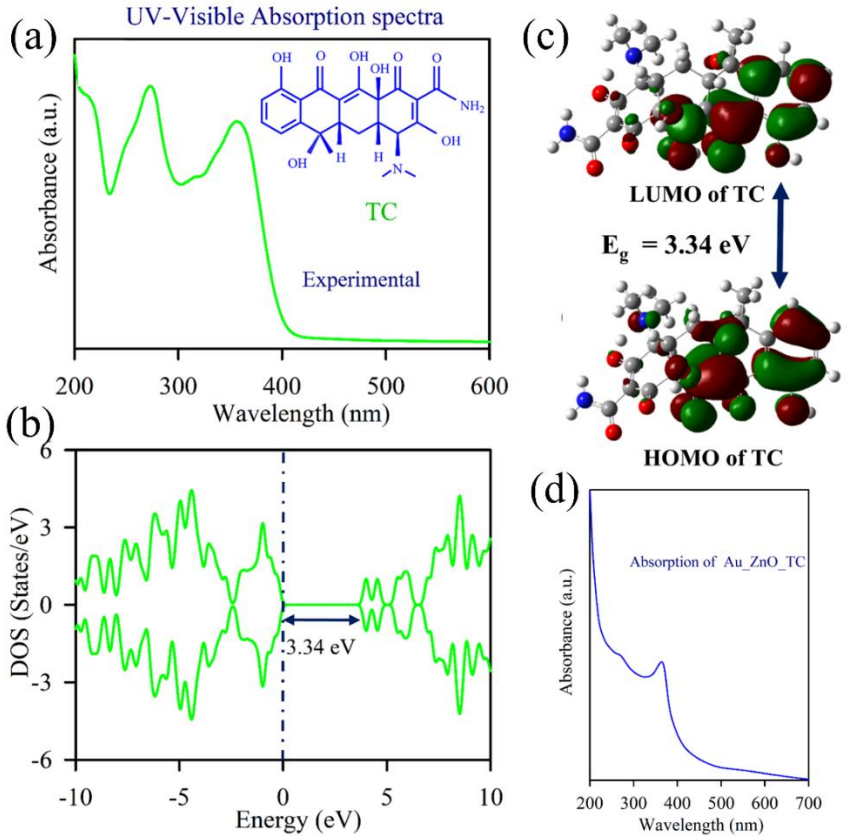

Figure 7.5: *(a) UV-vis absorbance of tetracycline (TC), inset shows structure of TC. (b) The density of states (DOS) plot of TC. (c) HOMO and LUMO of optimized geometrical structure of TC. Energy gap between HOMO and LUMO is 3.34 eV. (d) UV-Vis absorption spectra of Au_ZnO-TC nanohybrid.*

Next, TC has encapsulated on the surface of Au-decorated ZnO nanohybrid to make Au_ZnO-TC tri-hybrid. Figure 7.5a depicts the absorption spectra of TC which is measured experimentally in DMSO solvent and the inset shows the structure of TC. The absorption spectra of TC in DMSO exhibit three characteristic peaks at 220 nm, 270 nm and 355 nm corresponding to π-π* transitions. Figure 7.5b depicts total DOS of TC which is composed of the valence and conduction bands separated by an energy gap of 3.34 eV. Figure 7.5c

shows the electron delocalization of TC at HOMO and LUMO respectively. After encapsulation of TC with Au_ZnO hybrid, the charge transfer dynamics in the tri-hybrid have been performed. Figure 7.5d depicts the absorption spectra of Au_ZnO-TC tri-hybrid. Figure 7.6a depicts the room temperature steady-state emission spectrum of TC (Green), ZnO-TC (Red) and Au_ZnO-TC (Blue). Steady state emission of TC, ZnO-TC and Au_ZnO-TC have exhibited an emission maximum at 530 nm upon excitation at 409 nm.

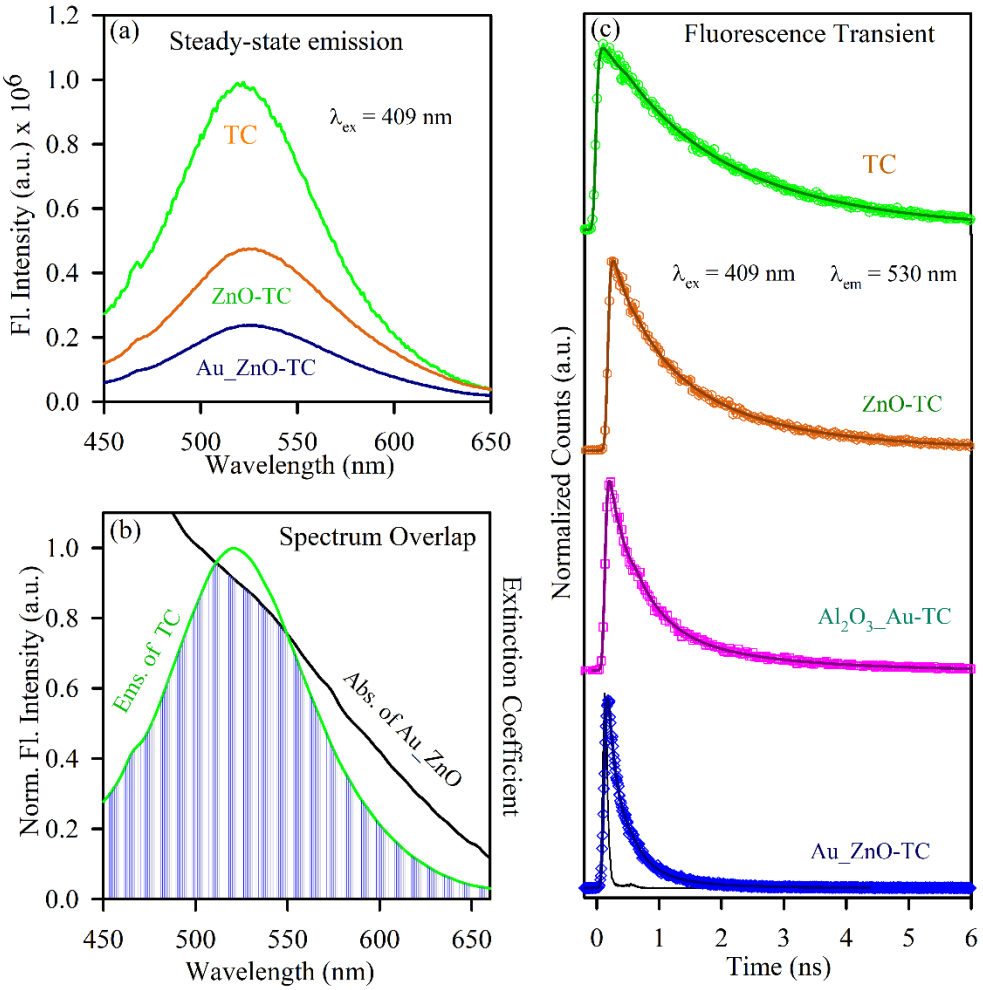

Figure 7.6: *(a) Room-temperature PL spectra (excitation at 405 nm) of TC (green), ZnO-TC (red) and Au_ZnO-TC (blue). (b) Spectral overlap of TC (donor) and Au-ZnO (acceptor). (c) The picosecond resolved fluorescence transient of TC (green), Al_2O_3-Au-TC (pink), ZnO-TC (red) and Au_ZnO-TC (blue). The excitation wavelength was 405 nm and the collection wavelength was 530 nm.*

In both cases, after the attachment of TC to the ZnO and Au_ZnO nanoparticles, the steady state emission intensity is significantly reduced. This may indicate the molecular level interactions present in the nanohybrid. The emission quenching

also signifies the presence of any excited state non-radiative process. However, the spectral overlap between the emission of TC and absorption of Au (Figure 7.6b) indicates the possibility of significant energy transfer between TC and Au. Figure 7.6c depicts the time-resolved fluorescence transients of all the samples. The time-resolved transient of TC has a two time component of 782 ps and 2153 ps with an average lifetime of 1865 ps which quenches significantly for ZnO-TC due to the presence of a faster time constant of ~43 ps (with 53% contribution). It is attributed to interfacial excited state electron transfer from the LUMO of TC to the conduction band (CB) of ZnO [39-41].

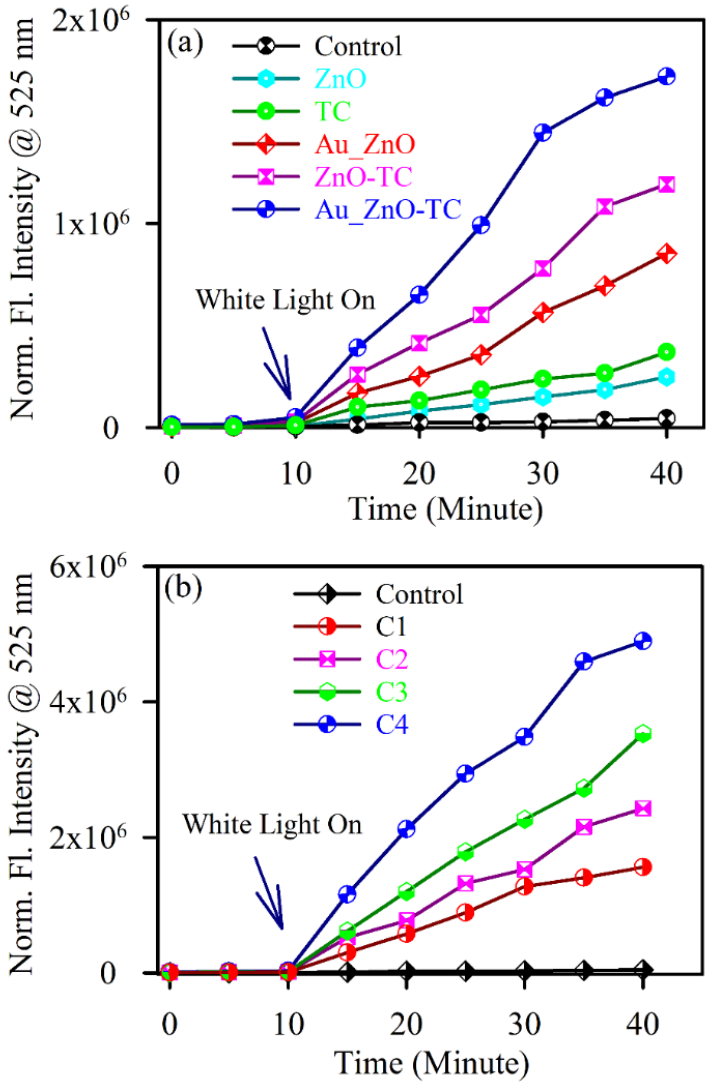

Figure 7.7: *(a) DCFH oxidation with respect to time with the addition of ZnO (cyan), TC (green), Au-TC (pink), Au-ZnO (red), Au_ZnO-TC (blue) and DCFH control (black). (b) Concentration-dependent DCFH oxidation of Au_ZnO-TC sample for four different concentrations. The experiment was performed in the dark for 10 minutes and then subsequent white-light irradiation for 30 minutes.*

In the case of Au_ZnO-TC tri-hybrid, the faster component of 52 ps attributes excited state photoelectron transfer [42]. It has to be stated that the time component of 272 ps could be an indicator of FRET from TC to Au nanoparticle [41]. To clarify FRET more specifically, we have introduced an insulator Al_2O_3 to make Au_Al_2O_3-TC tri-hybrid and measured time-resolved fluorescence transient. In this case, the faster time constant of 260 ps indicates the energy transfer from TC to Au nanoparticles as the possibility of an excited state photoelectron transfer process from TC to the Al_2O_3 insulator is insignificant. This implies that time constant of 260 ps (with contribution 36%) indicates the energy transfer from TC to Au.

Table 7.2: *Picosecond-resolved fluorescence transient lifetime. The excitation wavelength was 405 nm and the collection wavelength was 550 nm. Numbers in parentheses indicate relative contributions.*

Systems	τ_1 (ps)	τ_2 (ps)	τ_{avg} (ps)
TC	782 (21%)	2153 (79%)	1865
ZnO-TC	43 (54%)	291 (46%)	163
Au_Al_2O_3-TC	260 (36%)	1032 (64%)	785
Au_ZnO-TC	52 (34%)	272 (66%)	221

The fitting parameters of fluorescence transient are tabulated in Table 7.2. The efficiency of FRET is found to be 63% and FRET distance is found to be 1.9 nm which follows norms of FRET distance that is under 1-10 nm. Apart from that, the dipolar coupling between TC and Au also leads to electron transfer from Au to the conduction band of ZnO [43-45]. This indicates a huge extent of charge separation in the Au_ZnO-TC tri-hybrid upon excitation of TC using a visible light source. Enhancement of charge separation upon excitation of the Au_ZnO-TC tri-hybrid motivates us to measure the photoinduced generation of ROS. ROS production experiment has been performed using a well-known non-fluorescent marker dichlorofluorescein (DCFH). The change in ROS level is monitored by the enhancement of emission intensity peak at 525 nm for 10 minutes in the dark and then under irradiation of white light for 30 minutes. The enhancement of

ROS is observed in the presence of light for Au_ZnO-TC and ZnO-TC as compared to TC and other controls as shown in Figure 7.7a. The increment of ROS is occurred due to superoxide generated by free electrons from neighbouring oxygen molecules whereas hydroxyl radical is generated by holes from neighbouring water molecules [46-48].

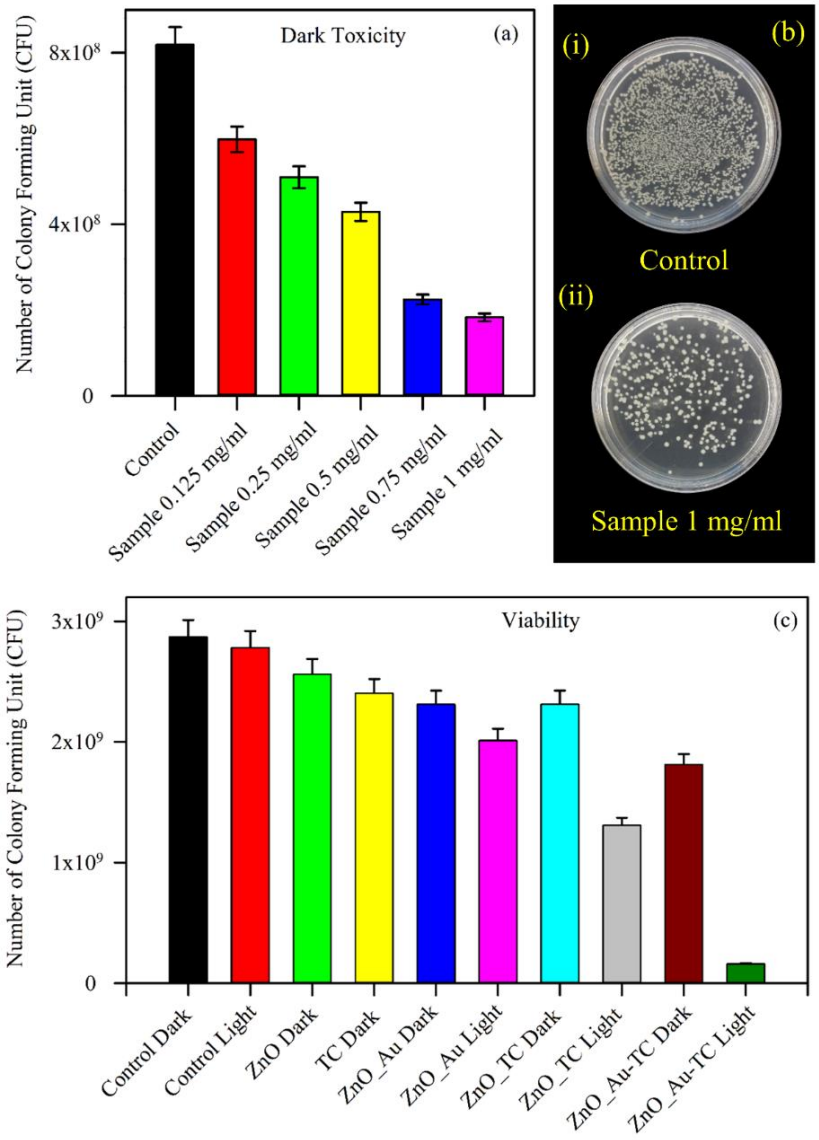

Figure 7.8: *(a) Optimization of bacterial viability in dark for different concentrations of Au_ZnO-TC samples with respect to control. (b) The images of S. hominis plates treated with Au_ZnO-TC sample; (i) the untreated plate of S. hominis bacteria, (ii) S. hominis bacteria treated by 1 mg/ml Au_ZnO-TC nanohybrid in the absence of light. (c) Bacterial viability of Au_ZnO-TC samples with respect to control.*

In case of tri-hybrid, concentration-dependent enhancement of ROS activity has also been performed for four different concentrations (C1, 5.2 µM; C2, 7.8 µM; C3, 10.4 µM and C4, 13.0 µM) at wavelength 525 nm) as depicted in Figure 7.7b.

The tri-hybrid shows greater ROS production capability when increasing the concentration which is due to a greater number of DCF formations with increasing concentration [49]. Besides the huge amount of charge separation in the Au_ZnO-TC nanohybrid upon excitation of TC, the white light (having a broad wavelength) irradiation facilitates direct excitation of Au which leads to electron migration process prom excited state of Au to CB of ZnO.

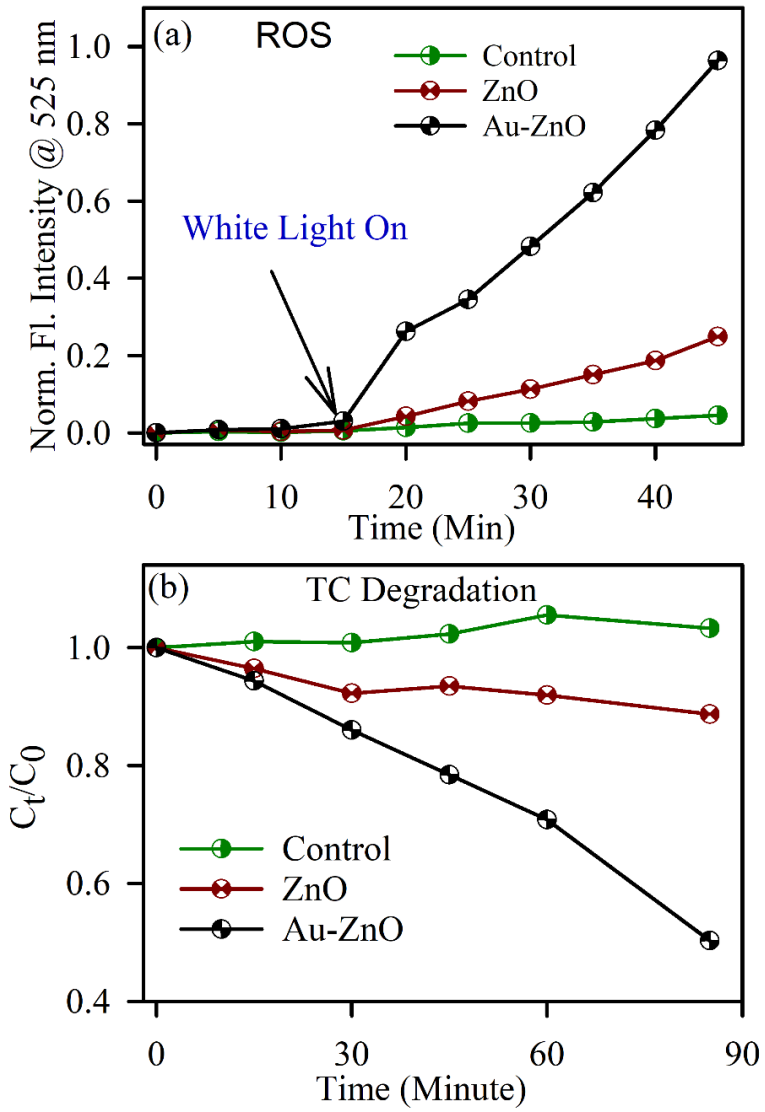

Figure 7.9: *(a) DCFH oxidation with respect to time with addition of ZnO (red), Au-ZnO (black) and DCFH control (green) under dark and subsequent white-light irradiation. (b) Kinetics of tetracycline degradation under white light illumination (control: green, ZnO: red and Au-ZnO: black).*

Overall, a greater extent of electron-hole separation in the Au_ZnO-TC nanohybrid induces a massive production of ROS under white light illumination (free electron combine with an oxygen molecule to generate the superoxide

radicals and holes are responsible for the generation of hydroxyl radicals from water molecule). Also, a significant amount of ROS production by Au_ZnO nanohybrid under white light supports the above explanation. The antibacterial activity of Au_ZnO-TC has been determined against *S. hominis* bacteria under white light irradiation. The dark toxicity nature of the samples has been checked by treated *S. hominis* bacteria with five different concentrations (0.125 mg/ml, 0.25 mg/ml, 0.5 mg/ml, 0.75 mg/ml and 1 mg/ml) of Au_ZnO-TC nanohybrid as shown in Figure 7.8a. Figure 7.8b depicts colony forming unit (CFU) image of *S. hominis* plates treated with Au_ZnO-TC sample; (i) control of *S. hominis* bacteria, (ii) 1 mg/ml sample of Au_ZnO-TC in the absence of light. The tri-hybrid has less antibacterial effect under dark for 0.25 mg/ml concentration with respect to controls.

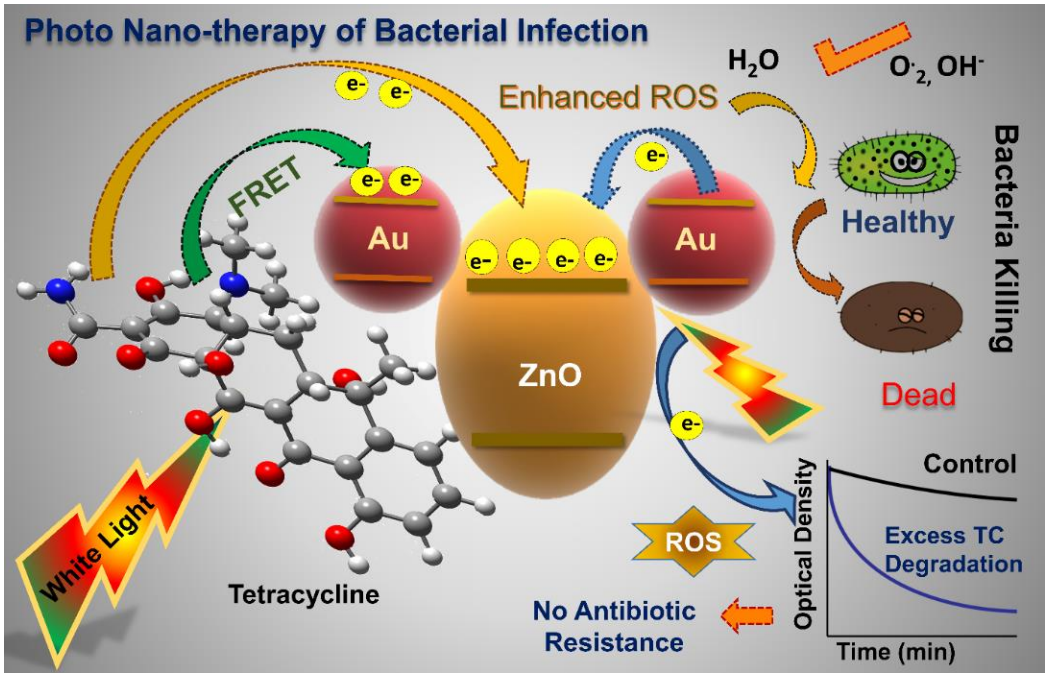

Scheme 7.2: *Schematic representation of photo nano-therapy of bacterial infection by Au_ZnO-TC tri-hybrids due to immense ROS production and metal hybrid (Au_ZnO) has the capability to destroy excess antibiotics which potentially reduces the chance of development of antibiotic resistance.*

Light irradiation treatment on *S. hominis* bacteria is carried out with the optimized concentration (0.25 mg/ml) of Au_ZnO-TC tri-hybrid. It shows enormous antimicrobial activity of Au_ZnO-TC nanohybrid in the presence of white light of wavelength 400-700 nm (89% in 30 minutes) due to enhanced ROS

production. The control experiments of only TC, ZnO, Au_ZnO and ZnO-TC have lesser antibacterial action against *S. hominis* in the presence of white light. Antibacterial experiments confirm the enhanced antimicrobial action of Au_ZnO-TC trihybrid. Furthermore, we found five times enhancement of ROS of Au_ZnO nanohybrid compared to ZnO in the presence of white light (Figure 7.9a). It motivates us to investigate TC degradation capability by Au_ZnO nanohybrid. It will help to degrade the remaining excess amount of TC, thus, the transmutation chances of TC antibiotic-resistant bacteria would be less. Figure 7.9b shows the kinetics of TC degradation by Au_ZnO hybrid due to ROS generation. The degradation percentage is found to be ~55% in 90 minutes, which implies that, after the treatment of bacterial infection, the excess amount of TC would be degraded by Au_ZnO. The results of this study confirm that the Au_ZnO-TC tri-hybrid nanomaterial has a potential antibacterial activity which further degrades the excess amount of TC by Au_ZnO in the presence of white light. The destroying excess antibiotic potentially reduces the chance of the development of antibiotic resistance.

7.3. Conclusion:

We have synthesized a new tri-hybrid material, Au-decorated ZnO nanoparticles attached to the TC drug. The morphology and composition of the samples are characterized by microscopic, ultrafast optical spectroscopic and DFT-based computational techniques. The DFT calculation of the hybrid material validates the experimental findings. We encapsulated an antibacterial agent TC with Au_ZnO system to make the Au_ZnO-TC tri-hybrid. The steady state photoluminescence and time-resolved fluorescence transient studies demonstrate the FRET from TC to Au as well as electron transfer from TC to ZnO in the Au_ZnO-TC tri-hybrid system. In addition to that the faster time resolved transient components of Au_Al_2O_3-TC further confirms FRET between TC and Au in Au_ZnO-TC tri-hybrid. It shows immense production of ROS in the presence of white light due to the enhanced charge transfer which improved the antibacterial activity of Au_ZnO-TC tri-hybrids against *S. hominis* bacteria.

Overall, the developed Au_ZnO-TC tri-hybrids show an enhanced antibacterial action due to immense ROS production and the metal hybrid (Au_ZnO) has capability to destroy excess antibiotics which potentially reduces the chance of development of antibiotic resistance.

References

[1] X. Xie, C. Mao, X. Liu, L. Tan, Z. Cui, X. Yang, S. Zhu, Z. Li, X. Yuan, Y. Zheng, K. W. K. Yeung, P. K. Chu, S. Wu, Tuning the bandgap of photo-sensitive polydopamine/Ag_3PO_4/Graphene oxide coating for rapid, noninvasive disinfection of implants, *ACS Cent. Sci.* 4 (2018) 724.

[2] H. Liu, J. Li, X. Liu, Z. Li, Y. Zhang, Y. Liang, Y. Zheng, S. Zhu, Z. Cui, S. Wu, Photo-sono interfacial engineering exciting the intrinsic property of herbal nanomedicine for rapid broad-spectrum bacteria killing, *ACS Nano* 15 (2021) 18505.

[3] C. Mao, Y. Xiang, X. Liu, Z. Cui, X. Yang, Z. Li, S. Zhu, Y. Zheng, K. W. K. Yeung, S. Wu, Repeatable photodynamic therapy with triggered signaling pathways of fibroblast cell proliferation and differentiation to promote bacteria-accompanied wound healing, *ACS Nano* 12 (2018) 1747.

[4] D. Welch, M. Buonanno, V. Grilj, I. Shuryak, C. Crickmore, A. W. Bigelow, G. Randers-Pehrson, G. W. Johnson, D. J. Brenner, Far-UVC light: A new tool to control the spread of airborne-mediated microbial diseases, *Sci. Rep.* 8 (2018) 2752.

[5] W. Bian, Y. Wang, Z. Pan, N. Chen, X. Li, W.-L. Wong, X. Liu, Y. He, K. Zhang, Y.-J. Lu, Review of functionalized nanomaterials for photothermal therapy of cancers, *ACS Appl. Nano Mater.* 4 (2021) 11353.

[6] Y. Qiao, X. Liu, B. Li, Y. Han, Y. Zheng, K. W. K. Yeung, C. Li, Z. Cui, Y. Liang, Z. Li, S. Zhu, X. Wang, S. Wu, Treatment of MRSA-infected osteomyelitis using bacterial capturing, magnetically targeted composites with microwave-assisted bacterial killing, *Nat. Commun.* 11 (2020) 4446.

[7] B. Huang, L. Tan, X. Liu, J. Li, S. Wu, A facile fabrication of novel stuff with antibacterial property and osteogenic promotion utilizing red phosphorus and near-infrared light, *Bioact. Mater.* 4 (2019) 17.

[8] A. K. Nanayakkara, H. W. Boucher, V. G. Fowler Jr, A. Jezek, K. Outterson, D. E. Greenberg, Antibiotic resistance in the patient with cancer: Escalating challenges and paths forward, *CA Cancer J. Clin.* 71 (2021) 488.

[9] Y. Ren, Y. Han, Z. Li, X. Liu, S. Zhu, Y. Liang, K. W. K. Yeung, S. Wu, Ce and Er Co-doped TiO_2 for rapid bacteria- killing using visible light, *Bioact. Mater.* 5 (2020) 201.

[10] I. Chopra, M. Roberts, Tetracycline antibiotics: Mode of action, applications, molecular biology, and epidemiology of bacterial resistance, *Microbiol. Mol. Biol. Rev.* 65 (2001) 232.

[11] M. N. Hasan, A. Bera, T. K. Maji, S. K. Pal, Sensitization of nontoxic MOF for their potential drug delivery application against microbial infection, *Inorg. Chim. Acta* 523 (2021) 120381.

[12] J. Li, Z. Li, X. Liu, C. Li, Y. Zheng, K. W. K. Yeung, Z. Cui, Y. Liang, S. Zhu, W. Hu, Y. Qi, T. Zhang, X. Wang, S. Wu, Interfacial engineering of $Bi_2S_3/Ti_3C_2T_x$ MXene based on work function for rapid photo-excited bacteria-killing, *Nat. Commun.* 12 (2021) 1224.

[13] M. R. Hamblin, H. Abrahamse, Tetracyclines: Light-activated antibiotics?, *Future Med. Chem.* 11 (2019) 2427.

[14] Y. He, Y.-Y. Huang, L. Xi, J. A. Gelfand, M. R. Hamblin, Tetracyclines function as dual-action light-activated antibiotics, *PLoS One* 13 (2018) e0196485.

[15] D. Han, Y. Li, X. Liu, K. W. K. Yeung, Y. Zheng, Z. Cui, Y. Liang, Z. Li, S. Zhu, X. Wang, S. Wu, Photothermy-strengthened photocatalytic activity of polydopamine-modified metal-organic frameworks for rapid therapy of bacteria-infected wounds, *J. Mater. Sci. Technol.* 62 (2021) 83.

[16] Y. Li, X. Liu, L. Tan, Z. Cui, X. Yang, Y. Zheng, K. W. K. Yeung, P. K. Chu, S. Wu, Rapid sterilization and accelerated wound healing using Zn^{2+} and graphene oxide modified g-C_3N_4 under dual light irradiation, *Adv. Funct. Mater.* 28 (2018) 1800299.

[17] K. Su, L. Tan, X. Liu, Z. Cui, Y. Zheng, B. Li, Y. Han, Z. Li, S. Zhu, Y. Liang, X. Feng, X. Wang, S. Wu, Rapid photo-sonotherapy for clinical treatment of bacterial infected bone implants by creating oxygen deficiency using sulfur doping, *ACS Nano* 14 (2020) 2077.

[18] W. Gao, Y. Chen, Y. Zhang, Q. Zhang, L. Zhang, Nanoparticle-based local antimicrobial drug delivery, *Adv. Drug Deliv. Rev.* 127 (2018) 46.

[19] W. Guan, L. Tan, X. Liu, Z. Cui, Y. Zheng, K. W. K. Yeung, D. Zheng, Y. Liang, Z. Li, S. Zhu, X. Wang, S. Wu, Ultrasonic interfacial engineering of red phosphorous–metal for eradicating MRSA infection effectively, *Adv. Mater.* 33 (2021) 2006047.

[20] S. Wei, Y. Qiao, Z. Wu, X. Liu, Y. Li, Z. Cui, C. Li, Y. Zheng, Y. Liang, Z. Li, S. Zhu, H. Wang, X. Wang, R. Che, S. Wu, Na^+ inserted metal-organic framework for rapid therapy of bacteria-infected osteomyelitis through microwave strengthened fenton reaction and thermal effects, *Nano Today* 37 (2021) 101090.

[21] C. Mao, Y. Xiang, X. Liu, Z. Cui, X. Yang, K. W. K. Yeung, H. Pan, X. Wang, P. K. Chu, S. Wu, Photo-inspired antibacterial activity and wound healing acceleration by hydrogel embedded with Ag/Ag@AgCl/ZnO nanostructures, *ACS Nano* 11 (2017) 9010.

[22] Y. Zhang, X. Liu, Z. Li, S. Zhu, X. Yuan, Z. Cui, X. Yang, P. K. Chu, S. Wu, Nano Ag/ZnO-incorporated hydroxyapatite composite coatings: Highly effective infection prevention and excellent osteointegration, *ACS Appl. Mater. Interfaces* 10 (2018) 1266.

[23] Y. Xiang, Q. Zhou, Z. Li, Z. Cui, X. Liu, Y. Liang, S. Zhu, Y. Zheng, K. W. K. Yeung, S. Wu, A Z-scheme heterojunction of ZnO/CDots/C_3N_4 for strengthened photoresponsive bacteria-killing and acceleration of wound healing, *J. Mater. Sci. Technol.* 57 (2020) 1.

[24] A. Nawaz, S. Goudarzi, M. A. Asghari, S. Pichiah, G. S. Selopal, F. Rosei, Z. M. Wang, H. Zarrin, Review of hybrid 1D/2D photocatalysts for light-harvesting applications, *ACS Appl. Nano Mater.* 4 (2021) 11323.

[25] S. A. Ahmed, M. N. Hasan, D. Bagchi, H. M. Altass, M. Morad, I. I. Althagafi, A. M. Hameed, A. Sayqal, A. E. R. S. Khder, B. H. Asghar, H. A. Katouah, S. K. Pal, Nano-MOFs as targeted drug delivery agents to combat antibiotic-resistant bacterial infections, *R. Soc. Open Sci.* 7 (2020) 200959.

[26] A. C. Gomathi, S. R. Xavier Rajarathinam, A. Mohammed Sadiq, S. Rajeshkumar, Anticancer activity of silver nanoparticles synthesized using aqueous fruit shell extract of Tamarindus indica on MCF-7 human breast cancer cell line, *J. Drug Deliv. Sci. Technol.* 55 (2020) 101376.

[27] Z.-Y. Zhang, Y.-D. Xu, Y.-Y. Ma, L.-L. Qiu, Y. Wang, J.-L. Kong, H.-M. Xiong, Biodegradable ZnO@polymer core–shell nanocarriers: pH-triggered release of doxorubicin *in vitro*, *Angew. Chem. Int. Ed.* 52 (2013) 4127.

[28] D. Bagchi, V. S. S. Rathnam, P. Lemmens, I. Banerjee, S. K. Pal, NIR-light-active ZnO-based nanohybrids for bacterial biofilm treatment, *ACS Omega* 3 (2018) 10877.

[29] M. N. Hasan, T. K. Maji, U. Pal, A. Bera, D. Bagchi, A. Halder, S. A. Ahmed, J. H. Al-Fahemi, T. M. Bawazeer, T. Saha-Dasgupta, S. K. Pal, Wide bandgap semiconductor-based novel nanohybrid for potential antibacterial activity: Ultrafast spectroscopy and computational studies, *RSC Adv.* 10 (2020) 38890.

[30] E. Lee, C. Kim, J. Jang, High-performance förster resonance energy transfer (FRET)-based Dye-sensitized solar cells: Rational design of quantum dots for wide solar-spectrum utilization, *Chem. Eur. J.* 19 (2013) 10280.

[31] S. Sarkar, A. Makhal, K. Lakshman, T. Bora, J. Dutta, S. Kumar Pal, Dual-sensitization via electron and energy harvesting in CdTe quantum dots decorated ZnO nanorod-based dye-sensitized solar cells, *J. Phys. Chem. C* 116 (2012) 14248.

[32] M. Ambapuram, R. Ramireddy, G. Maddala, S. Godugunuru, P. V. S. Yerva, R. Mitty, Effective upconverter and light scattering dual function $LiYF_4:Er^{3+}/Yb^{3+}$ assisted photoelectrode for high performance cosensitized dye sensitized solar cells, *ACS Appl. Electron. Mater.* 2 (2020) 962.

[33] S. A. Ahmed, M. N. Hasan, H. M. Altass, A. Bera, R. I. Alsantali, N. Pan, A. Y. A. Alzahrani, D. Bagchi, J. H. Al-Fahemi, A. S. Khder, S. K. Pal, Tetracycline encapsulated in Au nanoparticle-decorated ZnO nanohybrids for enhanced antibacterial activity, *ACS Appl. Nano Mater.* 5 (2022) 4484.

[34] A. Chatterjee, P. Kar, D. Wulferding, P. Lemmens, S. K. Pal, Flower-like BiOI microspheres decorated with plasmonic gold nanoparticles for dual detoxification of organic and inorganic water pollutants, *ACS Appl. Nano Mater.* 3 (2020) 2733.

[35] F. Hu, H. Lin, Z. Zhang, F. Liao, M. Shao, Y. Lifshitz, S.-T. Lee, Smart liquid SERS substrates based on Fe_3O_4/Au nanoparticles with reversibly tunable enhancement factor for practical quantitative detection, *Sci. Rep.* 4 (2014) 7204.

[36] T. Afshari, M. Mohsennia, Transition metals doped ZnO nanocluster for ethylene oxide detection: A DFT study, *Main Group Met. Chem.* 42 (2019) 113.

[37] O. V. de Oliveira, J. M. Pires, A. C. Neto, J. D. dos Santos, Computational studies of the $Ca_{12}O_{12}$, $Ti_{12}O_{12}$, $Fe_{12}O_{12}$ and $Zn_{12}O_{12}$ nanocage clusters, *Chem. Phys. Lett.* 634 (2015) 25.

[38] H. Y. Ammar, H. M. Badran, A. Umar, H. Fouad, O. Y. Alothman, ZnO nanocrystal-based chloroform detection: Density functional theory (DFT) study, *Coatings* 9 (2019) 769.

[39] S. Chaudhuri, S. Sardar, D. Bagchi, S. Dutta, S. Debnath, P. Saha, P. Lemmens, S. K. Pal, Photoinduced dynamics and toxicity of a cancer drug in proximity of inorganic nanoparticles under visible light, *ChemPhysChem* 17 (2016) 270.

[40] S. E. Koops, B. C. O'Regan, P. R. F. Barnes, J. R. Durrant, Parameters influencing the efficiency of electron injection in dye-sensitized solar cells, *J. Am. Chem. Soc.* 131 (2009) 4808.

[41] J. Patwari, A. Chatterjee, S. Sardar, P. Lemmens, S. K. Pal, Ultrafast dynamics in co-sensitized photocatalysts under visible and NIR light irradiation, *Phys. Chem. Chem. Phys.* 20 (2018) 10418.

[42] D. Bagchi, V. S. Rathnam, P. Lemmens, I. Banerjee, S. K. Pal, NIR-Light-active ZnO-based nanohybrids for bacterial biofilm treatment, *ACS omega* 3 (2018) 10877.

[43] P. Reineck, D. Gómez, S. H. Ng, M. Karg, T. Bell, P. Mulvaney, U. Bach, Distance and wavelength dependent quenching of molecular fluorescence by Au@ SiO2 core–shell nanoparticles, *ACS nano* 7 (2013) 6636.

[44] S. T. Kochuveedu, T. Son, Y. Lee, M. Lee, D. Kim, D. H. Kim, Revolutionizing the FRET-based light emission in core-shell nanostructures *via* comprehensive activity of surface plasmons, *Sci. Rep.* 4 (2014) 4735.

[45] W. R. Erwin, H. F. Zarick, E. M. Talbert, R. Bardhan, Light trapping in mesoporous solar cells with plasmonic nanostructures, *Energy Environ. Sci.* 9 (2016) 1577.

[46] Y. Chen, D. Zeng, K. Zhang, A. Lu, L. Wang, D.-L. Peng, Au–ZnO hybrid nanoflowers, nanomultipods and nanopyramids: One-pot reaction synthesis and photocatalytic properties, *Nanoscale* 6 (2014) 874.

[47] Z. Kang, X. Yan, L. Zhao, Q. Liao, K. Zhao, H. Du, X. Zhang, X. Zhang, Y. Zhang, Gold nanoparticle/ZnO nanorod hybrids for enhanced reactive oxygen species generation and photodynamic therapy, *Nano Research* 8 (2015) 2004.

[48] W. He, H.-K. Kim, W. G. Wamer, D. Melka, J. H. Callahan, J.-J. Yin, Photogenerated charge carriers and reactive oxygen species in ZnO/Au hybrid nanostructures with enhanced photocatalytic and antibacterial activity, *J. Am. Chem. Soc.* 136 (2014) 750.

[49] M. N. Hasan, A. Bera, T. K. Maji, D. Mukherjee, N. Pan, D. Karmakar, S. K. Pal, Functionalized nano-MOF for NIR induced bacterial remediation: A

combined spectroscopic and computational study, *Inorg. Chim. Acta* 532 (2022) 120733.

Chapter 8

Synthesis and Optical Spectroscopic Studies on Properties of Nanohybrids after Doping with Ions for their Potential Applications

8.1. Introduction:

Essential metals such as, cobalt (Co), iron (Fe), chromium (Cr), copper (Cu), nickel (Ni), manganese (Mn), molybdenum (Mo), zinc (Zn) and selenium (Se) are fundamental supplements that are essential for several physiological and biochemical purposes [1, 2]. Nevertheless, a portion of these substantial metals in high dosages can be dangerous to the body, while others (for example cadmium, mercury, lead, chromium, silver, and arsenic) in minute amounts, have incoherent impacts in the body causing critical and chronic toxicities in humans [3, 4]. Excess amounts of essential metals are source of neurotoxicity. Moreover, excess metal in the human body can generate free radicals which can increase the oxidative stress and can destroy lipids, proteins and DNA molecules. These free radicals also promote carcinogenesis. Excess amount of iron has largely been reported to be one of the reasons for death in children [5, 6] and has a long history of research in therapeutics [7, 8]. After the discovery of numerous oral medicines for iron toxicity, child mortalities are under control but rigorous poisonings due to excess iron still take place [9].

So far, chelation therapy is the most powerful and commonly utilized strategy for the treatment of substantial metal over-burden and related to the mitigation of several diseases such as Parkinson's, Alzheimer's, Wilson's ailment, and Friedreich's ataxia [10]. The most commonly utilized chelating agents such as $CaNa_2EDTA$ – 1985 [8]; BAL – 1949 [8]; DMSA – 1978 [11]; DMPS – 1958 [12] were utilized to treat metal over-burden issues for a long time. However, these chelators have adverse effects creating harmful impacts that may damage a few

fundamental organs [13, 14]. The accumulation of the substantial amount of metals in the cerebrum by some chelators can affect the intellectual capacity of teenagers [15]. Thus, nanoscience related innovation can open a new approach for the treatment of metal toxicity related issues [16, 17]. Various *in vitro* investigations have portrayed the capacity of metallic nanoparticles to tie or detect the excess amount of metals [6, 18]. For example, nanosized silver and gold particles can agglomerate with the bivalent metal ions such as mercury (Hg^{2+}), copper (Cu^{2+}), iron (Fe^{2+}) and lead (Pb^{2+}) which can shift the surface plasmon band, useful for detection purpose [19-21]. However, low biocompatibility limits their *in vivo* applications [19]. In the present study, we have developed new technique that could be a potential option for the treatment of substantial cationic metal poisoning.

Among all the cationic metals, iron is an essential mineral in the human body as it constitutes the important biological molecule hemoglobin and thus maintains the proper iron balance in the body which is important to regulate different physiological activities [22]. Nevertheless, iron is one of the heavy metals commonly known to produce hydroxyl radicals (•OH) [23]. Excess amount of iron leads to greater formation of free radicals that can cause carcinogenesis [24]. Iron-instigated free radicals can produce malignancy by oxidation of DNA, prompting to DNA damage [25]. In this work, through various spectroscopy tools, we have investigated the different properties of the synthesized Fe-Cur complex which provides us with the details of Fe-chelating action by promising chelator curcumin. We have also investigated whether the synthesized complex provides antioxidant activity. The role of metal particles in the antioxidant action of the complex is assessed in detail using a well-known radical scavenger 2, 2-diphenyl-1-picrylhydrazyl (DPPH) in aqueous media under light irradiation as well as under dark condition. This analysis reveals that the antioxidant activity of the curcumin increases after the chelation of Fe and consequent decrease is also observed in free radical generation under dark. We have extended our studies on ROS in an aqueous solution which show this complex does not generate any significant ROS in the dark. The results validate its acceptability as

a therapeutic agent. Femtosecond resolved fluorescence studies further highlight the mechanistic approach of the therapeutic activity of the metal-ligand complex. Through the photophysical study, it has been found that the ligand to metal charge transfer plays a key role to control the entire ROS generation and radical scavenging activity of the proposed complex. For a comparison of the activity and probable side effects of the Fe-Cur complex, we have introduced and investigated another transition metal complex with the ligand curcumin (Zn-Cur). Although, these two complexes are structurally similar, the difference in electronic distribution causes a decreased efficiency in the activities. The trend in radical scavenging activity is observed to be similar for both the metal curcumin complexes which validate the role of electron transfer in controlling the activities of the complex. Thus, the entire study provides a deep insight into the photophysical behaviour of a potential chelation therapeutic agent curcumin in mitigation of iron toxicity with validation of *in vitro* applications that may uncover a dual activity nanotherapeutic approach in the future.

8.2. Results and Discussion:

8.2.1. Combating Essential Metal Toxicity: Key Information from Optical Spectroscopy [15]: The schematic representation of Fe-Cur complexes is depicted in Figure 8.1a and the photographs of curcumin (yellow) and Fe-Cur (brown) in the DMSO solvent under visible light are shown in Figure 8.1b. The formation of metallo-organic complexes causes significant alterations in the electronic configuration of the free ligands. UV-visible absorption spectroscopy is a suitable method to determine complexation or metalation. Figure 8.1c represents the absorption spectra of $FeCl_3$ (blue) with an absorption peak of 340 nm and curcumin (black) with a peak of 435 nm in DMSO solvent. The inset shows the absorption maximum of $FeCl_3$ (blue) with an absorption peak of 390 nm and curcumin (black) appears at 440 nm in an aqueous solvent. The absorption peaks of the ligand curcumin can be assigned to a π–π^* transition from (HOMO-1) to (LUMO) and (HOMO) to (LUMO) respectively [26]. The blue

shift in the absorption spectra of curcumin after attachment to the metal particle provides a signature of the covalent attachment. For the Fe–curcumin, a clear peak can be observed at 440 nm, with a wide absorption peak at around 520 nm in DMSO as well as in water as shown in Figure 8.1c (red). Some earlier reports [27, 28] have depicted the comparative FTIR and NMR spectra of Fe-Cur with curcumin and concluded effective complex formation. The room temperature steady-state PL spectrum (Figure 8.2a) of curcumin (black) shows a peak at 520 nm upon excitation at 400 nm in DMSO solvent and the inset shows the same measurement in aqueous solvent. However, after metalation with iron, the steady-state emission intensity is significantly quenched (in both the solvents) in spite of the fact that the absorption peak of the complex in both the solutions are comparable.

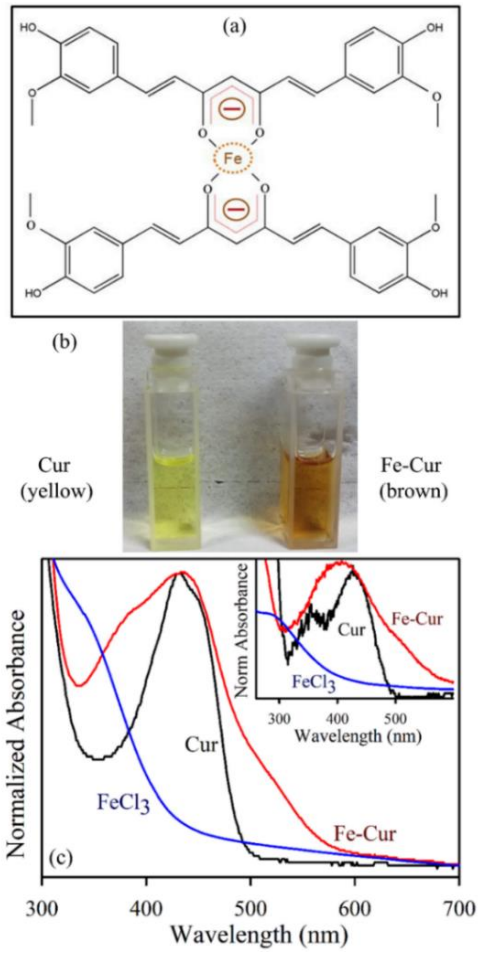

Figure 8.1: *(a) Schematic representation of Fe-Cur complexes. (b) Photographs of curcumin (Cur) and Fe–Cur in DMSO under visible light (c) Absorption spectra of $FeCl_3$ (blue), Cur (black), Fe–Cur (red) using DMSO as the solvent. Inset shows the absorption spectra of $FeCl_3$ (blue), Cur (black), and Fe–Cur (red) using water as the solvent.*

The observation leads to the possibility of non-radiative charge transfer [29]. Figure 8.2b shows the excitation spectra of all the samples in DMSO solvent and the inset shows the excitation of all the samples in an aqueous solvent. A significant decrease in intensity for both emission and excitation spectra after the metalation can be ascribed to the signature of complexation as well as non-radiative charge transfer from the ligand (Cur) to the chelated metal ion.

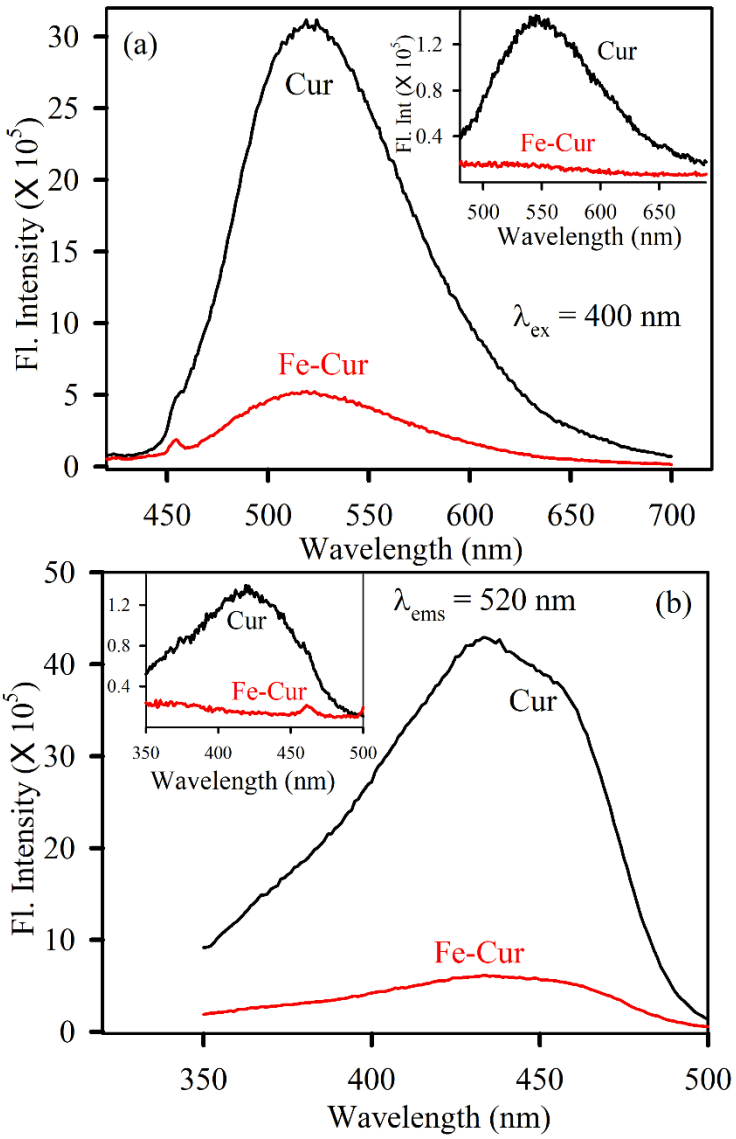

Figure 8.2: *(a) Room-temperature emission spectra of Cur (black), Fe–Cur (red) in DMSO are shown. The excitation wavelength was 400 nm. Inset shows the emission of the same samples using water as a solvent. (b) Room temperature excitation spectra of Cur (black), Fe–Cur (red) in DMSO are shown. The emission wavelength was set at 530 nm. Inset shows the excitation of the same samples using water as a solvent.*

There is also a possibility of the development of a new energetically low lying charge-transfer state due to the electronic transition from curcumin to the

chelated metal. The curcumin moiety having delocalized π-electron density behaves as a donor to the positively charged metal center (which has empty d-orbitals) behaving as an acceptor and exhibiting a ligand to metal charge transfer band (LMCT) [30, 31].

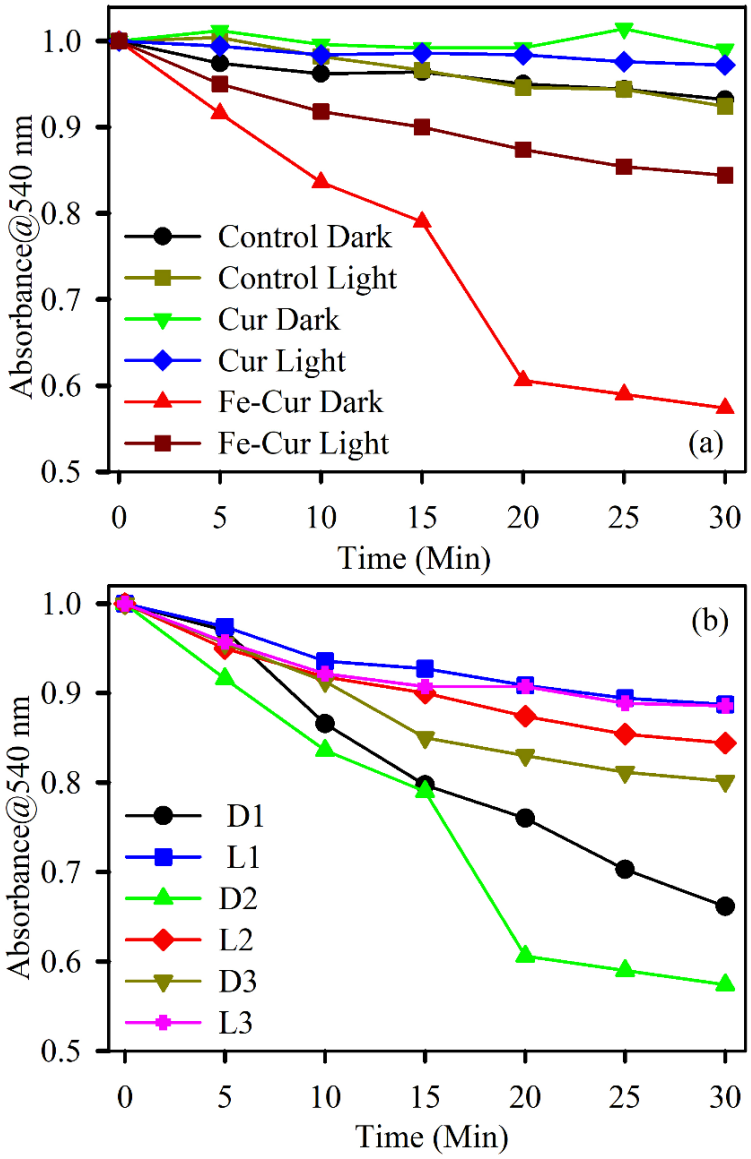

Figure 8.3: *Absorption kinetics of DPPH degradation (monitored at 540 nm) (a) in the absence of light using samples Cur (green), Fe–Cur (red) and in the presence of green light with Cur (blue), Fe–Cur (brown). (b) In the absence and presence of light using samples Fe–Cur with variable concentration.*

Figure 8.3a demonstrates the antioxidant activities of curcumin and Fe–Cur complex in the dark as well as under green light irradiation under constant stirring conditions. The antioxidant activity of samples is observed by the decolorization kinetics of stable free radical DPPH in ethanol-water mixture [32].

DPPH, a stable free radical having violet colour, is reduced to $DPPH_2$, which is yellow in colour, due to donation of an H-atom from polyphenolic antioxidants to the radical [33]. As the DPPPH assay is performed under stirring conditions, there is no possibility of precipitation.

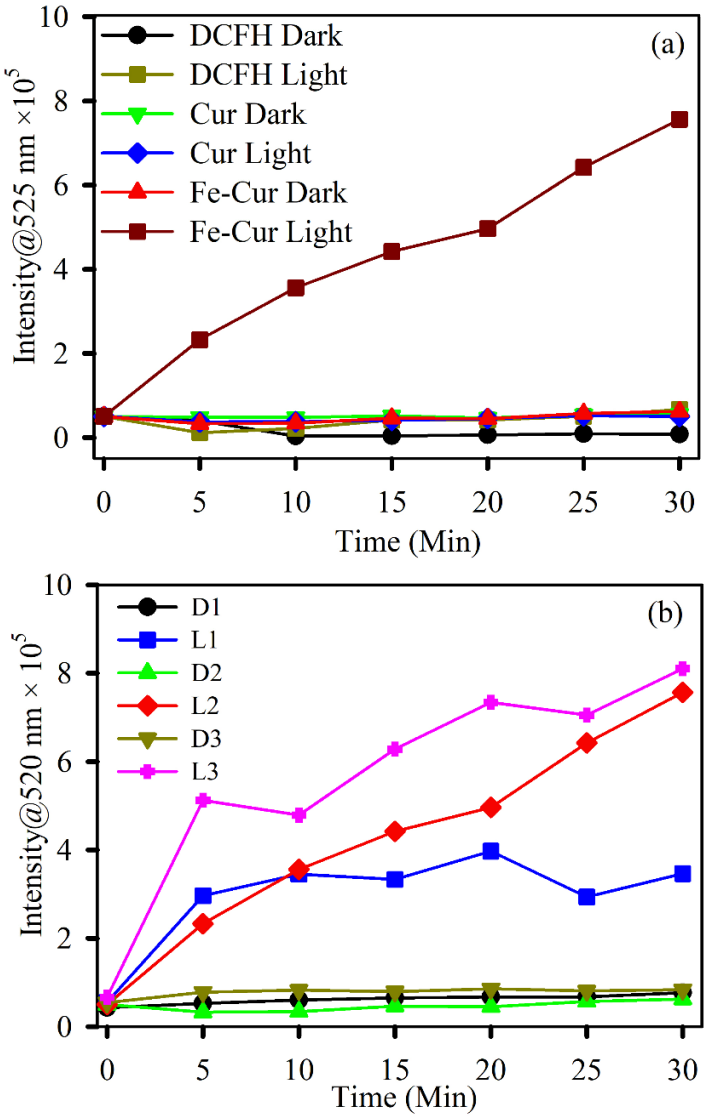

Figure 8.4: *DCFH oxidation (monitored at 520 nm) with time in absence and presence of light with (a) the samples Cur (green) and Fe-Cur (red) and in presence of light with Cur (blue), Fe–Cur (brown), (b) using samples Fe–Cur with variable concentration. The excitation wavelength was 488 nm.*

Figure 8.3a shows an increase in radical scavenging activity for Fe-Cur in the dark whereas under green light conditions no effect has been observed in this assay. The electronic configuration of Fe (at ground state) allows it to capture electron density from the peripheral O-H bond and initiate the breaking of peripheral O-H bond [26]. Thus, it can show more antioxidant properties.

However, in case of light irradiated system, the electronic configuration alters significantly in Fe-Cur complex. This may induce stability in the complex which could lead to less electron affinity of the metal center, which causes a lower antioxidant activity. Thus, the improved anti-oxidant property for Fe–Cur in dark credits to a more vulnerable ArO–H bond in curcumin and a resulting simpler H-atom loss process [34]. The dose-dependent antioxidant activities of Fe-Cur have been performed up to three different concentrations (OD 0.07, 0.10 and 0.15) as shown in Figure 8.3b. It has been observed that the antioxidant capability of Fe-Cur increases more for the concentration of OD 0.10 compared to the other two concentrations in the dark (Figure 8.3b). The results demonstrate that Fe–Cur serves as an extremely effective free-radical scavenger compared to free curcumin in water in the absence of light.

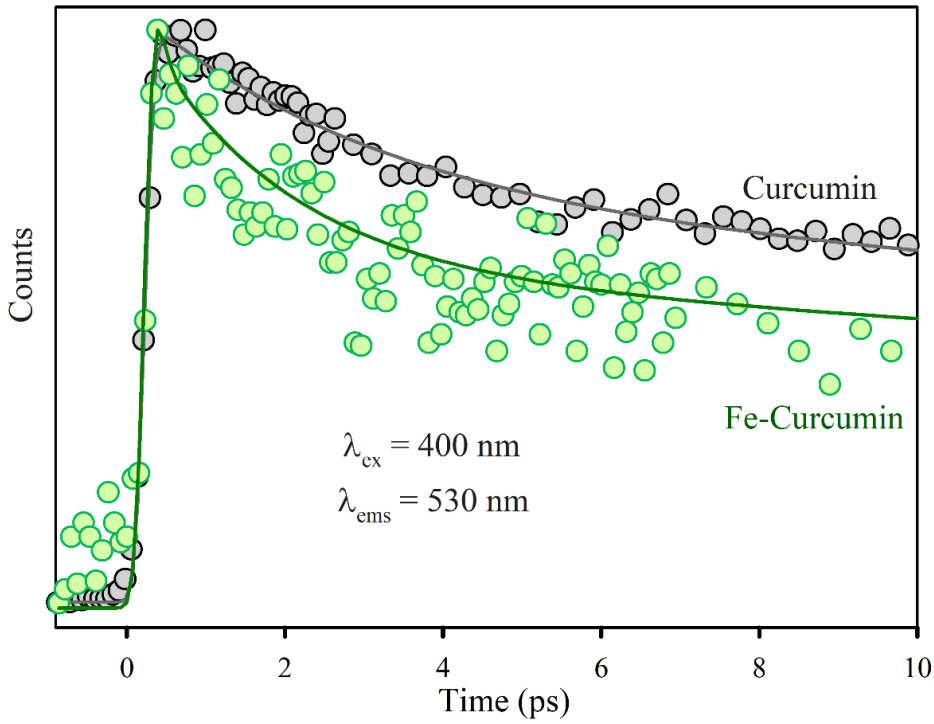

Figure 8.5: *Femtosecond resolved fluorescence transients of Cur (grey), Fe–Cur (green) in DMSO. The excitation wavelength was at 400 nm and the detection wavelength was at 530 nm. The circles are experimental data, and the solid lines are the best multiexponential fit.*

We have assessed the ROS generation capability by Fe-Cur with respect to curcumin by performing the DCFH assay in the presence of light and dark as well. The rise in the emission intensity of DCF which is the oxidized form of DCFH has been monitored to quantify the amount of ROS in the system. Fe-Cur

complex shows 8.5 times additional ROS generation compared to curcumin under the green light irradiated condition, as represented in Figure 8.4a. The dose-dependent capability of Fe-Cur has been performed up to three different concentrations (OD 0.07, 0.10 and 0.15) as shown in Figure 8.4b. It has been observed that the ROS generation capability of Fe-Cur increases with increasing concentration (Figure 8.4b) in the presence of green light. Fe-Cur almost doesn't generate any ROS in the absence of light.

Table 8.1: *Lifetime of femtosecond-resolved fluorescence transients of Cur and Fe-Cur complexes, detected at 530 nm (PL maxima) upon excitation at 400 nm wavelength. Numbers in parentheses indicate relative contributions.*

System	τ_1 (ps)	τ_2 (ps)	τ_3 (ps)	τ_{avg} (ps)
Cur	3.19 (32%)	73.50 (68%)	-	50.50
Fe-Cur	0.09 (32%)	1.82 (28%)	62 (40%)	25.60

Femtosecond resolved fluorescence transients of Fe-Cur samples have been measured to find out the excited state dynamics of the complex which provide further evidence of the metal ligand chelation. The femtosecond resolved decay profiles of the free ligand curcumin and the Fe-Cur complex are compared in Figure 8.5.

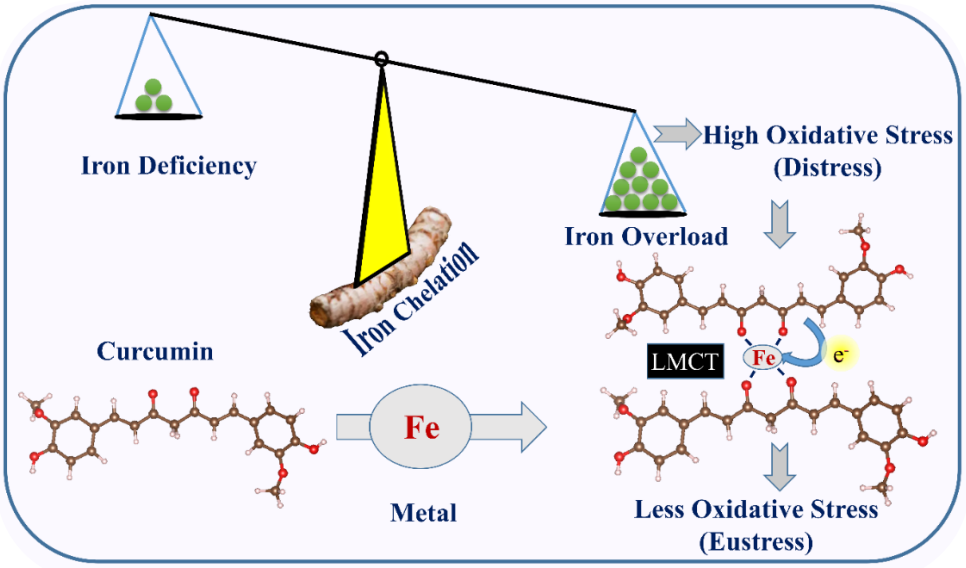

Scheme 8.1: *Schematic view of iron chelation by the formation of Fe-Cur complex leading to efficient radical scavenging activity for the effective treatment of iron overload diseases.*

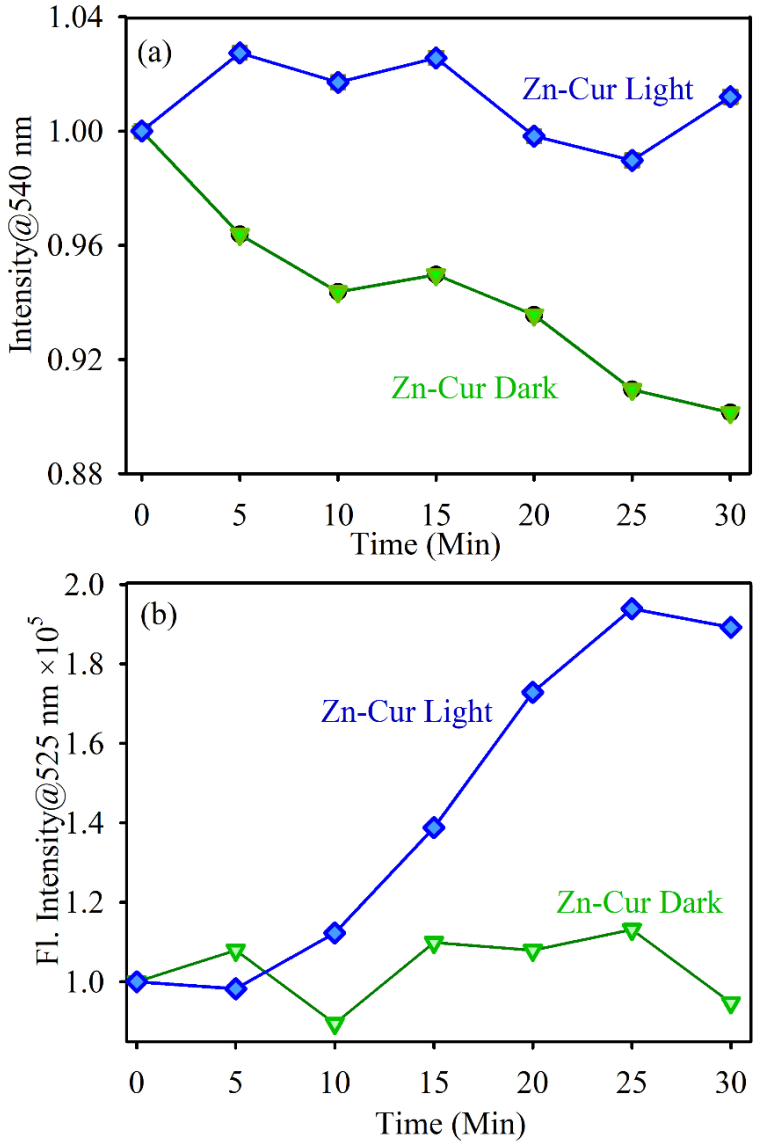

Figure 8.6: *(a) Depicts the absorption kinetics of DPPH degradation (monitored at 520 nm) in the absence and presence of light using Zn-Cur. (b) DCFH in the absence and presence of light using samples Zn–Cur. The excitation was at 488 nm.*

The fluorescence decay of curcumin is fitted by a double exponential decay with a lifetime of 3.2 ps (faster part: mark of solvation dynamics) and another 73.5 ps (longer part: sign for excited state intramolecular H atom transfer ESIHT) [35]. The average lifetime of the system is 50.5 ps. The femtosecond resolved decay profile of Fe-Cur shows a faster time component of 0.09 ps and the corresponding average lifetime is 25.6 ps. The lifetime components of the fluorescence transients are summarized in Table 8.1. The faster timescale in the decay pattern of the Fe-Cur complex could be ascribed to the electron transfer from the ligand to the chelated metal centre [36]. Therefore, this electron transfer

process can be correlated to enhanced antioxidant activity and photoinduced ROS generation by Fe-Cur. Additionally, we have performed an antioxidant activity and photoinduced ROS generation by Zn-Cur complex in order to compare its activity with the Fe-Cur one. It has been found that the antioxidant activity of Zn-Cur is increasing under dark but the increment is much less as compared to Fe-Cur. The trend is due to the presence of a stronger O-H bond in the case of the Zn-Cur complex as Zn(II) has a filled *d*-orbital and shows lower interactions compared to Fe(II) [37]. Figure 8.6b shows the ROS generation capability of Zn-Cur in the presence of green light (blue) and the absence of light (red). The ROS of Zn-Cur is increasing but the ability is much less than Fe-Cur. Therefore, antioxidant activity and photoinduced ROS generation by Zn-Cur is consistent with the Fe-Cur results. However, the activity of Fe-Cur is far better than Zn-Cur.

8.3. Conclusion:

In summary, the biocompatible ligand curcumin shows a high affinity to chelate with metallic Fe. Curcumin is known to have less or minimal side effects. So, it can be used as an alternative to conventional chelating agents. The Fe-Cur has enhanced antioxidant activity and negligible ROS generation capability in the dark. The prominent ligand to metal charge transfer in the case of the Fe-Cur complex is found to be the mechanistic pathway to control the radical scavenging and the ROS generation trends. The proposed mechanism has further been validated by a comparison of activity with the structural analogue Zn-Cur. Thus, the electron rearrangement process in the Fe-Cur complex leading to efficient radical scavenging activity may pave a new way for the effective treatment of iron overload diseases and can be considered as an alternative medicine.

References

[1] P. C. Nagajyoti, K. D. Lee, T. Sreekanth, Heavy metals, occurrence and toxicity for plants: A review, *Environ. Chem. Lett.* 8 (2010) 199.

[2] K. Soetan, C. Olaiya, O. Oyewole, The importance of mineral elements for humans, domestic animals and plants-A review, *Afr. J. Food Sc.* 4 (2010) 200.

[3] M. Mahurpawar, Effects of heavy metals on human health, *Int. J. Res.* 530 (2015) 1.

[4] V. Mudgal, N. Madaan, A. Mudgal, R. Singh, S. Mishra, Effect of toxic metals on human health, *Open Nutraceut J.* 3 (2010) 94.

[5] P. B. Tchounwou, C. G. Yedjou, A. K. Patlolla, D. J. Sutton, Heavy metal toxicity and the environment in molecular, clinical and environmental toxicology, *Springer*, New York, 2012.

[6] D. N. Juurlink, M. Tenenbein, G. Koren, D. A. Redelmeier, Iron poisoning in young children: Association with the birth of a sibling, *CMAJ* 168 (2003) 1539.

[7] R. A. Wuana, F. E. Okieimen, Heavy metals in contaminated soils: A review of sources, chemistry, risks and best available strategies for remediation, *ISRN Ecol.* 2011 (2011) 1.

[8] A. Adhikari, P. Biswas, S. Mondal, M. Das, S. Darbar, A. M. Hameed, A. Alharbi, S. A. Ahmed, S. Sankar Bhattacharya, D. Pal, S. Kumar Pal, A smart nanotherapeutic agent for *in vitro* and *in vivo* reversal of heavy-metal-induced causality: Key information from optical spectroscopy, *ChemMedChem* 15 (2020) 420.

[9] Centers for disease control and prevention (CDC), deaths associated with hypocalcemia from chelation therapy--Texas, Pennsylvania, and Oregon, 2003-2005, *Morb. Mortal. Wkly. Rep.* 55 (2006) 204.

[10] F. Zahir, S. J. Rizwi, S. K. Haq, R. H. Khan, Low dose mercury toxicity and human health, *Environ. Toxicol. Pharmacol.* 20 (2005) 351.

[11] E. Friedheim, J. Graziano, D. Popovac, D. Dragovic, B. Kaul, Treatment of lead poisoning by 2, 3-dimercaptosuccinic acid, *Lancet* 312 (1978) 1234.

[12] H. V. Aposhian, D. C. Bruce, W. Alter, R. C. Dart, K. M. Hurlbut, M. M. Aposhian, Urinary mercury after administration of 2, 3-dimercaptopropane-1-sulfonic acid: Correlation with dental amalgam score, *FASEB J.* 6 (1992) 2472.

[13] H. V. Aposhian, R. M. Maiorino, D. Gonzalez-Ramirez, M. Zuniga-Charles, Z. Xu, K. M. Hurlbut, P. Junco-Munoz, R. C. Dart, M. M. Aposhian, Mobilization of heavy metals by newer, therapeutically useful chelating agents, *Toxicology* 97 (1995) 23.

[14] G. Liu, M. R. Garrett, P. Men, X. Zhu, G. Perry, M. A. Smith, Nanoparticle and other metal chelation therapeutics in alzheimer disease, *Biochim. Biophys. Acta* 1741 (2005) 246.

[15] S. A. Ahmed, M. N. Hasan, D. Bagchi, H. M. Altass, M. Morad, R. S. Jassas, A. M. Hameed, J. Patwari, H. Alessa, A. Alharbi, S. K. Pal, Combating essential metal toxicity: Key information from optical spectroscopy, *ACS Omega* 5 (2020) 15666.

[16] S. S. Pasha, L. Fageria, C. Climent, N. P. Rath, P. Alemany, R. Chowdhury, A. Roy, I. R. Laskar, Evaluation of novel platinum(II) based AIE compound-encapsulated mesoporous silica nanoparticles for cancer theranostic application, *Dalton Trans.* 47 (2018) 4613.

[17] J. E. Hutchison, Greener nanoscience: A proactive approach to advancing applications and reducing implications of nanotechnology, *ACS Nano* 2 (2008) 395.

[18] Y. Wang, F. Yang, X. Yang, Colorimetric detection of mercury(II) ion using unmodified silver nanoparticles and mercury-specific oligonucleotides, *ACS Appl. Mater. Interfaces* 2 (2010) 339.

[19] C.-Y. Lin, C.-J. Yu, Y.-H. Lin, W.-L. Tseng, Colorimetric sensing of silver(I) and mercury(II) ions based on an assembly of tween 20-stabilized gold nanoparticles, *Anal. Chem.* 82 (2010) 6830.

[20] X. Xue, F. Wang, X. Liu, One-step, room temperature, colorimetric detection of mercury (Hg^{2+}) using DNA/nanoparticle conjugates, *J. Am. Chem. Soc.* 130 (2008) 3244.

[21] F. Li, J. Wang, Y. Lai, C. Wu, S. Sun, Y. He, H. Ma, Ultrasensitive and selective detection of copper(II) and mercury(II) ions by dye-coded silver nanoparticle-based SERS probes, *Biosens. Bioelectron.* 39 (2013) 82.

[22] D. H. Nies, Microbial heavy-metal resistance, *Appl. Microbiol. Biotechnol.* 51 (1999) 730.

[23] G. A. Engwa, P. U. Ferdinand, F. N. Nwalo, M. N. Unachukwu, Mechanism and health effects of heavy metal toxicity in umans in poisoning in the modern world-new tricks for an old Dog?, *IntechOpen*, Vienna, 2019.

[24] V. Lobo, A. Patil, A. Phatak, N. Chandra, Free radicals, antioxidants and functional foods: Impact on human health, *Pharmacogn. Rev.* 4 (2010) 118.

[25] G. Bhasin, H. Kauser, M. Athar, Iron augments stage-I and stage-II tumor promotion in murine skin, *Cancer Lett.* 183 (2002) 113.

[26] D. Bagchi, S. Chaudhuri, S. Sardar, S. Choudhury, N. Polley, P. Lemmens, S. K. Pal, Modulation of stability and functionality of a phyto-antioxidant by weakly interacting metal ions: Curcumin in aqueous solution, *RSC Adv.* 5 (2015) 102516.

[27] N. Bicer, E. Yildiz, A. A. Yegani, F. Aksu, Synthesis of curcumin complexes with iron(III) and manganese(II), and effects of curcumin–iron(III) on alzheimer's disease, *New J. Chem.* 42 (2018) 8098.

[28] M. I. Khalil, A. M. Al-Zahem, M. H. Al-Qunaibit, Synthesis, characterization, Mössbauer parameters, and antitumor activity of Fe(III) curcumin complex, *Bioinorg. Chem. Appl.* 2013 (2013).

[29] A. Bera, D. Bagchi, S. K. Pal, Improvement of hotostability and NIR activity of cyanine dye through nanohybrid formation: Key information from ultrafast dynamical studies, *J. Phys. Chem. A* 123 (2019) 7550.

[30] A. Giri, N. Goswami, C. Sasmal, N. Polley, D. Majumdar, S. Sarkar, S. N. Bandyopadhyay, A. Singha, S. K. Pal, Unprecedented catalytic activity of Mn_3O_4 nanoparticles: Potential lead of a sustainable therapeutic agent for hyperbilirubinemia, *RSC Adv.* 4 (2014) 5075.

[31] J. Patwari, A. Chatterjee, S. Sardar, P. Lemmens, S. K. Pal, Ultrafast dynamics in co-sensitized photocatalysts under visible and NIR light irradiation, *Phys. Chem. Chem. Phys.* 20 (2018) 10418.

[32] S. Chaudhuri, S. Batabyal, N. Polley, S. K. Pal, Vitamin B2 in nanoscopic environments under visible light: Photosensitized antioxidant or phototoxic drug?, *J. Phys. Chem. Lett.* 118 (2014) 3934.

[33] S. Chaudhuri, S. Sardar, D. Bagchi, S. S. Singha, P. Lemmens, S. K. Pal, Sensitization of an endogenous photosensitizer: Electronic spectroscopy of riboflavin in the proximity of semiconductor, insulator, and metal nanoparticles, *J. Phys. Chem. A* 119 (2015) 4162.

[34] X.-Z. Zhao, T. Jiang, L. Wang, H. Yang, S. Zhang, P. Zhou, Interaction of curcumin with Zn(II) and Cu(II) ions based on experiment and theoretical calculation, *J. Mol. Struct.* 984 (2010) 316.

[35] R. Adhikary, P. Mukherjee, T. W. Kee, J. W. Petrich, Excited-state intramolecular hydrogen atom transfer and solvation dynamics of the medicinal pigment curcumin, *J. Phys. Chem. B* 113 (2009) 5255.

[36] T. K. Maji, M. N. Hasan, S. Ghosh, D. Wulferding, C. Bhattacharya, P. Lemmens, D. Karmakar, S. Kumar Pal, Development of a magnetic nanohybrid for multifunctional application: From immobile photocatalysis to efficient photoelectrochemical water splitting: A combined experimental and computational study, *J. Photochem. Photobiol. A* 397 (2020) 112575.

[37] M. A. Addicoat, G. F. Metha, T. W. Kee, Density functional theory investigation of Cu(I)-and Cu(II)-curcumin complexes, *J. Comput. Chem.* 32 (2011) 429.

List of Publications

A. In Peer Reviewed International Journal

1. **M. N. Hasan**, T. K. Maji, U. Pal, A. Bera, D. Bagchi, A. Halder, S. A. Ahmed, J. H. Al-Fahemi, T. M. Bawazeer, T. Saha-Dasgupta, and S. K. Pal
"Wide bandgap semiconductor based novel nanohybrid for potential antibacterial activity: Ultrafast Spectroscopy and Computational Studies"
RSC Advances 10 (2020) 38890.

2. **M. N. Hasan**, A. Bera, T. K. Maji, D. Mukherjee, N. Pan, D. Karmakar and S. K. Pal
"Functionalized Nano-MOF for NIR Induced Bacterial Remediation: A Combined Spectroscopic and Computational Study"
Inorganica Chimica Acta 532 (2022) 120733.

3. **M. N. Hasan**, F. Sorgenfrei, N. Pan, D. Phuyal, M. Abdel-Hafiez, S. K. Pal, A. Delin, P. Thunstrom, D. D. Sarma, O. Eriksson and D. Karmakar
"Re-dichalcogenides: Resolving Conflicts of their Structure-property Relationship"
Advanced Physics Research 1 (2022) 2200010.

4. S. A. Ahmed[#], **M. N. Hasan**[#], H. M. Altass, A. Bera, R. I. Alsantali, N. Pan, A. Y. A. Alzahrani, D. Bagchi, J. H. Al-Fahemi, A. S. Khder and S. K. Pal
"Tetracycline Encapsulated in Au Nanoparticle-decorated ZnO Nanohybrids for Enhanced Antibacterial Activity"
ACS Applied Nano Materials 5 (2022) 4484–4492.
([#] Authors made equal contribution).

5. **M. N. Hasan**, A. Bera, T. K. Maji and S. K. Pal
"Sensitization of nontoxic MOF for their potential drug delivery application against microbial infection"
Inoganica Chimica Acta 523 (2021) 120381.

6. S. A. Ahmed, **M. N. Hasan**, D.Bagchi, H. A. Altass, M. Morad, R. S. Jassas, A. M. Hameed, J. Patwari, H. Alessa, A. Alharbi, Ahmed and S. K. Pal "Combating Essential Metal Toxicity: Key Information from Optical Spectroscopy"
ACS Omega 5 (2020) 15666.

7. S. A. Ahmed, **M. N. Hasan**, D. Bagchi, H. M. Altass, M. Morad, I. I. Althagafi, A. M. Hameed, A. Sayqal, A. S. Khder, B. H. Asghar, H. A. Katouah, and S. K. Pal
"Nano MOFs as targeted drug delivery agents to combat antibiotic resistant bacterial infections"
Royal Society Open Science 7 (2020) 200959.

8. S. A. Ahmed, D. Bagchi, H. A. Katouah, **M. N. Hasan**, H. M. Altass and S. K. Pal
"Enhanced Water Stability and Photoresponsivity in Metal-Organic Framework (MOF): A Potential Tool to Combat Drug-resistant Bacteria"
Scientific Reports – Nature 9 (2019) 19372.

9. * T. K. Maji, **M. N. Hasan**, S. Ghosh, D. Wulferding, C. Bhattacharya, P. Lemmens, D. Karmakar and S. K. Pal
"Development of a Magnetic Nanohybrid for Multifunctional Application: From Immobile Photocatalysis to Efficient Photoelectrochemical Water Splitting: A Combined Experimental and Computational Study"
Journal of Photochemistry and Photobiology A: Chemistry 397 (2020) 112575.

10. * A. Banerjee, S. Singh, R. Ghosh, **M. N. Hasan**, A. Bera, L. Roy, N. Bhattacharya, A. Halder, A. Chattopadhyay, S. Mukhopadhyay, A. Das, H. M. Altass, Z. Moussa, S. A. Ahmed and S. K. Pal
"A portable spectroscopic instrument for multiplexed monitoring of acute 2 water toxicity: Design, testing and evaluation"
Review of Scientific Instruments 93 (2022) 115105.

11. * A. Bera, **M. N. Hasan**, A. Chatterjee, D. Mukherjee and S. K. Pal
"Dual-Sensitization via Electron and Energy Harvesting in a Nanohybrid for Improvement of Therapeutic Efficacy"
ACS Physical Chemistry Au 2 (2022) 171–178.

12. * N. Pan, L. Roy, **M. N. Hasan**, A. Banerjee, R. Ghosh, M. A. Alsharif, B. A. Asghar, R. J. Obaid, A. Chattopadhyay, R. Das, S. A. Ahmed and S. K. Pal
"Unraveling an Ultrafast Electron Transport Mechanism in a Photocatalytic 'Micromachine' for their Potential Light Harvesting Applications"
Micromachines 14 (2023) 980.

13. * A. Bera, **M. N. Hasan**, N. Pan, R. Ghosh, R. Alsantali, H. M. Altass, R J. Obaid, S. A. Ahmed and S. K. Pal
"Implementation of surface functionalization of MnS nanoparticle for achieving of novel optical properties and Improving Therapeutic Potential"
RSC Advances 12 (2022) 20728 - 20734.

14. * D. Mukherjee, G. Chakraborty, **M. N. Hasan**, U. Pal, P. Singh, T. Rakshit, R. I. Alsantali, T. Saha-dasgupta, S. A. Ahmed, R. Das and S. K. Pal
"Reversible photoswitching of spiropyran in biomolecular interfaces: A combined spectroscopy and computational study
Journal of Photochemistry and Photobiology A: Chemistry (2022) 113958.

15. * N. Pan, S. Ghosh, **M. N. Hasan**, S. A. Ahmed, A. Chatterjee, J. Patwari, C. Bhattacharya, J. Qurban, A. Khder, and S. K. Pal
"Plasmon-Coupled Donor-Acceptor type Organic Sensitizer based Photoanodes for Enhanced Photovoltaic Activity: Key information from Ultrafast Dynamical Study"
ACS Energy & Fuels 36 (2022) 9272–9281.

16. * A. Bera, **M. N. Hasan**, U. Pal, D. Bagchi, T. K. Maji, T. Saha-Dasgupta, R. Das and S. K. Pal
"Fabrication of nanohybrids toward improving therapeutic potential of a NIR photo-sensitizer: An optical spectroscopic and computational study"
Journal of Photochemistry and Photobiology A: Chemistry 424 (2022) 113610.

17. * R. Ghosh, D. Mukherjee, G. Ghosh, **M. N. Hasan**, A. Chattopadhyay, R. Das and S. K. Pal
"Mimicking Cellular Fusion in A Microfluidic Channel Via Time-Resolved Chemiluminescence"

Journal of Photochemistry and Photobiology A: Chemistry 441 (2023) 114731.

18. * D. Mukherjee, **M. N. Hasan**, R. Ghosh, G. Ghosh, A. Bera, E. S. Prasad, A. Hiwale, P. Vemula, R. Das and S. K. Pal
"Decoding the Kinetic Pathways Towards Lipid/DNA Complex of Alkyl-alcohol Cationic lipids formed in a Microfluidic Channel"
The Journal of Physical Chemistry B 126 (2022) 588–600.

19. * S. Singh, A. Halder, A. Banerjee, **M. N. Hasan**, A. Bera, O. Sinha, S.K. Ghosh, A. Mitra, S. K. Pal
"An Optical Scattering Based Cost-Effective Approach Towards Quantitative Assessment of Turbidity and Particle Size Estimation In Drinking Water Using Image Analysis"
Journal of Environmental Science and Engineering 62 (2020) 891-899.

20. * D. Mukherjee, D. Paul, S. Sarker, **M. N. Hasan**, R. Ghosh, S. Prasad, P. Vemula, R. Das, A. Adhikary, S. K. Pal and T. Rakshit
"Polyethylene Glycol-Mediated Fusion of Extracellular Vesicles with Cationic Liposomes for the Design of Hybrid Delivery Systems"
ACS Applied Bio Materials 4 (2021) 8259–8266.

21. * A. Banerjee, D. Mukherjee, **M. N. Hasan**, S. Mukhopadhyay, D. Karmakar, R. Das, A. Chattopadhyay and S. K. Pal
"Interaction of Chlorophyll with Artificial Colorants: Key Insights on the Toxicity from Electronic Spectroscopy" *Nanoscience and Nanotechnology: Open Access* (2023).

B. Conference Proceeding/Symposium

1. **M. N. Hasan**, F. Sorgenfrei, N. Pan, S. K. Pal, A. Delin, P. Thunstrom, D. D. Sarma, O. Eriksson and D. Karmakar
"Controversies and contradictions in Rhenium Dichalcogenides: First-principles pathway towards solutions"
Psi-k Conference, **EPFL, Lausanne, Switzerland** (2022) C5.15.

2. **M. N. Hasan**, F. Sorgenfrei, N. Pan, S. K. Pal, A. Delin, P. Thunstrom, D. D. Sarma, O. Eriksson, D. Karmakar
"Resolving Conflicts in Rhenium Dichalcogenides (ReS_2 and $ReSe_2$)",
Bulletin of the American Physical Society, **Las Vegas, USA.** (2023)

3. **M. N. Hasan**, Q. Xu, A. Delin, A. Bergmann, S. K. Pal, P. M. Oppeneer, M. Pereiro, O. Eriksson and D. Karmakar
"Magnetism in Kagome Superconductors"
***Psi-k Conference,* EPFL, Lausanne, Switzerland** (2022) C3.23.

4. N. Pan, **M. N. Hasan**, M. Pereiro, S. K. Pal, A. Delin, O. Eriksson, D. Karmakar
"New series of magnetic hydroxide semiconductor"
***Psi-k Conference,* EPFL, Lausanne, Switzerland** (2022) C3.35

5. N. Pan, **M. N. Hasan**, M. Pereiro, P. Thunstrom, S. K. Pal, A. Delin, O. Eriksson and D. Karmakar
"Hydroxide Semiconductors: New Series of van der Waals Magnets"
***Bulletin of the American Physical Society*, Las Vegas, USA** (2023)

C. Manuscript Communicated

1. * **M. N. Hasan**, R. Bharati, J. Hellsvik, A. Delin, S. K. Pal, A. Bergman, S. Sharma, I. D. Marco, M. Pereiro, P. Thunström, P. M. Oppeneer, O. Eriksson and D. Karmakar
"Magnetism in AV_3Sb_5 (Cs, Rb and K) - I: Origin and Consequences for the Strongly Correlated Phases" (In peer review).

2. * **M. N. Hasan**, F. Sorgenfrei, N. Pan, D. Phuyal, M. Abdel-Hafiez, S. K. Pal, A. Delin, P. Thunstrom, D. D. Sarma, O. Eriksson and D. Karmakar
"Metallic Transition in Rhenium Dichalcogenides (ReS_2 and $ReSe_2$) at High Pressure:" (Communicated).

3. * **M. N. Hasan**, R. Bharati, J. Hellsvik, A. Delin, S. K. Pal, A. Bergman, S. Sharma, I. D. Marco, M. Pereiro, P. Thunström, P. M. Oppeneer, O. Eriksson and D. Karmakar
"Kagome Superconductor: AV_3Sb_5 (Cs, Rb and K)" (Communicated).

4. * D. Karmakar, M. Pereiro, **M. N. Hasan**, R. Bharati, J. Hellsvik, A. Delin, S. K. Pal, A. Bergman, S. Sharma, I. D. Marco, P. Thunström, P. M. Oppeneer and O. Eriksson
"Magnetism in AV_3Sb_5 (Cs, Rb and K) – II: Complex Texture of the Dynamical Magnetic Properties" (Communicated).

* Not included in the thesis

List of National/International Conference/Workshop

1. Contributed in an oral presentation on "Resolving Conflicts in Rhenium Dichalcogenides (ReS_2 and $ReSe_2$)" in the APS March Meeting 2023, March 5–10, 2023 (in person) and March 20–22, 2023 (Virtual) at Las Vegas, Nevada, USA.

2. Oral presentation delivered on "Rhenium Dichalcogenides: Resolving Conflicts of Their Structure-Property Relationship" in an international conference "Divergent Quantum Materials, Methods and Applications (DQMMA2023)", from 2nd – 4th February 2023, Nanu Beach Resort, Goa 403713, India.

3. Contributed in oral presentation on "Resolving disputes in Rhenium Dichalcogenides: A First-principles Study" and participated in workshop in an international conference 'Evolution of Electronic Structure Theory & Experimental Realization (EESTER-2023)' during 4th – 12th January 2023 of August 2022 in IIT Madras & SRM IST KTR, Chennai, India.

4. Oral presentation delivered on "Metallic Transition in Rhenium Dichalcogenides" in an international conference "EHPRG 2022", from 5th to 8th of September 2022, Uppsala University, Uppsala, Sweden.

5. Contributed in oral presentation on "Controversies and contradictions in Rhenium Dichalcogenides: First-principles pathway towards solutions" and presented two posters in an international conference 'Psi-k 2022" from 22nd to 25th of August 2022 in SwissTech Convention Center, EPFL, Lausanne, Switzerland.

6. Poster presentation delivered in an international Conference on "Frontiers In Materials for Technological Applications (FIMTA-2021)" (Virtual) from 4th – 6th August 2021 at CSIR-IMMT, Bhubaneswar, India. ***(Best Poster Award)***

7. Participated in an international conference on "Advanced Materials for Better Tomorrow (AMBT 2021)" (Virtual) from 13th -17th July 2021 held at Indian Institute of Technology, BHU, Varanasi, India.

8. Poster presentation delivered in an International Conference on Nano Science and Nano Technology (ICONSAT 2020) from 5th – 7th March 2020 held at SN Bose National Centre for Basic Sciences, Kolkata, India.

9. Poster presentation delivered in an international Conference On "Smart Materials For Sustainable Technology (SMST 2020)" from 22nd – 25th February 2020 held at Bagmallo Beach Resort, Goa, India.

10. Oral Presentation delivered in an International workshop on Physics of Semiconductor Devices (IWPSD 2019) during 17th – 20th December 2019 held at Novotel Hotel and Residences, Kolkata, India.

11. Poster presentation delivered in an International Science Festival-2019, Young Scientist' Conference, during 5th – 7th November 2019 held at Biswa Bangla Convention Centre, New Town, Kolkata 700156, India.

12. Participated in a workshop on "Nanolithography and Nanofabrication" organized by RAITH INDIA, Bangalore in cooperation with S. N. Bose National Centre for Basic Sciences, held on 9th July 2019 at Kolkata, India.